UNIVERSITÀ DEGLI STUDI DI ROMA "TOR VERGATA"

FACOLTA' DI INGEGNERIA

DOTTORATO DI RICERCA IN

INGEGNERIA DELL'ENERGIA - AMBIENTE

CICLO DEL CORSO DI DOTTORATO

Titolo della tesi

Simulazione numerica di sistemi di celle a combustibili ad ossidi solidi

Nome e Cognome del dottorando

DANIELE COLOCCINI

A.A. 2009/2010

Docente Guida/Tutor: Prof. V. Rocco

Coordinatore: Prof. F. Gori

- Contents

Introduction……3

1 Solid Oxide Fuel Cell……4
- 1.1 Introduction……4
- 1.2 Fuel Cell Stacking……6
- 1.3 Auxiliary components……7
- 1.4 Fuel Cell Types……8

2 **3D SOFC Model**……10
- 2.1 Introduction……10
- 2.2 Fuel Cell Description……10
- 2.3 Experimental Setup……12
- 2.4 Numerical Model……14
- 2.5 Model validation and results……25
- 2.6 Using Syngas as Fuel……34
- 2.7 Model validation and results……49

3 **SOFC System**……67
- 3.1 Introduction……67
- 3.2 Description of the system……70
- 3.3 Plant configuration feed with methane (CASE A)……81
- 3.4 Plant configuration feed with anode recirculation (CASE B)……94
- 3.5 SOFC system feed by biogas……107

4 **Stack of SOFC**……119
- 4.1 Introduction……119
- 4.2 General aspect……120
- 4.3 Thermal consideration……121
- 4.4 Assembling criteria……132
- 4.5 Contact issues……144
- 4.6 Conclusion……155

5 **After burner integration**……157
- 5.1 Geometry of the model……157
- 5.2 Chemical model……159
- 5.3 Model Description……163
- 5.4 Results Analysis……173
- Appendix: Arrhenius law coefficient calculation……173

6 **Conclusions**……174

Introduction;

With the rising concern about greenhouse gas emissions, many countries are pursuing efforts to develop more sustainable energy systems to replace conventional combustion heat engines. Solid oxide fuel cell (SOFC) power generation shows great promise to serve as an alternative in the near future. Since SOFC operation relies on electrochemical reactions, its electrical efficiency is not limited by temperature as in the case of conventional heat engines. Therefore, the electrical efficiency obtained from a SOFC is typically greater and more stable than that obtained from conventional heat engines. Furthermore, additional efficiency can be gained by incorporating a steam/gas turbine cycle to recover heat from the hot gas exhausted from SOFCs because they operate at high temperatures between 800 and 1000°C. Fuel flexibility with SOFCs also presents advantages over other types of fuel cells such as polymer electrolyte membrane fuel cells (PEMFCs). In fact, the carbon monoxide present in the fuel gas is not harmful to SOFCs, and it can also act as a fuel. Therefore, a variety of hydrocarbon-based fuels or their syngas derivatives, such as natural gas, biomass and coal, can efficiently be used in SOFCs. Biomass and coal are gasified to form syngas, essentially containing a mixture of H_2, CO, CO_2, H_2O, N_2 and eventually H_2S. This syngas can then be used as a fuel in SOFC. However, H_2S must be scrubbed before the syngas is fed to the SOFC to prevent rapid degradation of the SOFC performance. Depending on the type of coal and biomass, the composition of syngas strongly varies so affecting the SOFC performance. Moreover, carbon formation is a problem that can limit SOFC performance when fed with syngas. This is due to the Boudouard reaction which converts CO to carbon on the anode surface. Therefore, properly operating strategies to limit carbon formation have to be considered.

In this work a mathematical model of hydrogen and syngas fed solid oxide fuel cells (SOFC) under stationary regime is presented. It is well known that diffusion, ohmic and activation overpotentials affect the fuel cell ideal efficiency, during cell operation. Hence, the aim of this thesis is to provide, for a given set of data describing the geometry of the cell and the operating conditions, an estimate of the losses and where they occur. Moreover, it is possible to develop a sensitivity analysis, allowing the definition of the influence on the cell performance of the most affecting parameters. Accordingly, the numerical tool can be considered as a design tool.

Several 2D and 3D numerical simulation of SOFCs have already been described, based on mathematical models under different simplifying assumption. In these works, as in the present work, the temperature distribution, concentration of the species and electrical current are obtained in the unit cell itself.. The originality of the present work is that it allows the evaluation of the local distribution of temperature, electric potential and concentration on a three dimensional computational domain, representing an anode-supported solid oxide fuel cell. The overall SOFC model consists of three sub-models:

- the fluid dynamic sub-model;
- the electrochemical sub-model;
- the thermal sub-model;

and the solution technique of both the electrochemical sub-model and the overall model is innovative, using a finite element discretization scheme to do it.

1. Solid Oxide Fuel Cell

1.1. Introduction

Fuel cells are electrochemical devices that directly convert chemical energy stored in fuels into electrical energy. Power generation is theoretically produced with high efficiency and low environmental impact. Fuel cells are not limited by thermodynamic limitations of heat engines such as the Carnot efficiency. Moreover, as combustion is avoided, fuel cells produce power with very low pollutant emission. However, unlike batteries the reductant and oxidant in fuel cells must be continuously replenished to allow continuous operation. Fuel cells bear significant resemblance to electrolysers. In fact, some fuel cells operate in reverse as electrolysers, yielding a reversible fuel cell that can be used for energy storage.

Fuel cells could, in principle, operate with a wide variety of fuels and oxidants. Of particular interest are the fuel cells that use common fuels (or their derivatives) or hydrogen as reductants, and air the oxidants.

Fuel cell power systems are usually constituted by:

- Unit cells, in which the electrochemical reactions take place;
- Stacks, in which individual cells are modularly combined by electrically connections to form units with the desired output capacity;
- Auxiliary components as, for example, reformer, air compressor, etc…

1.1.1. Unit cells

Unit cell is the core of a fuel cell. These devices convert the chemical energy electrochemically stored in a fuel into electrical energy. The basic physical structure of a fuel cell consists of an electrolyte layer in contact with an anode and a cathode on either side (PEN). A schematic representation of a unit cell with the reactant/product gases and the ion conduction flow directions through the cell is shown in Figure 1-1.

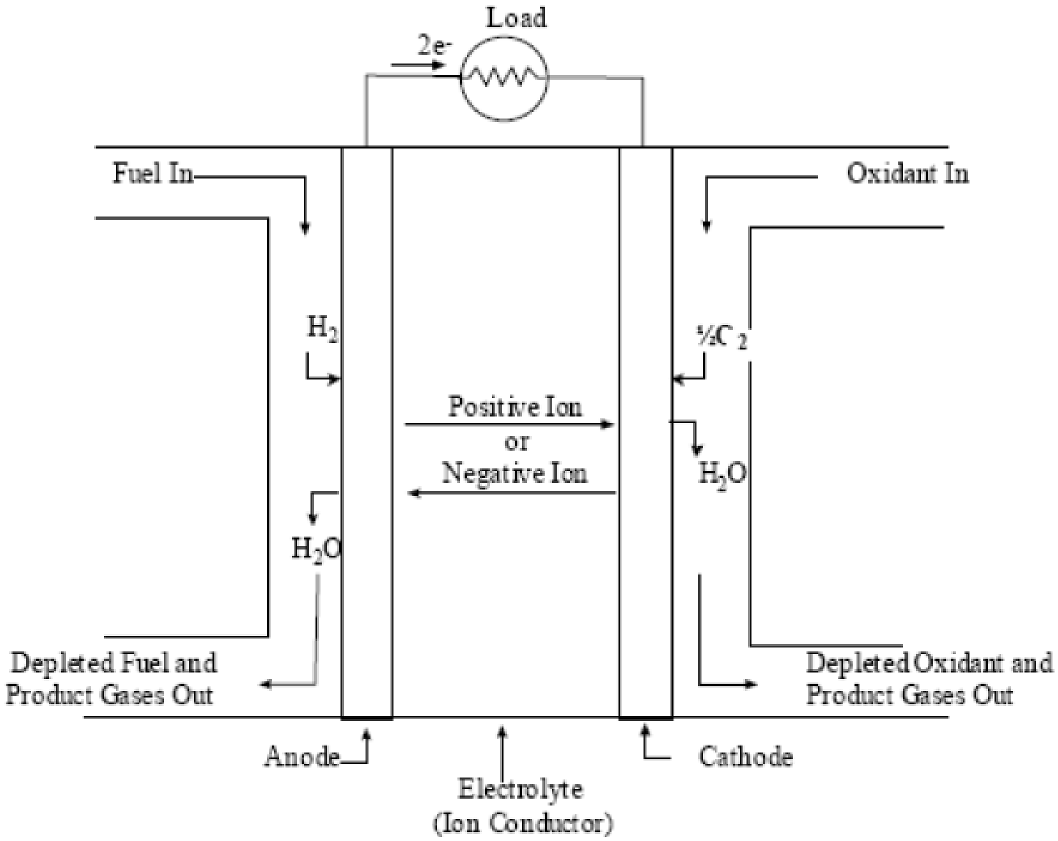

Figure 1-1 Schematic of an individual fuel cell

In a typical fuel cell, fuel is fed continuously to the anode and an oxidant is fed continuously to the cathode. The electrochemical reactions take place at the electrodes to produce electric current through the electrolyte. Although a fuel cell is similar to a typical battery for many aspect, it is very different. The battery is an energy storage device in which all the energy available is stored within the battery itself (at least the reductant). The battery stops to produce electrical energy when the chemical reactants are consumed (i.e., discharged). A fuel cell, on the other hand, is an energy conversion device to which fuel and oxidant are supplied continuously. In principle, the fuel cell produces power as long as fuel is supplied.

Fuel cells are classified according to the choice of electrolyte and fuel, which in turn determines the electrode reactions and the type of ions that carry the current across the electrolyte. Appleby and Foulkes [1] observe that, in theory, any substance which can be chemically oxidised and that can be continuously supplied can also be galvanically burned as fuel at the anode of a fuel cell. Similarly, oxidant can be any fluid that can be reduced at a sufficient rate. Though the direct use of conventional fuels in fuel cells would be desirable, most of the fuel cells today under development use gaseous hydrogen, or a synthesis gas rich in hydrogen, as a fuel. Hydrogen has a high reactivity for anode reactions, and can be produced chemically from a wide range of fossil and renewable fuels, as well as via electrolysis. The most common oxidant is gaseous oxygen, available from air.

The most critical part of the fuel cell is the three phase interface (TPB) where reactions occur. This area must be exposed to the reactant, be in electrical contact with the electrode, be in ionic contact with the electrolyte, and contain sufficient electro-catalyst for the reaction to proceed at the desired rate. The density of these regions and the nature of these interfaces play a critical role in the electrochemical performance of both liquid and solid electrolyte fuel cells:

- In liquid electrolyte fuel cells, the reactant gases diffuse through a thin electrolyte film that wets portions of the porous electrode and electrochemically reacts on the electrode surface. If the porous electrode contains an excessive amount of electrolyte, the electrode may "flood" reducing the transport of gaseous species in the electrolyte phase to the reaction sites. The consequence is a reduction in electrochemical performance of the porous electrode. Thus, a balance has to be respected among the electrode, electrolyte, and gaseous phases in the porous electrode structure.

- In solid electrolyte fuel cells, the challenge is to engineer a large number of catalyst sites into the interface that are electrically and ionically connected to the electrode and the electrolyte, respectively. In most successful solid electrolyte fuel cells, a high-performance interface requires the use of an electrode characterized by a mixed conductivity (i.e. it conducts both electrons and ions).

Over the past twenty years, the unit cell performance of at least some of the fuel cell technologies has been dramatically improved. These developments resulted from improvements in the three-phase boundary, obtained reducing the thickness of the electrolyte, and developing improved electrode and electrolyte materials which broaden the temperature range over which the cells can be operated.

Moreover, the electrolyte not only transports dissolved reactants to the electrode, but also conducts ionic charge between the electrodes, and thereby completes the cell electric circuit as illustrated in Figure 1-1. It also provides a physical barrier to prevent the fuel and oxidant gas streams from directly mixing. The functions of porous electrodes, other than to providing a surface for electrochemical reactions, are:

- conduct electrons from or into the three-phase interface once they are formed (so an electrode must be made of materials that have good electrical conductance);

- ensure that reactant gases are equally distributed over the cell;

- ensure that reaction products are efficiently led away to the bulk gas phase.

As a consequence, the electrodes are typically made of porous material. At low temperatures, only a few and relatively rare and expensive materials provide sufficient electro-catalytic activity. Accordingly, catalysts are deposited in small quantities at the interface. In high-temperature fuel cells, the electro-catalytic activity of the bulk electrode material is often enough.

Though a wide range of fuel cell geometries has been considered, most fuel cells under development now are either planar (rectangular or circular) or tubular (either single or doubleended and cylindrical or flattened).

1.1.2. Fuel cell stacking

For most practical fuel cell applications, unit cells must be combined in a modular fashion into a cell stack to achieve the voltage and power output level required for the application. Generally, the stacking involves connecting multiple unit cells in series via electrically conductive interconnects. Different stacking arrangements have been developed.

Planar-Bipolar Stacking

The most common fuel cell stack design is the so-called planar-bipolar arrangement (Figure 1-2). Individual unit cells are electrically connected with interconnections. Because of the configuration of a flat plate cell, the interconnection becomes a separator plate with two functions:

- to provide an electrical series connection between adjacent cells, specifically for flat plate cells;

- to provide a gas barrier that separates the fuel and oxidant of adjacent cells.

In many planar-bipolar designs, the interconnection also includes channels that distribute the gas flow over the cells. The planar-bipolar design is electrically simple and leads to short electronic current paths (which helps to minimize cell resistance).

Planar-bipolar stacks can be further characterized according to arrangement of the gas flow:

- Cross-flow. Air and fuel flow perpendicular to each other;

- Co-flow. Air and fuel flow parallel and in the same direction. In the case of circular cells, this means that the gases flow radially outward;

- Counter-flow. Air and fuel flow parallel but in opposite directions. Again, in the case of circular cells this means radial flow.

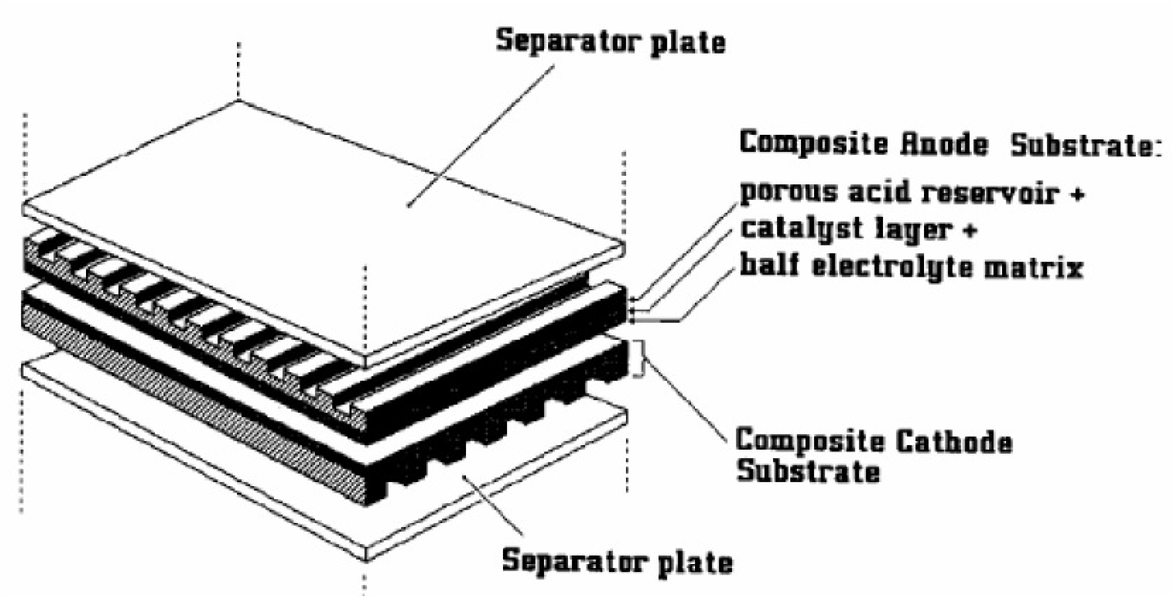

Figure 1-2 Expanded view of a basic fuel cell unit in a fuel cell stack

The choice of gas-flow arrangement depends on the type of fuel cell, the application, and other considerations. Finally, the manifolding of gas streams to the cells in bipolar stacks can be achieved in various ways:

- Internal: the manifolds run through the unit cells.

- Integrated: the manifolds do not penetrate the unit cells but are integrated in the interconnects.

- External: the manifold is completely external to the cell, much like a wind-box.

Stacks with Tubular Cells

Especially for high-temperature fuel cells, stacks with tubular cells have been developed (Figure 1-3). Tubular cells have significant advantages in sealing and in the structural integrity of the cells. However, they represent a special geometric challenge to the stack designer to achieve high power density and short current paths. In one of the earliest tubular designs, the current is tangentially conducted around the tube. Interconnections between the tubes are used to form rectangular arrays of tubes. Alternatively, the current can be conducted along the axis of the tube, in which case interconnection is done at the end of the tubes. To minimize the length of electronic conduction paths for individual cells, sequential series connected cells are being developed. The cell arrays can be connected in series or in parallel.

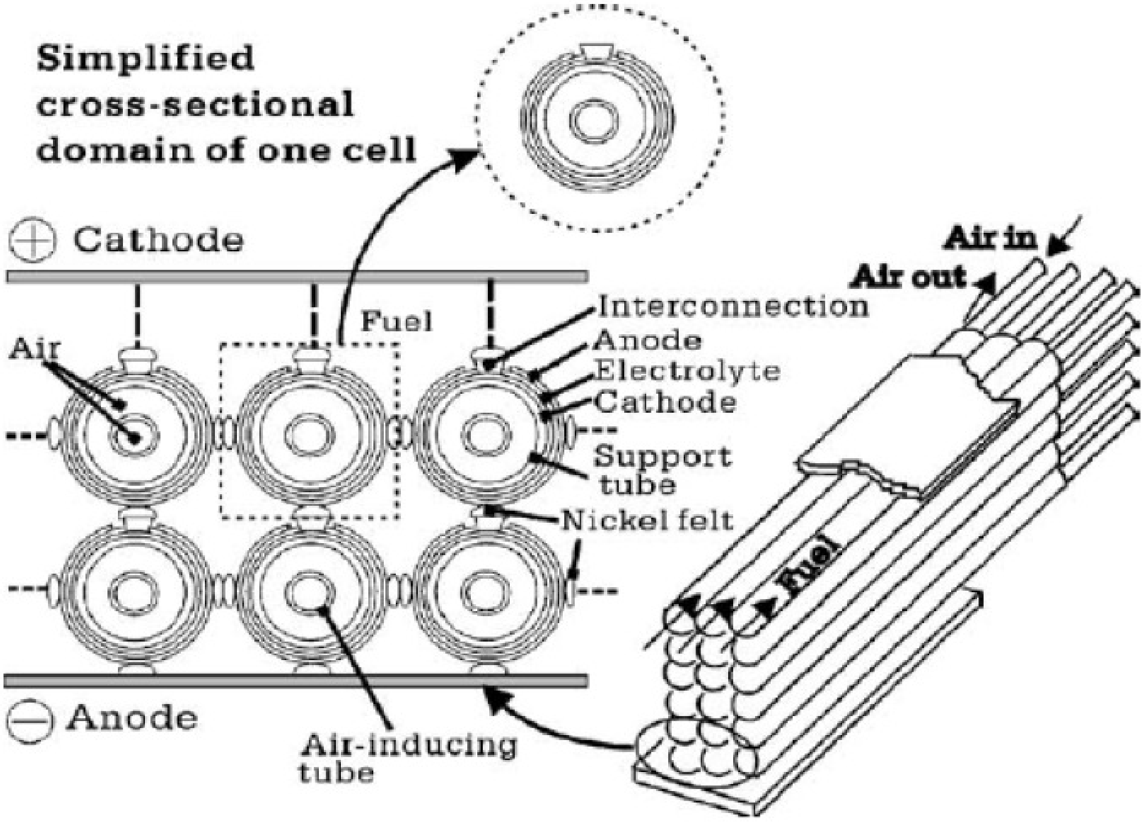

Figure 1-3 Orientation of a tubular SOFC in a cell stack

To avoid the packing density limitations associated with cylindrical cells, some tubular stack designs use flattened tubes.

1.1.3. Auxiliary components

In addition to the stack, practical fuel cell systems require several other sub-systems and components; the so-called balance of plant (BoP). Together with the stack, the BoP forms the fuel cell system. The arrangement of the BoP strongly depends on the fuel cell type, the fuel choice, and the application. In addition, specific operating conditions and requirements of individual cell and stack designs determine the BoP characteristics. Furthermore, other components are:

- Fuel preparation system. Except when pure fuels (such as pure hydrogen) are used, fuel preparation is required, usually involving the removal of impurities and thermal conditioning. In addition, many fuel cells that use fuels other than pure hydrogen require fuel processing, such as reforming, in which the fuel reacts with some oxidant (usually steam or air) to form a hydrogen-rich anode feed mixture.

- Air supply system. In most practical fuel cell systems, this includes air compressors or blowers as well as air filters.

- Thermal management system. All fuel cell systems require careful management of the fuel cell stack temperature.

- Water management system. Water is needed in some parts of the fuel cell, while overall water is a reaction product. A water circuit is often requested.

- Electric power conditioning equipment. Since fuel cell stacks provide a variable DC voltage output that is typically not directly usable for the load, electric power conditioning is typically required.

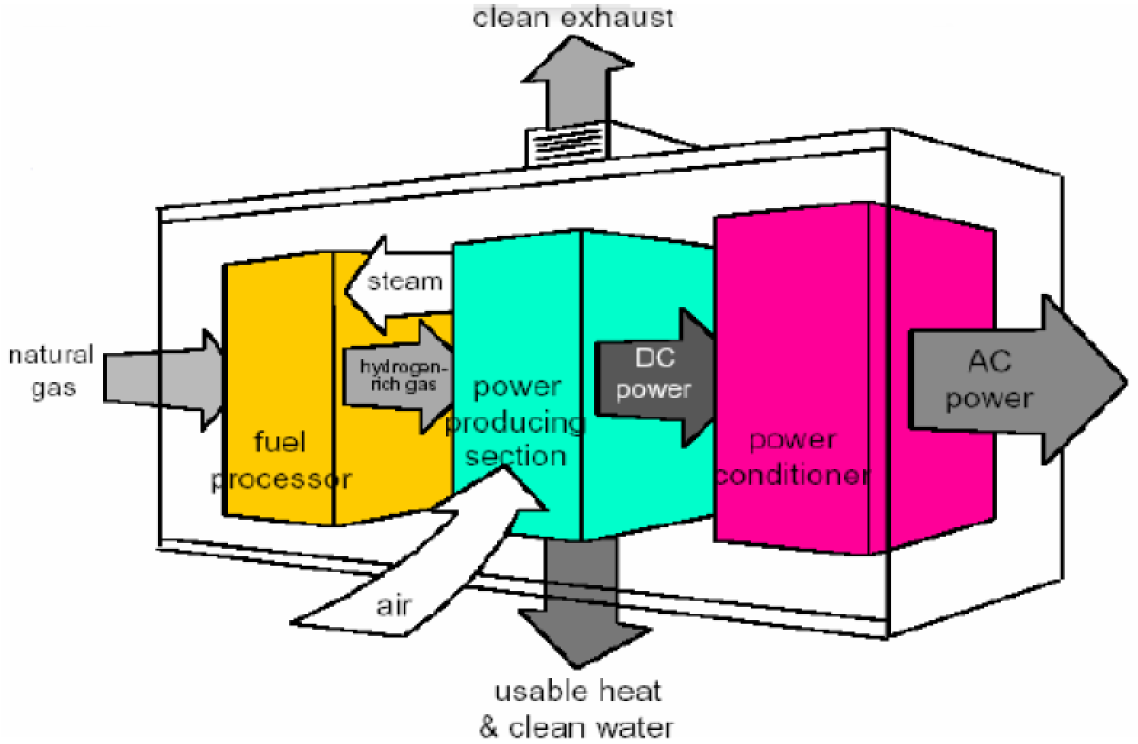

Figure 1-4 Fuel cell power plant major processes

Figure 1-4 shows a scheme of a fuel cell power plant. Beginning with fuel processing, a conventional fuel (natural gas, other gaseous hydrocarbons, methanol, naphtha, or coal) is cleaned, then converted into a gas containing hydrogen. Energy conversion occurs when dc electricity is generated by means of individual fuel cells combined in stacks or bundles. A varying number of cells or stacks can be matched to a particular power application. Finally, power conditioning converts the electric power from dc into regulated dc or ac for consumer use.

1.1.4. Fuel cell types

The most common classification of fuel cells is by the type of electrolyte used in the cells and includes:

- polymer electrolyte fuel cell (PEFC)
- alkaline fuel cell (AFC)
- phosphoric acid fuel cell (PAFC)
- molten carbonate fuel cell (MCFC)
- solid oxide fuel cell (SOFC).

Broadly, the choice of electrolyte dictates the operating temperature range of the fuel cell. The operating temperature and useful life of a fuel cell dictate the physicochemical and thermo mechanical properties of materials used in the cell components (i.e., electrodes, electrolyte, interconnect, current collector, etc.). Aqueous electrolytes are limited to temperatures of about 200°C or lower because of their high vapor pressure and rapid degradation at higher temperatures. The operating temperature also plays an important role in dictating the degree of fuel processing required. In low-temperature fuel cells, all the fuel must be converted to hydrogen prior to entering the fuel cell. In addition, the anode catalyst in low temperature fuel cells (mainly platinum) is strongly poisoned by CO. In high-temperature fuel cells, CO and even CH_4 can be internally converted to hydrogen or even directly oxidized electrochemically.

Table 1-1 provides an overview of the key characteristics of the main fuel cell types.

	PEFC	**AFC**	**PAFC**	**MCFC**	**SOFC**
Electrolyte	Hydrated Polymeric Ion Exchange Membranes	Mobilized or Immobilized Potassium Hydroxide in asbestos matrix	Immobilized Liquid Phosphoric Acid in SiC	Immobilized Liquid Molten Carbonate in LiAlO2	Perovskites (Ceramics)
Electrodes	Carbon	Transition metals	Carbon	Nickel and Nickel Oxide	Perovskite and perovskite / metal cermet
Catalyst	Platinum	Platinum	Platinum	Electrode material	Electrode material
Interconnect	Carbon or metal	Metal	Graphite	Stainless steel or Nickel	Nickel, ceramic, or steel
Operating Temperature	40 – 80 °C	65°C – 220 °C	205 °C	650 °C	600-1000 °C
Charge Carrier	H^+	OH^-	H^+	$CO_3^=$	$O^=$
External Reformer for hydrocarbon fuels	Yes	Yes	Yes	No, for some fuels	No, for some fuels and cell designs
External Shift conversion of CO to hydrogen	Yes, plus purification to remove trace CO	Yes, plus purification to remove CO and CO_2	Yes	No	No
Prime Cell Components	Carbon-based	Carbon-based	Graphite-based	Stainless-based	Ceramic
Product Water Management	Evaporative	Evaporative	Evaporative	Gaseous Product	Gaseous Product
Product Heat Management	Process Gas + Liquid Cooling Medium	Process Gas + Electrolyte Circulation	Process Gas + Liquid cooling medium or steam generation	Internal Reforming + Process Gas	Internal Reforming + Process Gas

- 2. 3D SOFC Model

2.1. Introduction

In the anode supported disk-shape SOFC study, the main objective was to have a better understanding of the phenomena occurring within the cell. For this reason, an extensive analysis of all the physical variables of each domain was performed. For sake of simplicity, the model was implemented in a 2D-simplified domain, and some limitations of such simplification were underlined, thus a 3D simulation was already identified as the next step for a better understanding of the operational-related phenomena.

The main objective of the present work is to improve anode-supported SOFC study, implementing it in a 3D domain, thus obtaining more accurate results, and, in addiction, attaining in-depth understanding of some operational-related phenomena, not analyzable in the 2D domain. In particular, an extensive analysis of the fluid-dynamics within the gas channel, and the related implication for the fuel cell performance are performed.

While in the 2D implementation, reported in [4], there was no prediction of the cell temperature, and an iso-thermal condition was assumed, in the present study, the energy balance within the fuel cell is also considered, and the temperature distribution is deduced.
Furthermore, while in [4], the model was validated by comparison with one polarization curve experimentally obtained, in the present study, the model results are compared with more than one experimental J-V curve.

2.2. Fuel cell description

The fuel cell analyzed in the present study is a disk-shape anode-supported SOFC, currently produced by InDec B.V. As illustrated in Figure 4-1, anode material is a cermet of Ni and YSZ, nickel oxide doped with yttrium stablilized zirconia, 8% yttrium (NiO/8YSZ). Cathode is composed of two layers: one made of 8YSZ with strontium-doped $LaMnO_3$ (8YSZ/LSM) and one of LSM. The electrolyte consists of dense 8YSZ.

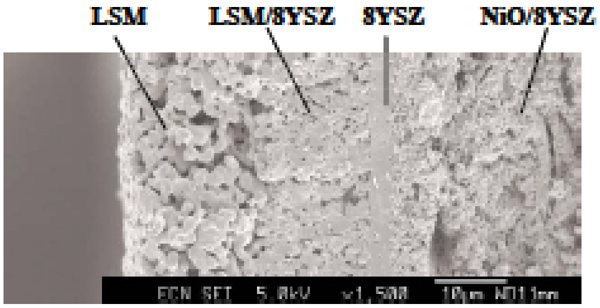

Figure 4-1 Anode, cathode and electrolyte layers of the single cells

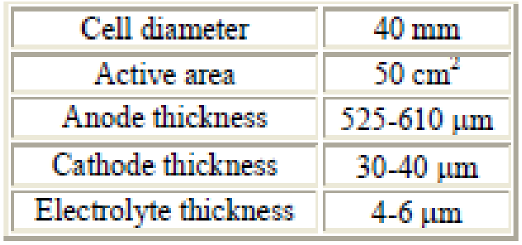

Cell diameter	40 mm
Active area	50 cm^2
Anode thickness	525-610 μm
Cathode thickness	30-40 μm
Electrolyte thickness	4-6 μm

Table 4-1 Main geometrical characteristics of the SOFC single cell

The main geometrical characteristics of the fuel cell are reported in Table 4-1, while a schematic of the whole apparatus is depicted in Figure 4-2.

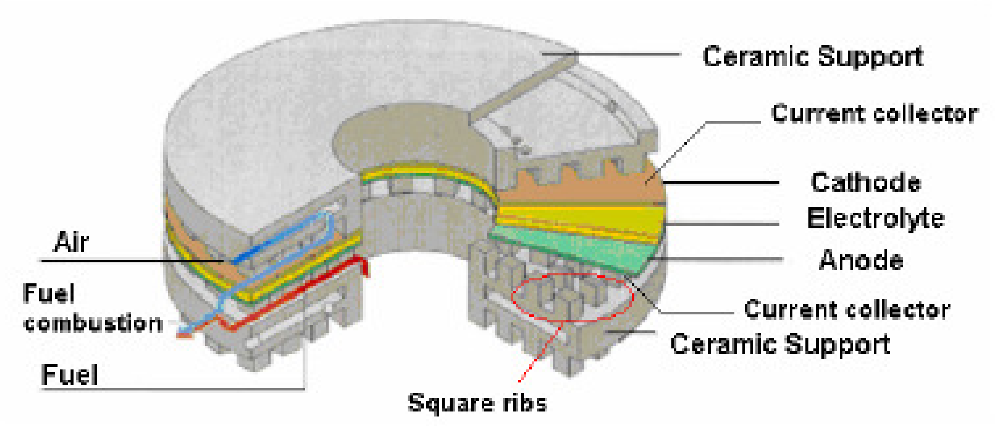

Figure 4-2 Schematic of the whole SOFC apparatus

The single cell is arranged in sealess. Through the use of two alumina tubes perpendicular to the fuel cell plane, not shown in Figure 4-2, anodic and cathodic gases come in contact, respectively, with the anode and cathode in a small circular region, where the flux configuration changes into radial. Then, anodic and cathodic flows merge together at the cell outlet, where, due to the high temperature, combustion of the unoxidized hydrogen is takes place. Although cell cylindrical geometry leads to consider the gas flow as purely radial, this is an idealized condition that does not take place in the cell. The gas channels, in fact, are not realized in a radial configuration, but as a channel grid, as described in details in Section 4.3.

The deviation of the flux from a pure radial configuration, can lead to several consequences on the operational conditions of the fuel cell, thus affecting the resulting performance.

- First of all, if the gas is not well distributed within the cell surface, some parts of the cell are characterized by a higher reaction rate, compared to other surface zones. This implies the existence of preferred zones for the electrochemical reaction, and, consequently, of local high current density, which reduces the overall cell voltage.

- Secondly, a high reaction rate in some parts of the cell causes temperature gradients and, consequently, thermal stresses, which can cause the mechanical failure of the cell itself [5,6,7].

- Finally, the existence of some preferred zones for the electrochemical reaction implies that a part of the fuel cell is not completely exploited.

Such phenomena can be identified and quantified, only if the numerical model is developed in 3D.

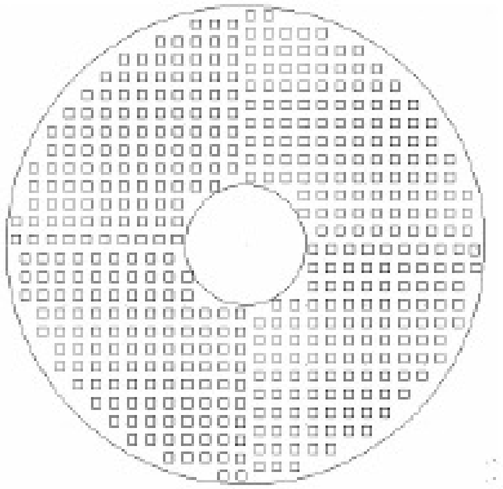

Figure 4-3 Gas channel geometry

Figure 4-4 Details of the cathodic current collector

2.3. Experimental setup

The single cell described in Section 4.2. is embedded in a cell housing made of alumina. The surfaces of the cell housing are in contact with the fuel cell, and act as gas channels, i.e. they guide the gas from the internal part of the disk towards the outlet. Figure 4-3 shows the gas channels details. The geometry of the gas channels, as already mentioned, does not allow the gas to follow a pure radial direction, thus the effect of the preferred reactions zones needs to be quantified. Manufacturing a gas channel with an increasing cross-section would be more complex and more expensive than the present solution, thus it is highly desirable to understand the consequence on the fuel cell performance of the present geometry. The results of such analysis are presented in Section 4.5. As illustrated in Figure 4-4, the current is collected on the electrode surface through a mesh, which is interposed between the electrode surface and the pins delimiting the gas channels. The mesh is made of Platinum at the cathode side and of Ni at the anode side.

Figure 4-5 Single cell test rig set-up

The cell housing is embedded in an electric furnace, which guarantees the desired fuel cell operating temperature. Figure 4-5 depicts the complete test-rig employed at the University of Perugia for testing the single cell. The electric load applied to the single cell is varied through the use of a potentiometer. Anodic and cathodic gas mixtures are obtained from laboratory-quality hydrogen, oxygen and nitrogen stored in gas cylinders outside the laboratory. Before entering the single cell, hydrogen is saturated at room temperature, and then heated-up to 110 °C to avoid water condensation in the gas line. The test rig is also equipped with a peristaltic pump, a water mass flow controller, and an evaporator apparatus for dedicated tests where the water content in the anode needs to be varied. However, for the present study, hydrogen is saturated at room temperature. Mass flow controllers, electrical load, gas and furnace temperature are controlled through an in-house software realized in Visual Basic, and the results are stored in a dedicated file. Experimental results obtained at University of Perugia testing laboratory are shown in Figure 4-6 and 4-7.

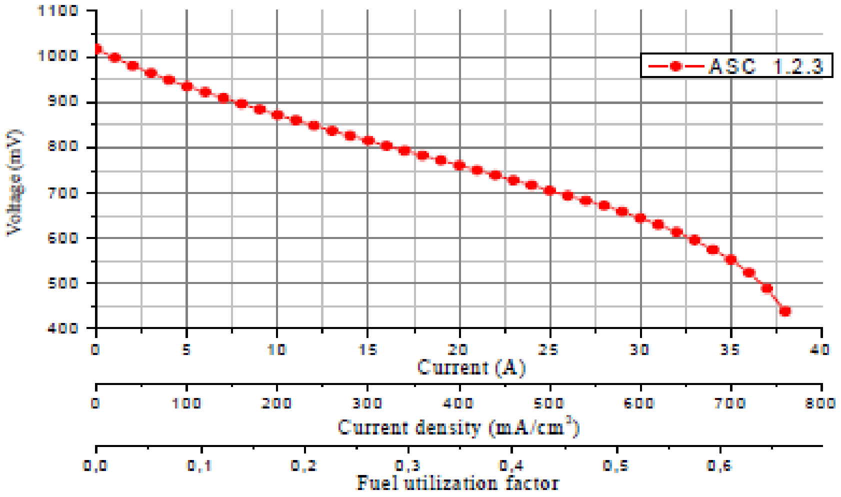

Figure 4-6 Polarization curve

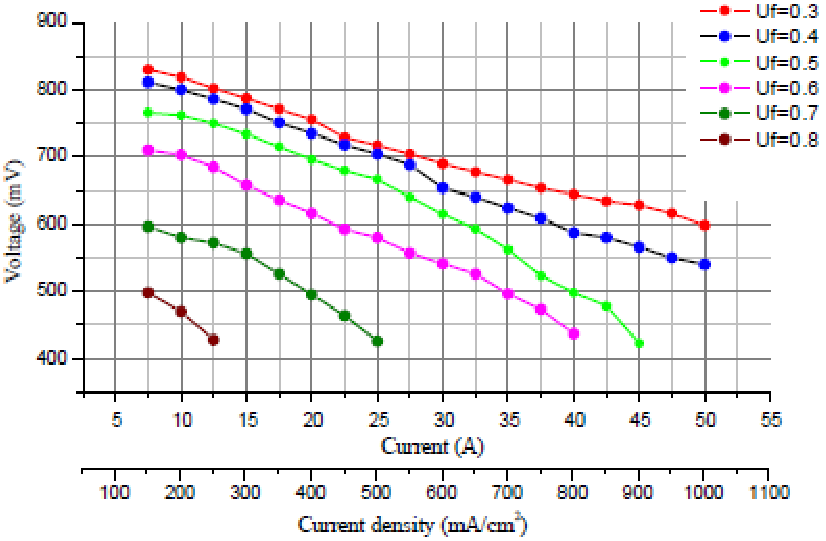

Figure 4-7 Current-voltage curves with constant fuel (U_f) and oxidant (U_{ox}) utilization coefficients

2.4. Numerical model

The single cell described in Section 4.2. is schematically considered to be composed of five domains, namely the flow channels (air and fuel), two porous electrodes (cathode and anode), and the electrolyte. In this work, a detailed numerical model is applied to each sub-domain where the governing equations are directly solved applying appropriate interface conditions.

Hydrogen is considered as the only fuel, thus the following reaction takes place at the anode:

$$(1)\quad H_2 + O^{2-} \rightarrow H_2O + 2e^-$$

where the oxygen ion is made available by the following oxidant reduction reaction that occurs at the cathode side:

$$(2)\quad \frac{1}{2}O_2 + 2e^- \rightarrow O^{2-}$$

Reactions occur at the so-called triple-phase-boundary (TPB) where there is the simultaneous presence of electrons, ions and gases. In the present model the TPBs is regarded as an infinite thin layer between the electrode and the electrolyte interface.

The electrons released from reaction (1) flow from the reaction zone (typically very close to the anode/electrolyte interface) to the current collector, through the anode. At the cathode side, these electrons flow from the current collector to the cathodic reaction zone, where reaction (2) takes place. The main processes within the fuel cell are drawn in Figure 4-8.

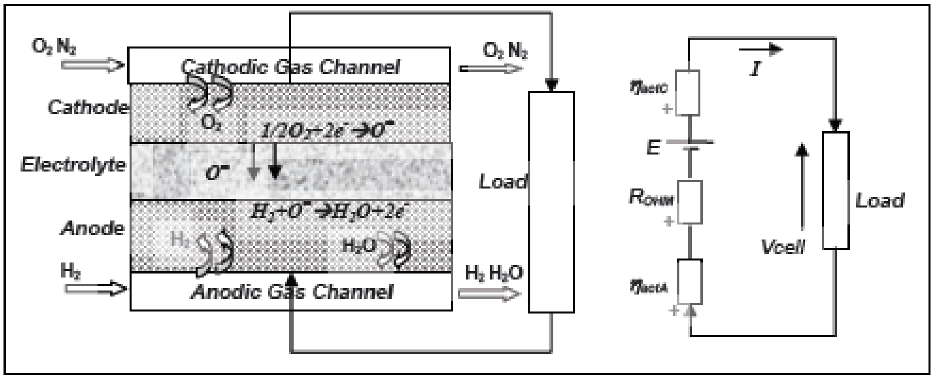

Figure 4-8 Schematic of fuel cell processes

slice which can be considered the smallest non-repeating geometrical pattern, as reported in Figure 4-9. Accordingly, as better explained in Section 4.4.4., periodic boundary conditions have been set.

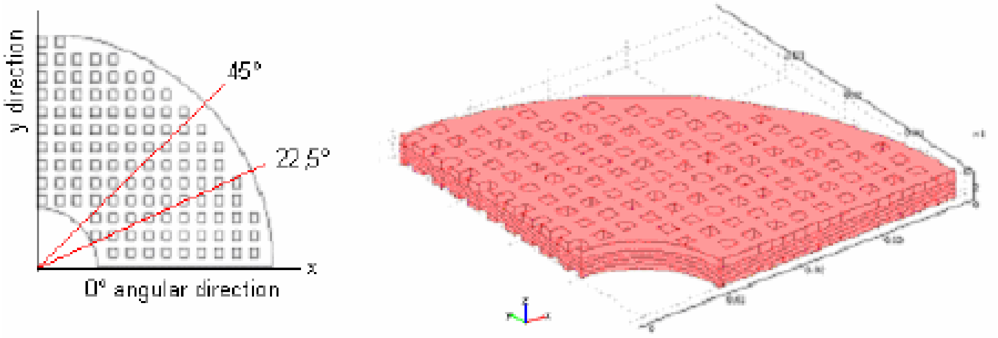

Figure 4-9 Computational 3D domain (and geometric directions)

The presented model is based on the following assumptions:

1. steady state conditions;
2. ohmic losses within the current collectors are neglected;
3. laminar and incompressible flow in the flow channels
4. radiation heat exchange is neglected ;
5. the electrochemical reactions are confined to the electrode-electrolyte interface ;

Assumption 2 is justified by the high electrical conductivity of the current collectors, compared to those of the electrodes. Assumption 3 is justified by the fact that gas speed in SOFC gas channels is wherever very low [14] and the density variation is not related to compression [3] Radiation heat exchange between gas and solid can be neglected if compared to convective heat transfer phenomena, as shown in [15], while assumption 5 is due to the high ionic conductivity of the electrolyte compared to the electrodes, which reduces the ability of oxygen ions to migrate through the electrodes.

In Figure 4-10 a schematic representation of the different domains together with the governing equations is reported. The overall SOFC model consists of three sub-models:

- the fluid dynamic sub-model;
- the electrochemical and mass transfer sub-model;
- the thermal sub-model.

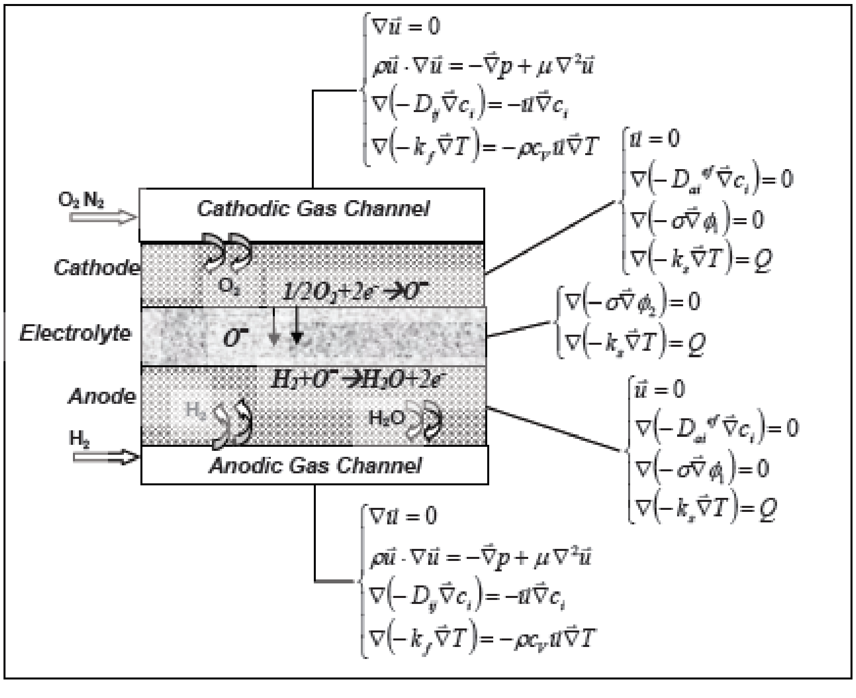

Figure 4-10 Schematic of governing equations applied to each domain

2.4.1. Fluid dynamic sub-model

Gas Channels. The task of the gas channel is to uniformly deliver the gas on the electrode surface. The fuel flow in the gas channels is modeled applying the equation of state and the mass and momentum conservation principles, i.e..

. (3) (4)

$$\nabla \vec{u} = 0$$

$$\rho \vec{u} \cdot \nabla \vec{u} = -\nabla p + \mu \nabla^2 \vec{u}$$

where $\vec{u}$ is the velocity vector, p the pressure, ρ and μ fluid density and viscosity, respectively. Since gases in SOFCs are far from the critic conditions, perfect gas equation of state is employed;

$$\rho = \frac{p}{RT \sum y_i / m_i}$$

$$\mu = \sum y_i \mu_i$$

Electrodes. Considering that the total pressure change within the electrodes is negligible (dp/dz ≈ 0), it is assumed that the mass transport through the porous media is driven only by diffusion [17].

2.4.2. Electrochemical sub-model

Mass balance

The electrochemical reaction ideal voltage depends on the reactants partial pressure at the triple phase boundaries through the Nernst law. The reactants concentration at the electrode/electrolyte interface (assumption 5) is evaluated through the species balance as follows:

(7) $$\nabla\left(c_i \vec{u}\right) = -\nabla \vec{N}_i + R_i$$

where i denotes the generic i-th specie (hydrogen, oxygen or water), N is the molar diffusive flux, and R the volume specie source term.

Gas channels. The molar flux is mainly convective in the gas flow direction and diffusive from the channel to the porous media. The diffusive mass flux is modeled through the Fick's law:

(8) $$\vec{N}_i = -D_{ij} + R_i$$

where D_{ij} is the mass diffusion coefficient, which is calculated through the Fuller-Schettler-Gidding correlation:

$$D_{ij} = \frac{0.143 \cdot 10^{-6} T^{1.75}}{p M_{ij}^{1/2} \left(v_i^{1/3} + v_j^{1/3}\right)}$$

(9)

where :

$$(10)\ M_{ij} = 2\left(\frac{1}{m_i} + \frac{1}{m_j}\right)^{-1}$$

v_i and m_i are the species Fuller diffusion volume and the molecular weight, respectively.

Electrodes. As discussed before, the molar flux is mainly diffusive [17]:

$$(11)\ \vec{N}_i = -D_{ai}^{eff}\,\vec{\nabla} c_i$$

The diffusion coefficient in the porous medium is composed of a binary diffusion coefficient D_{ai}^{eff} and of the Knudsen diffusion coefficient D_{ikn}^{eff} [16]

$$(12)\ \frac{1}{D_{ai}^{eff}} = \left(\frac{1}{D_{ij}^{eff}} + \frac{1}{D_{iKn}^{eff}}\right)$$

where the binary diffusion coefficient depends on the porosity (ε), and tortuosity (τ):

$$(13)\ D_{ij}^{eff} = \frac{\varepsilon}{\tau} D_{ij}$$

and Knudsen diffusion coefficient can be calculated through [16]:

$$(14)\ D_{iKn}^{eff} = \frac{\varepsilon}{\tau} 97 r_p \sqrt{\frac{T}{m_i}}$$

Charge balance

Electrodes. Since the electrochemical reactions are considered to take place at electrode/electrolyte interface, only electron transport takes place in the electrode domain. The electric potential (scalar), φ, and the current density (vector), J, are related each other by the Ohm's law:

$$(15)\ \vec{J} = -\sigma \vec{\nabla} \phi$$

where σ is the conductivity of the electrode. Charge conservation is coupled with expression (15) :

$$(16)\ \nabla \vec{J} = 0$$

Electrolyte. In this domain, no mass transport takes place, thus only the ionic potential and current density need to be calculated. Expressions (15) and (16), defined for the electrode, are employed also for modeling the ionic flux within the electrolyte.

Interface electrochemical reactions

Electrochemical reactions are specified here as boundary conditions at electrode-electrolyte interfaces for the balance equations (7) and (15). The local current density distribution is given by the Bulter-Volmer equation:

$$(17)\quad J\cdot \vec{n} = J_0\left[\exp\left(\vartheta_A \frac{F}{RT}\eta_{ACT}\right)-\exp\left(-\vartheta_C \frac{F}{RT}\eta_{ACT}\right)\right]$$

where ϑ_i is the product of the number of transferred electrons in the single elementary rate-limiting step (η_{BV}) and the charge-transfer coefficient (α), J_0 is the exchange current density, and η_{ACT} is the activation overpotential. The two key parameters are the charge-transfer coefficient and the exchange current density. The first ones are defined following the approach reported in [10] for a LMS cathode and a Ni/YSZ cermet anode. The exchange current density is expressed as a function of the local species partial pressure. A preliminary evaluation of different approaches has shown that the model proposed by Costamagna et al.[10] best interprets the cell behavior. The model proposed by Yamamura et al.[12] is considered to evaluate the anodic exchange current:

$$(18)\quad J_{0A} = \gamma_A\left(\frac{p_{H2}}{p}\right)\cdot\left(\frac{p_{H2O}}{p}\right)^{-0.5}\cdot\exp\left(-\frac{E_{actA}}{RT}\right)$$

The cathodic exchange current is defined according to the formulation reported in [13] :

$$(19)\quad J_{0C} = \gamma_C\left(\frac{p_{O2}}{p}\right)^{0.25}\cdot\exp\left(-\frac{E_{actC}}{RT}\right)$$

The activation overpotential η_{ACT} is calculated as the local difference between the relative electrode potential and the same value evaluated under ideal conditions.

$$(20)\quad \eta_{ACT} = \left(\phi_{electrode}-\phi_{electrolyte}\right)-V_{id}$$

V_{id} is the reversible potential for the semi-electrochemical reactions (1) and (2), respectively:

$$(21)\quad V_{id,A} = \frac{RT}{2F}\ln\frac{p_{H2O}}{p_{H2}}$$

$$(22)\quad V_{id,C} = E^{0,T} + \frac{RT}{2F}\ln\left(p_{O2}\right)^{0.5}$$

Where:

$$(23)\quad E^{0,T} = \frac{-\Delta G^{0,T}}{2F}$$

$E^{0,T}$ and $\Delta G^{0,T}$ are respectively the ideal potential and the Gibbs free energy at standard pressure p and temperature T, F is the Faraday constant and 2 are the electrons transferred. Finally, the Faraday's law is used to evaluate the molar flux at the anode/electrolyte interface:

$$(24)\quad \begin{cases} N_{H2} = \dfrac{-J_A}{2F} \\ N_{H2O} = \dfrac{J_A}{2F} \end{cases}$$

and at the cathode/electrolyte interface:

(25) $$N_{O2} = \frac{-J_C}{4F}$$

Electrochemical sub-model solution algorithm

The electrochemical sub-model solution algorithm is based on charge conservation, which imposes the equality between anode/electrolyte and cathode/electrolyte interface consumption or formation of charge. This can be described by the anodic and cathodic current density J. Once assigned a test value to the Nernst voltage (species concentration at the TPB) and to the electrode potential (electric problem), the fluctuating electrolyte potential allows determining, in an iterative process, the local activation overpotential (Eq. 20). By this way the equality of the anodic and cathodic local current density is obtained. In Figure 4-11 a comprehensive representation of all the governing equations solving the electrochemical problem in the different domains together with the boundary conditions is reported.

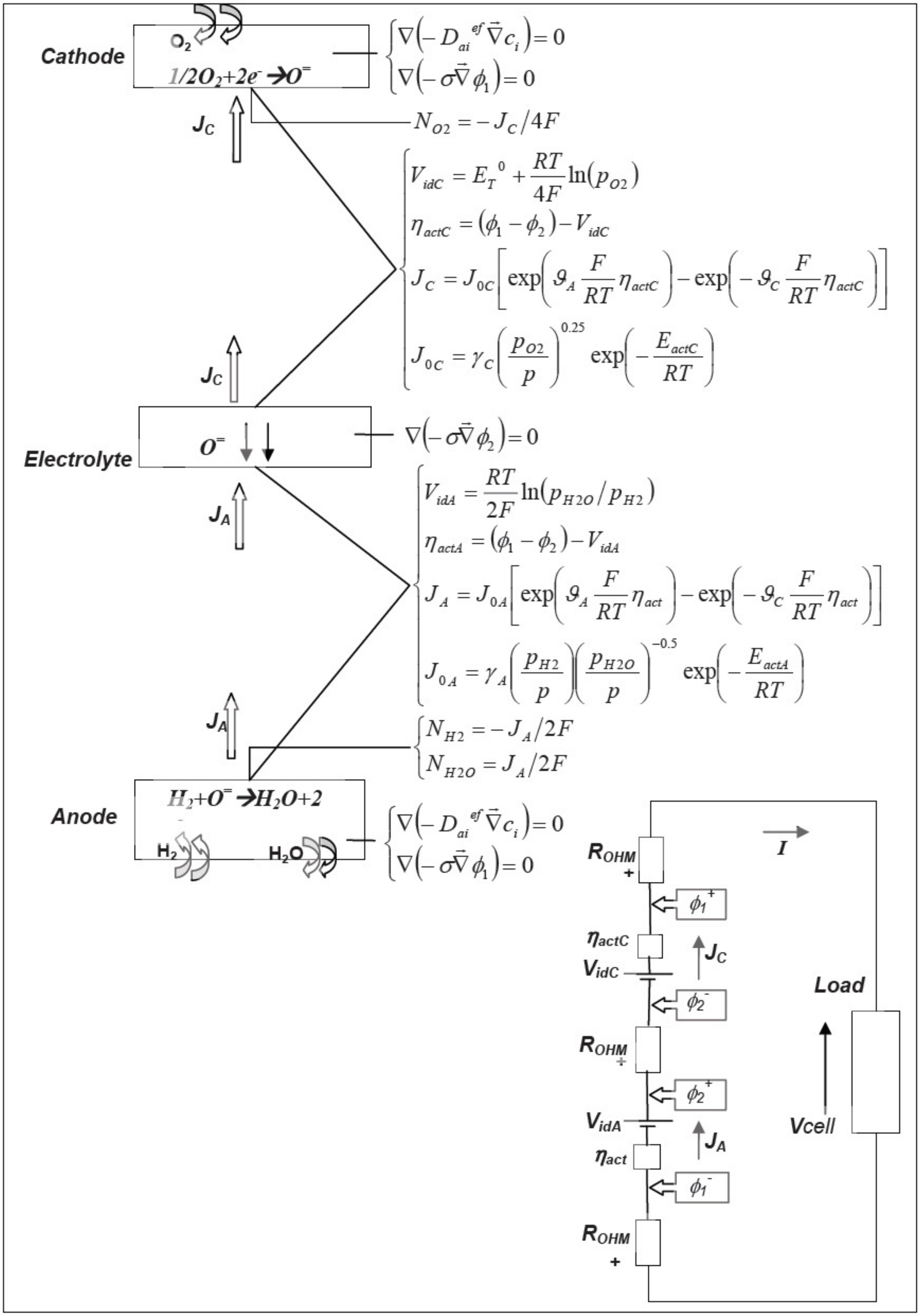

Figure 4-11 Schematic of governing equations together with the boundary conditions solving the electrochemical problem

2.4.3. Thermal sub-model

The thermal sub-model allows calculating the local temperature distribution, which affects the fuel cell performance by means of the electrochemical reaction rate, the electrode overpotential, the electrical and ionic conductivity and fluid properties.

Heat is generated inside the solid structure and is predominantly removed by convection heat transfer with the air and fuel flowing in the channels. Even if the operating temperature is high, we assume that radiation is negligible in comparison with the other heat transfer mechanisms [15].The temperature profile is obtained through the energy equation:

$$\text{(26)}\quad \rho c_v \vec{u}\cdot\vec{\nabla} T = -\nabla \vec{q} + Q$$

where q is the conductive heat flux, and Q is the ohmic heat source given by:

$$\text{(27)}\quad Q = \sigma \vec{\nabla}\phi \vec{\nabla}\phi$$

The conductive heat flux is expressed by the Fourier's law:

$$\text{(28)}\quad q = -k\vec{\nabla} T \quad \begin{cases} k = k_f & \left(gas\,channels \right) \\ k = k_s & \left(solids \right) \end{cases}$$

Finally, the interface electrochemical reactions introduce the following boundary heat sources:

- reversible heat generation at the anode:

$$\text{(29)}\quad q_{rev} = T\Delta S \left(\frac{J}{2F} \right)$$

- irreversible heat generation at both the anode and the cathode:

$$\text{(30)}\quad q_{irr} = \eta_{act} J$$

The external boundary conditions of this sub-model are reported in Figure 4-12.

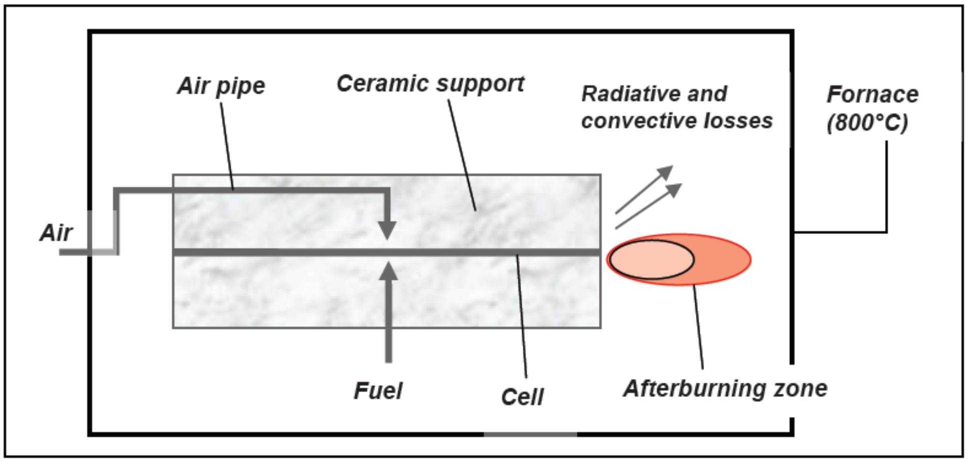

Figure 4-12 External boundary conditions for the thermal sub-model

2.4.4. External boundary conditions

The external boundary conditions on V, T, c_i and $\vec{u}$ are defined as follows:

Inlet: Inlet conditions are defined by the operating conditions, summarized in Table 4-3

Lateral: Periodic conditions are considered on the lateral boundary as the analyzed geometry is the smallest non-repeating geometrical pattern of the whole cell (see Figure 4-9).

Top/bottom: No slip condition is imposed to the velocity field and as the SOFC ceramic support is considered at thermal equilibrium with the external furnace then giving a constant temperature value.

Outlet: Convective fluxes are considered at the cell outside. The convection and radiation heat exchange mechanisms between the solid structure and the external furnace are considered:

$$(31)\ q_{conv} = h_c\left(T_f - T\right)$$

$$(32)\ q_{rad} = f\sigma_{rad}\left(T_f^4 - T^4\right)$$

where h_C, f, and σ_{rad} are, respectively, the convective heat transfer coefficient, the total emissivity, and the Stefan–Boltzmann constant. T_f is the furnace temperature. Furthermore, the combustion of the non-oxidized fuel mass as it meets oxygen at the cell outlet provides another heat source.

Afterburning - The afterburning heat source is evaluated as follows:

$$(33)\ q_{afterburning} = \frac{\left(H_{2Out} - H_i\right)}{S_{anode}}$$

Where:

$$(34)\ H_{2out} = \rho\left[H_{2in} - \frac{I}{2F}\right]$$

Therefore, on the polarization curve basis, starting from the knowledge of the total current and of H_{2in}, the afterburning heat source and the function $q_{afterburning} = f(V_{cell})$ can be defined.

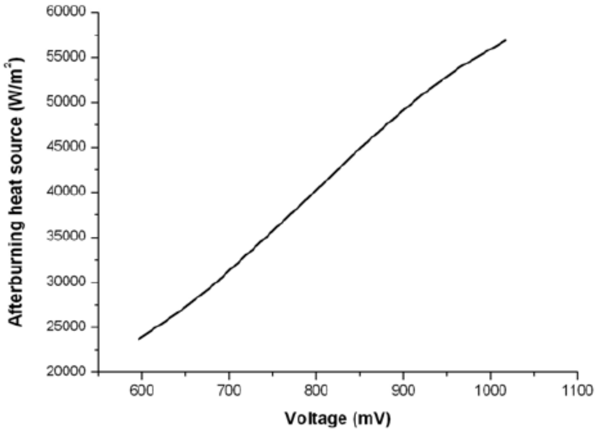

Figure 4-13 Afterburning heat source as function of cell voltage

Inlet gas temperature – Inlet hydrogen temperature is directly available on the basis of the experimental measurements as a thermocouple is located close to the SOFC inlet. On the other hand, air inlet temperature is not measured. Accordingly, a 0D model has been developed. Air is delivered to the cathode from the external ambient through a pipe of 4 mm diameter and 9 cm length, embedded in the furnace. The air heating is evaluated through a simple 0D thermal balance that leads to [18]:

$$(35)\quad T_{out} = T_f - \left(T_f - T_{in}\right)\exp\left(\frac{-h_c A}{\dot{m} c_p}\right)$$

where the thermo-physical properties are evaluated in function of temperature through an iterative way. Results are summarized in Table 4-2 and it is worth of noting that air reaches the equilibrium with the furnace at 800°C.

Table 4-2 Results of air heating iterative calculation

Oxygen volume flow	12 Nl/h
Logarithmic mean temperature	$T_{ml} = \left(T_{out} - T_{in}\right) \Big/ \ln\left(\frac{T_{out} - T_T}{T_{in} - T_T}\right) = 785.26\ °\mathrm{C}$
Mean speed	$\bar{u} = 4\dot{m} / \bar{\rho}\left(\pi D^2\right) = 1.027\ \mathrm{m/s}$
Reynolds number	$\mathrm{Re} = \bar{u} D \bar{\rho} / \bar{\mu} = 31.048$
Nusselt number [18]	$Nu = 3.66$
Convection coefficient	$h = Nu \cdot k / D = 179.50\ \mathrm{W/m^2K}$
Pipe air outlet temperature	$T_{out} = T_T - \left(T_T - T_{in}\right)\exp\left(-hA/\dot{m}c_p\right) = 800\ °\mathrm{C}$

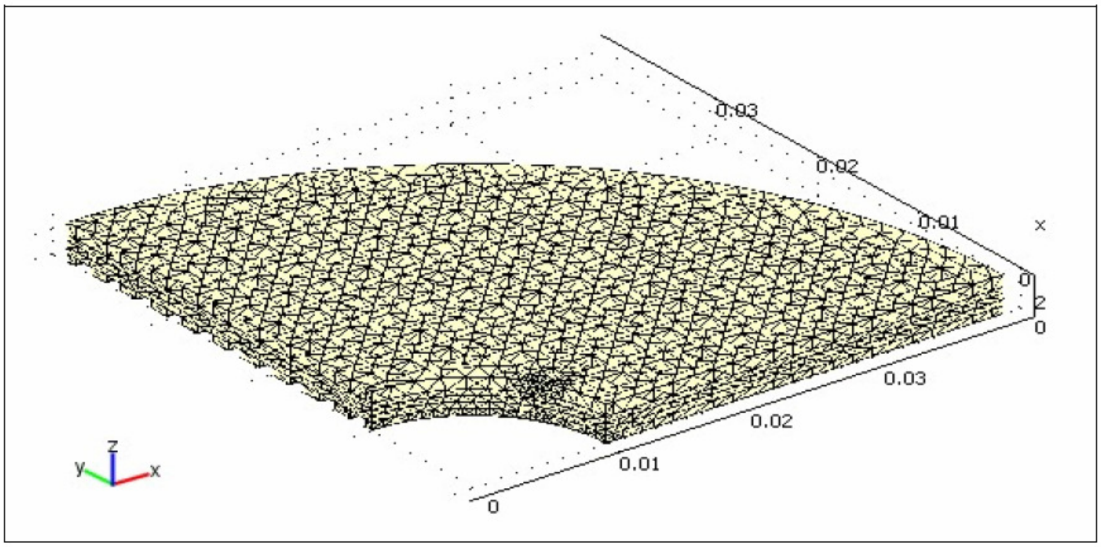

Figure 4-14 Computational mesh

2.4.5. Solution technique

A finite element computational package, FEMLAB, is used to solve the described non-linear system of equation. A 3D unstructured triangular mesh is considered in the present calculations. The mesh is composed of 43785 elements and is sketched in Figure 4-14. The results have been checked for grid sensitivity and the trends are observed to be consistent in all the investigated cases in terms of polarization curve as the numerical results are included within a 3% of difference when increasing the grid detail level.

The iterative solution algorithm is reported in Figure 4-15. As it is possible to notice, even if the model sub-problems are fully coupled, to perform an efficient management of computer resources and to reduce the computational time, the numerical convergence is reached in an iterative way, called “frozen fields”. The electrochemical sub-model is firstly solved starting from a tentative velocity and a temperature profile, so evaluating species distribution and electrochemical quantities. These data are exchanged with the fluid dynamic sub-model and the thermal sub-model. This process is repeated until convergence is reached.

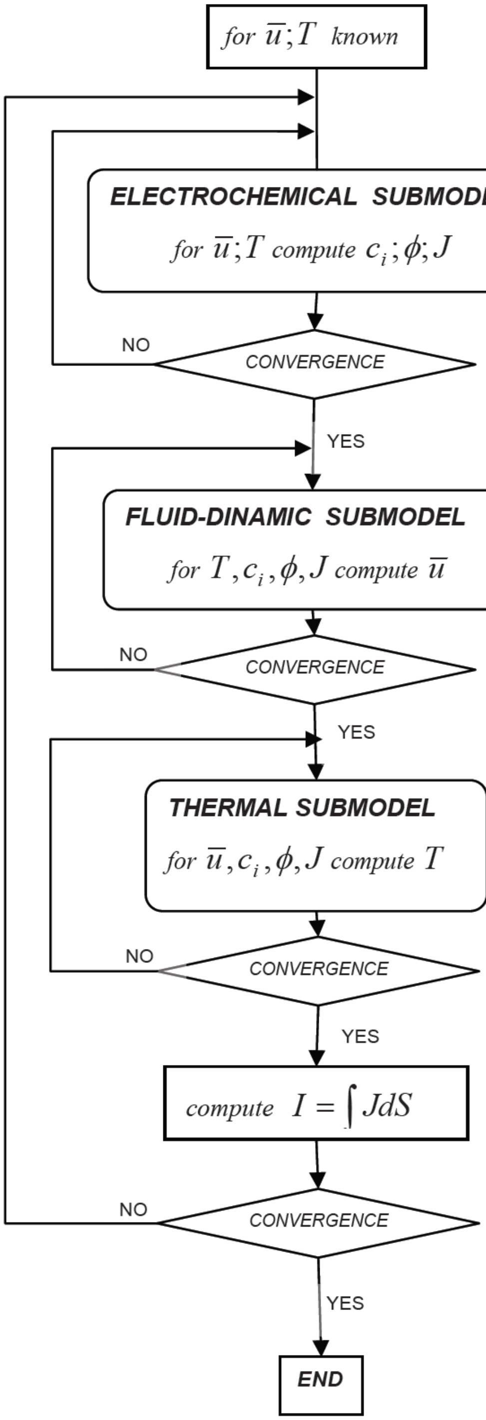

2.5. Model validation and results

This section presents the comparison between the numerical data provided by the 3D numerical code and the experimental data of the single cell ASC1.

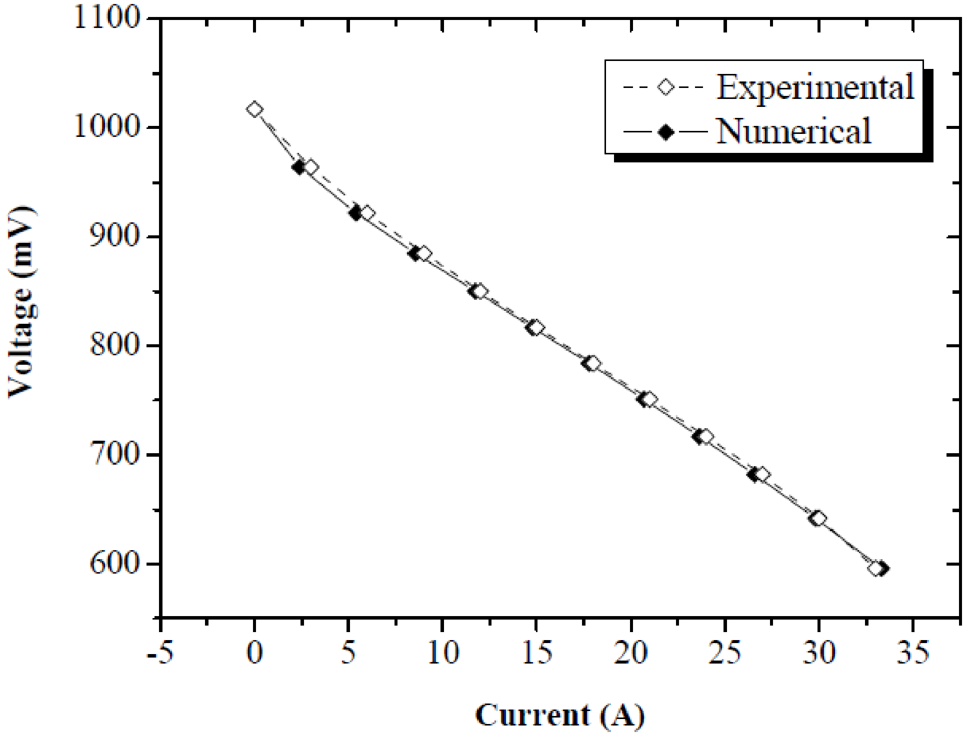

Figure 4-16 Numerical and experimental polarisation curve

4.5.1. Model validation

As deeply discussed literature [10], the open-circuit voltage (OCV) calculated through the Nernst equation on the basis of experimental reactant concentrations is slightly higher than the experimental one. Therefore, the updating phase is started by imposing the experimental value of the open-circuit voltage (OCV). The difference between the experimental and calculated open circuit voltage is 7.8% and is kept as a constant for all of the calculations.

Then the numerical model has been updated on the basis of the experimental characteristic curve at constant fuel and oxidant flow rates (H_2=24 Nl/h; O_2=12 Nl/h) so that different points along the curve correspond to different utilization factors. In this phase the best performing species diffusion and current exchange formulations have been chosen. As already mentioned, the Fick's law (Eq.11) and the Costamagna approach for the exchange current (Eq. 18 and 19) allowed to correctly predict the actual fuel cell operation. The adjustable parameters were the constants γ_A and γ_C in the anodic and cathodic exchange current (Eq. 18 and 19) and the diffusion coefficients by means of the porous microstructure characteristics, it being understood that the tuning process has been performed by varying the parameters within literature values. The whole set of input parameters is reported in Table 4-4.

Figure 14 demonstrates that the experimental and numerical polarisation profiles are mostly coincident, as the difference between experimental and numerical cell total current is everywhere lower than 0.6A, so clearly indicating a proper updating phase. However this is not enough to declare that the developed numerical model is valid and reliable. To establish the range of validity and the accuracy of the code it is necessary, in fact, to verify that the numerical simulation allow to predict the fuel cell behaviour at different operating conditions, without changing the adjustable parameters values found in the updating phase.

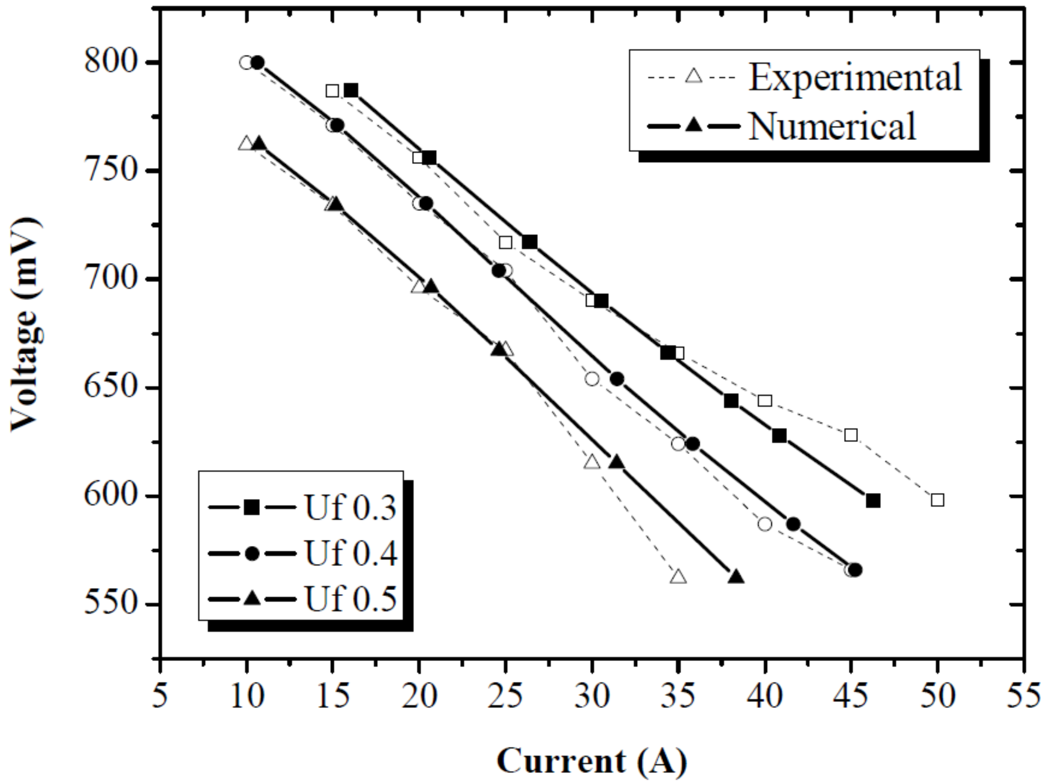

Figure 4-17 Numerical and experimental current-voltage curves with constant fuel (U_f) and oxidant (U_{ox}) utilization coefficients

Therefore, the code validation has been carried out by comparing numerical and experimental data varying both fuel flow rate and utilisation coefficient, defined as follows:

$$U_f = \frac{J}{J_t}$$

being J the actual current density (on the basis of the amount of reactants consumed) and J_t the theoretically expected current density assuming that the overall reaction in the fuel cell is complete. Since each mole of hydrogen that reacts in the anode frees two moles of electrons, the fuel utilisation factor can be correlated to the inlet hydrogen flow rate as:

$$U_f = \frac{J}{(2F)H_2}$$

Using the inlet oxygen flow rate, the oxidant utilization coefficient:

$$U_{ox} = \frac{J}{(4F)O_2}$$

has been kept constant to 0.4 that ensure enough oxygen at the highest current density.

Figure 4-17 presents the comparison between numerical and experimental results for three current density-voltage curves with constant fuel and oxidant utilization coefficients (U_f = 0.3,0.4,0.5 and U_{ox} = 0.4) and variable flow rates. The agreement between numerical and experimental data is excellent in most cases. Larger differences can be observed at high current densities for U_f = 0.3 and 0.5, while the numerical curve at U_f=0.4 is almost superimposed to the numerical one. The percentage errors between numerical and experimental is everywhere within 5% and less than 2% for U_f=0.4, thus demonstrating a wide range of validity of the numerical code.

It is important to underline that the polarisation curves of Figure 4-17 used to validate the present code represent a hard and important benchmark test. Even if the characteristic curve of Figure 4-16 it is usually used to benchmark different cell types, in fact, it cannot be used to analyse cell performance like the increase in voltage internal losses. This happens because by increasing the current flow with fixed gas input, the cell is forced to work with increasing utilization factors, thus mixing the effects of fuel and losses on voltage variations. On the other hand, the performance analysis at constant fuel utilisation factor is of particular interest since it allows to quantify the portion of voltage decrease only due the increasing losses.

Moreover, the polarisation curves at constant fuel utilisation factor allow the identification of the cell optimal operating range. It is, in fact, worth of noting, that the curves linear theoretical slope is modified because of thermal effects at the higher current densities and because of humidification effects at the lower current densities. It is important to observe that for a current greater than 30 A the polarization effects become significant in comparison to the non reacted hydrogen afterburning effect. This heat source is quickly dispersed in the furnace, so producing only a remarkable edge effect. On the other hand, also the humidification effects can be highlighted, as they are strictly connected with the hydrogen velocity when enters in the hydrogen humidifier.

4.5.2. Analysis of results

Once validated the model, the advantages of a multidimensional numerical approach can be exploited observing the following maps.

Flow field: Flow field streamlines are reported in Figure 4-18. The presence of the ribs strongly affects the flow field. In fact, preferential flow directions can be observed along the x and y directions. In the central zone, due to the cell geometry, the flow is mostly broken so reducing the reactants feeding efficiency.

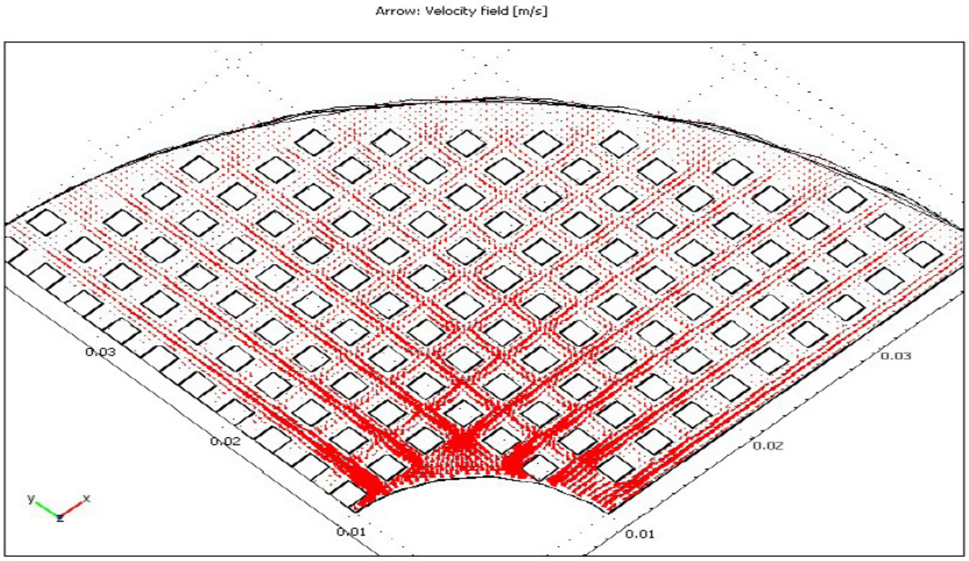

Figure 4-18 Flow field arrows on the cathodic side (O_2=12Nl/h, cell voltage 0.8V, total current 18 A)

Species concentration: Hydrogen and oxygen concentration along the gas channels are reported in Figures 4-19. Highest values are located at the cell inlet, while a progressive O_2 and H_2 concentration decreasing is observed moving to the cell outlet.

In Figure 4-20 and 4-21, respectively, hydrogen and oxygen concentration at the electrode/electrolyte interface are shown. It is worth of noting that a lower concentration of the reacting species is observed under the ribs. This phenomenon can be explained considering that the diffusion in the porous electrodes can be considered as the combinations of two effects:

- cross-plane diffusion.
- in-plane diffusion .

Under the ribs the species diffusion in the direction orthogonal to the cell plan, i.e. cross-plane diffusion, is obviously impossible. Hence, the reactants concentration on the electrode/electrolyte interface locally decreases, so reducing the overall cell performance. The ribs effect is significant at any operating condition, but it becomes predominant at high fuel utilization.

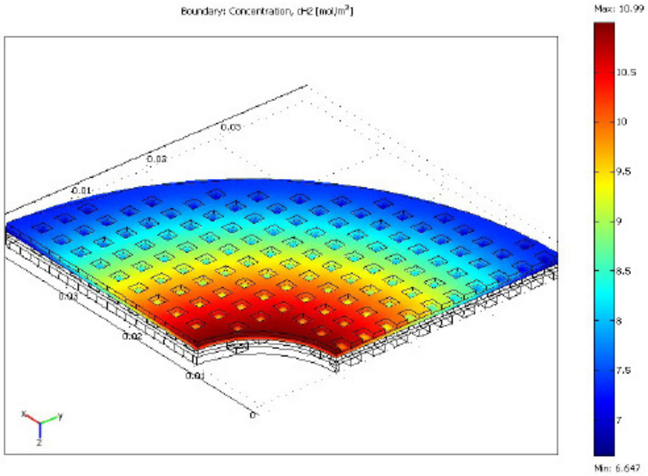

Hydrogen concentration along the fuel channels (H_2=24 Nl/h, cell voltage 0.8V, total current 18 A)

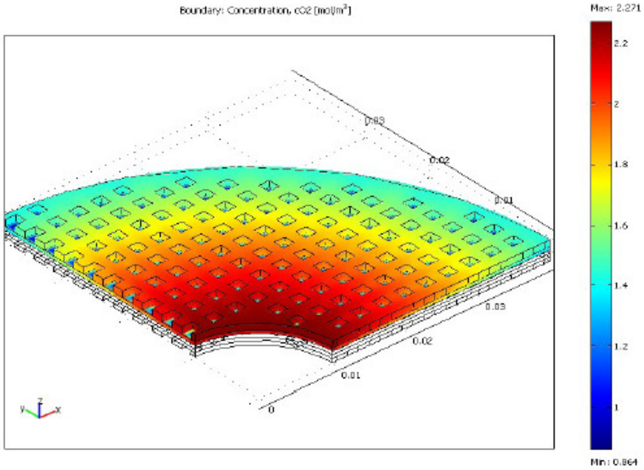

Oxygen concentration along the air channels (O_2=12 Nl/h, cell voltage 0.8V, total current 18 A)

Figure 4-19 Hydrogen, and oxygen concentration along the gas channels

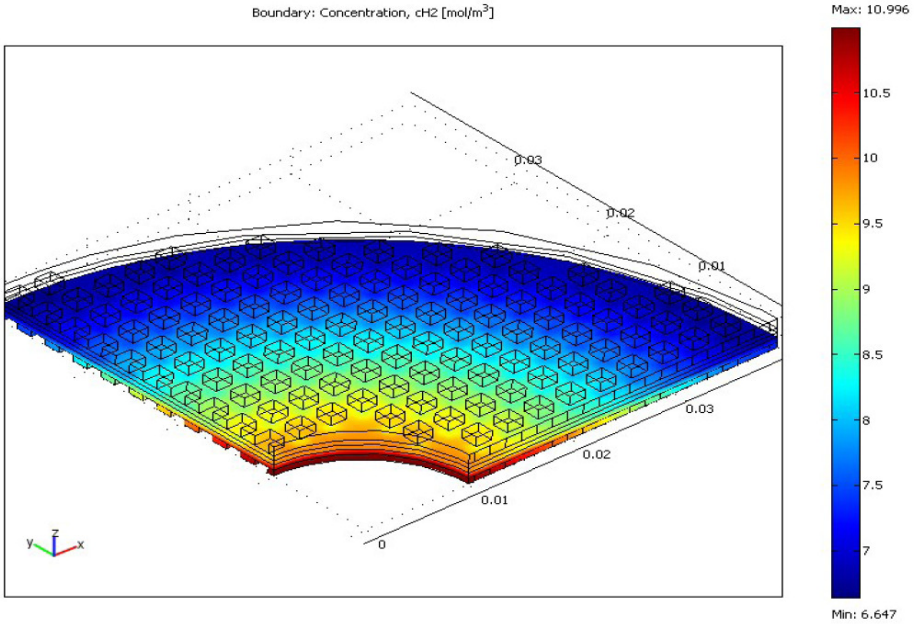

Figure 4-20 Hydrogen concentration at anode/electrolyte interface

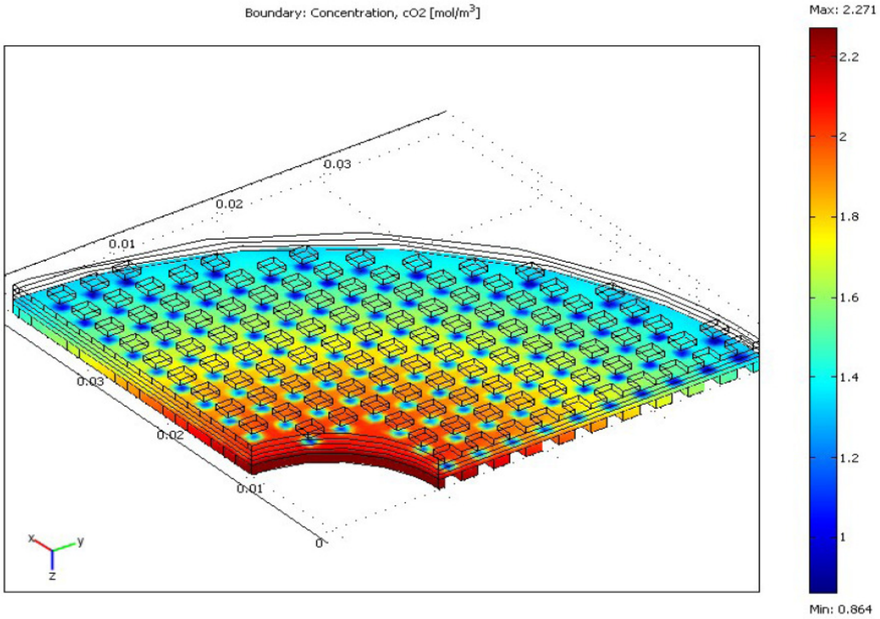

Figure 4-21 Oxygen concentration at cathode/electrolyte interface

For better accuracy, in Figure 4-22 and 4-23 a slice view of reactants concentration along the 0°, 22,5° and 45° angular direction is given. Moreover, comparing the figures, it can be observed that cross-plane and in-plane diffusion effects are more important at the cathode than at the anode because of the lower diffusivity.

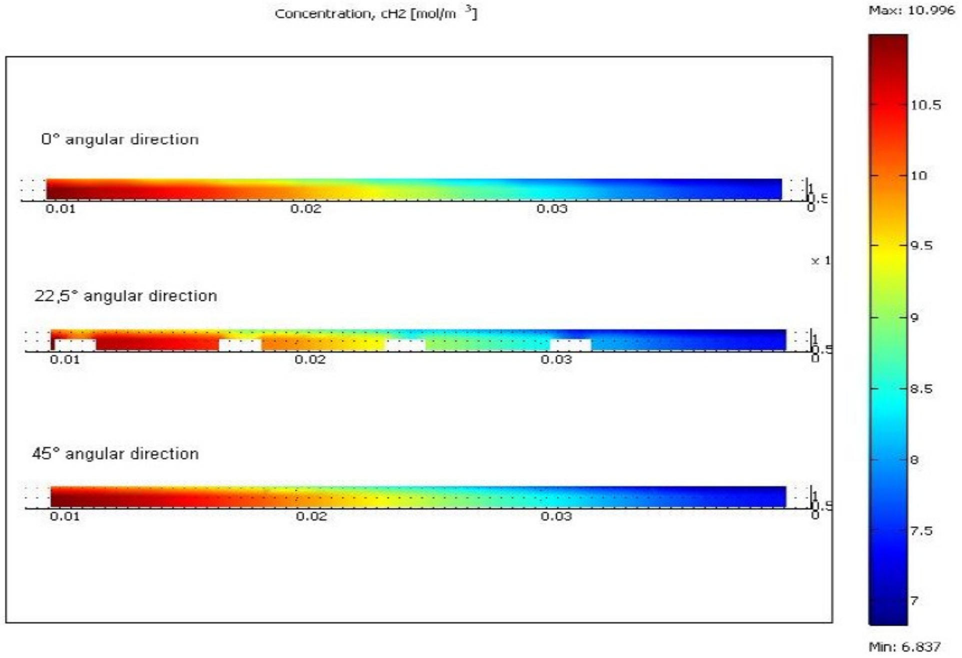

Figure 4-22 Hydrogen concentration along 0°, 22.5°, and 45° angular direction

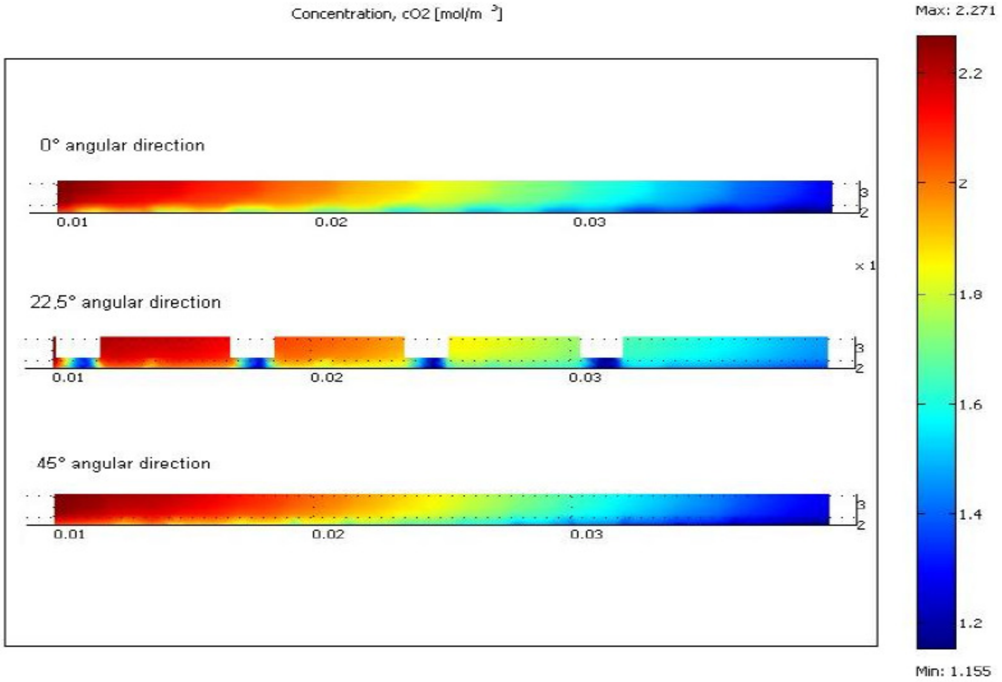

Figure 4-23 Oxygen concentration along 0°, 22.5°, and 45° angular direction

Current density: Figure 4-24 shows the current density distribution at the cathode/electrolyte interface. The current density is not uniform being affected by the hydrogen and oxygen distributions and by the electrolyte resistance which is, in turns dependent on the temperature. Because of the previously discussed reasons, under the ribs the produced current is smaller than elsewhere. Furthermore, around the ribs, it is possible to observe that the produced current is characterized by a local increase. This effect is related to the local flow deceleration which, in turn causes a local increase in the species concentrations together with greater species diffusion perpendicularly to the cell plane.

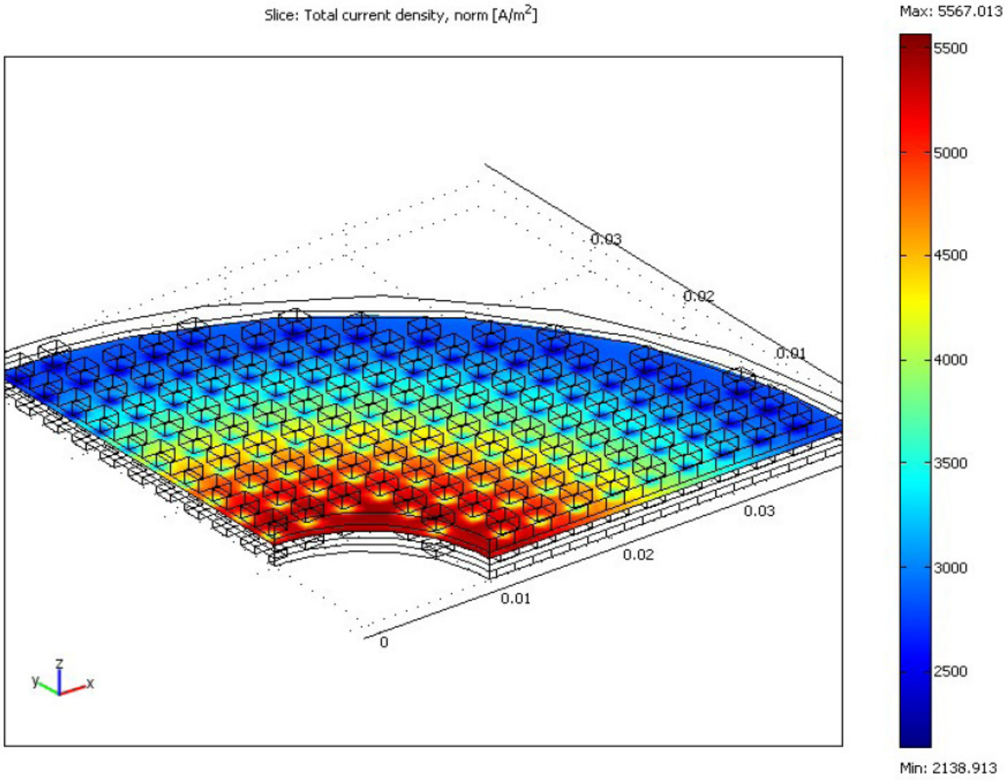

Figure 4-24 Current density distribution (cell voltage 0.8V, total current 18 A)

Temperature distribution: In Figure 4-25 and 4-26 the temperature distribution at the cell middle plane is reported for two operating conditions. It can be seen that the fuel cell does not work at uniform temperature but a difference between maximum and minimum temperature of appreciatively 25°C is detectable. The highest temperature is located towards the cell outlet. This information is of primarily importance in SOFC as it allows getting information for thermally-induced stresses due to steady state thermal gradients.

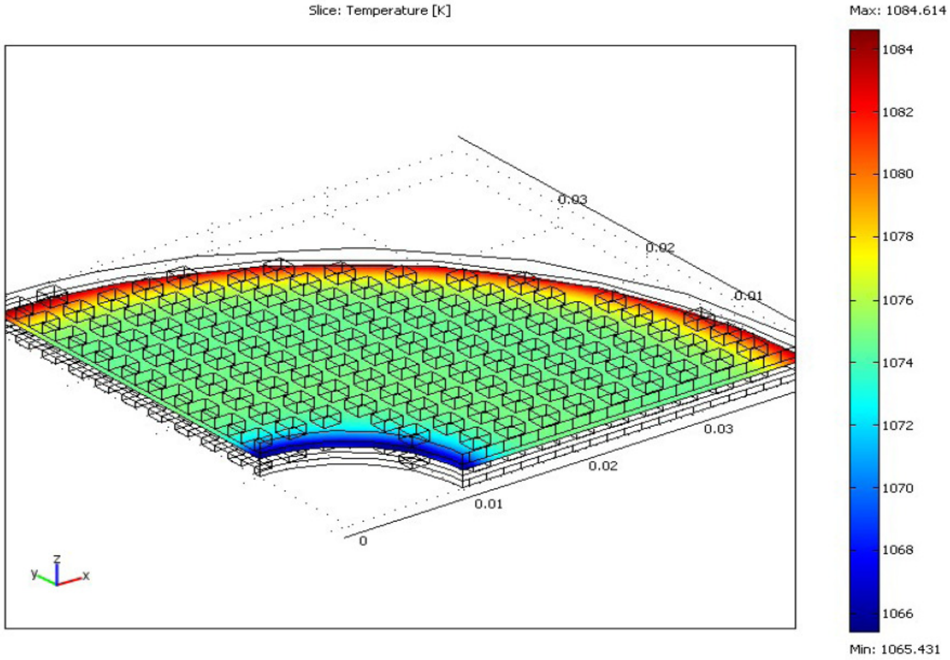

Figure 4-25 Temperature distribution (cell voltage 0.8V, total current 18 A)

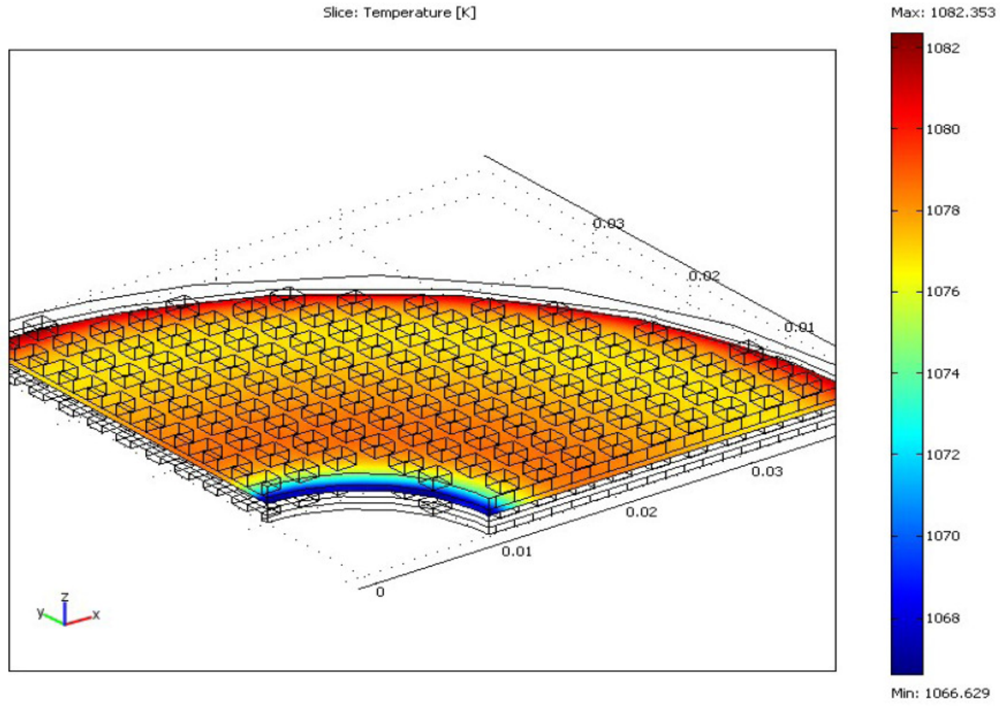

Figure 4-26 Temperature distribution (cell voltage 0.6V, total current 33 A)

Furthermore, the high is the overall temperature the higher is the current density. The temperature non-uniform distribution is enhanced by the non reacted hydrogen afterburning reaction. Comparing the two operating conditions, it can be observed that the temperature rise at the cell outlet is higher for lower current densities, that imply poorer reactants consumption and higher after-burn thermal flux.
In the following tables, the cell operating parameters for the polarization curve and model input parameters found in the updating phase are summarized.

Table 4-3 Cell operating parameters for the polarization curve

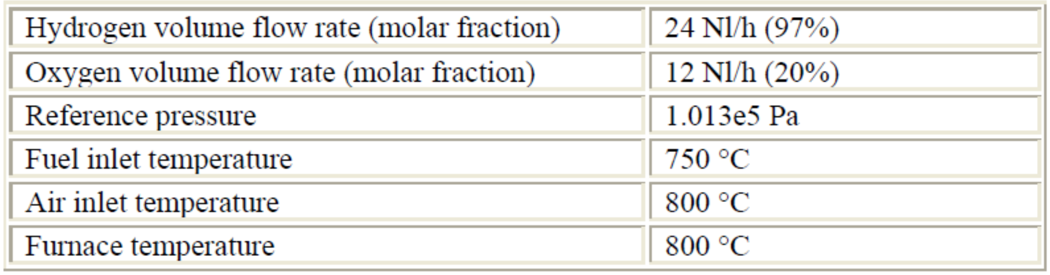

Hydrogen volume flow rate (molar fraction)	24 Nl/h (97%)
Oxygen volume flow rate (molar fraction)	12 Nl/h (20%)
Reference pressure	1.013e5 Pa
Fuel inlet temperature	750 °C
Air inlet temperature	800 °C
Furnace temperature	800 °C

Table 4-4 Cell operating parameters

Gas thermo-physic properties [8]	
Oxygen viscosity	1.668e-5+3.108e-8*T [Pas]
Nitrogen viscosity	1.435e-5+2.642e-8*T [Pas]
Hydrogen viscosity	6.162e-6+1.145e-8*T [Pas]
Water viscosity	4.567e-6+2.209e-8*T [Pas]
Oxygen specific heat at constant volume	2.201e4+4.936*T [J/kmolK]
Nitrogen specific heat at constant volume	1.910e4+5.126*T [J/kmolK]
Hydrogen specific heat at constant volume	1.829e4+3.719*T [J/kmolK]
Water specific heat at constant volume	2.075e4+12.15*T [J/kmolK]
Oxygen thermal conductivity	0.01569+5.690e-4*T [W/mK]
Nitrogen conductivity	0.01258+5.444e-5*T [W/mK]
Hydrogen thermal conductivity	0.08525+2.964e-4*T [W/mK]
Water thermal conductivity	-0.01430+9.782e-5*T [W/mK]
Fuller binary diffusion coefficients [9]	
Oxygen Fuller diffusion volume	16.3
Nitrogen Fuller diffusion volume	18.5
Hydrogen Fuller diffusion volume	6.12
Water Fuller diffusion volume	13.1

Porous media microstructure [10]	
Porosity	30 %
Tortuosity	10
Porous radium	0.5e-6 m
Electrokinetic parameters [10]	
Ideal potential	0.8961 V
Anodic preexponential coefficient	1.6e9
Cathodic preexponential coefficient	3.9e9
Anodic activation energy	120 J/mol
Cathodic activation energy	120 J/mol
Anode charge transfer coefficient	$\theta_{a,}$ =2; θ_c= 1
Cathode charge transfer coefficient	θ_a =1.4 θ_c = 0.6
Electrical conductivities [11]	
Anode electrical conductivity	9.5e7/T*exp(-1150/T) [$Ohm^{-1}m^{-1}$]
Electrolyte electrical conductivity	3.34e4*exp(-E_el/T) [$Ohm^{-1}m^{-1}$]
cathode electrical conductivity	4.2e7/T*exp(-1200/T) [$Ohm^{-1}m^{-1}$]
Solid parts thermal conductivities [11]	
Anode thermal conductivity	3 W/mK
Electrolyte thermal conductivity	2 W/mK
Cathode thermal conductivity	3 W/mK
Heat exchange coefficients	
Thermal convective coefficient	5 W/m^2K
Thermal radiative emissivity	0.3

2.6 Using Syngas As Fuel

An attractive and practicable way of biomass utilization for energy production is gasification integrated with solid oxide fuel cell. This technology seems to have the possibility to reach high efficiencies based on a fundamentally clean and renewable fuel. Nowadays, the main interest of wood waste gasification is the production of syngas fuel (CO and H_2). Syngas is of particular interest if used as fuel in the high temperature fuel cell like SOFC. SOFC, in fact, is a high temperature fuel cell in which CO can be directly used as fuel, because of the rapid electrode kinetics and the lower need for high catalytic activity. Accordingly, it offers fuel flexibility and high efficiency [9].

The great part of models in literature [16, 15, 2] suppose that only H_2 is oxidized at the anode while CO and/or CH_4, if existing, are respectively shifted and reformed to produce H_2. On the contrary, Khaleel [9] and Petruzzi [17], for example, introduced the direct oxidation of the carbon monoxide using the parallel electrical circuit analogy. Petruzzi [17] adopted empirical correlations as reported by Achenbach [8] to estimate the anodic and cathodic polarization assuming a low activation polarization in addition of a neglected concentration polarization. Whereas Khaleel [9] used analytical expressions for activation and concentration polarizations, assuming the same concentration polarization for H_2–H_2O and CO–CO_2 systems to determine a relation between H_2 and CO currents. Zhu [18] elaborated a general mathematical model which accommodates arbitrary gas mixtures using iterative procedure to determine the pressure and concentration gradients.

The present study is the evolution of the hydrogen fed SOFC model, described in Chapter 4. The main objective of this work phase is to implement, in the hydrogen SOFC model, the chemical reactions occurring in the anode channel (i.e. water gas shift) and the direct oxidation of the carbon monoxide at the TPB. By this way, it is possible to predict SOFC performance when fed with pre-reformed fuel containing at least H_2 CO H_2O, and CO_2.

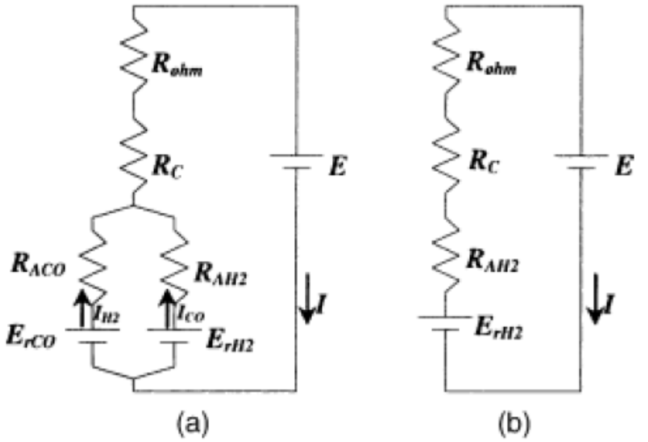

(a) (b)

Figure 5-1 Equivalent circuit for the simultaneous H_2 and CO oxidation (a) and H_2 oxidation (b) approach described by Petruzzi [17]

Like hydrogen fed SOFC model, the syngas fed one is applied on 3D domain, thus obtaining accurate results. In particular, it allows calculating the amount of current produced by CO oxidation and by H_2 oxidation. The fluid-dynamics within the gas channel is again deeply analyzed, and temperature distribution is influenced by polarization effects, afterburning reactions and chemical reaction inside the fuel channel.

The lack of experimental data and literature reports about simultaneous oxidation of CO and H_2, prevents a rigorous validation of this model. Some studies have to be still performed, but this work, whose results are compared with more than one experimental J-V curve, goes in that direction.

2.6.1 Experimental setup

Experimental J-V curves, obtained at University of Perugia testing laboratory, are shown in Figure 5-2. The SOFC apparatus described in detail in Section 4.2. and 4.3. is embedded in an electric furnace, which guarantees the desired fuel cell operating temperature. The electric load applied to the single cell is varied through the use of a potentiometer. Anodic and cathodic gas mixtures are obtained from laboratory-quality H_2, CO, CO_2, O_2, and N_2 stored in gas cylinders outside the laboratory. The water content in the anode is varied through the use of a peristaltic pump, a water mass flow controller, and an evaporator apparatus. Mass flow controllers, electrical load, gas and furnace temperature are controlled through an in-house software realized in Visual Basic, and the results are stored in a dedicated file.
In Figure 5-2, the red line limits the region where experimental data are consistent, as better explain in Section 5.4.1.

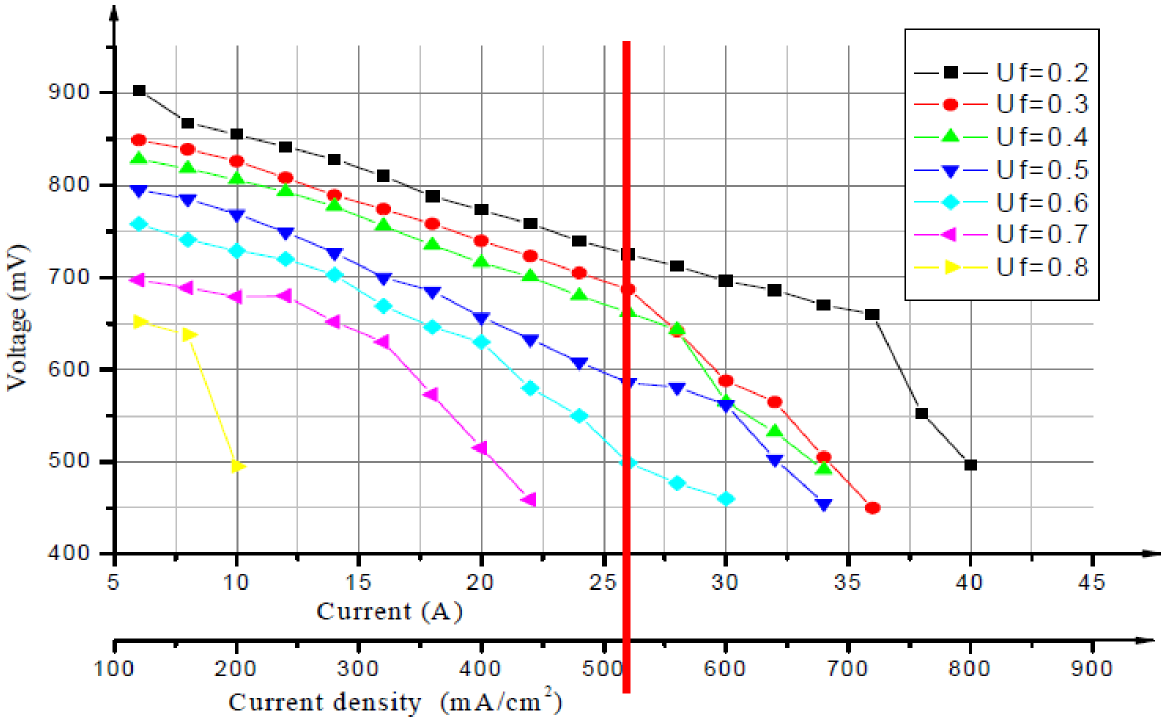

Figure 5-2 Current-voltage curves with constant fuel (U_f) and oxidant (U_{ox}) utilization coefficients

2.6.2 Numerical model

For the single cell described in Section 5.2., a detailed numerical model was carried out. As discussed in Section 4.4., the set of mathematical equations describing the electrochemical and physical phenomena has been solved on a disk slice which can be considered the smallest non-repeating geometrical pattern (see Figure 4-9).
The single cell is again schematically considered to be composed of five domains, namely the flow channels (air and fuel), two porous electrodes (cathode and anode), and the electrolyte, as shown in Figure 5-3. The governing equations applied to each sub-domain have been directly solved applying appropriate interface conditions.

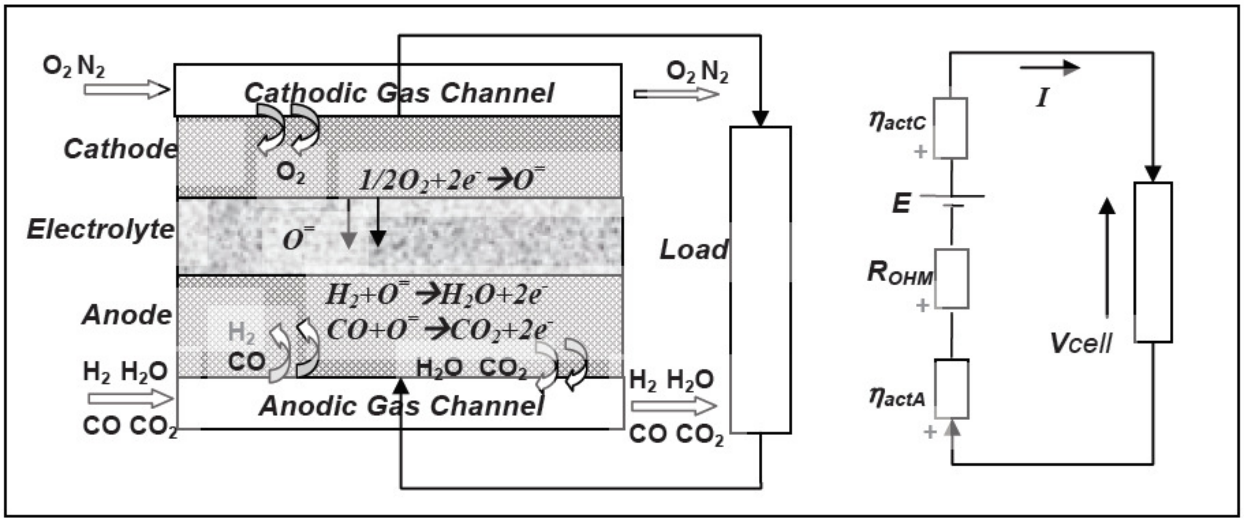

Figure 5-3 Schematic of fuel cell processes

During SOFC operation, oxygen from the air channel diffuses through the porous cathode to the electrons, ions and gases three-phase boundaries where is reduced to oxygen ion (O^{2-}). In the present model the TPBs is regarded as an infinite thin layer between the electrode and the electrolyte interface.

$$(1)\ \frac{1}{2}O_2 + 2e^- \rightarrow O^{2-}$$

Oxygen ion is then transported to the anode/electrolyte interface through the ion-conducting electrolyte. Simultaneously, H_2 and/or CO fuel diffuses through the porous anode to the anode/electrolyte interface, where it is oxidized electrochemically to produce H_2O and/or CO_2.

$$(2)\ H_2 + O^{2-} \rightarrow H_2O + 2^{e-}$$

$$(3)\ CO + O^{2-} \rightarrow CO_2 + 2^{e-}$$

These products are then transported back to the fuel channel through the porous anode structure. The electrons released from reaction (2) and (3) flow from the reaction zone to the current collector, through the anode. At the cathode side, these electrons flow from the current collector to the cathodic reaction zone, where reaction (1) takes place.

As the fuel is syngas (H_2, H_2O, CO, CO_2) the water gas shift reactions take place within the anode gas channel as follows:

$$(4)\ CO + H_2O \rightarrow CO_2 + H_2 \quad \left(\Delta H_{WGSR} = -41 kJ/mol\right)$$

The presented model is based on the following assumptions:

1. steady state conditions;
2. ohmic losses within the current collectors are neglected;
3. laminar and incompressible flow in the flow channels
4. radiation heat exchange is neglected
5. the electrochemical reactions are confined to the electrode-electrolyte interface
6. the water gas shift reactions occur only at the fuel channel.

Assumption 2 is justified by the high electrical conductivity of the current collectors, compared to those of the electrodes. Assumption 3 is justified by the fact that gas speed in SOFC gas channels is wherever very low [9] and the density variation is not related to compression [1] Radiation heat exchange between gas and solid can be neglected if compared to convective heat transfer phenomena, as shown in [10], while assumption 5 is due to the high ionic conductivity of the electrolyte compared to the electrodes, which reduces the ability of oxygen ions to migrate through the electrodes. Due to the inlet syngas composition, reported in Table 5.1, and to the cell anode supported structure, in previous numerical tests it was found that the anode layer shift reactions are negligible in comparison whit fuel channel ones.

In Figure 5-4 a schematic representation of the different domains together with the governing equations is reported. The overall SOFC model consists of three sub-models:

- the fluid dynamic sub-model;

- the electrochemical and mass transfer sub-model;

- the thermal sub-model.

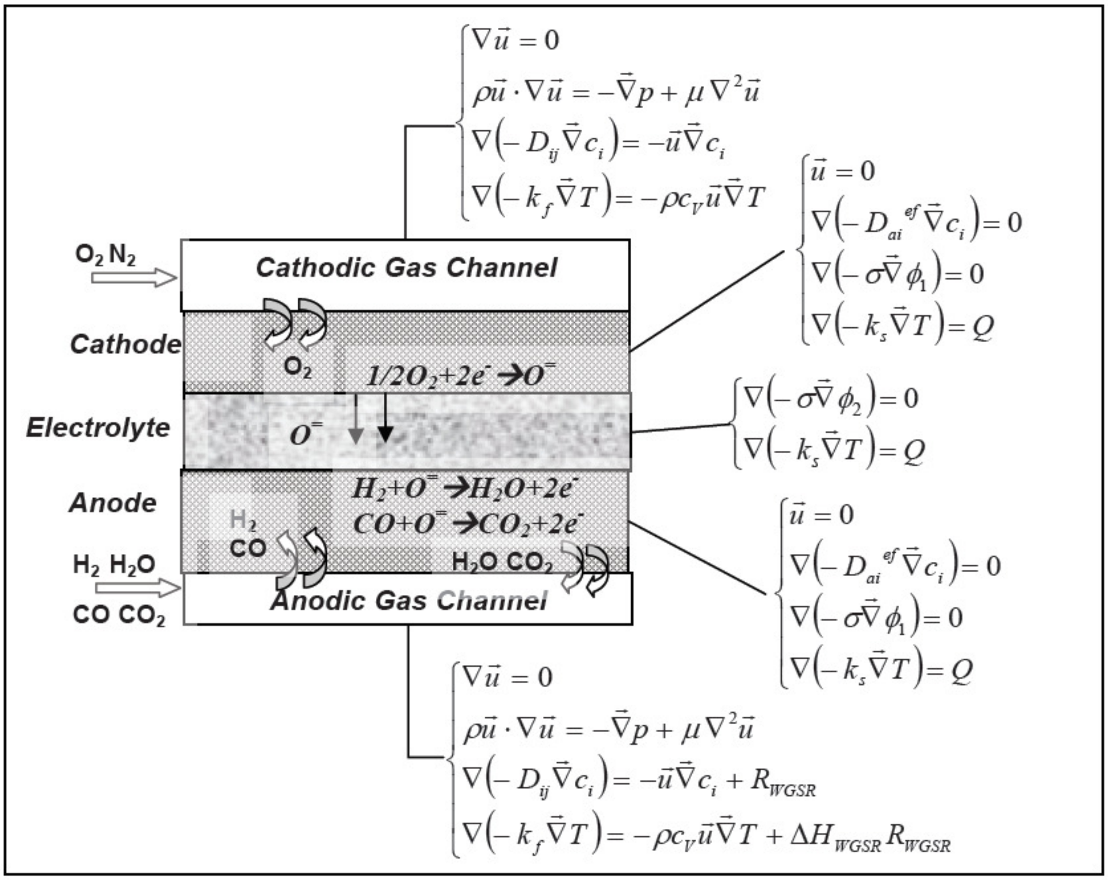

Figure 5-4 Schematic of governing equations applied to each domain

2.6.3 Fluid dynamic sub-model

Gas Channels. The task of the gas channel is to uniformly deliver the gas on the electrode surface. The fuel flow in the gas channels is modeled applying the equation of state and the mass and momentum conservation principles, i.e..

$$\nabla \vec{u} = 0$$

(5) (6)

$$\rho \vec{u} \cdot \nabla \vec{u} = -\nabla p + \mu \nabla^2 \vec{u}$$

where is the velocity vector, p the pressure, ρ and μfluid density and viscosity, respectively. Since gases in SOFCs are far from the critic conditions, perfect gas equation of state is employed $\vec{u}$

$$\rho = \frac{p}{RT \sum y_i / m_i}$$

$$\mu = \sum y_i \mu_i$$

<u>Electrodes.</u> Considering that the total pressure change within the electrodes is negligible (dp/dz ≈ 0), it is assumed that the mass transport through the porous media is driven only by diffusion [12].

2.6.4. Electrochemical sub-model

Mass balance

The electrochemical reaction ideal voltage depends on the reactants partial pressure at the triple phase boundaries through the Nernst law. The reactants concentration at the electrode/electrolyte interface (assumption 5) is evaluated through the species balance as follows:

(9) $$\nabla\left(c \vec{u} \right) = -\nabla \vec{N}_i + R_i$$

where i denotes the generic i-th specie (H_2, H_2O, CO, CO_2, O_2), N is the molar diffusive flux, and R the volume specie source term.

<u>Gas channels</u>.

The molar flux is mainly convective in the gas flow direction and diffusive from the channel to the porous media. The diffusive mass flux is modeled through the Fick's law:

(10) $$\vec{N}_i = -D_{im} \vec{\nabla} c_i$$

where the mixture diffusion coefficient D_{im} takes into account of the diffusion of each species in the gas mixture. The mixture diffusion coefficient of each species *k,* which derives from the Stefan–Maxwell relation, is calculated as [3]:

(11) $$D_{i,m} = \frac{(1 - y_i)}{\sum_{j \neq i} \frac{y_j}{Di_j}}$$

The binary mass diffusion coefficient is given by the Fuller-Schettler-Gidding correlation:

$$D_{ij} = \frac{0.143 \cdot 10^{-6} T^{1.75}}{p M_{ij}^{1/2} \left(v_i^{1/3} + v_j^{1/3} \right)} \quad (12)$$

where

$$(13) \quad M_{ij} = 2\left(\frac{1}{m_i} + \frac{1}{m_j} \right)^{-1}$$

v_i and m_i are the Fuller diffusion volume and the molecular weight of the species i, respectively.

<u>Electrodes</u>. As discussed before, the molar flux is mainly diffusive [12]:

$$(14) \quad \vec{N}_i = -D_{ai}^{eff} \vec{\nabla} c_i$$

The diffusion coefficient in the porous medium is composed of a mixture diffusion coefficient and of the Knudsen diffusion coefficient D_{ikn}^{eff} [11]

$$\frac{1}{D_{ai}^{eff}} = \left(\frac{1}{D_{ij}^{eff}} + \frac{1}{D_{iKn}^{eff}} \right)$$

where the binary diffusion coefficient depends on the porosity (ε), and tortuosity (τ):

$$D_{ij}^{eff} = \frac{\varepsilon}{\tau} D_{ij}$$

and Knudsen diffusion coefficient can be calculated through [11]:

$$D_{iKn}^{eff} = \frac{\varepsilon}{\tau} 97 r_p \sqrt{\frac{T}{m_i}}$$

Water-gas shift reaction (WGSR)

Since, in a SOFC, the shift reaction takes place at high temperatures, it can be assumed to occur very quickly and to be almost in equilibrium [14]. Lehnert et al. [14] reported experimental results for the forward velocity constants k_S^+ and the backward velocity constants k_S^- for the chemical reactions at three different temperatures. Habeman and Young [15] developed empirical correlations for velocity constants with Arrhenius curve fitting technique using experimental data of Lehnert et al. [14] in the temperature range $900<T<1300$K

.

The rate expression R_{WGSR} for shift reaction (reaction 4) can be defined as [13, 11]:

$$(18) \quad R_{WGSR} = k_{WGSR} \left(p_{H2O} p_{CO} - \frac{p_{H2O} p_{CO2}}{k_{eqWGSR}} \right)$$

where k_{WGSR} is the rate constant and $K_{\mathrm{eq,WGSR}}$ the equilibrium constant for the WGSR. The following expression for $\mathrm{k}_{\mathrm{WGSR}}$ has been gotten by fitting an Arrhenius curve to the experimental data given in [11]:

$$(19)\ k_{WGSR} = k_S^+ = 0.0171\exp\left(-\frac{103191}{RT}\right)$$

The temperature dependence of $K_{\mathrm{eq,WGSR}}$ is given by:

$$(20)\ k_{pS} = \frac{k_S^+}{k_S^-} = \exp\left(-0.2935Z^3 + 0.6351Z + 0.3169\right)$$

where

$$(21)\ Z = \frac{1000}{T(K)} - 1$$

Charge balance

Electrodes. Since the electrochemical reactions are considered to take place at electrode/electrolyte interface, only electron transport takes place in the electrode domain. The electric potential (scalar), φ, and the current density (vector), J, are related each other by the Ohm's law:

$$(22)\ \vec{J} = -\sigma\vec{\nabla}\phi$$

where σ is the conductivity of the electrode. Charge conservation is coupled with expression (22) :

$$(23)\ \nabla\vec{J} = 0$$

Electrolyte. In this domain, no mass transport takes place, thus only the ionic potential and current density need to be calculated. Expressions (22) and (23), defined for the electrode, are employed also for modeling the ionic flux within the electrolyte.

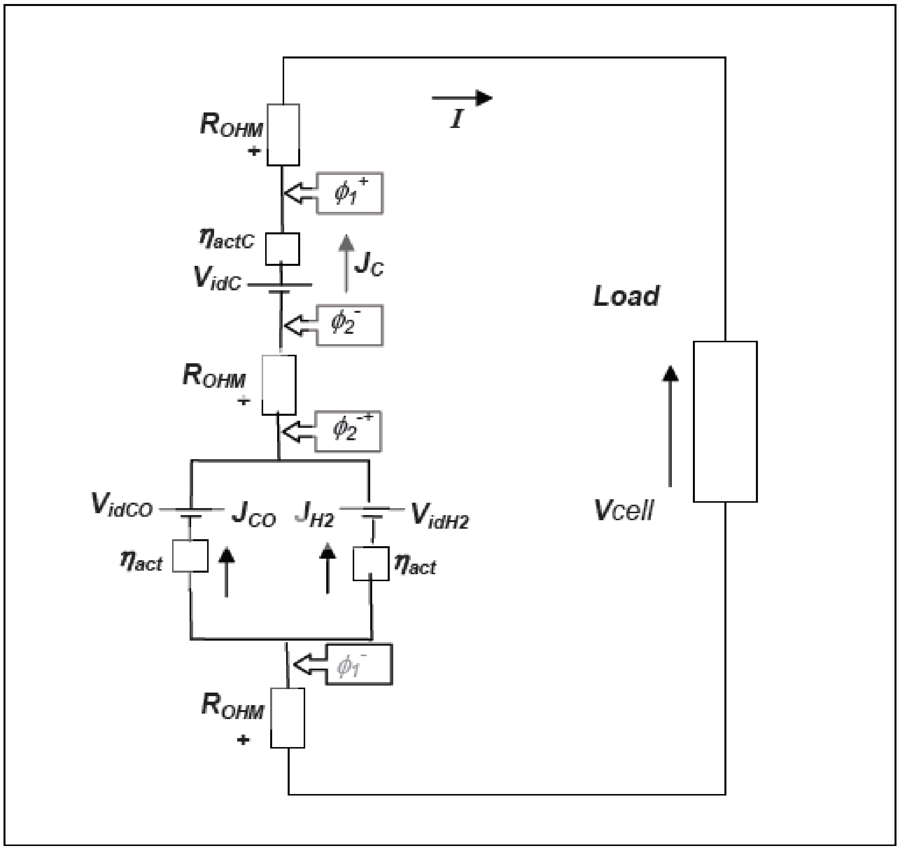

Figure 5-5 Parallel electrical circuit analogy to model simultaneous H_2 and CO oxidation

Interface electrochemical reactions

Using parallel electrical circuit analogy, shown in Figure 5-5, to model the simultaneous H_2 and CO oxidation, the half electrochemical reactions (1), (2), (3) are separately discussed. The electrochemical reaction rate is expressed by the Butler-Volmer Equation:

$$(24)\quad J\cdot\vec{n} = J_0\left[\exp\left(\vartheta_A \frac{F}{RT}\eta_{ACT}\right) - \exp\left(-\vartheta_C \frac{F}{RT}\eta_{ACT}\right)\right]$$

where ϑ_i is the product of the number of transferred electrons in the single elementary rate-limiting step (η_{BV}) and the charge-transfer coefficient (α), J_0 is the exchange current density, and η_{ACT} is the activation overpotential. The two key electrokinetic parameters are the charge-transfer coefficient and the exchange current density. The first one is defined following the approach reported in [5] for a LMS cathode and a Ni/YSZ cermet anode. The exchange current density is expressed as a function of the local species partial pressure.

It is worth of noting that in the hydrogen fed SOFC model updating phase (see Section 4.5.1.), oxygen reduction and hydrogen oxidation have been already characterized. However, for reader's convenience, the equations to be used are here reported.

Oxygen reduction reaction

The oxygen reduction (reaction 1) exchange current density model is given by Achenbach [8]:

$$(25)\quad J_{0C} = \gamma_C \left(\frac{p_{O2}}{p} \right)^{0.25} \cdot \exp\left(-\frac{E_{actC}}{RT} \right)$$

The activation overvoltage η_{act} for O_2 reduction is defined as:

$$(26)\quad \eta_{ACT} = \left(\phi_{electrode} - \phi_{electrolyte} \right) - V_{id}$$

where $V_{id,C}$ is the reversible potential for O_2 reduction:

$$(27)\quad V_{id,C} = \frac{RT}{2F} \ln\left(p_{O2} \right)$$

H_2 and CO oxidation reactions

The hydrogen oxidation (reaction 2) exchange current density model is chosen in accordance with Yamamura et al. [7]:

$$(28)\quad J_{0A} = \gamma_A \left(\frac{p_{H2}}{p} \right) \cdot \left(\frac{p_{H2O}}{p} \right)^{-0.5} \cdot \exp\left(-\frac{E_{actA}}{RT} \right)$$

The activation overvoltage η_{act} for H_2 oxidation is defined as:

$$(29)\quad \eta_{id,H2} = \left(\phi_{anode} - \phi_{electrolyte} \right) - V_{id,H2}$$

where $V_{id,H2}$ is the reversible potential for H_2 oxidation:

$$(30)\quad V_{id,H2} = -E_{0,H2} + \frac{RT}{2F} \ln\left(\frac{p_{H2O}}{p_{H2}} \right)$$

and E^0_{H2} is the ideal potential at standard pressure p and temperature T for H_2 oxidation.

Although the reaction mechanisms of CO oxidation (reaction 3) have been less studied than that of H_2 oxidation, it is believed that the rate-determining step for CO oxidation is similar to that for H_2 oxidation [19]. Setoguchi et al. [20] found that the exchange current density for CO oxidation is the same as that of H_2 oxidation if the partial pressure p_{O2} is similar in both the oxidation processes. This suggests that the exchange current density of CO oxidation can be described by a similar correlation to that of H_2 oxidation, i.e.:

$$(31)\quad J_{0,CO} = \gamma_{H2} \left(\frac{p_{CO}}{p} \right) \left(\frac{p_{CO2}}{p} \right)^{0.25} \cdot \exp\left(-\frac{E_{act,H2}}{RT} \right)$$

However, it was recently found that CO oxidation has a much higher overpotential than H_2 oxidation for the same current density and the difference cannot be attributed to differences in concentration overpotential [21]. This observation agrees with that of Matzusaki et al. [22] who found the rate of CO oxidation to be 2–3 times less than that of H_2 oxidation over the entire range of overpotential and the same partial pressure p_{O2}. Based on this argument, the rate of CO oxidation reaction used in this model is assumed to be 3 times less than that for H2 oxidation reaction, i.e.

$$(32)\ J_{0,CO} = \gamma_{H2}\left(\frac{p_{CO}}{p}\right)\left(\frac{p_{CO2}}{p}\right)^{0.25} \exp\left(-\frac{E_{act,H2}}{RT}\right)$$

The activation overvoltage η_{act} for CO oxidation is defined as

$$(33)\ \eta_{CO} = \left(\phi_{anode} - \phi_{electrolyte}\right) - V_{id,CO}$$

where $V_{id,CO}$ is the reversible potential for H_2 oxidation:

$$(34)\ V_{id,CO} = -E_{0,CO} + \frac{RT}{2F}\ln\left(\frac{p_{CO2}}{p_{CO}}\right)$$

and E^0_{CO} is the ideal potential at standard pressure p and temperature T for CO oxidation.

Finally, the Faraday's law is used to evaluate the molar flux. Since H_2 and CO are oxidized separately at the anode/electrolyte interface, their molar flux will be respectively equal to:

$$(35)\ \begin{cases} N_{H2} = -J_{H2}/2F \\ N_{H2O} = J_{H2}/2F \end{cases}$$

$$(36)\ \begin{cases} N_{CO} = -J_{CO}/2F \\ N_{CO2} = J_{CO}/2F \end{cases}$$

At the cathode/electrolyte interface:

$$(37)\ N_{O2} = -J_C/4F$$

By the charge conservation and the parallel electrical circuit analogy, it results:

$$(38)\ J_c = J_A = J_{H2} + J_{CO}$$

Electrochemical sub-model closure condition

The closure condition of the electrochemical sub-model is given by charge conservation, which imposes the equality between anode/electrolyte and cathode/electrolyte interface consumption-formation of charge, through Eq. 38. This can be described by the anodic and cathodic current density J. Once assigned a test value to the Nernst voltage (species concentration at the TPB) and to the electrode potential (electric problem), the fluctuating electrolyte potential allows determining, in an iterative process, the local activation overpotential η_{act} for each electrochemical reaction. By this way, the equality of the anodic and cathodic local current density is obtained.

In Figure 5-6 a comprehensive representation of all the governing equations solving the electrochemical problem in the different domains together with the boundary conditions is reported.

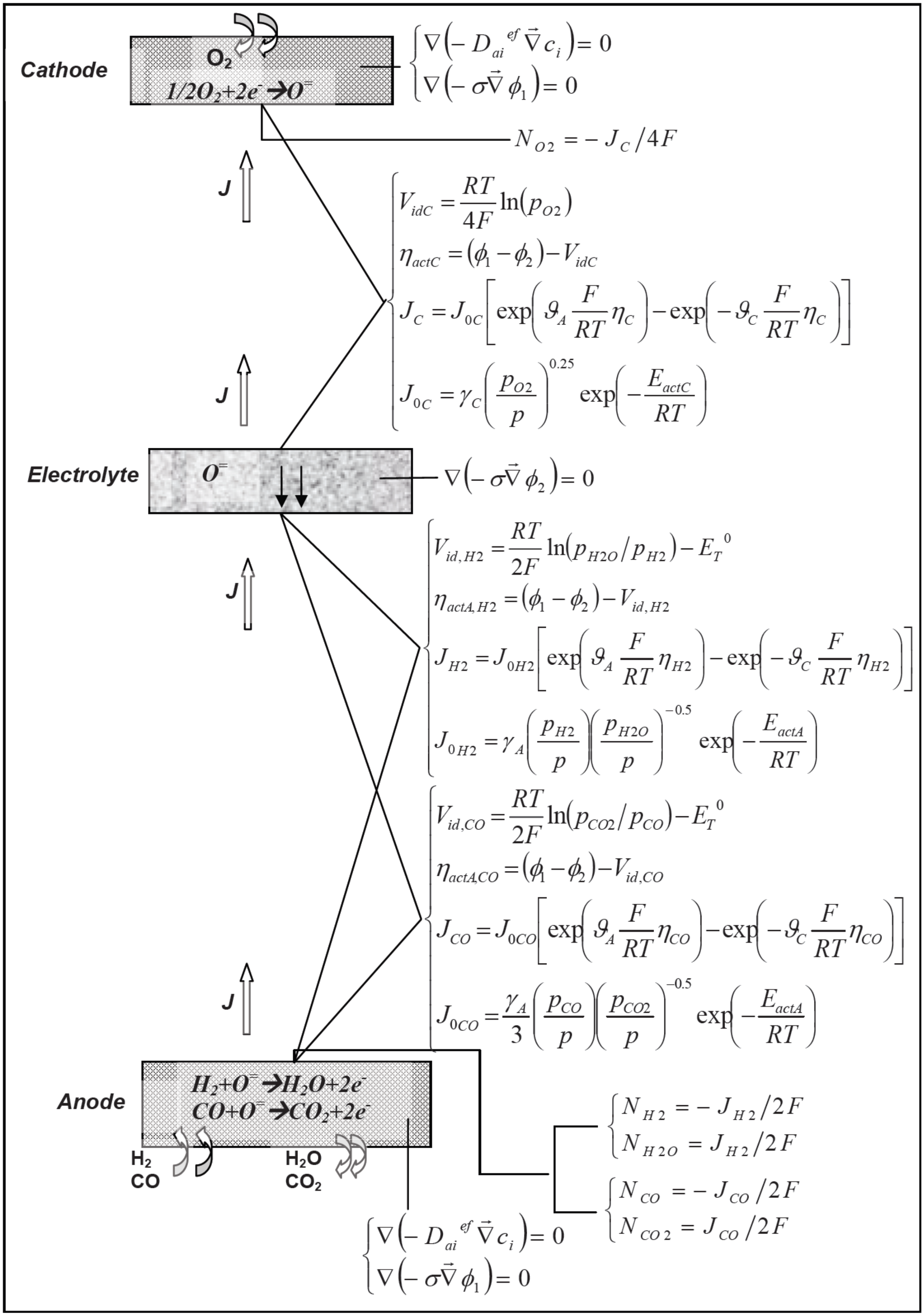

$$\begin{cases}\nabla\left(-D_{ai}{}^{ef}\vec{\nabla}c_i\right)=0\\ \nabla\left(-\sigma\vec{\nabla}\phi_1\right)=0\end{cases}$$

$$N_{O2}=-J_C/4F$$

$$\begin{cases}V_{idC}=\dfrac{RT}{4F}\ln\left(p_{O2}\right)\\ \eta_{actC}=\left(\phi_1-\phi_2\right)-V_{idC}\\ J_C=J_{0C}\left[\exp\left(\vartheta_A\dfrac{F}{RT}\eta_C\right)-\exp\left(-\vartheta_C\dfrac{F}{RT}\eta_C\right)\right]\\ J_{0C}=\gamma_C\left(\dfrac{p_{O2}}{p}\right)^{0.25}\exp\left(-\dfrac{E_{actC}}{RT}\right)\end{cases}$$

$$\nabla\left(-\sigma\vec{\nabla}\phi_2\right)=0$$

$$\begin{cases}V_{id,H2}=\dfrac{RT}{2F}\ln\left(p_{H2O}/p_{H2}\right)-E_T{}^0\\ \eta_{actA,H2}=\left(\phi_1-\phi_2\right)-V_{id,H2}\\ J_{H2}=J_{0H2}\left[\exp\left(\vartheta_A\dfrac{F}{RT}\eta_{H2}\right)-\exp\left(-\vartheta_C\dfrac{F}{RT}\eta_{H2}\right)\right]\\ J_{0H2}=\gamma_A\left(\dfrac{p_{H2}}{p}\right)\left(\dfrac{p_{H2O}}{p}\right)^{-0.5}\exp\left(-\dfrac{E_{actA}}{RT}\right)\end{cases}$$

$$\begin{cases}V_{id,CO}=\dfrac{RT}{2F}\ln\left(p_{CO2}/p_{CO}\right)-E_T{}^0\\ \eta_{actA,CO}=\left(\phi_1-\phi_2\right)-V_{id,CO}\\ J_{CO}=J_{0CO}\left[\exp\left(\vartheta_A\dfrac{F}{RT}\eta_{CO}\right)-\exp\left(-\vartheta_C\dfrac{F}{RT}\eta_{CO}\right)\right]\\ J_{0CO}=\dfrac{\gamma_A}{3}\left(\dfrac{p_{CO}}{p}\right)\left(\dfrac{p_{CO2}}{p}\right)^{-0.5}\exp\left(-\dfrac{E_{actA}}{RT}\right)\end{cases}$$

$$\begin{cases}N_{H2}=-J_{H2}/2F\\ N_{H2O}=J_{H2}/2F\end{cases}$$

$$\begin{cases}N_{CO}=-J_{CO}/2F\\ N_{CO2}=J_{CO}/2F\end{cases}$$

$$\begin{cases}\nabla\left(-D_{ai}{}^{ef}\vec{\nabla}c_i\right)=0\\ \nabla\left(-\sigma\vec{\nabla}\phi_1\right)=0\end{cases}$$

Figure 5-6 Schematic of governing equations together with the boundary conditions solving the electrochemical problem

2.6.5 Thermal sub-model

The thermal sub-model allows calculating the local temperature distribution, which affects the fuel cell performance by means of the electrochemical reaction rate, the electrode overpotential, the electrical and ionic conductivity and fluid properties.

Heat is generated inside the solid structure and by the shift reaction, and it is predominantly removed by convection heat transfer with the air and fuel flowing in the channels. Even if the operating temperature is high, we assume that radiation is negligible in comparison with the other heat transfer mechanisms [10]. The temperature profiles is obtained through the energy equation:

$$(39)\quad \rho c_v \vec{u}\cdot\vec{\nabla} T = -\nabla \vec{q} + Q$$

where is the conductive heat flux, and Q is composed of the ohmic volumetric heat source:

$$(40)\quad Q = \sigma \vec{\nabla}\phi \vec{\nabla}\phi$$

and of the heat generated by WGSR (reaction 4). When the reaction rate R_{WGSR} is determined, this term is expressed by:

$$(41)\quad Q = \Delta H_{WGSR} R_{WGSR}$$

The conductive heat flux is expressed by the Fourier's law:

$$(42)\quad q = -k\vec{\nabla} T \quad \begin{cases} k = k_f & \left(gas\,channels\right) \\ k = k_s & \left(solids\right) \end{cases}$$

Finally, the interface electrochemical reactions introduce the following boundary heat sources:

- reversible heat generation at the anode:

$$(43)\quad q_{irr} = T\Delta S_T (J/2F)$$

- irreversible heat generation at both the anode and the cathode:

$$(44)\quad q_{irr} = \eta_{act} J$$

The external boundary conditions of this sub-model are reported in Figure 4-12.

2.6.6 External boundary conditions

The external boundary conditions on V, T, c_i and $u_\rightarrow$ are defined as follows:

Inlet: Inlet conditions are defined by the operating conditions, summarized in Table 5-1

Lateral: Periodic conditions are considered on the lateral boundary as the analyzed geometry is the smallest non-repeating geometrical pattern of the whole cell (see Figure 4-9).

Top/bottom: No slip condition is imposed to the velocity field and as the SOFC ceramic support is considered at thermal equilibrium with the external furnace then giving a constant temperature value.
Outlet: Convective fluxes are considered at the cell outside. The convection and radiation heat exchange mechanisms between the solid structure and the external furnace can be expressed as:

$$(45)\quad q_{conv} = h_c\left(T_F - T\right)$$

$$(46)\quad q_{rad} = f\,\sigma_c\left(T_F{}^4 - T^4\right)$$

where h_C, *f*, and σ_{rad} are, respectively, the convective heat transfer coefficient, the total emissivity, and the Stefan–Boltzmann constant. T_F is the furnace temperature. Another heat source is given by the combustion of the non-oxidized fuel mass as it meets oxygen at the cell outlet.

Afterburning – By considering a complete CO consumption-shift conversion in the cell, the afterburning heat source is evaluated as follows:

$$(47)\quad q_{afterburning} = \frac{\left(H_{2out}\cdot H_i\right)}{S_{anode}}$$

where

$$(48)\quad H_{2out} = \rho\left[\left(H_2 + CO\right)_{in} - \frac{I}{2F}\right]$$

Therefore, on the polarization curve basis, starting from the knowledge of the current and of $\left(H_2 + CO\right)_{in}$, the afterburning heat source and the function $q_{afterburning} = f\,(Vcell)$ can be defined.

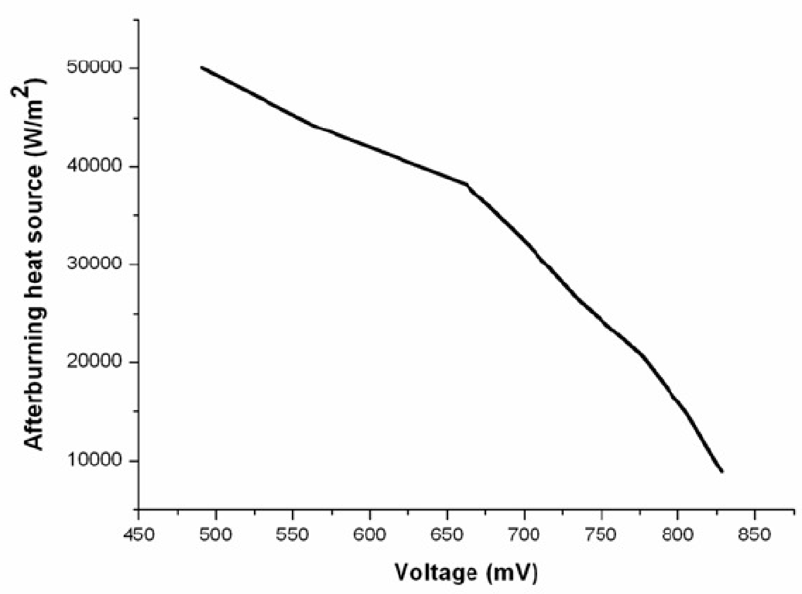

Figure 5-7
Afterburning heat source as function of cell voltage

Inlet gas temperature – Inlet hydrogen temperature is directly available on the basis of the experimental measurements as a thermocouple is located close to the SOFC inlet. On the other hand, air inlet temperature is not measured. Accordingly, a 0D model has been developed. Calculation and results are summarized in Section 4.4.4., where it was found that air reaches the equilibrium with the furnace at 800°C.

2.6.7 Solution technique

A finite element computational package, FEMLAB, is used to solve the described non-linear system of equation. A 3D unstructured triangular mesh is considered in the present calculations. To allow numerical solution, it was necessary to reduce the mesh elements number in comparison whit the hydrogen fed SOFC case. Thus, the mesh is composed of 24900 elements and is sketched in Figure 5-8. The results have been checked for grid sensitivity and the trends are observed to be consistent in all the investigated cases in terms of polarization curve as the numerical results are included within a 5% of difference when increasing the grid detail level.

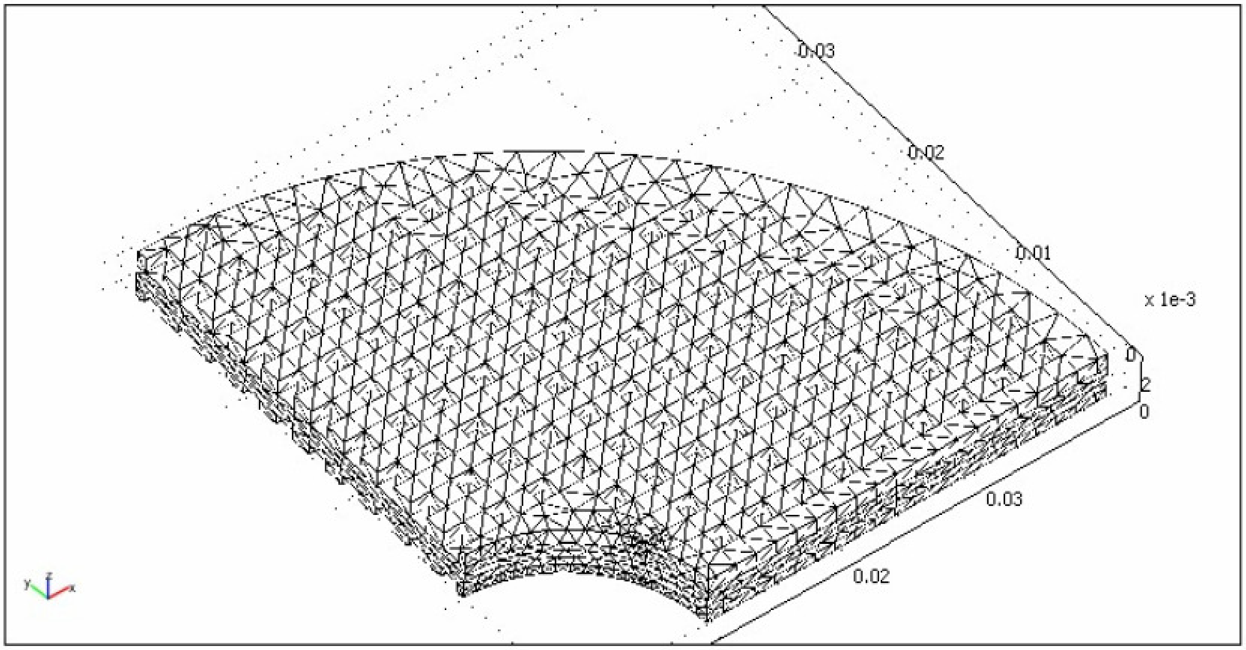

Figure 5-8 Computational mesh

The iterative solution algorithm is reported in Figure 5-9. As it is possible to notice, even if the model sub-problems are fully coupled, to perform an efficient management of computer

resources and to reduce the computational time, the numerical convergence is reached in an iterative way, called “frozen fields”. The electrochemical sub-model is firstly solved starting from a tentative velocity and a temperature profile, so evaluating species distribution and electrochemical quantities. These data are exchanged with the fluid dynamic sub-model and the thermal sub-model. This process is repeated until convergence is reached.

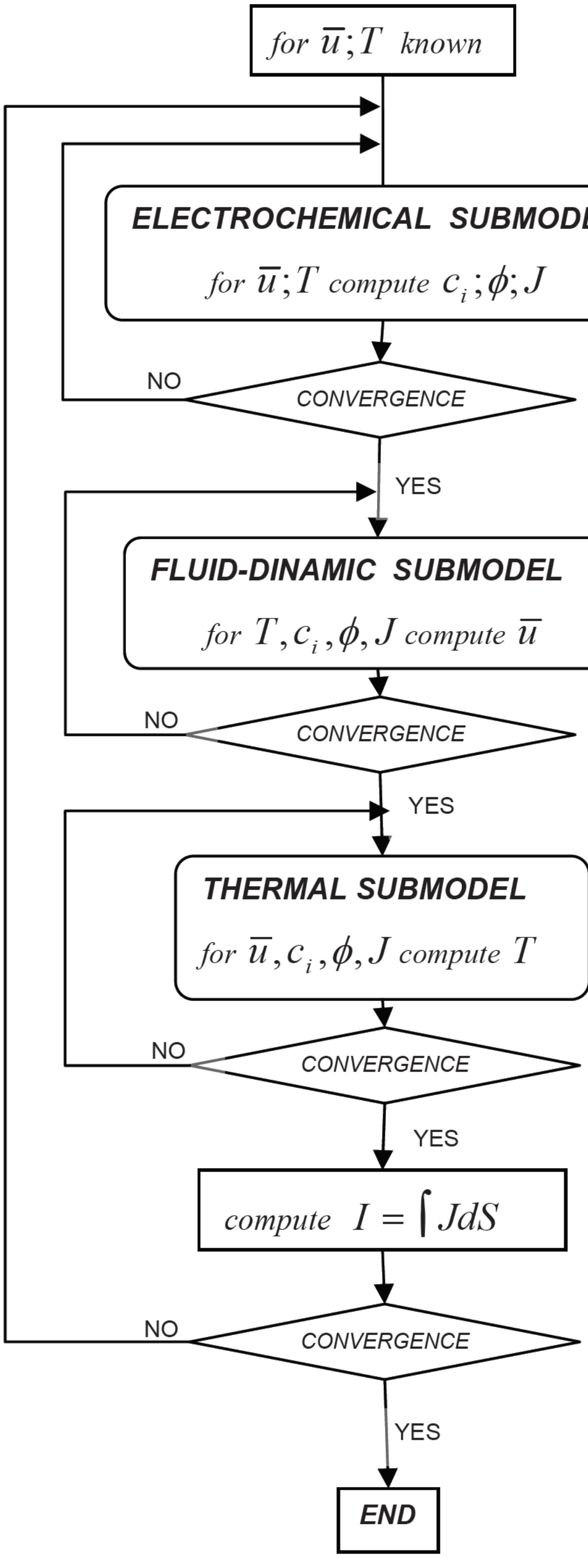

Figure 5-9 Solution algorithm

2.7 Model validation and results

This section presents the comparison between the numerical data provided by the 3D numerical code and the experimental data of the single cell ASC1.

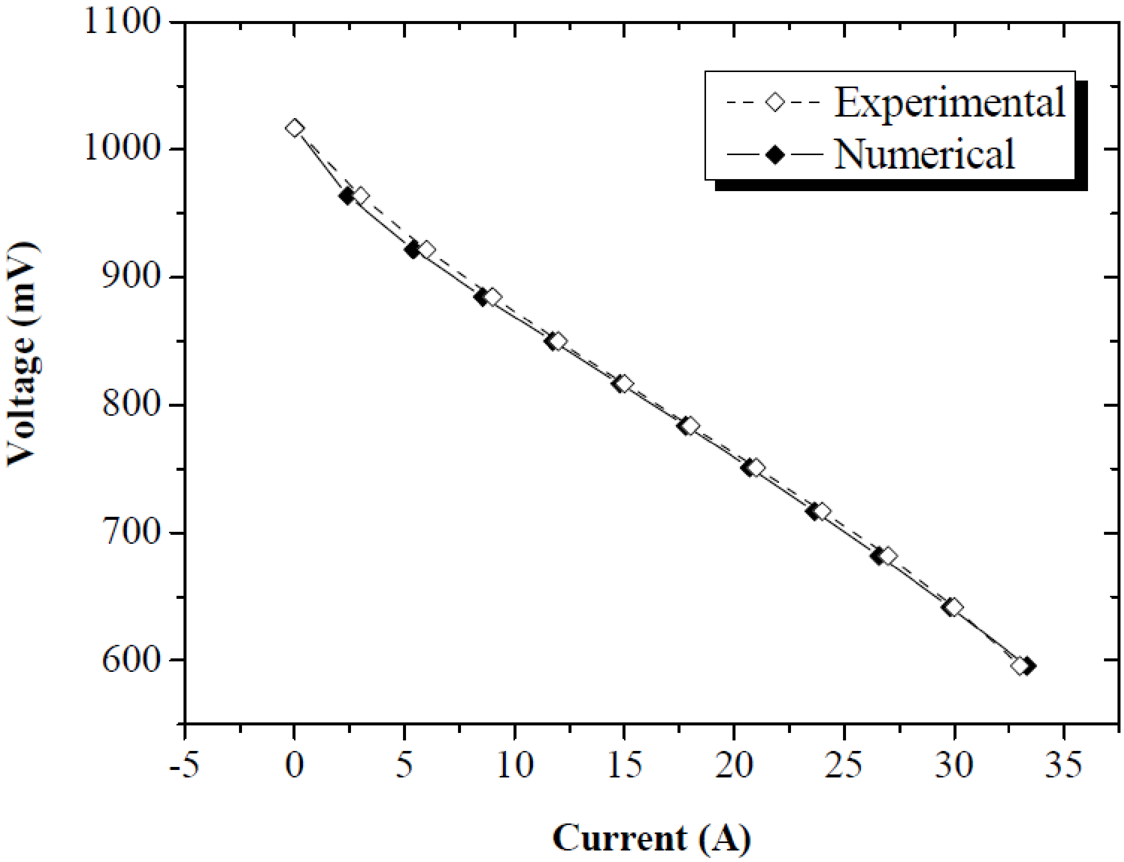

Figure 5-10 Numerical and experimental polarisation curve for updating phase

2.7.1 Model validation

The University of Perugia testing laboratory procedure to verify cell stability (cell update) is based on hydrogen fed SOFC polarization curve, even if the cell is subsequently fed whit pre-reformed gases. Following this approach, the model updating phase is made on the same testing laboratory polarization curve. As this cell operation has been well established in the dedicated study (see Section 4.5.1.), as reported in Figure 5-10 , the whole set of input parameters obtained for SOFC using hydrogen as fuel are still valid. For reader convenience, they are reported in Table 5-2.

It is important to underline that the use of the same polarisation curves obtained in Section 4.5.1. for the syngas fed SOFC updating phase represent a hard and important benchmark test. The good accordance between experimental and numerical results, shown in the following, demonstrates the numerical code wide range validity.

The model validation has been carried out by comparing numerical and experimental data varying both fuel flow rate and utilisation coefficient, defined as follows:

$$U_f = \frac{J}{J_f}$$

being J the actual current density (on the basis of the amount of reactants consumed) and J_t the theoretically expected current density assuming that the overall reaction in the fuel cell is complete. Since each mole of hydrogen or carbon monoxide that reacts in the anode frees two moles of electrons, the fuel utilisation factor can be correlated to the inlet flow rate as:

$$U_f = \frac{J}{(2F)(H_2 + CO)}$$

To determine each reacting species flow rate , the carbons factor, $C_f = \frac{CO}{(H_2 + CO)}$ has been set constant to 0.2.

Using the inlet oxygen flow rate, the oxidant utilization coefficient, $U_{ox} = \frac{J}{4F \cdot O_2}$, has been kept constant to 0.4 that ensure enough oxygen at the highest current density.

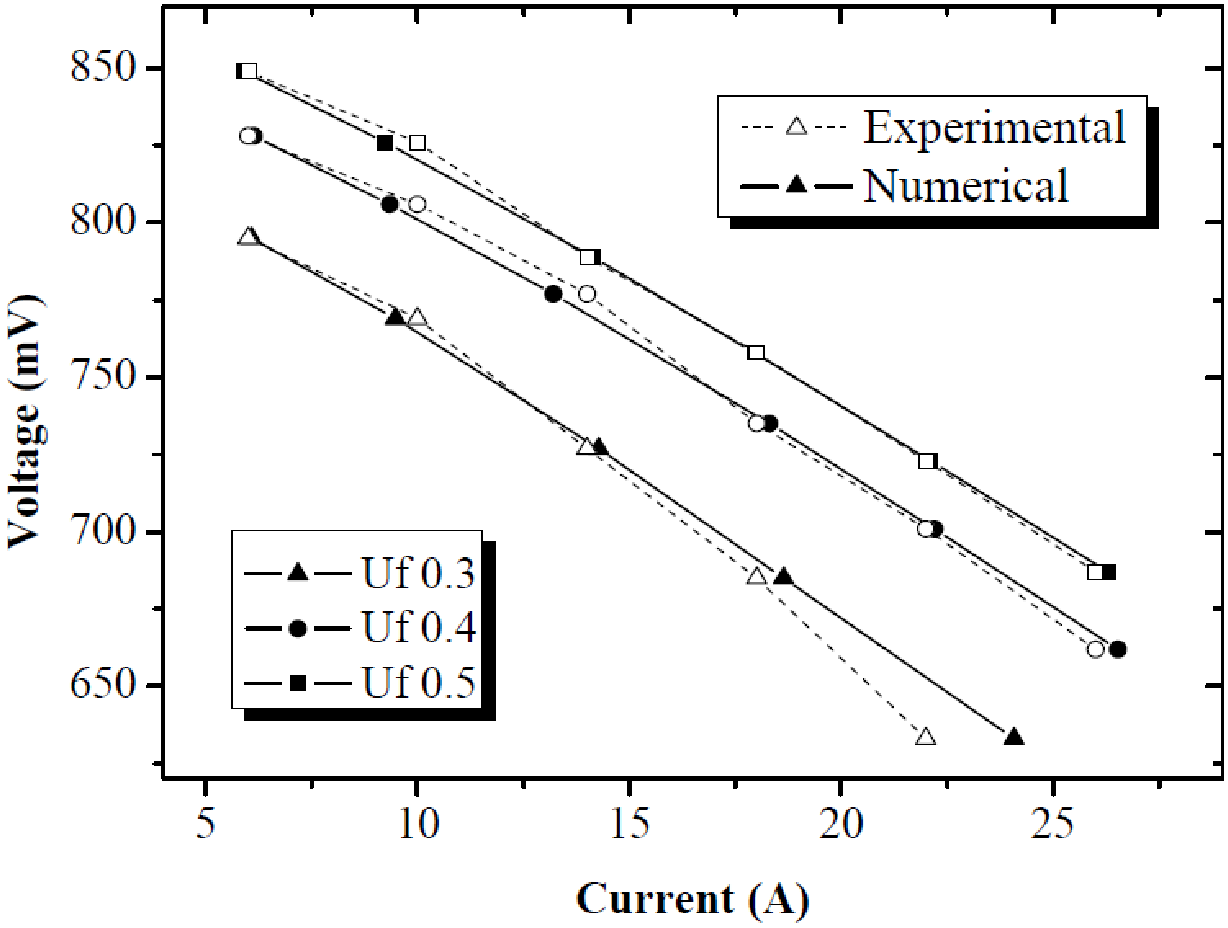

Figure 5-11 Numerical and experimental current-voltage curves with constant fuel (U_f) and oxidant (U_{ox}) utilization coefficients

Figure 5-11 presents the comparison between numerical and experimental results for three current density-voltage curves with constant fuel and oxidant utilization coefficients (U_f = 0.3,0.4,0.5 and U_{ox} = 0.4) and variable flow rates. In comparison to the available data (see Figure 5-2), the numerical results have been considered till to 26 A. After this value (red line of Figure 5-2) the experimental results introduce an inexplicable cell performance decrease, thus they have been considered not enough consistent. In the range just defined, the agreement between numerical and experimental data is excellent. Little differences can be observed at high current densities for U_f = 0.5, while the numerical profile at U_f=0.4 and 0.3 is almost superimposed to the numerical one. The percentage errors between numerical and experimental is everywhere within 5%.

About syngas fed SOFC, the great part of models in the literature [16, 15, 2] supposes that only H_2 is oxidized at the anode when CO is shifted to produce H_2. Contrary, this code considers the direct oxidation of the carbon monoxide together with hydrogen oxidation, by using the parallel electrical circuit analogy.

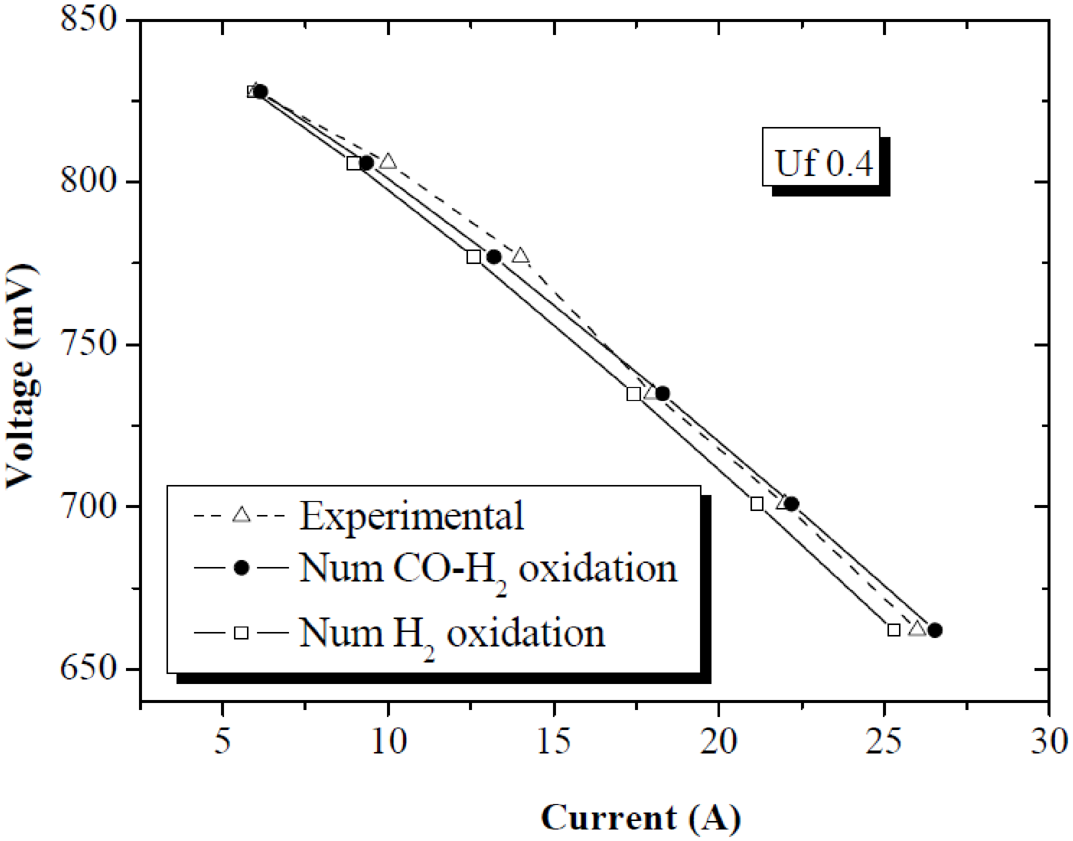

Figure 5-12 Numerical and experimental current-voltage curve for H_2 oxidation and the simultaneous H_2-CO oxidation (considering WGS within fuel channel in both cases)

In Figure 5-12, two numerical curves are compared to the experimental data. The first profile is derived supposing that CO is only shifted while the second one is obtained considering both the CO shifting and direct oxidation. Carbon monoxide direct oxidation, negligible for low current density, at high current becomes an effect to be absolutely considered. By this way, it can be seen the importance of H_2 and CO simultaneous oxidation models to correctly predict the syngas fed SOFC behaviour.

The 3D numerical code, here dealt with, allows also calculating the amount of current produced by CO oxidation and by H_2 oxidation. In Figure 5-13, the two contributions are separately drawn. It is worth of noting that the relationship between the numerical CO total current versus the cell total current is constant to 12.5%, in all the investigated operating condition. About this value, L. Petruzzi et al. [17] found a contribution of the CO of 13.8% on current basis, for the operating conditions of 0.8 V and 72 W single cell electrical power. In that case, the fuel mixture composition was of 24%CO, 26%H_2, 46%N_2, 1.5%H_2O, 2.5%CO_2 volume.

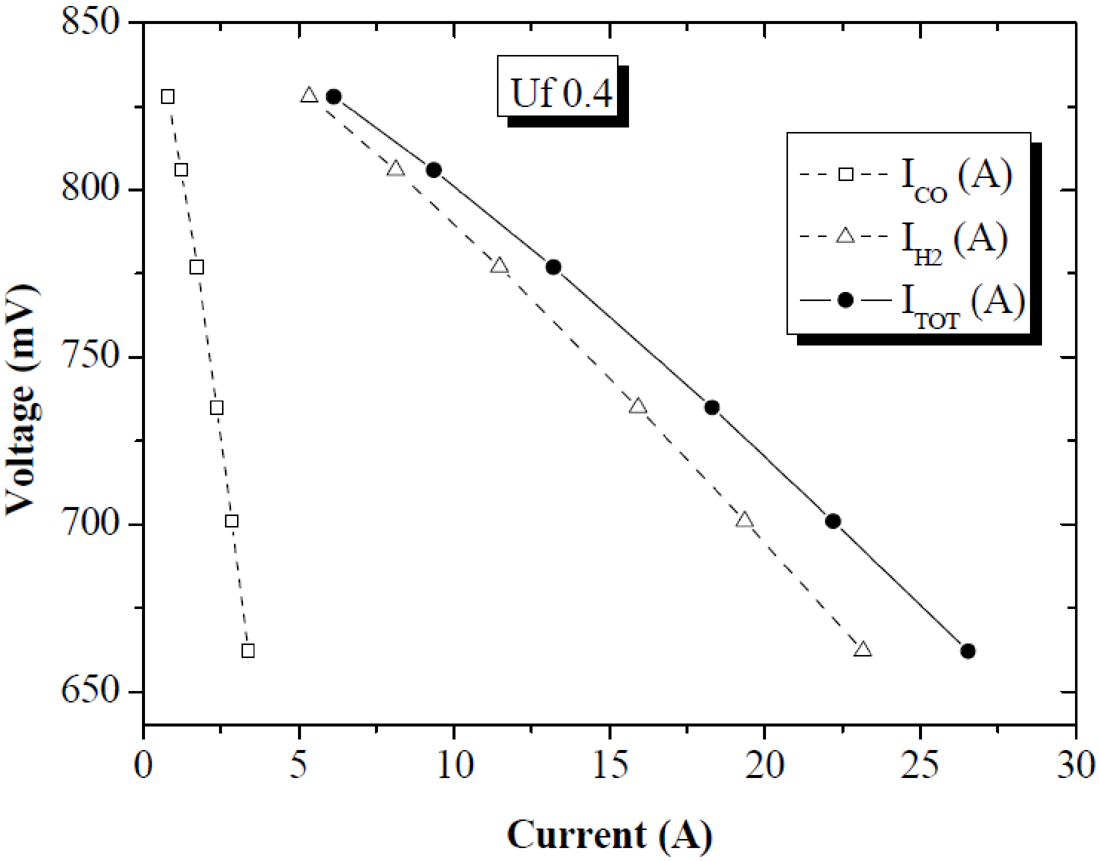

Figure 5-13 Hydrogen and carbon monoxide contributions to cell performance

2.7.2 Analysis of results

Once validated the model, the following maps show some aspects occurring at cell operation condition summarized in Table 5-1.

Flow field: Flow field vectors are reported in Figure 5-14. The presence of the ribs strongly affects the flow field. Preferential flow directions can be observed along the x and y directions; while the flow is mostly broken in the central zone. This reduces reactants feeding efficiency.

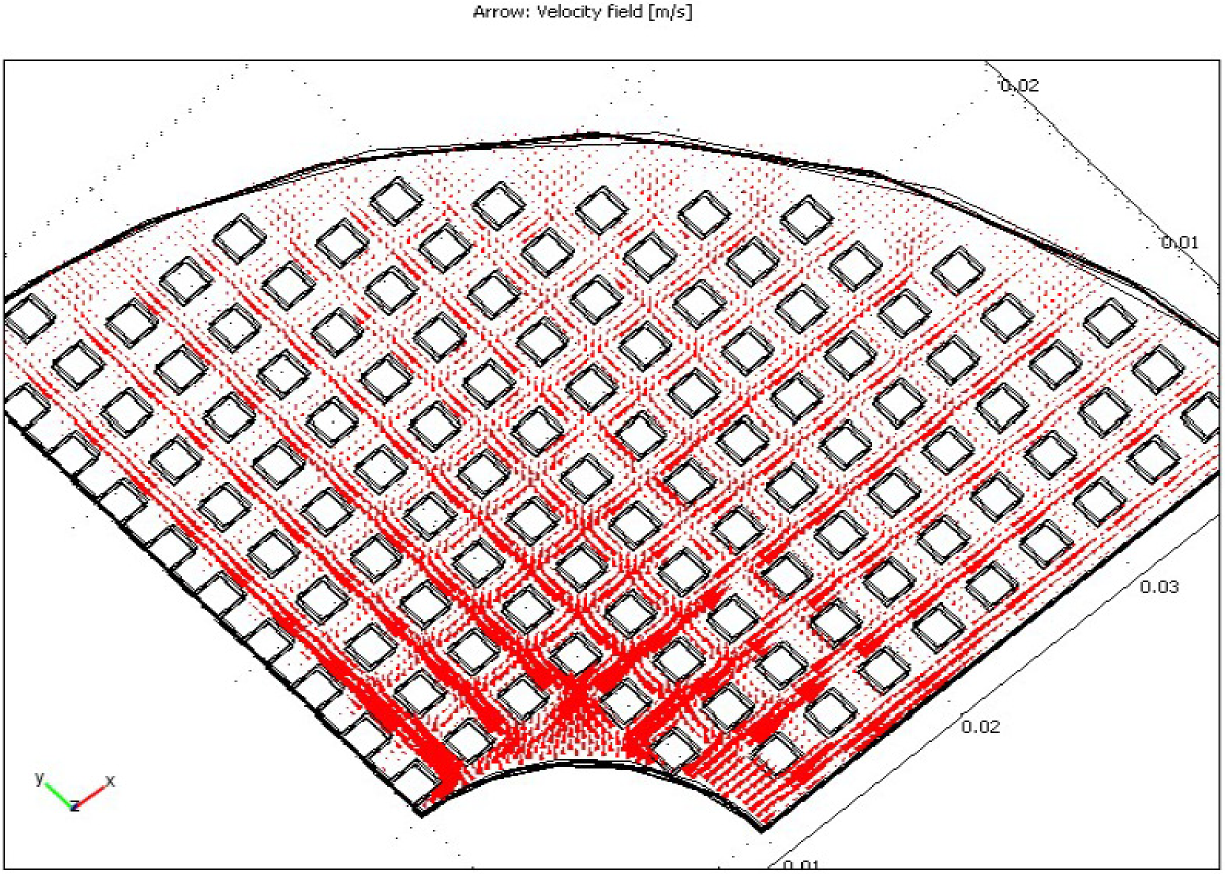

Figure 5-14 Flow field arrows on the cathodic side

(O_2=11.5 Nl/h, cell voltage 0.7V, total current 22 A)

Water-gas shift reaction: The shift reaction rate R_{WGSR} is shown in Figure 5-15. The carbon monoxide conversion in hydrogen is almost positive elsewhere, and it increases moving to the cell outlet because of the major H_2 electrochemical consumption with respect to CO. At the cell outlet, the afterburning produced increase of temperature (see Figure 5-26) inverts the reaction direction.

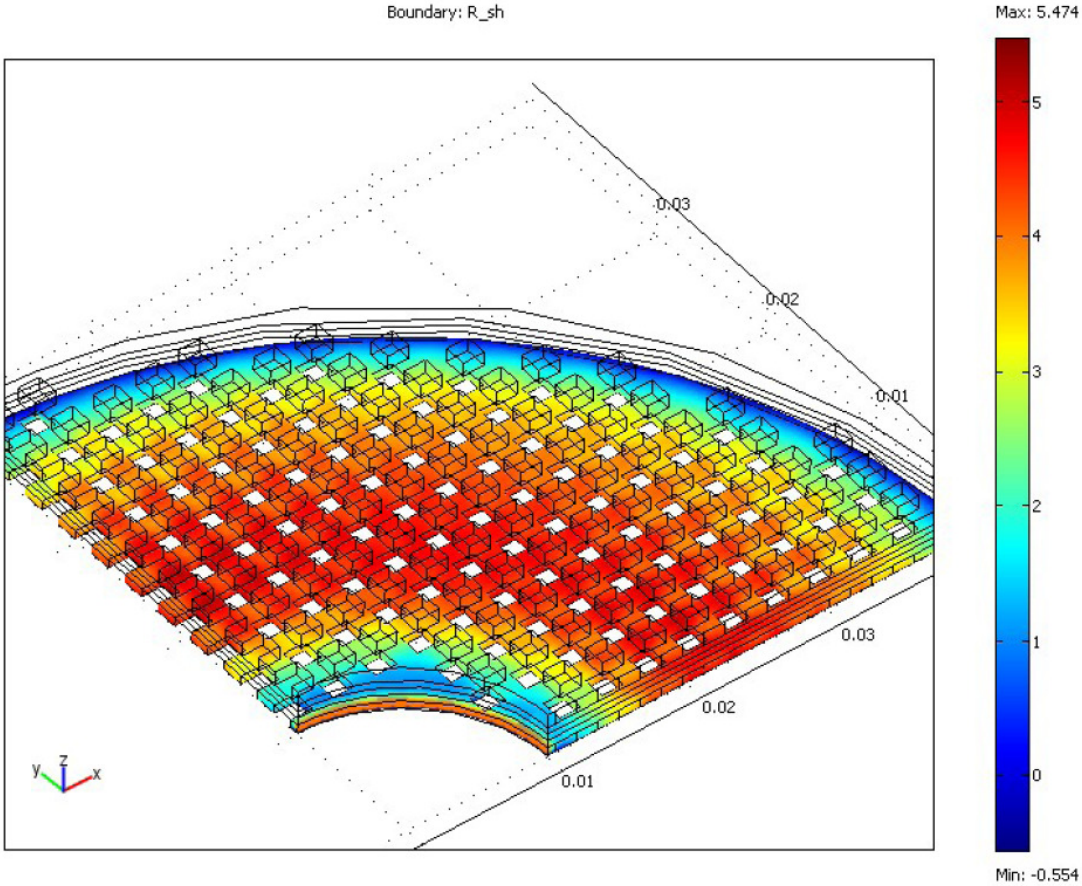

Figure 5-15 Shift reaction rate within the fuel channel

(H_2=18.45 Nl/h, CO=4.60 Nl/h, cell voltage 0.7V, total current 22 A)

Species concentration: Reactants (H_2, CO, O_2) concentration along the gas channels are reported in Figures 5-16. Highest values are located at the cell inlet, while a progressive hydrogen, carbon monoxide and oxygen consumption is observed moving to the cell outlet.

Hydrogen, carbon monoxide, and oxygen concentration at the electrode/electrolyte interface are shown in Figure 5-17, 5-18 and 5-19, respectively. It is worth of noting that a lower concentration of the reacting species is observed under the ribs. Cross-plane and in-plane diffusion effects, described in Section 4.5.2. , prevent species diffusion under the ribs. Hence, the reactants concentration on the electrode/electrolyte interface locally decreases, so reducing the overall cell performance. The ribs effect is significant at any operating condition, but it becomes predominant at high fuel utilization.

For better accuracy, in Figure 5-20, 5-21 and 5-22 a slice view of reactants concentration along the 0°, 22.5° and 45° angular direction is given. Moreover, comparing the figures, it can be observed that cross-plane and in-plane diffusion effects are more important for carbon monoxide and oxygen than for hydrogen because of their lower diffusivity.

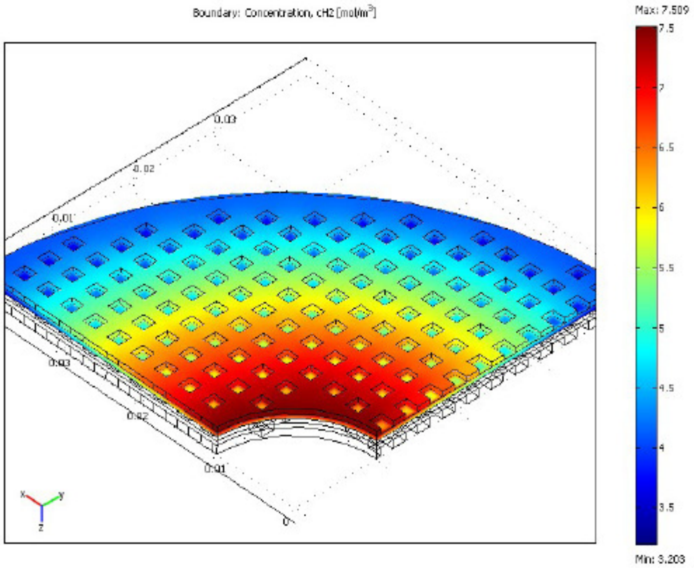

Hydrogen concentration along the fuel channels (H_2=18.45 Nl/h, cell voltage 0.7V, total current 22 A)

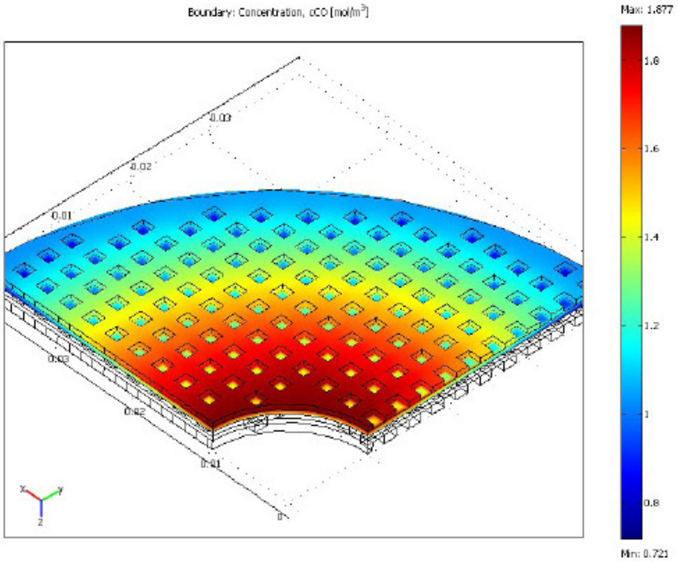

Carbon monoxide concentration along the fuel channels (CO=4.60 Nl/h, cell voltage 0.7V, total current 22 A)

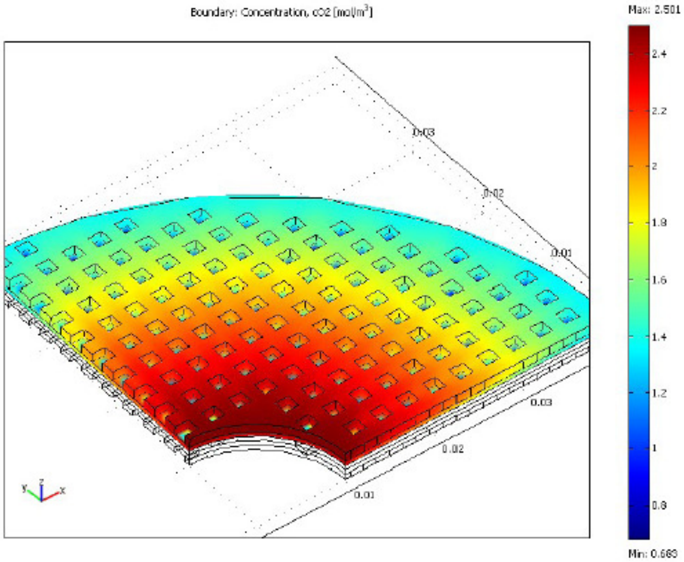

Oxygen concentration along the air channels (O_2=11.5 Nl/h, cell voltage 0.7V, total current 22 A)

Figure 5-16 Hydrogen, carbon monoxide, and oxygen concentration along gas channels

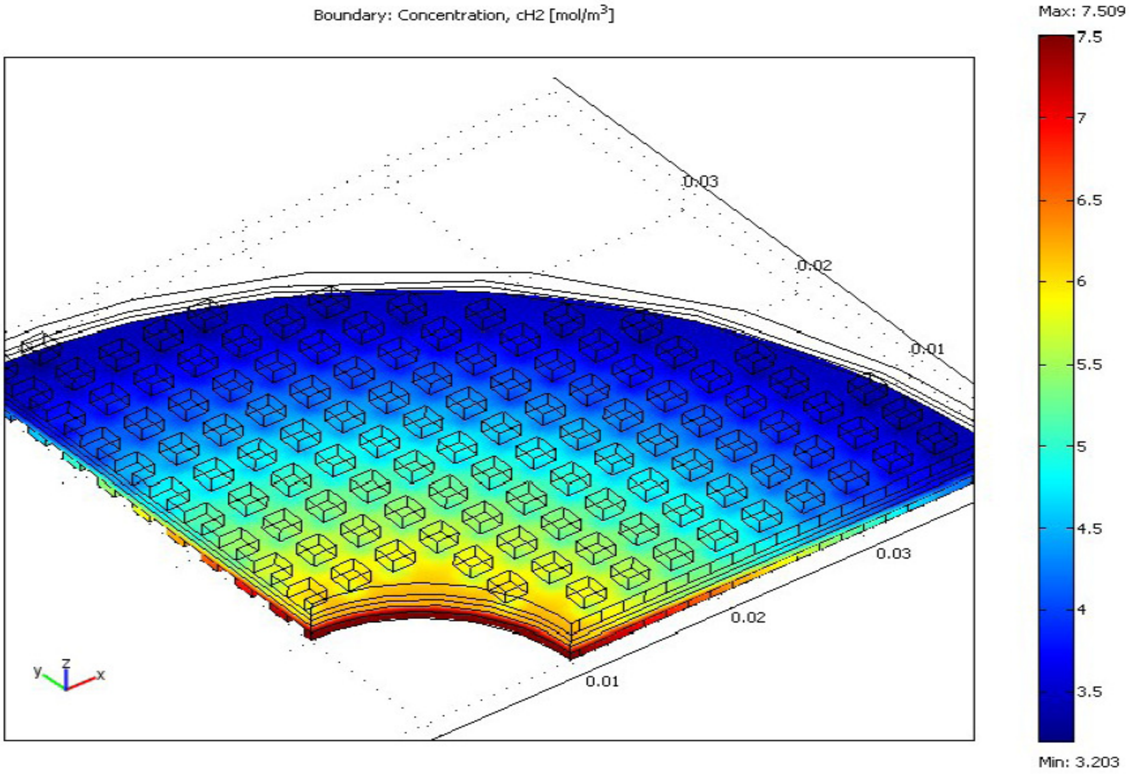

Figure 5-17 Hydrogen concentration at anode/electrolyte interface

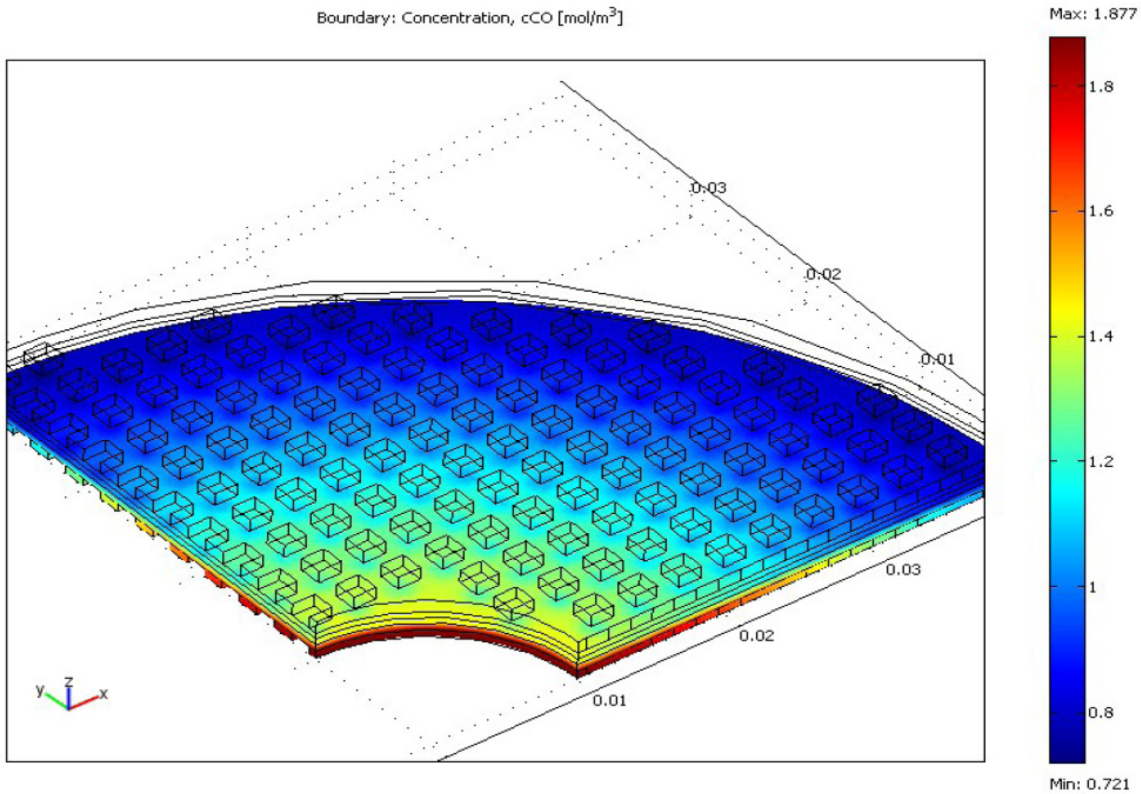

Figure 5-18 Carbon monoxide concentration at anode/electrolyte interface

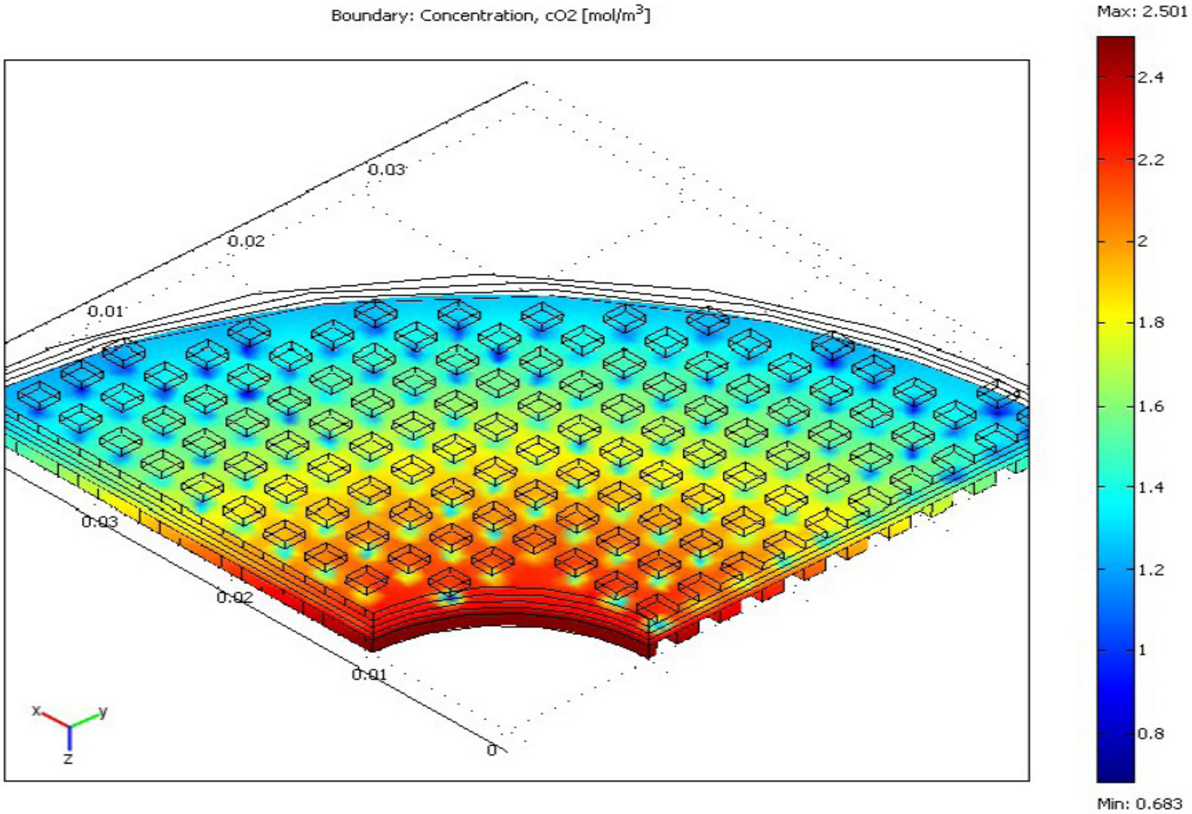

Figure 5-19 Oxygen concentration at cathode/electrolyte interface

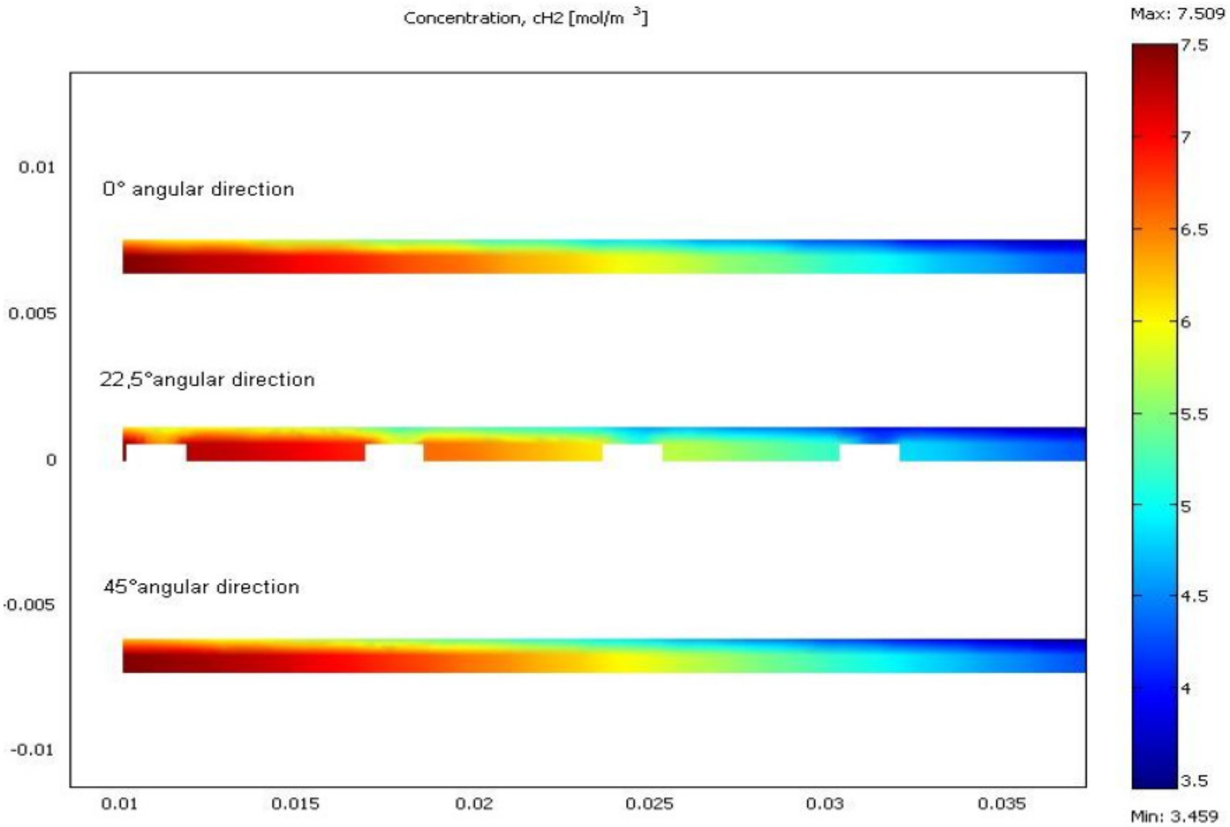

Figure 5-20 Hydrogen concentration along 0°, 22.5°, and 45° angular direction

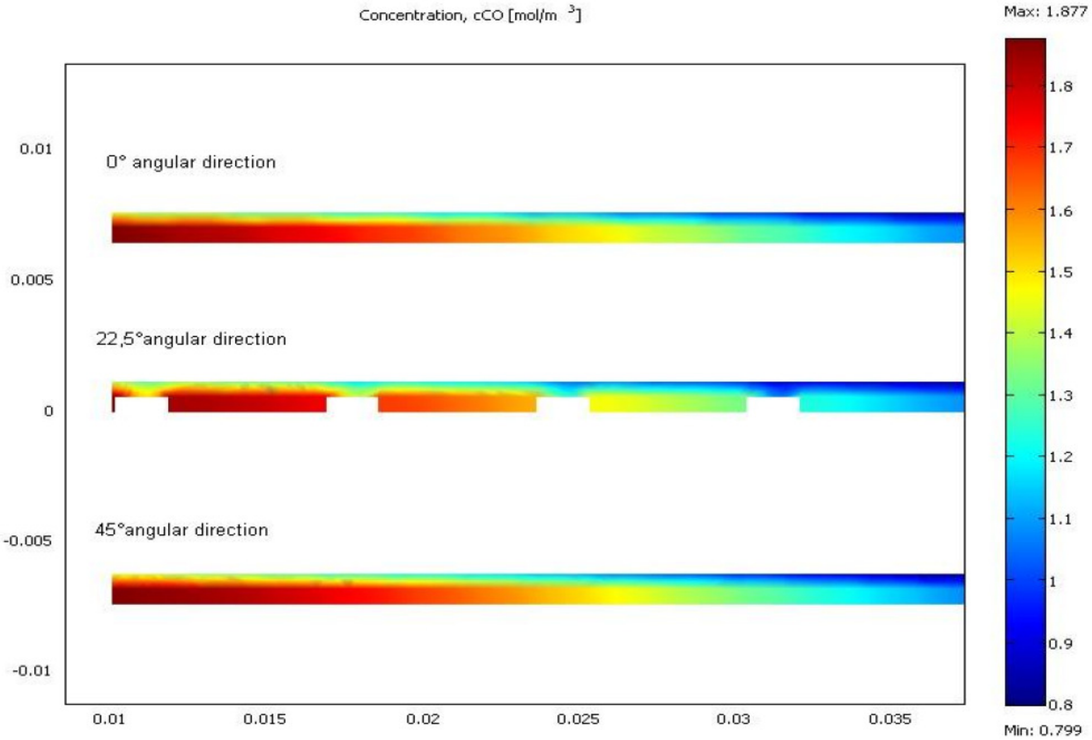

Figure 5-21 Carbon monoxide concentration along 0°, 22.5°, and 45° angular direction

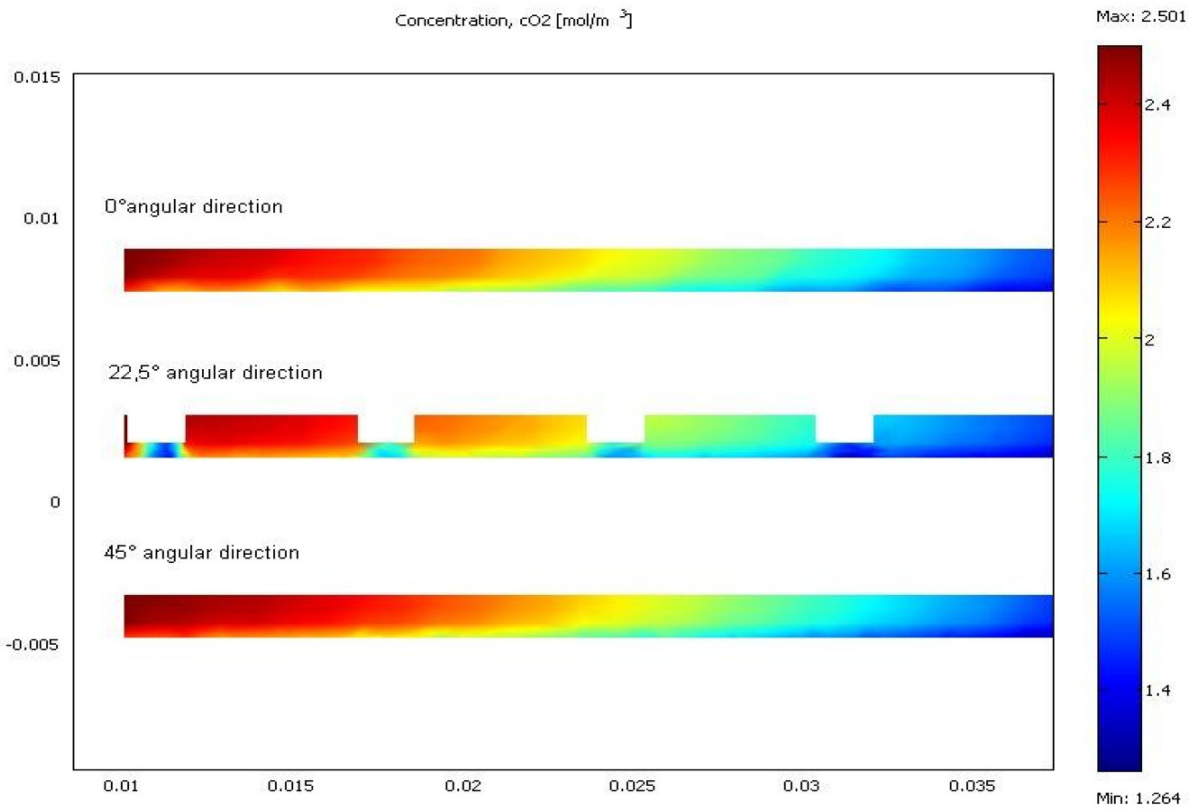

Figure 5-22 Oxygen concentration along 0°, 22.5°, and 45° angular direction

Current density: The total current density distribution at the cathode/electrolyte interface is shown in Figure 5-23. The current density is not uniform as it is affected by the H_2, CO, O_2 distributions and by the electrolyte resistance which is, in turn dependent on temperature. Because of the previously discussed reasons, under the ribs the produced current is smaller than elsewhere. Furthermore, around the ribs, it is possible to observe that the produced current is characterized by a localized peak, as explained in Section 4.5.2.

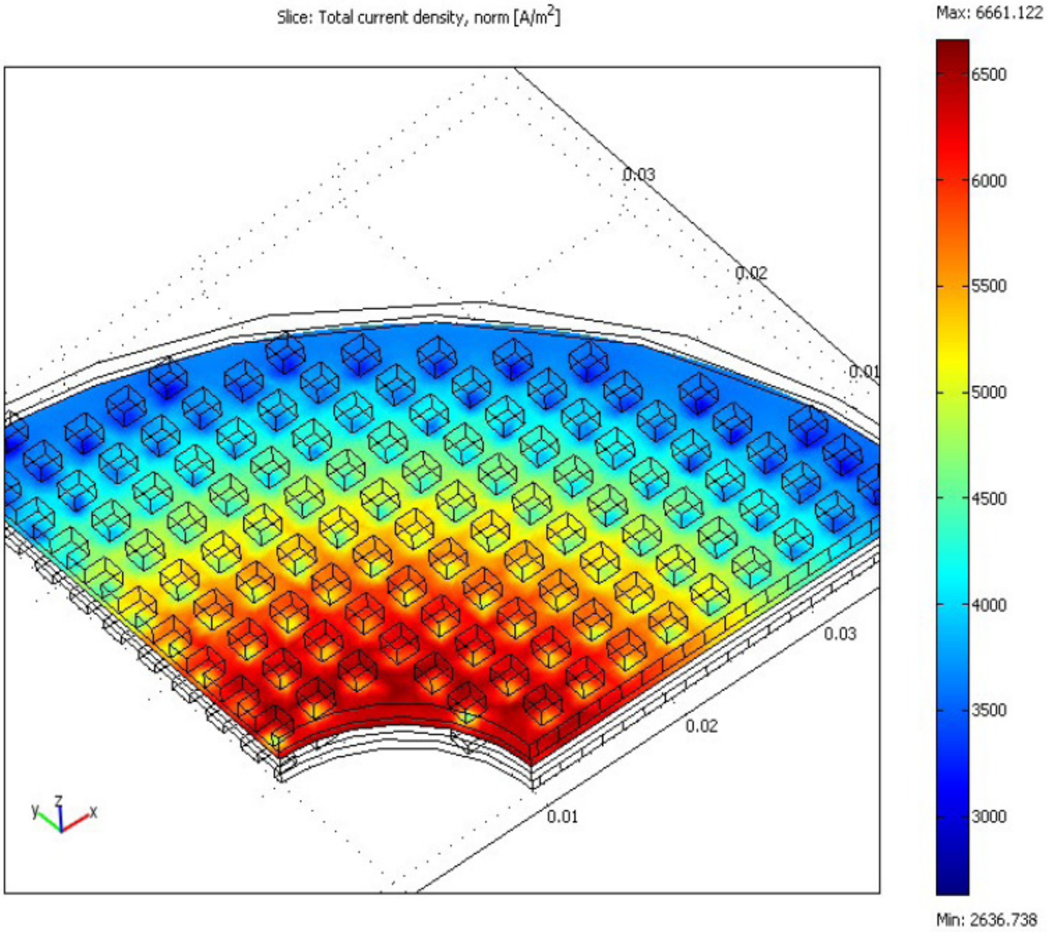

Figure 5-23 Current density distribution (cell voltage 0.7V, total current 22 A)

In Figures 5-24, and 5-25 the hydrogen and carbon monoxide produced current distribution at the anode/electrolyte are reported. Even if the spatial distributions are quite similar, it is of interest the different scale is to be emphasized (12.5% of the total cell current is produced by CO). In all the investigated operating condition, this relationship remains constant.

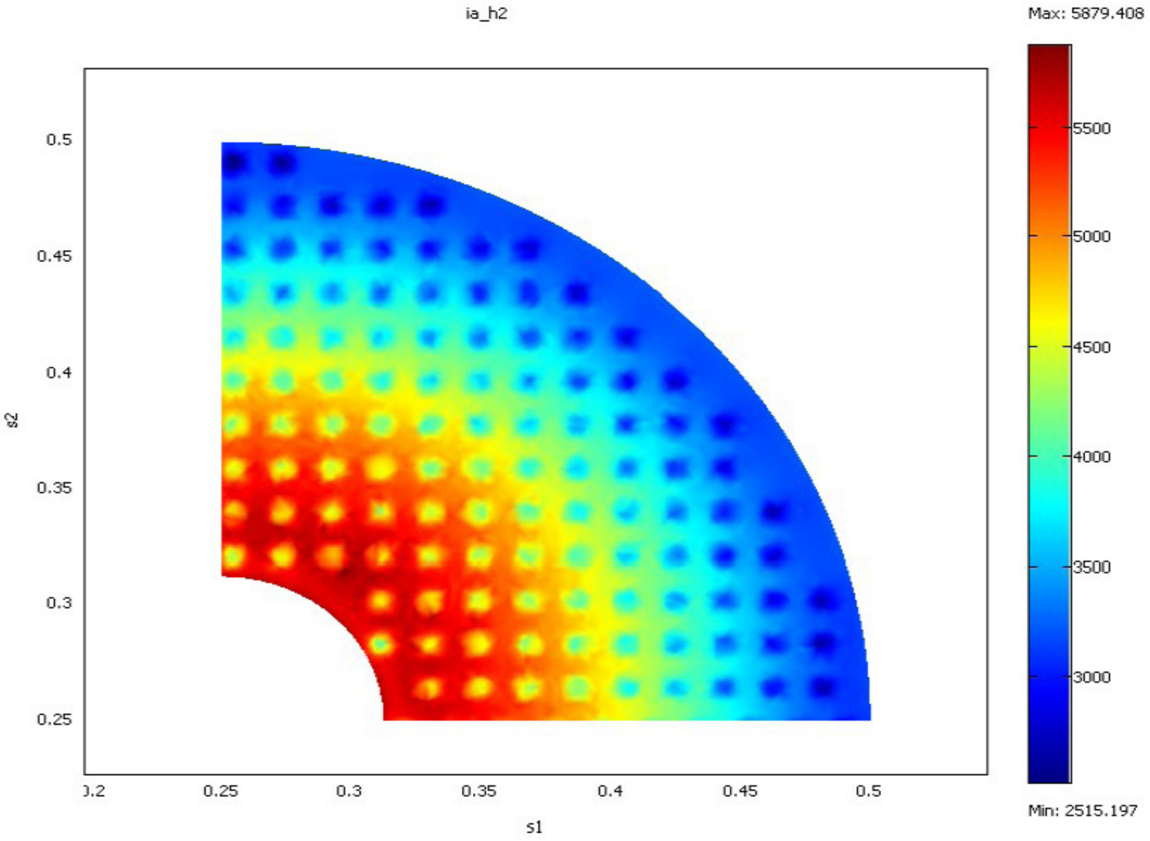

Figure 5-24 Hydrogen current distribution (cell voltage 0.7V, total current 22 A)

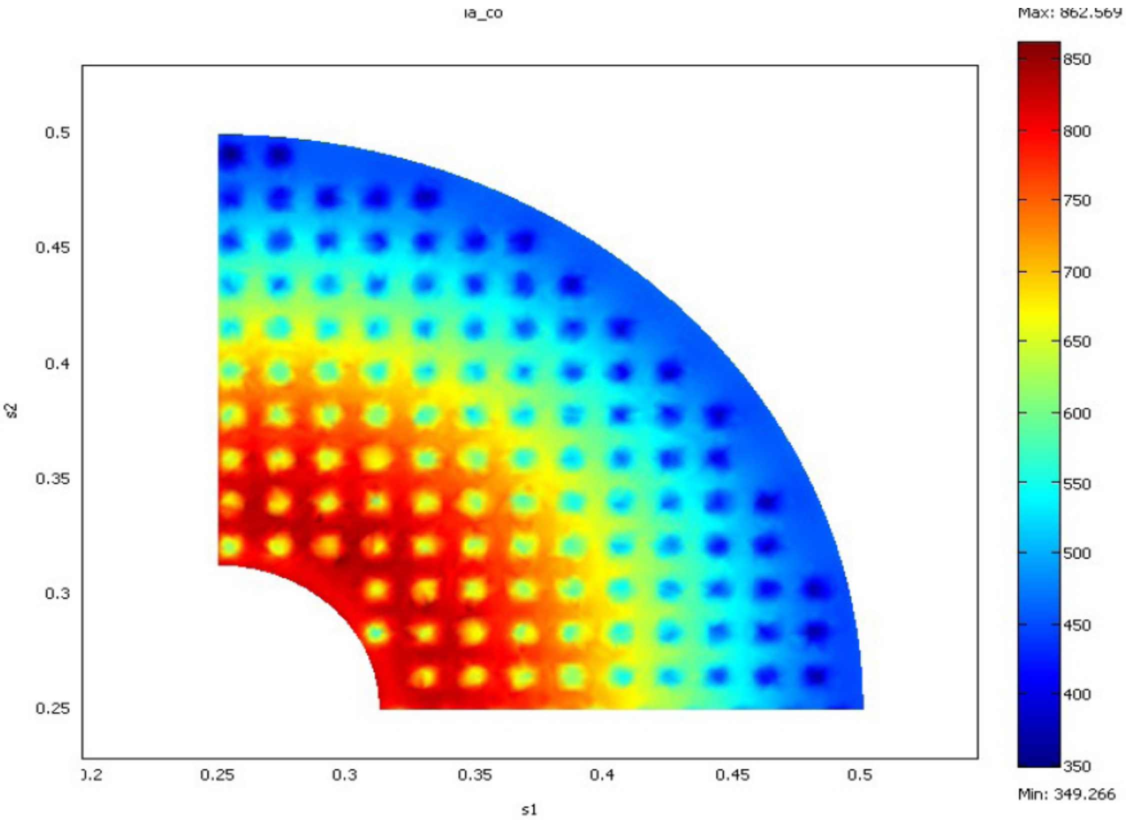

Figure 5-25 Carbon monoxide current distribution (cell voltage 0.7V, total current 22 A)

Temperature distribution: In Figure 5-26 the temperature distribution at the cell middle plane is shown. It can be seen that the fuel cell temperature is not uniform, and the highest temperature is located towards the cell outlet because of the non reacted hydrogen afterburning reaction. The shift reactions heating makes this temperature field hardly greater than hydrogen SOFC case one (see Figure 4-25).

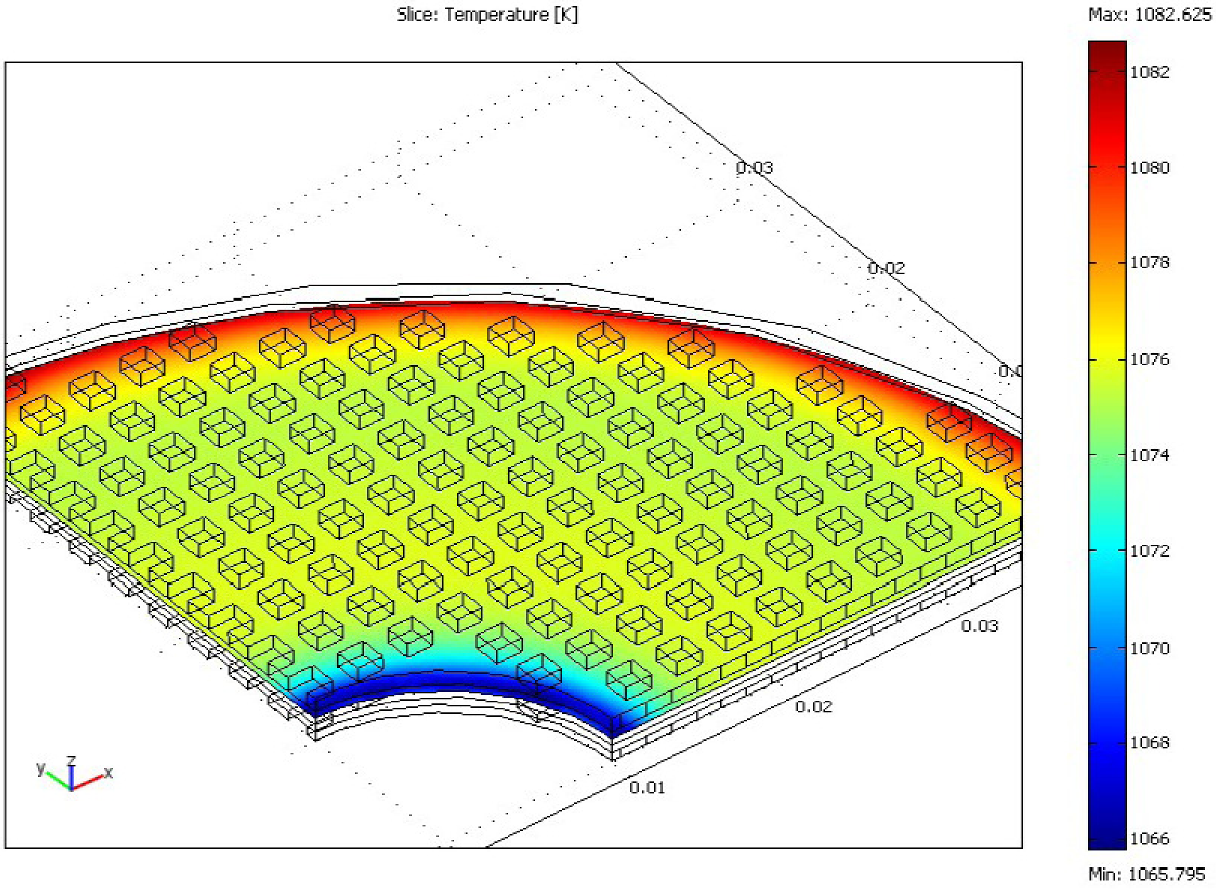

Figure 5-26 Temperature distribution (cell voltage 0.7V, total current 22 A)

In the following tables, the cell operating parameters for the polarization curve and model input parameters found in the updating phase are summarized.

Table 5-1 Cell operating parameters for the polarization curve

Hydrogen volume flow rate (molar fraction)	18.45 Nl/h (63 %)
Carbon monoxide volume flow rate (molar fraction)	4.60 Nl/h (15.8 %)
Carbon dioxide volume flow rate (molar fraction)	1.30 Nl/h (4.4 %)
Water volume flow rate (molar fraction)	4.90 Nl/h (16.8 %)
Oxygen volume flow rate (molar fraction)	11.5 Nl/h (21 %)
Reference pressure	1.013e5 Pa
Fuel inlet temperature	780 °C
Air inlet temperature	800 °C
Furnace temperature	800 °C

Table 5-2 Cell operating parameters

Gas thermo-physic properties [3]	
Oxygen viscosity	1.668e-5+3.108e-8*T [Pas]
Nitrogen viscosity	1.435e-5+2.642e-8*T [Pas]
Hydrogen viscosity	6.162e-6+1.145e-8*T [Pas]
Water viscosity	4.567e-6+2.209e-8*T [Pas]
Carbon monoxide viscosity	1.399e-5+2.582e-8*T
Carbon dioxide viscosity	1.273e-5+2.822e-8*T
Oxygen specific heat at constant volume	2.201e4+4.936*T [J/kmolK]
Nitrogen specific heat at constant volume	1.910e4+5.126*T [J/kmolK]
Hydrogen specific heat at constant volume	1.829e4+3.719*T [J/kmolK]
Water specific heat at constant volume	2.075e4+12.15*T [J/kmolK]
Carbon monoxide heat at constant volume	1.966e4+5.019*T [J/kmolK]
Carbon dioxide heat at constant volume	23690+31.01*T-8.875e-3*T^2 [J/kmolK]
Oxygen thermal conductivity	0.01569+5.690e-4*T [W/mK]
Nitrogen conductivity	0.01258+5.444e-5*T [W/mK]
Hydrogen thermal conductivity	0.08525+2.964e-4*T [W/mK]
Water thermal conductivity	-0.01430+9.782e-5*T [W/mK]
Carbon monoxide conductivity	0.01275+5.384e-5*T [W/mK]
Carbon dioxide conductivity	0.005485+6.272e-5*T [W/mK]
Fuller binary diffusion coefficients [4]	
Oxygen Fuller diffusion volume	16.3
Nitrogen Fuller diffusion volume	18.5
Hydrogen Fuller diffusion volume	6.12
Water Fuller diffusion volume	13.1
Carbon monoxide diffusion volume	18
Carbon dioxide diffusion volume	26.7

Porous media microstructure [5]	
Porosity	30 %
Tortuosity	10
Porous radium	0.5e-6 m
Electrokinetic parameters [5]	
Ideal potential	0.8961 V
Anodic preexponential coefficient	1.6e9
Cathodic preexponential coefficient	3.9e9
Anodic activation energy	120 J/mol
Cathodic activation energy	120 J/mol
Anode charge transfer coefficient	$\theta_{a,}$ =2; θ_c= 1
Cathode charge transfer coefficient	θ_a =1.4 θ_c = 0.6
Electrical conductivities [6]	
Anode electrical conductivity	9.5e7/T*exp(-1150/T) [$Ohm^{-1}m^{-1}$]
Electrolyte electrical conductivity	3.34e4*exp(-E_el/T) [$Ohm^{-1}m^{-1}$]
cathode electrical conductivity	4.2e7/T*exp(-1200/T) [$Ohm^{-1}m^{-1}$]
Solid parts thermal conductivities [6]	
Anode thermal conductivity	3 W/mK
Electrolyte thermal conductivity	2 W/mK
Cathode thermal conductivity	3 W/mK
Heat exchange coefficients	
Thermal convective coefficient	5 W/m^2K
Thermal radiative emissivity	0.3

- 3. SOFC Systems

3.1 Introduction;

In this chapter are analyzed a complete model of SOFC able to describe the functioning of the whole fuel cell system; secondary to this work are presented a resume to evaluate a general evaluation of the system changing main parameters.

The system is composed by three main parts:

- fuel section treatment to convert fuel to a gas with high hydrogen presence.

- An electrochemical section composed by sofc fuel cell to produce electric energy;

- An inverter to convert electric energy produced in alternate current and connect the system to the electric network;

To complete the system, a heat recovery system are inserted: this can be used to satisfy heat needed during fuel conversion, or other cogeneration applications.

In the present work, the different system components are modelled using a generic approach with different details level; to reduce computational requirements of the model, the single cell functioning has been reduced to a 2D model;
Regarding fuel treatment, the model used is mono-dimensional, in flow direction, to determine temperature and composition along the reformer and at cell stack consequently.
For the other components (heat exchangers, burners, etc), has been used a thermo-dynamic phenomenal approach;
In the picture below are shown the block diagram of the examined system:

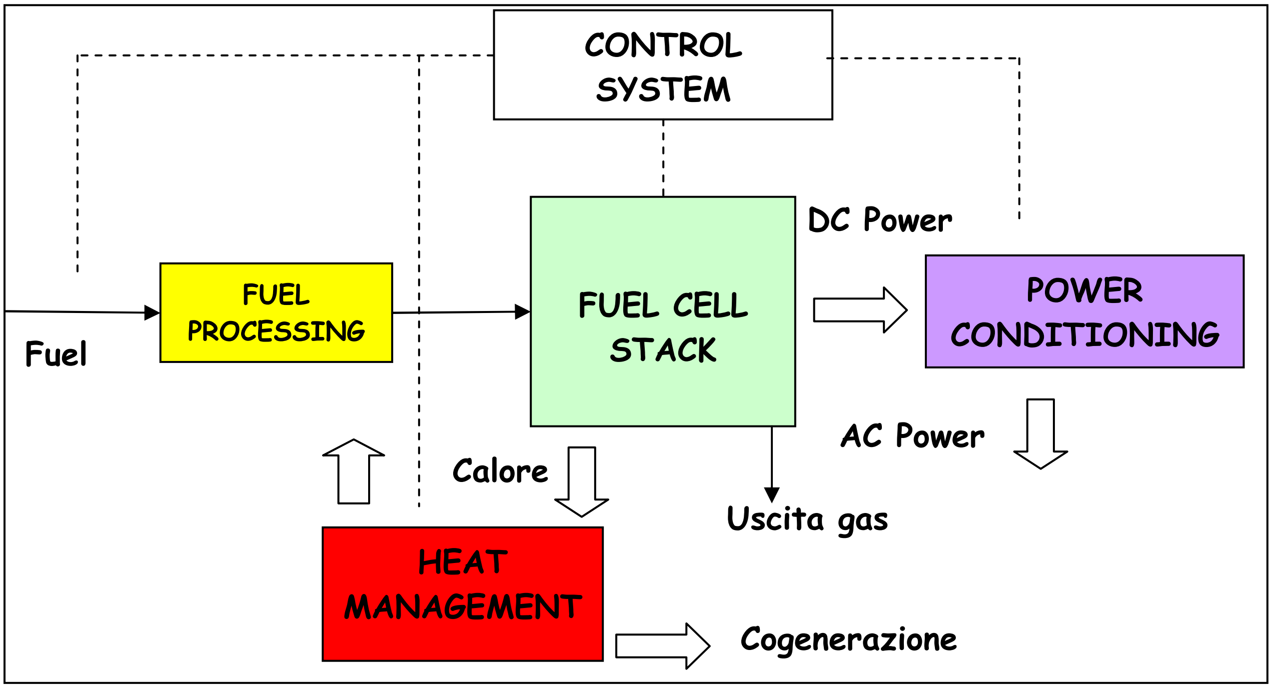

Figura 1 SOFC system scheme

Fuel section treatment;

The fuel processing section, is used to convert fuel (liquid, gaseous or solid) to a gas compatible to the sofc cell necessity; this feature implies an hydrogen directly feeding, produced by industrial processes, or of course a fuel processing section, that converts to hydrogen (and carbon monoxide), standard hydro-carbon fuels as methane. Properties needed of this system to be compatible whit SOFC cells, are high conversion efficiency, high hydrogen and CO production, compacters, lightness and low time response;
Generally, the fuel processing unit is strangely related to the fuel type: in the present work, fuel considered are natural gas, biogas, and syngas.

Fuel treatment are divided in two steps:

- de-sulphur section (including also ammonia, halogens removal) to prevent catalyst poisoning;
- pre-reforming reactor;

De-sulphuring phase;

Natural gas contains sulphurs smellers, intentionally introduced to identify easily any gas loss. These are a poison for some cell materials and the have to be removed using zinc oxide catalytic bed, or hydro-de-sulphurs, if needed; zinc oxides are able to remove mercapthane and disulphurs, but for some other components hydro-de-sulphurs are needed for complete cleaning, and conversion in sulphidric acid H_2S before catalytic bed;
In this study are considered a not continuous de-sulphur, constituted by two containers installed in parallel as per picture below, and functioning alternatively:

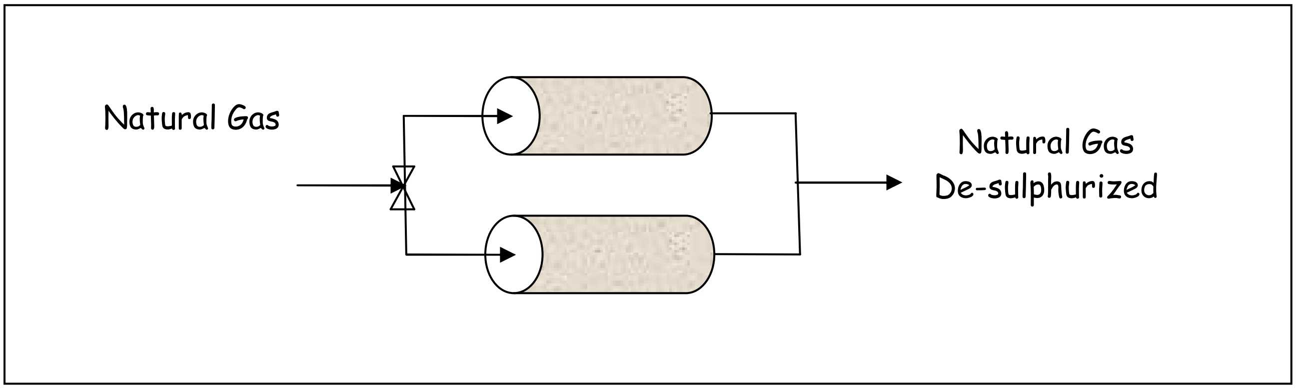

Figure 2 desulphurizer

While one cartridge are working, the other are regenerated through an high temperature flow;
Most used techniques to sulphur removal is physical-chemical adsorption , where sulphur compost are kept on adsorption material surface after the chemical reaction; Adsorption material can be change according to its porosity influencing dimension and design of the cartridge.

Main parameters to evaluate de-sulphur cartridge performance are:

- Adsorber type: active carbon, zeolite, ZnO, Fe(OH)3. The active carbon can used with caustic materials to improve their performance: from the other side, disadvantage of this material are the low ignition temperature;

- Breakthrough capacity, normally expressed in [g adsorbed/g adsorber], that quantify maximum quantity of unwanted material that can be kept from adsorbing material, in this case are sulphur composition (mainly H_2S).

- Gas Hourly Space Velocity (GHSV): this velocity, expressed in h^{-1}, define the ratio between volumetric flow through reactor and total adsorber volume. As greater is the GHSV, as soon saturation conditions will be reached.

From these parameters, other important information regarding the system can be obtained:

- passing time;
- saturation time;
- Outlet sulphur content;
- Pressure losses;

Important factors that influence the process efficiency are: flux humidity, initial content of contaminants, oxygen concentration, ph, temperature.
From energetic point of view there are different kind of process, from low temperature process (environment temperature in air presence) to high temperature (H2S oxidation in a temperature range between 100-250 °C, and dry condition at low oxygen concentration); Adsorption process of H2O is exothermic. In water absence this value is fixed between 40 kJ/mol and 50 kJ/mol (depending from kind of active carbon); This value can increase with porosity of adsorber material.
When the adsorber material (in this case active carbon) arrive at saturation conditions, must be regenerated by sulphur free flux through the adsorber bed. This regeneration process can be thermal or in water.
In the first one the inert gas are heated to 500-600 °C an then used to clean the reactor; the process starts around 450°C. However, to reconstruct the initial condition of the active carbon, or almost to a value around 90-95 %, can be obtained with a selective gasification with water vapour at 800-850 °C. In this case H2S are completely removed. This second method of course imply an higher complexity of the system.

Pre-reforming reactor;

Steam reforming process is the most used to obtain hydrogen from a hydrocarbons: to have an idea of the importance of this process, 48% of hydrogen needing is produced using this process. This process can be used with different kind of fuel molecule as propane, butane, and diesel gasoil (catalysts are needed in this last case). Steam reforming process allow to obtain higher hydrogen concentration.

Here below are reported main reaction involved and relatively energy produced (or needed);

$$CH_4 + H_2O \rightarrow 3H_2 + CO \qquad \Delta H=206.2\ \text{kJ mol}^{-1}$$

Shift reaction:

$$CO + H_2O \rightarrow CO_2 + H_2 \qquad \Delta H=-41.2\ \text{kJ mol}^{-1}$$

Steam reforming reactions, are furthered by catalyst with Ni base in a Al2O3 support.

This process is highly endothermic, so the reaction equilibrium is highly moved to the left at low temperature, and the best performance are obtained in temperature between 750 and 1000 °C.

Al2O3 support is one of the most choice because its high surface and thermal stability at high temperature required.

The process steps are here reported:

- Natural gas (the one consider in this study) are compressed to values of about 1.5, 2 atm (efficiency compression considered: 0.7).
- Natural gas are mixed to water vapour, in high excess respect natural gas (low ratio can cause solid carbon creation during the process); high steam values, moreover, encourage a good temperature value before reactor inlet, increasing converting efficiency;
- Steam-methane mixture, starts conversion inside reactor, thanks to catalyst ad heat from outside; in the table below the main reaction occurring along the reactor:

Reactions	**$\Delta H_{298,15}$[kJmol^{-1}]**
$CH_4+H_2O \leftrightarrow CO+3H_2$	206.1
$CO+H_2O \leftrightarrow CO_2+H_2$	-41.15
$CH_4+2H_2O \leftrightarrow CO_2+4H_2$	165
$CH4_4+CO_2 \leftrightarrow 2CO+2H_2$	247.3
$CH_4+3CO_2 \leftrightarrow 4CO+2H_2O$	330
$CH_4 \leftrightarrow C+2H_2$	74.8
$2CO \leftrightarrow C+CO_2$	-173.3
$CO+H_2 \leftrightarrow C+2H_2O$	-131.3
$CO_2+2H_2 \leftrightarrow C+2H_2O$	-90.13
$CH_4+2CO \leftrightarrow 2C+2H_2O$	-15.3
$CH_4+2CO \leftrightarrow 3C+2H_2O$	-187.6

Tabella 1 Reaction involved in reforming reactor

As anticipated, to avoid solid carbon formation, steam-methane ration are kept to values around 2, consequently the favourite reactions remains the monoxide carbon shift, and methane reforming;

3.2 Description of the system:

Considered reactor use as catalyst Ni/Mg-Al2O3;
Reaction rates of each reaction involved in the model are given below (expressed in kmol/kg$_{cat}$):

Reforming reaction:

$$r_1 = \frac{k_1}{{p_{H_2}}^{2.5}}\left(p_{CH_4} p_{H_2O} - \frac{{p_{H_2}}^3 p_{CO}}{k_{e,1}} \right) \cdot \frac{1}{{Q_r}^2}$$

Shift reaction:

$$r_2 = \frac{k_2}{p_{H_2}}\left(p_{CO}p_{H_2O} - \frac{p_{H_2}p_{CO_2}}{k_{e,2}}\right)\cdot\frac{1}{Q_r^{\ 2}}$$

With:

$$Q_r = 1 + K_{CO}p_{CO} + K_{H_2}p_{H_2} + K_{CH_4}p_{CH_4} + \frac{K_{H_2O}p_{H_2O}}{p_{H_2}}$$

- p_i partial pressure of species i;
- $k_j = k_{0j}\exp\left(\frac{-E_j}{RT}\right)$ kinetic constant of reactions.
- Other kinetic constant for i-reaction are reported in next table, E_i is the activation energy:

Reaction	k_{0j} [kmol/kg cat h]	E_j [kJ/kmol]
1	$4.225 \cdot 10^{15}$bar $^{-1.5}$	240100
2	$1.955 \cdot 10^{6}$bar$^{0.5}$	67130

Tabella 2 kinetics costants

Reaction	Equilibrium constant
1	$5.75 \cdot 10^{12}\exp(-11476/T)$ (bar^2)
2	$1.26 \cdot 10^{-2}\exp(4639/T)$

Tabella 3 equilibrium constant

- $K_I = K_{0i}\exp\left(\frac{-\Delta H_i}{RT}\right)$ is adsorbtion constant of species i

Specie	K_{0i} [bar^{-1}]	H_i [kJmol^{-1}]
CH_4	$6.56 \cdot 10^{-4}$	-38280
CO	$8.23 \cdot 10^{-5}$	-70650
H_2	$6.12 \cdot 10^{-9}$	-82900
H_2O	$1.77 \cdot 10^{5}$ bar	88680

Tabella 4 adsorbing constant

Consumption velocity (or generation velocity) of i species are obtained adding the production rate (or consumption) of each reaction.
Analyzing reaction rate for each species:

$$r_{CH_4} = -r_1$$
$$r_{CO} = r_1 - r_2$$
$$r_{H_2} = 3r_1 + r_2$$
$$r_{H_2O} = -r_1 - r_2$$
$$r_{CO_2} = r_1$$

Simulation model;

reformer model, simulate a mono dimensional reactor; equation that describe process are reported as follow:

$$\frac{dF_{CH_4}}{dW} = -r_1$$
$$\frac{dF_{CO}}{dW} = -r_2 + r_1$$
$$\frac{dF_{CO_2}}{dW} = -r_2$$
$$\frac{dF_{H_2O}}{dW} = -r_1 - r_2$$
$$\frac{dF_{H_2}}{dW} = 3r_1 + r_2$$
$$\frac{dT}{dW} = \frac{-\Delta H_1 r_1 - \Delta H_2 r_2}{\sum_j F_j c_{pj}}$$

Where:

- F_j molar flux of species i [kmol/h]
- r_i velocity of reaction i
- ΔH_i entalpy of reaction i [kJ/mol]
- cp_j specific heat of species i

with the following reactor entering conditions:
per W=0 it's possible to write:
$F_j=F_{j0}$
$T=T_0$
With hypothesis of constant pressure.
In the following table are resumed all conditions considered in the model:

Inlet CH_4 flow	0.00017
Ratio S/C	2.17
Initial reactor temperature	850 °C
Reactor pressure	2.9 atm
Total cathalist weight	0.6 g
Reactor lenght	40 cm

The model described, allows to have concentration values for each species along the reactor axis; concentration values are reported in the graph below;
Percentage of conversion is about 25% with 650°C temperature. In a SOFC system the ratio between internal reforming and pre-reforming have to be optimized, in relation to experimental data, moreover, recirculation gases coming from anode side can be used to eliminate steam generation and its consumption; both cases (with ad without anode recirculation) are analyzed in this model, focusing performance and control parameters;

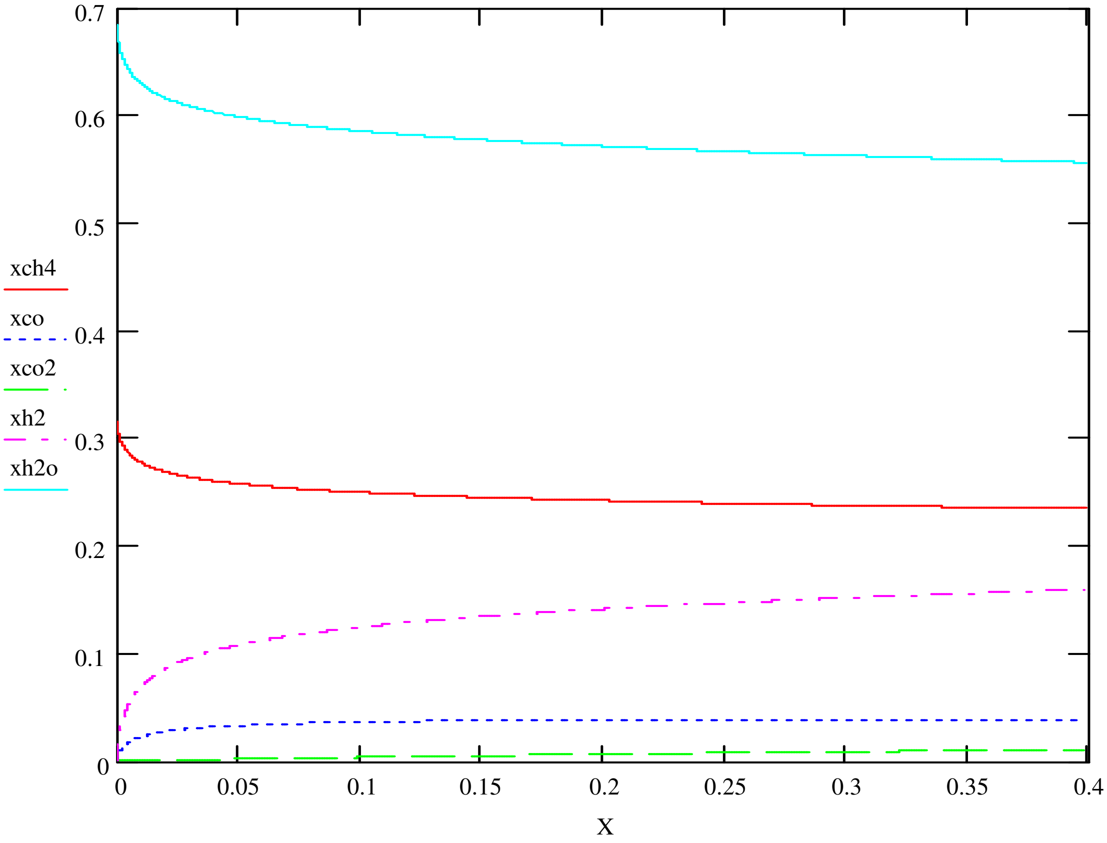

Figura 3 Molar fraction along reformer axis

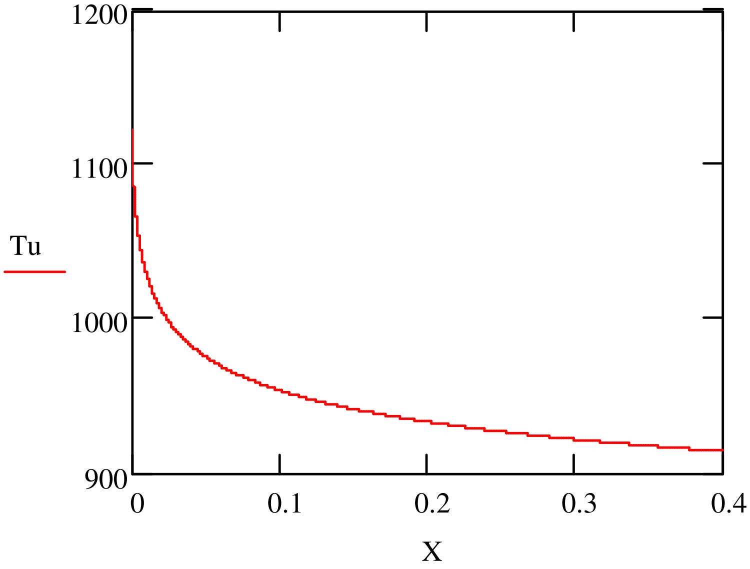

Figura 4 reformer temperature along axis

In next picture are shown how is important inlet temperature for CH4 conversion; increasing temperature, kinetics are promoted, obtaining higher conversion percentages. Higher flows, instead, get worse to reforming performance, because passage time is reduced.

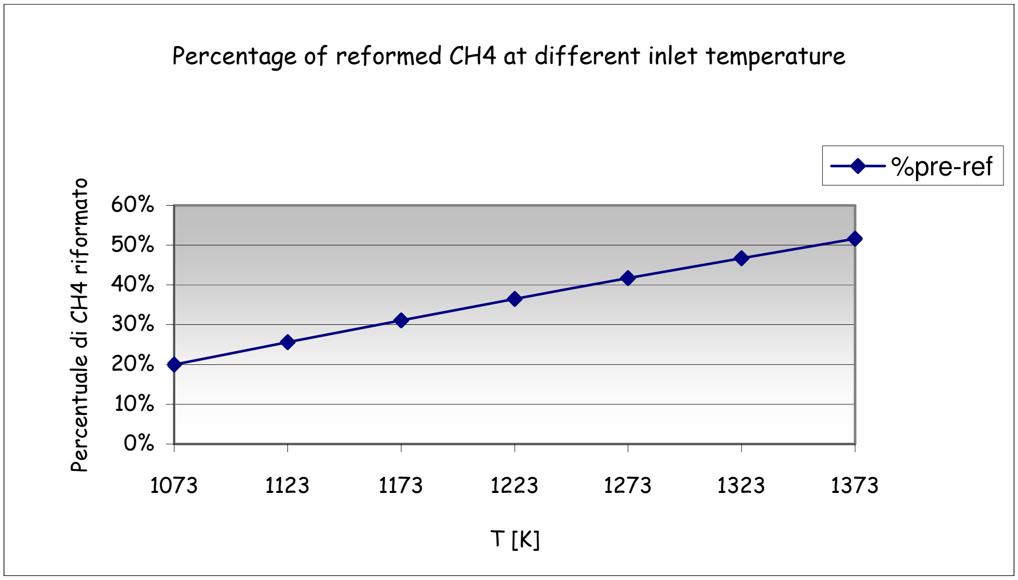

Figura 5 reformed CH4 according inlet temperature

This last point is evidenced in next graph where conversion rate is decreasing with flow rate; temperature in this case is fixed to 1230°C;

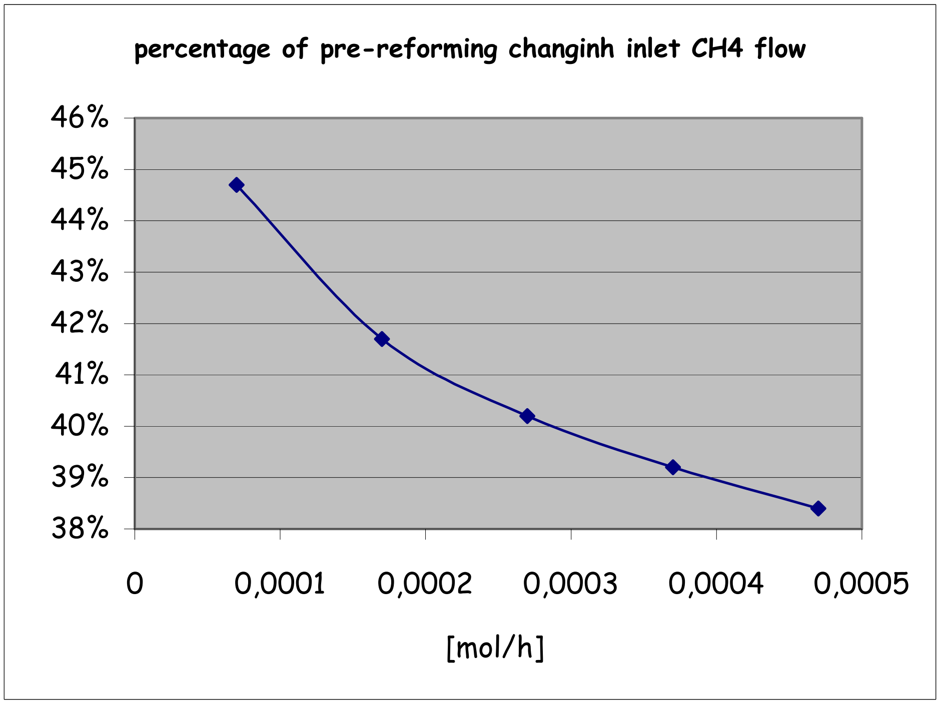

Figura 6 Percentage of pre-reforming changing inlet flow

After-burner

In this model has been inserted also and afterburner that simply consist in a burner connected to the anodic flow exiting the cell and to the cathode exiting flow to burn out remaining species not consumed in the cell; This component represent another heat source that can be used for other purpose;
Equation involved are the follow:

$$H_2 + \frac{1}{2}O_2 \rightarrow H_2O$$

Reazione 1

$$CO + \frac{1}{2}O_2 \rightarrow CO_2$$

Reazione 2

With enthalpy of 245,8 kJ/mol first reaction and 243 J/mol to the second.
In this model, all anodic flux enter in the after burner, while from cathode side, are used just the amount of gas necessary for remaining hydrogen and CO combustion;
Air necessary to after burner are calculated from stoichiometry of two reaction above;

Power connection

This other part of the model is needed to convert continue current generated from the stack, in alternate current at desired tension and frequency;
Generally this stage is represented by a dc/dc converter (elevator chopper), a battery set and a final inverter.
Chopper connected after the stack, is needed to rise the voltage and to actuate the control of the system, changing power required from the system and consequently point of work of the stack; battery set between chopper and inverter are needed to have a quick response of the system and allow the stack to pass the transitory phase, according with its inertia;

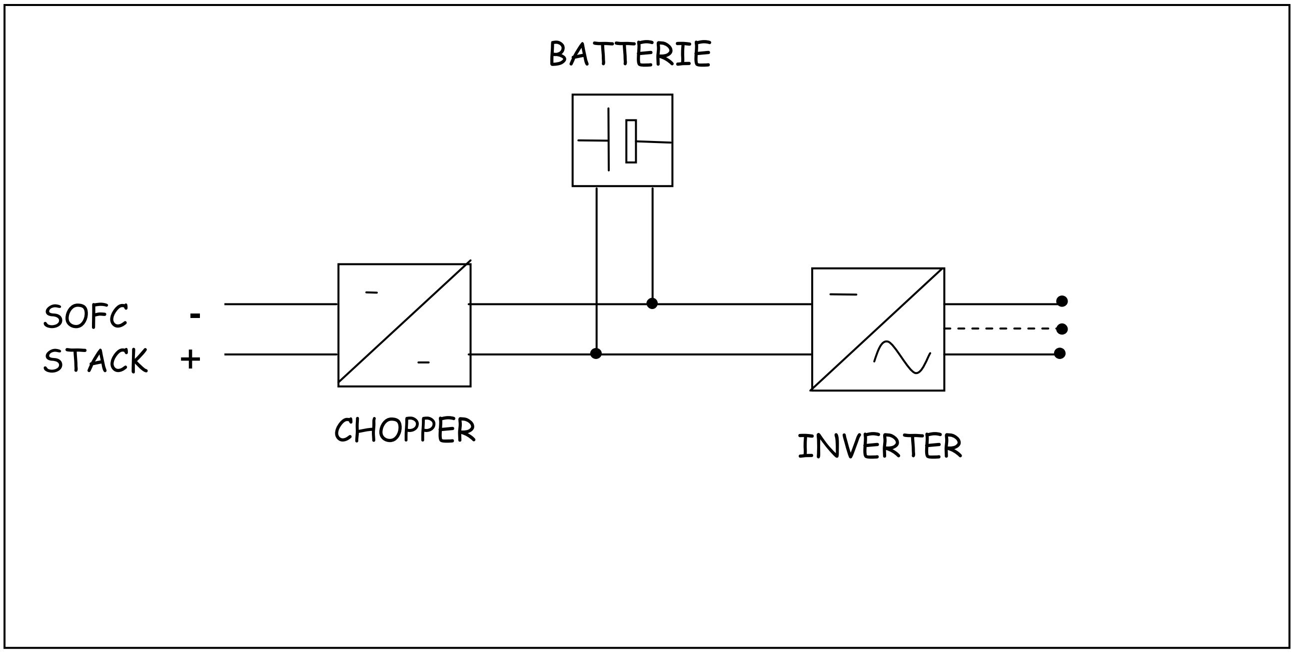

Figura 7 Power management section

Control system

Control system are divided in three main areas: central control, power control, back-up control. The whole system are controlled by a PLC, needed to avoid:

- reach too high temperatures
- pressure gradient too high between anodic and cathode flux
- low ratio steam/carbon in pre-reformer section
- excesses thermal stress

while for the normal control system, main parameters are:

- fuel valve control
- air flow control
- anode flow recirculation
- air flow to afterburner
- required/produced power

SOFC Systems fed by poor gases;

One of advantages of SOFC system are flexibility regarding fuel used: hydrogen, natural gas, but also biogas, garbage gas, gas from carbon, methanol and many others opportunely treaded;
Using of fuels o biomasses derived from urban waste material can be a valid solution to recover energy from human activity.
Biogas comes from anaerobic fermentation of organic waste, with high methane content. Other species can be carbon dioxide (approximately in the same methane quantity), and many others gases as hydrogen, oxygen, nitrogen, carbon monoxide, ammonia, hydrogen sulphureous, water vapour, and traces of other components.

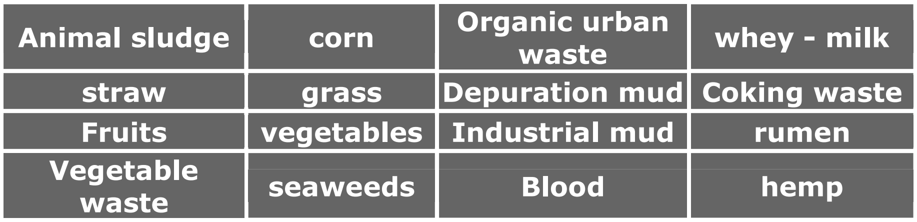

Animal sludge	corn	Organic urban waste	whey - milk
straw	grass	Depuration mud	Coking waste
Fruits	vegetables	Industrial mud	rumen
Vegetable waste	seaweeds	Blood	hemp

Tabella 5 biomass usefull for biogass production

Biological process needed to obtain final biogas starting from organic substances, is quite widespread in nature, also know as anaerobic digestion.
For what explained this kind of gas can be used in SOFC system cause it's high energetic content;

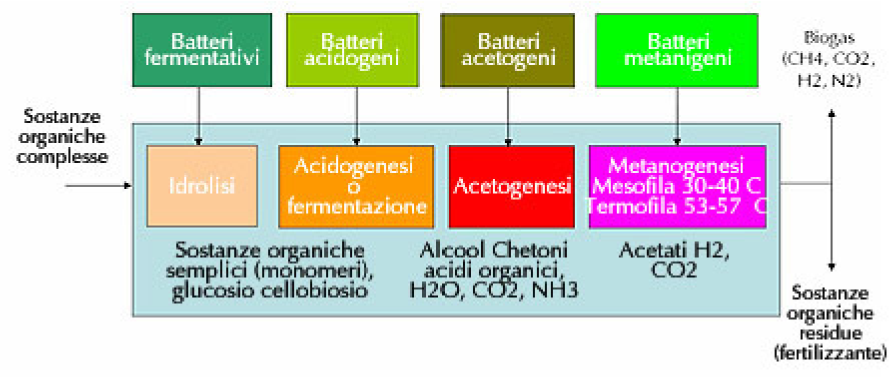

Figura 8Processo di digestone anaerobica

Energy recovering from biomasses can occurs also through the gasification process.
This is a thermal process that must be controlled by a limited oxygen quantity (to obtain a partial combustion) in a closed chamber, as per picture below.

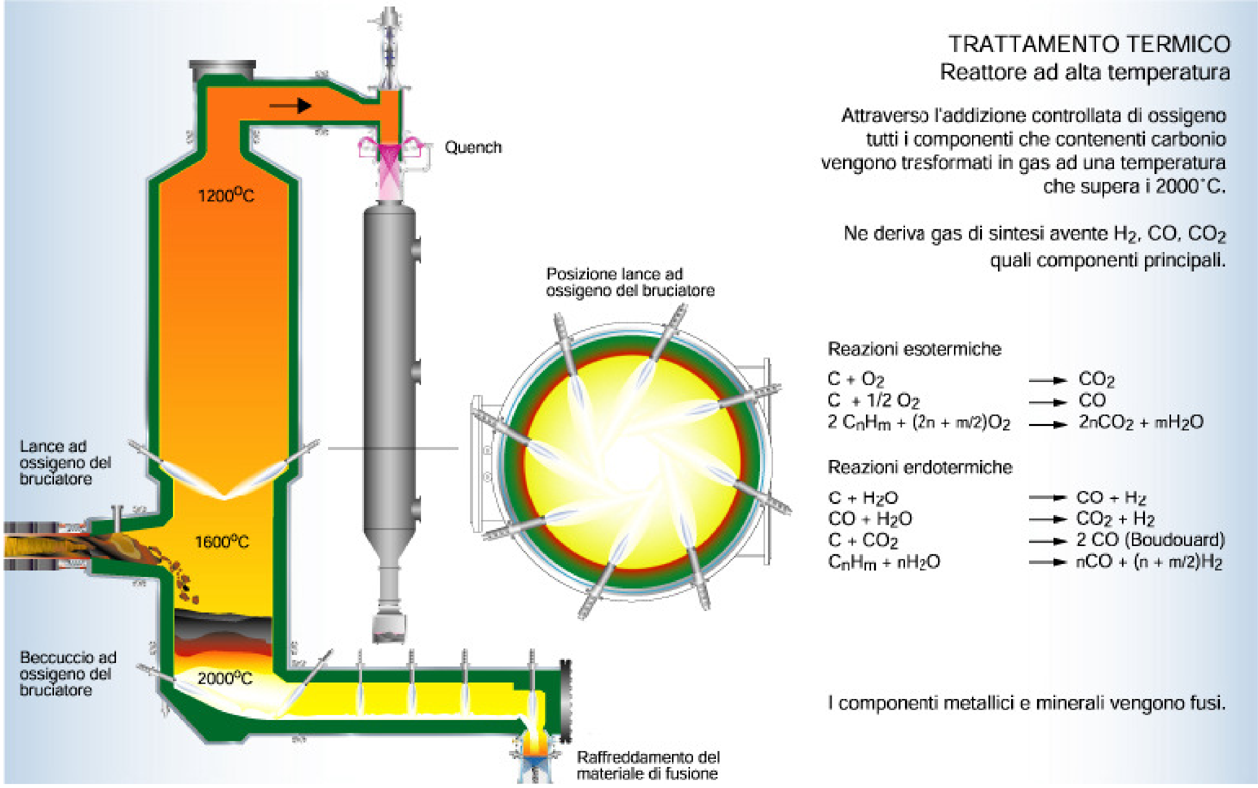

Figura 9 gasification reactor

Gasification process, transform organic material in syn-gas, that could be used as energetic vector or other chemical synthesis; In this case, combustion process, does not produce solid residual and hashes, ashes and dioxins neither; Material entering in gasification chamber became a gas with the following properties:

- medium-low calorific power (4-15 MJ/Nm3), mainly composed by CO and H2
- solid residual (char) is lisciviable, in according with European normative;

This kind of plants, does not release liquid or muddy effluent, the one taken back from cleaning system can be put in glass form;

Gasification process can be used with solid urban wastes and specific materials, as cultivations rape, sunflower, ecc;

However, in case the feeding fuel is biogas, the SOFC stack system remains the one exanimate because mainly composed by CH4, CO, CO2, H2, and must be partially reformed before entering the stack.

In gasification case, instead, reforming phase is not necessary because percentage of natural gas is quite low and can be used only the internal reformer;

A SOFC system with cogeneration the electrical efficiency based on low calorific fuel power can be 45-50%, while the electric and thermal efficiency can arrive to 90%;

Pollution emission for this kind of system can be negligible, but not if CO2 are considered.

In next pages are reported a model test using the parameters in the table to set boundary conditions; Performance of the system have been evaluated with and without anodic recirculation;

Technical specifications	
Fuel	Gas Naturale
Output Voltage	220V @50Hz
Fuel consumption (without recirculation)	9,88 mol/h
Fuel consumption (with recirculation)	8,4 mol/h
Active area (for each cell)	100 cm^2
Voltage (for each cell)	0,7V
Cell Number	40

Tabella 6 Technical specification SOFC plant

Methane flux within the cell is about 9,32 mol$_{CH4}$/h; considering composition of natural gas reassumed in table, natural gas flux is 9,88 mol/h, equivalent to 0,212 Nm^3/h

Fuel consumption	0,212Nm^3/h
Fuel energetic content	8302kJ/h
Temperature	15°C
Pressure	1,1 atm
Sulphur content	115mg/m^3
	147ppm
Composition	
Methane	94,4%
Ethane	2,5%
Propane	0,2%
Iso pentane	0,03%
Pentane	0,01%
Hexane	0,01%
Nitrose	1,6%
Carbon dioxide	0,7%
Iso buthane	0,03%

Tabella 7 inflet flow composition

3.3 Plant configuration feed with methane (CASE A)

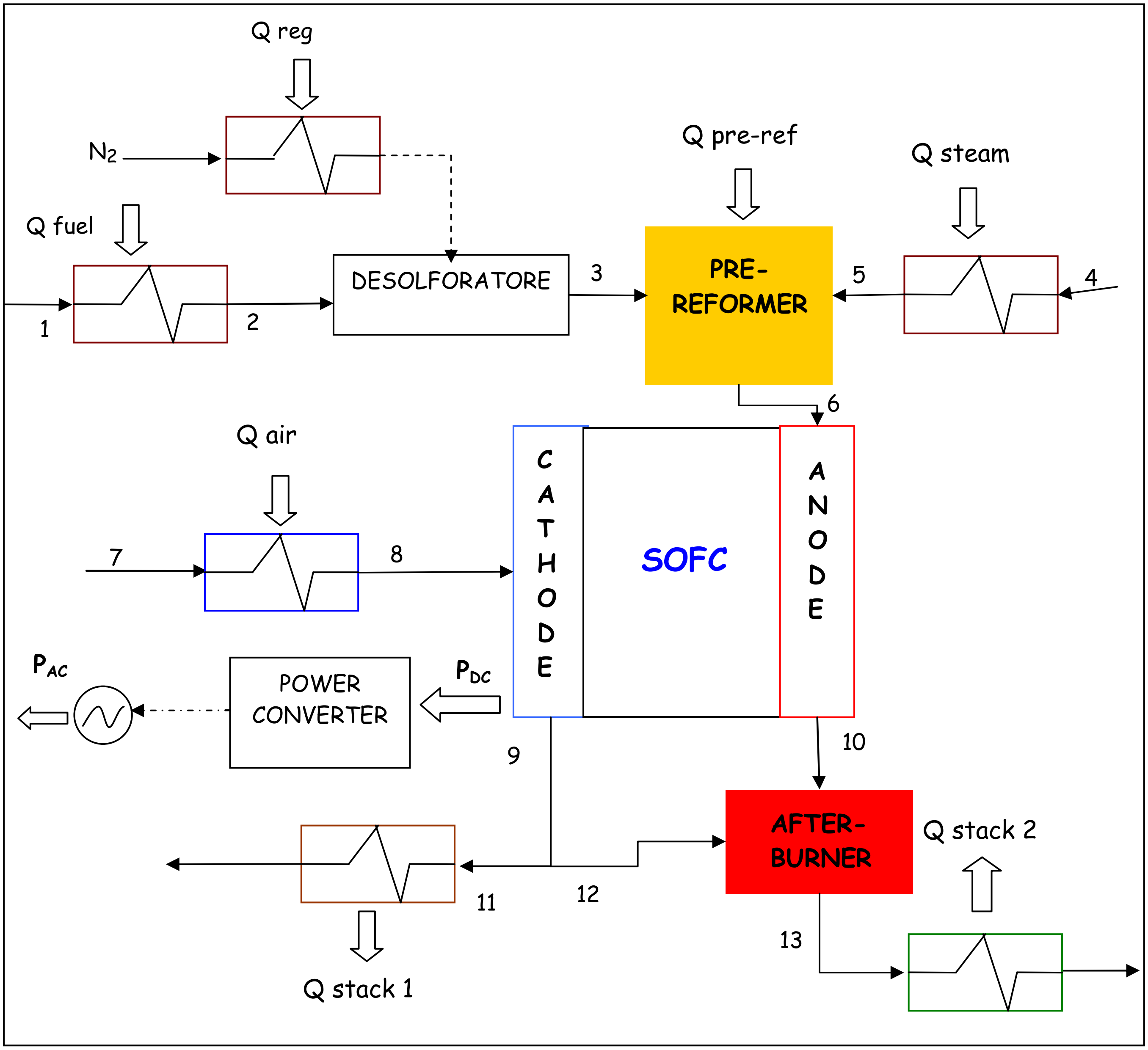

Figura 10 Plant configuration without anodic recirculation

This first plant configuration is characterized by the presence of steam generation needed in external reformed, without anodic recirculation; plant performance has been evaluated changing percentage of reformed methane, in particular has been considered 35%, 25% and 15% conversion ratio. Fuel inlet gas properties are the follow:

1	
Inlet fuel parameters	
Fuel	Gas naturale
Fuel flowrate	9,88mol/h
Temperature	20°C

Pressure	1,1 atm
S/C ratio	2,4

Tabella 8 inlet fuel data

Since the fuel is available to environment temperature (20°C) warming up is necessary before de-sulphur entering; this heating require about 40 thermal W. Fixed a sulphur concentration of 1 ppm an esteem of heat released is not relevant (about 0,0094 W); Counter must be taken in account heat necessary to sulphur cartridge regeneration; considering thermal de-adsorbing, and regeneration time of about 1 hour and half every 4 days with 0,282 Nm^3/h of nitrogen at 800 °C, heat needed is about 70 W.

2	
Fuel heating	
Flowrate	9,88mol/h
Exit temperature	250°C
Inlet T	20°C
Q fuel	**40,2 W**

Tabella 9 fuel heating

3	
Desulphuration exit flow	
Flowrate mol/h	9,88mol/h
Temperature	250°C
Pressure atm	1,1
Sulphur content	1 ppm
Q reg	**70 W**

Tabella 10 fuel properties exiting desulphuration

Air flow editing the cartridge are mixed with steam inserted in pre-reforming reactor. Have been consider a rector with dimensions of 0,4m length and 6 grams of catalysing; steam required is 23,71 mol/h.
In next table are reported water characteristic at inlet:

4	
Inlet Water	
Flowrate	23,71 mol/h
Temperature	20°C

Tabella 11 water inlet parameter

5	
Steam generation	
Pressure	1 atm
Steam flowrate	23,71 mol/h
Inlet water temperature	20 °C

Exit steam temperature	110°C
Q nedeed	**325 W**

Tabella 12 exit flow from steam generation

Heat needed to produce 23,71 mol/h of steam at 110°C, considering an heat exchanger efficiency of 95% is 325 thermal W.
According to reforming ratio desired, different heat quantity are needed:

6			
Pre-reformer	**35%**	**25%**	**15%**
Exit flowrate	38,6 mol/h	37,05 mol/h	35,6 mol/h
Exit temperature	785 °C	785°C	781 °C
Composition			
CH4	19%	22,00%	25%
CO	6,40%	4,60%	2,80%
CO2	0,00100%	0,0007%	0,0004%
H2	19,60%	14,10%	8,60%
H2O	54,80%	59,30%	63,70%
Q nemee	**588 W**	**495 W**	**435 W**

Tabella 13 flow properties from pre-refomer

As from the previous table, decreasing pre-reforming ratio, also the heat requirement decrease, passing from 588W to 435W. Must kept clear that it's not possible to arrive too low with pre-reforming conversion to avoid formation of solid carbon in the cell, that would cause a damage and an decreasing of cell performance. For firs case examined (35% of pre-reforming), species concentrations are reported following;

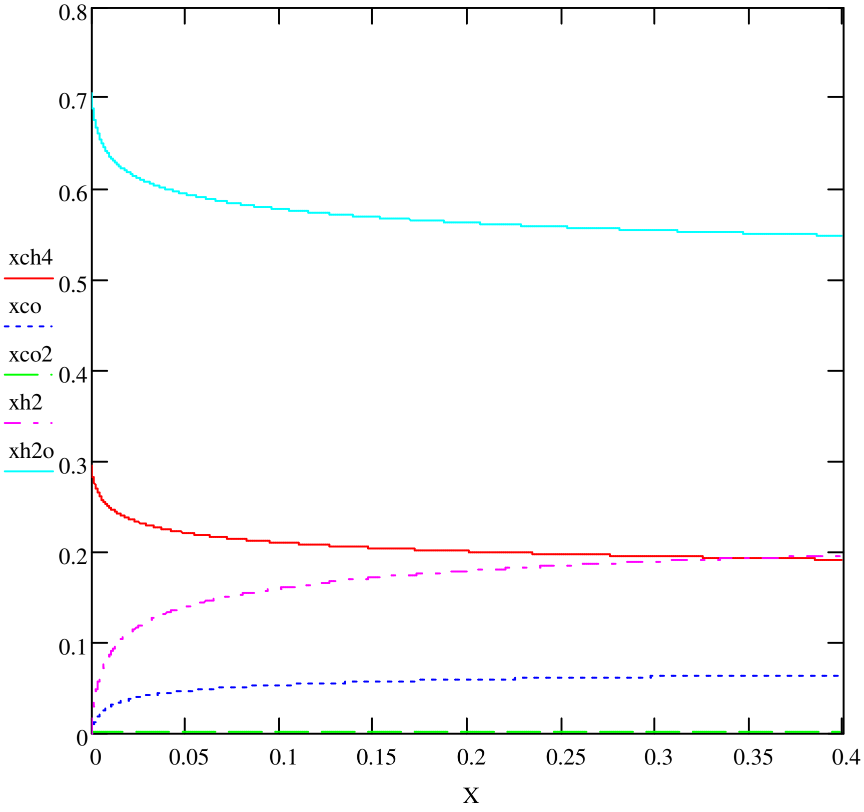

Figura 11 molar fraction in reformer (35% pre-ref)

Decreasing temperature, velocity of CH4 conversion decrease as well. Considering high temperature, shift reaction is quite slow, producing high CO quantity: for SOFC cell, this is not a poison for the cell, but on contraries can be used as fuel.

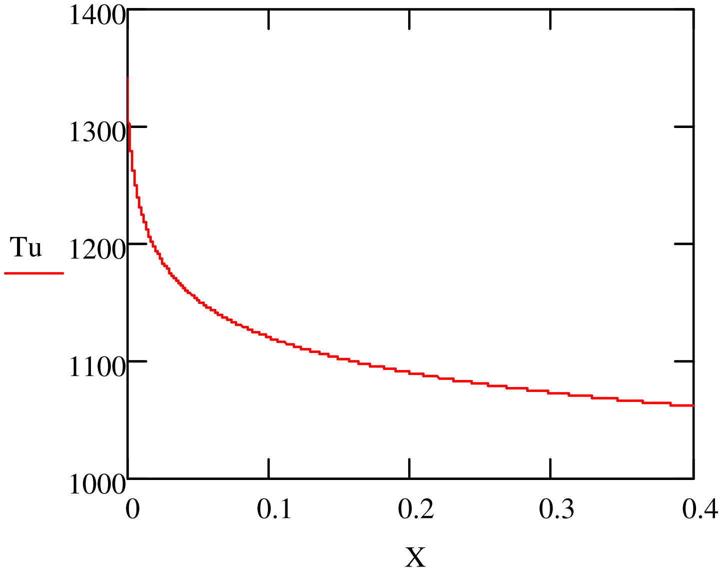

Figura 12 temperature along reformer axis [K] (35% pre-ref)

Power generation section;

This part of the plant comprise the cell stack and after-burner. Stack is feed with flow exiting from pre-reformer, while afterburner with the one exiting from the cell;

Fuel Cell Stack	**35%**	**25%**	**15%**
Inlet flow mol/h	**38,13**	**35,95**	**34,51**
Single cell active area cm^2	100	100	100
Cells number	40	40	40
Current density A/cm^2	0,428	0,3816	0,293
Cell voltage V	0,66	0,66	0,66
Cell power W	28,248	25,1856	19,3314
Stack power kW	**1,13**	**1,0074**	**0,773**
Uf	83%	75%	57%
Air excess	10%	10%	10%
Electric efficiency	49,30%	43%	35,00%

Tabella 14 Stack performance

In next pages tables are reported results obtained changing inlet flow composition. Are shown negative effect of too low pre-reforming ratio that cause a decreasing of current supplied from the stack. Higher CH4 concentration in fuel cause a cell cooling and less energy produced consequently. Fuel utilization factor drops, without considering carbon deposition on cell surface (especially with a CH4 conversion ratio lower than 15%).
Temperature trend (and also molar fractions, and current density) in 35%, 25% and 15% reformer conversion cases are reported in pictures below;

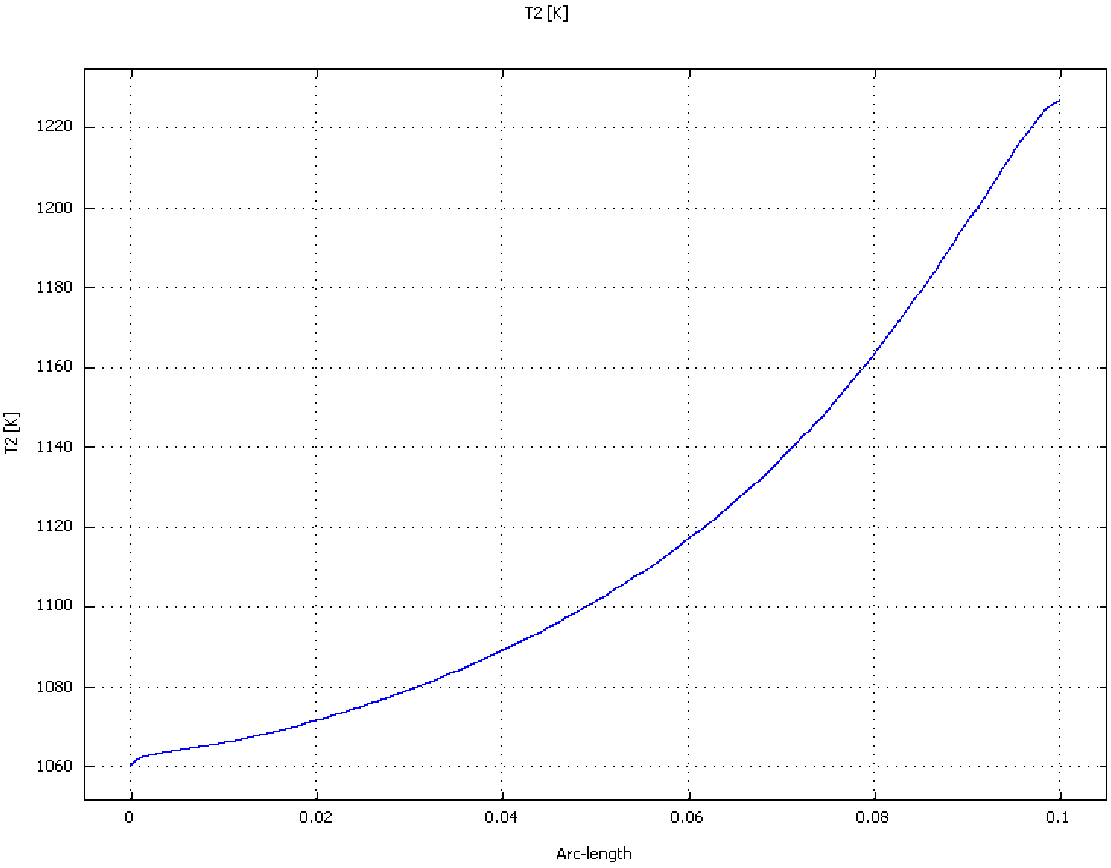

Figura 13 tempertaure at electrolyte-anode interface (35% pre-ref)

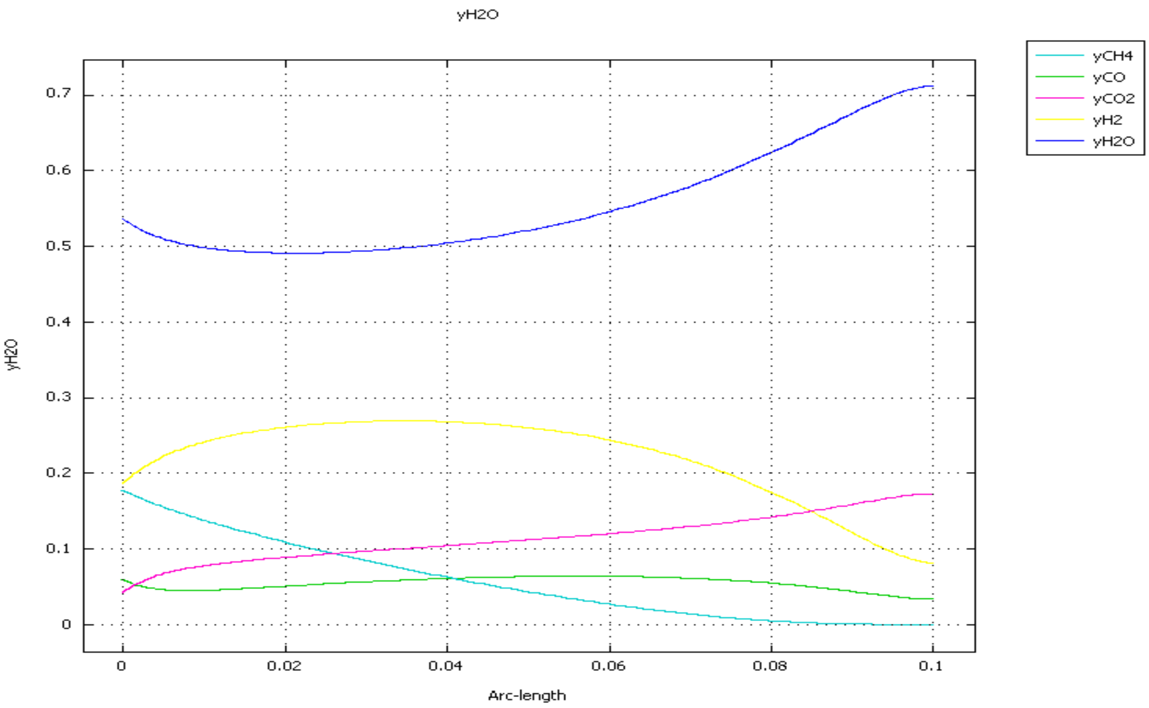

Figura 14 molar fractions at electrolyte-anode interface (35% pre-ref)

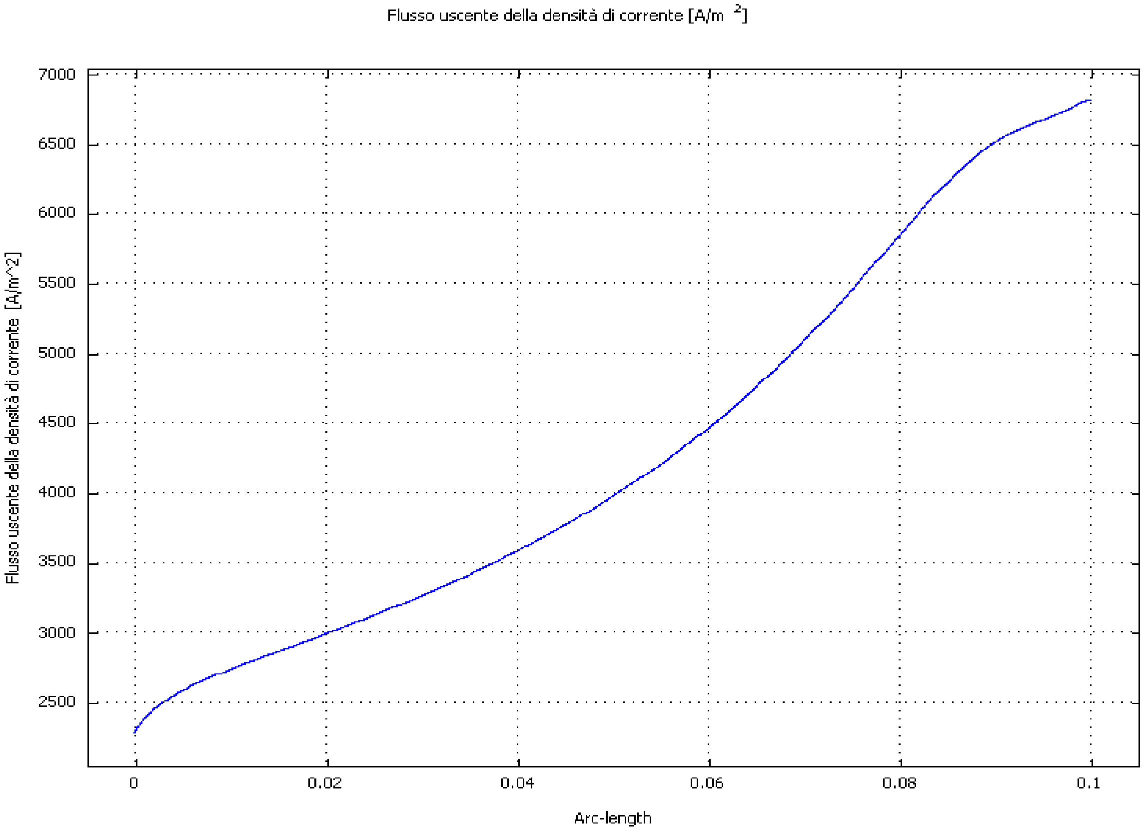

Figura 15 current density [A/m^2] (35% pre-ref)

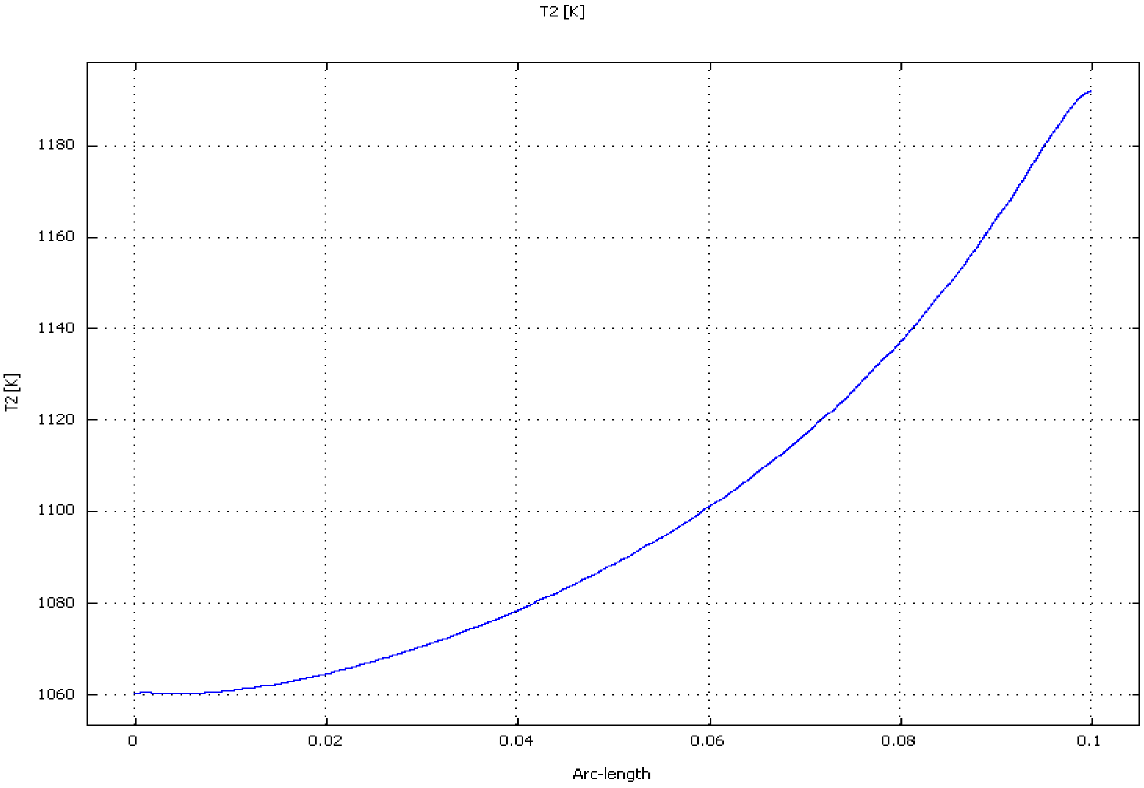

Figura 16 tempertaure at electrolyte-anode interface (25% pre-ref)

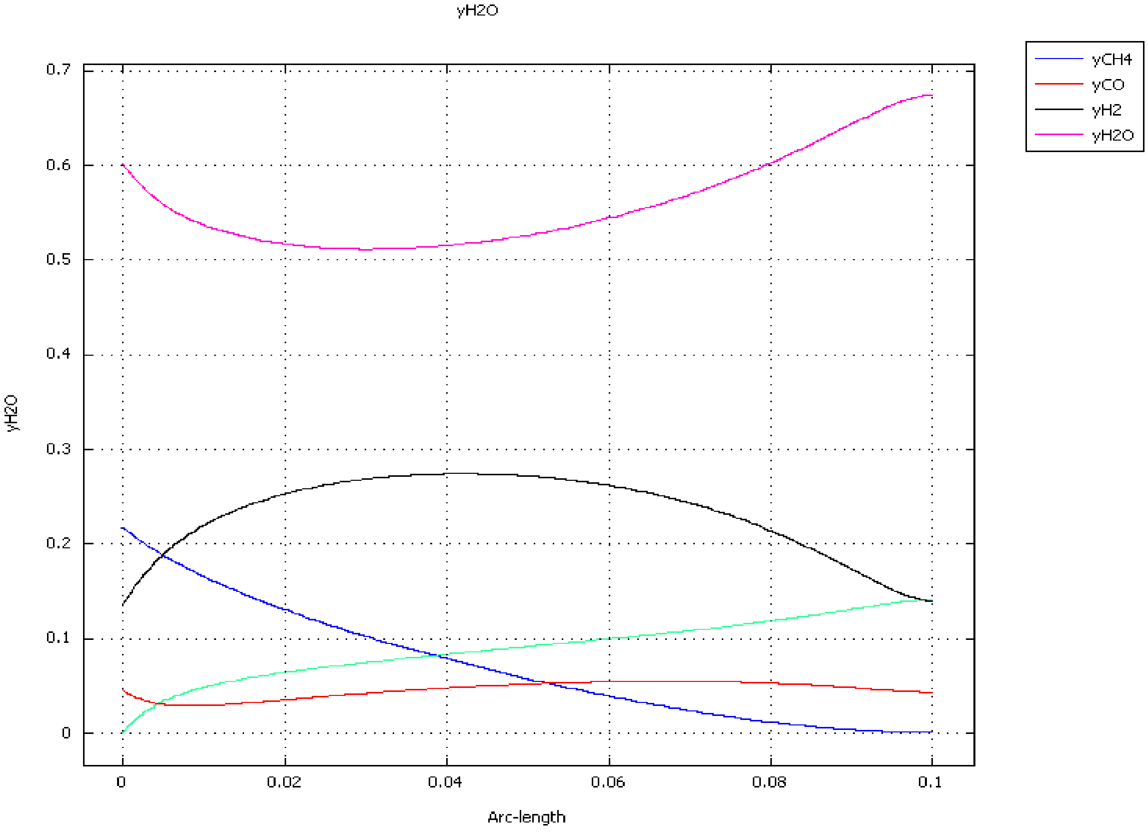

Figura 17 molar fraction at electrolyte-anode interface (25% pre-ref)

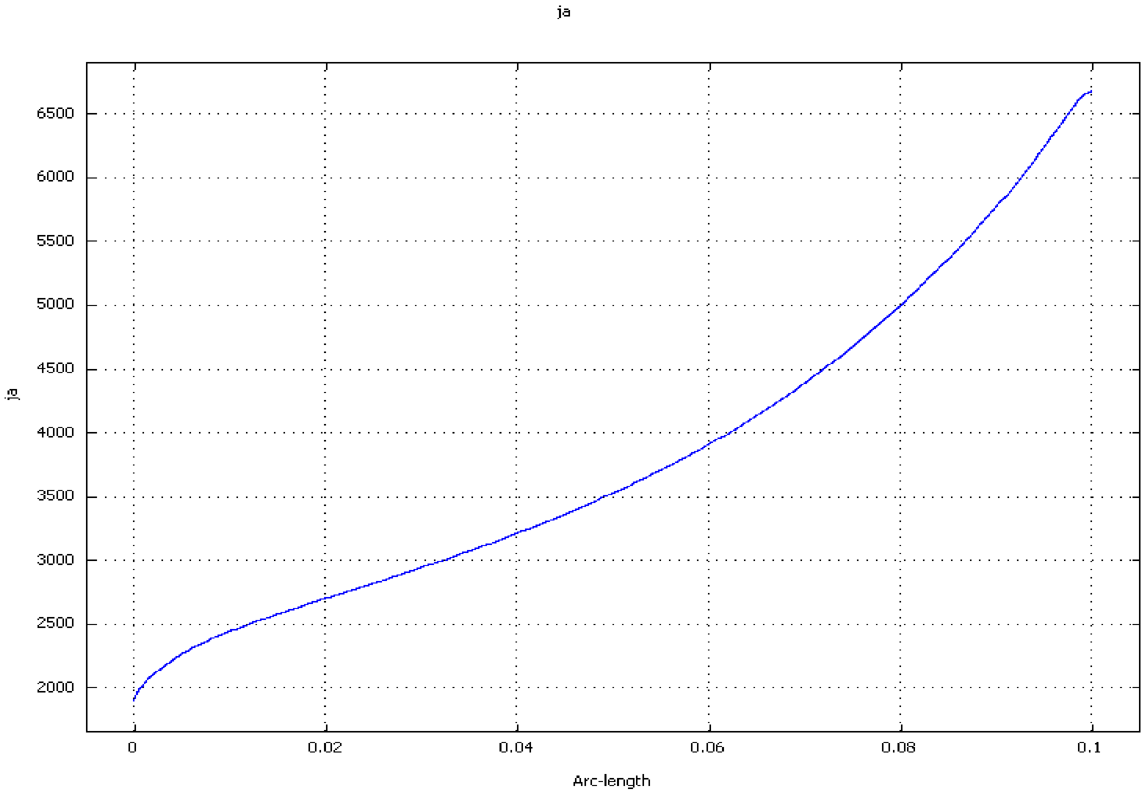

Figura 18 current density [A/m^2] (25% pre-ref)

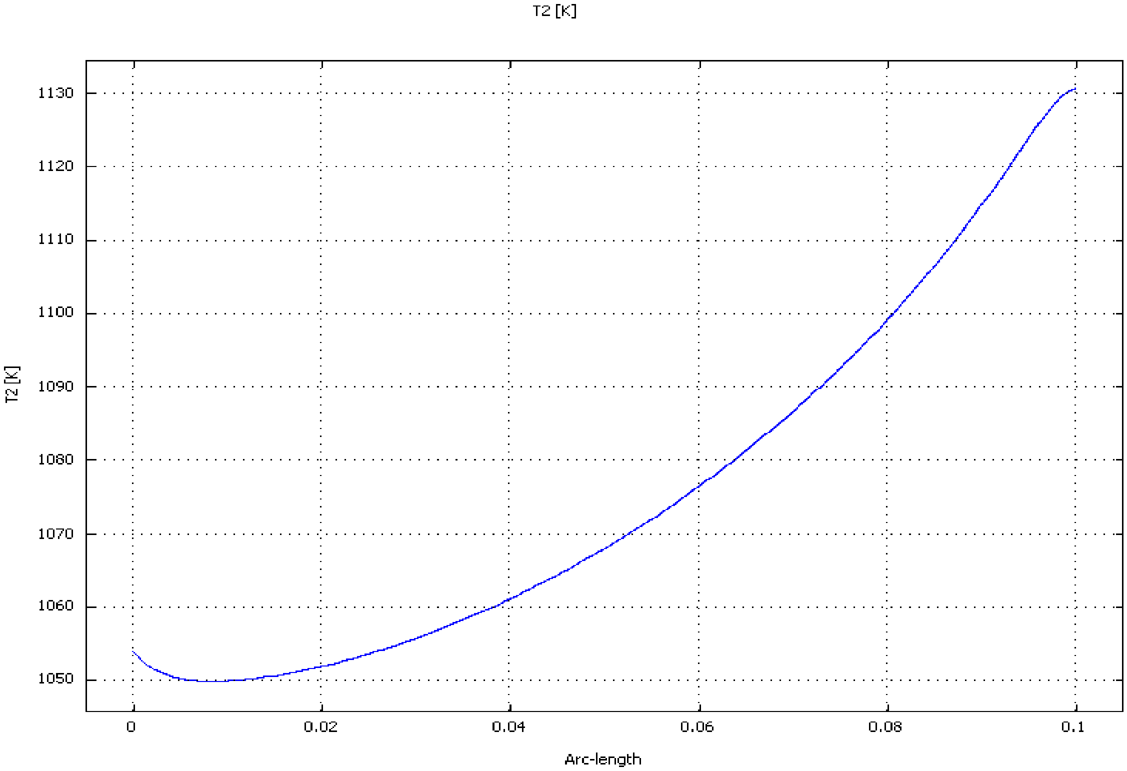

Figura 19 tempertaure at electrolyte-anode interface (15%pre-ref)

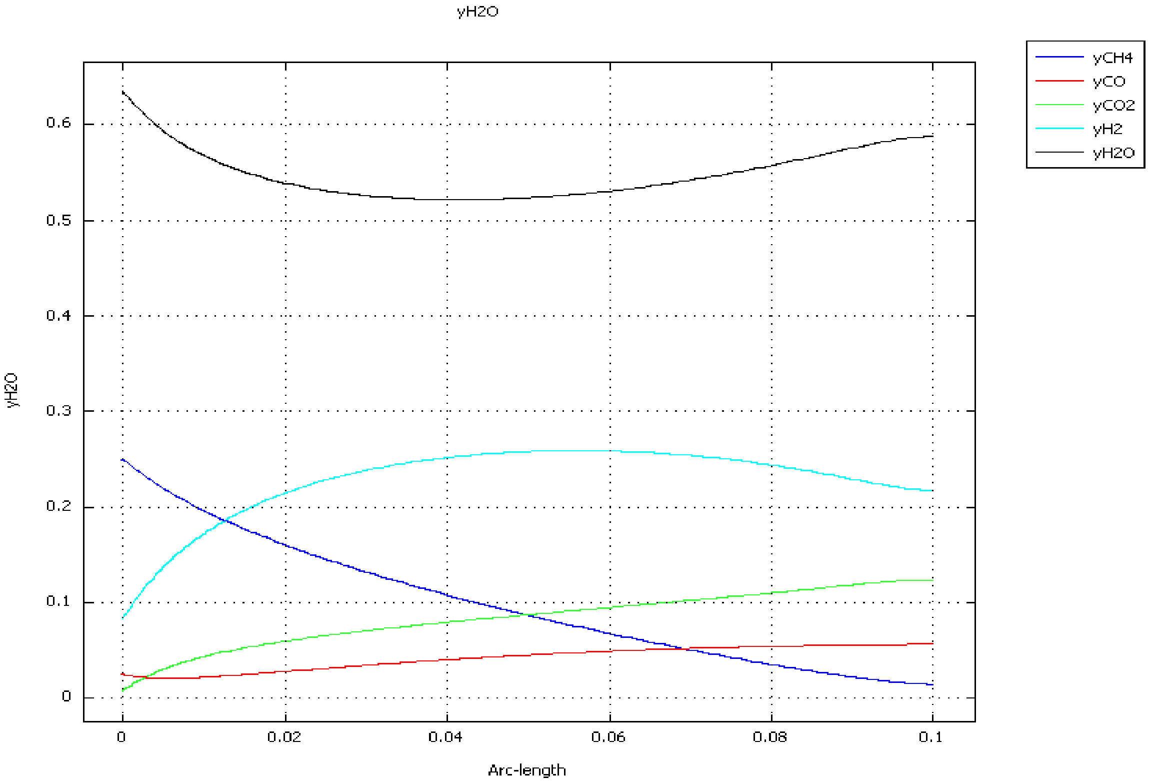

Figura 20 molar fractions at electrolyte-anode interface (15% pre-ref)

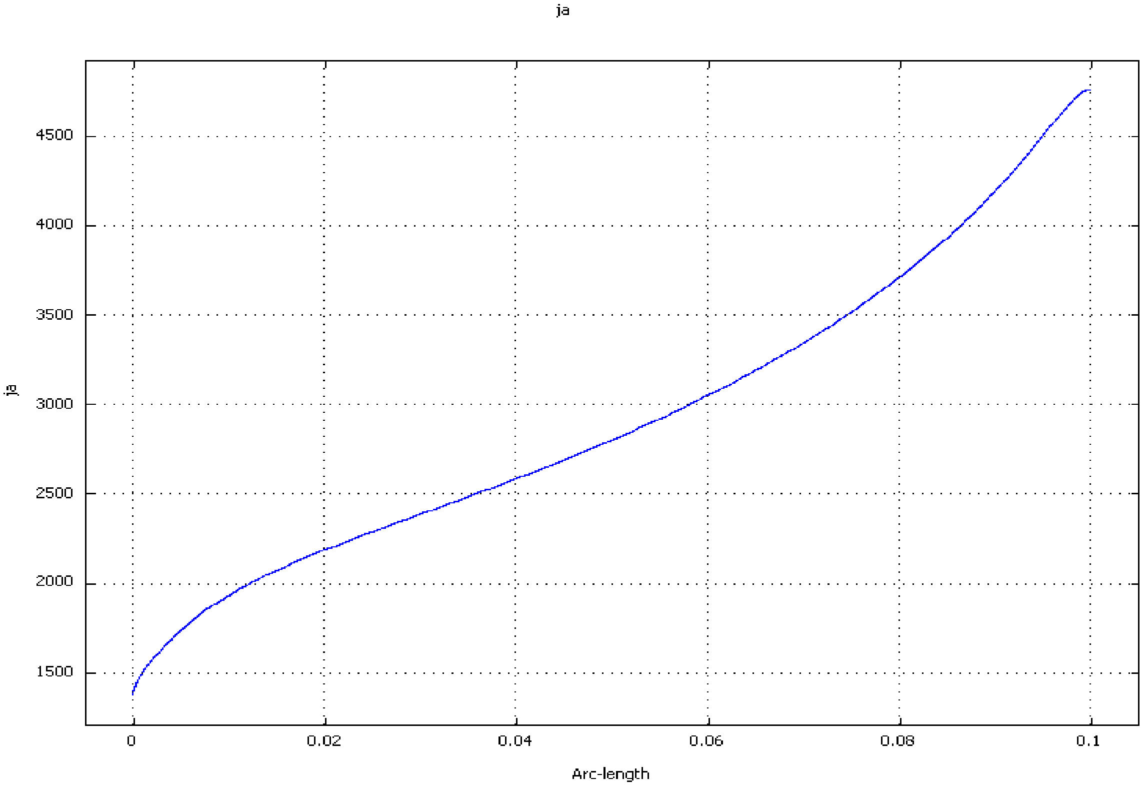

Figura 21 Densità di corrente [A/m^2] (15% pre-ref)

10 **Anode exit**	**35%**	**25%**	**15%**
Flusso in uscita mol/h	53,8	52,11	50,9
Temperatura	949	918	857
Composizione			
H2O	70%	67,40%	58%
H2	9,40%	14%	22,00%
CO	3,64%	4,77%	5,65%
CO2	17,06%	14,33%	13,95%
9 **Cathode exit**	**35%**	**25%**	**15%**
Flusso aria in uscita	518	518	520,3
Temperatura	937	893	857
Composizione			
O2	18,60%	18,90%	19,20%
N2	81,40%	81,10%	80,80%

Tabel 15 anode and cathode exit flows

Compositions and temperatures at anode editing are shown in previous table. As is possible to observe, exit temperature decrease at reforming ratio increasing inside the cell. Exiting flow moreover, is rich of H2 until a 21,1% when pre-reforming percentage is fixed at 15%.

	35%	**25%**	**15%**
Post combustion			
moli aria	22,62	34,356	42,744
moli comb	53,8	52,11	51,8
Tair °c	937	893	865
Tcomb	949	906	873
Q disponibile DT	**1505 W**	**1674 W**	**1781 W**
T	1435°C	1621°C	1770 °C
13 **composizione in uscita**			
H2O	61,70%	56,10%	51,80%
CO2	16%	13%	12,20%
N2	22,30%	30,90%	36,00%

Tabel 16 Post combustion properties

In the same plant configuration, all the anodic flow enter in the after burner, while from cathode point of view, are considered only the percentage needed to complete combustion of H2 and CO with 1,2 air excess; remaining part is used as heat source;

11	**35%**	**25%**	**15%**

Cathode flow By-passed			
mol/h	495,38	483,644	477,556
Temperatura °C	937	893	865
Composizione			
O2	18,60%	18,90%	19,20%
N2	81,40%	81,10%	80,80%
Q stack 1	**4875 W**	**4718 W**	**4635 W**

Tabel 17 Flusso catodico by-passato

	35%	**25%**	**15%**
flowrate [moli/h]	9,88	9,88	9,88
Lower calorific heat [MJ/Jg]	50,1	50,1	50,1
mcHi [W]	2199,95	2199,95	2199,95
Qreg [W]	70	70	70
Qfuel [W]	40,2	40,2	40,2
Qpre-ref [W]	588	495	435
Qsteam [W]	315	315	315
Qair [W]	3970	3970	3970
Q1[W]	4471	4164	3833
Q2 [W]	1257	1493	1758
P_{AC} [W]	1066,59	946,98	726,86
P+Q	1811,39	1613,78	1487,66
rend I principio	82,34%	73,36%	67,62%
Q disponibile [W]	744,8	666,8	760,8
T media K	1133	1027,5	1022,5
Exergia	548,9	473,41	539
rend II principio	73,4%	64,5%	57,4%

Tabella 18 CASE A results

Results for case A, of plant considered without anode recirculation are reported in previous table.

As anticipated, a decreasing of reformer percentage implies a decreasing of the whole performances; in fact, even if supported by a thin increasing of available heat for post combustion (related to higher H2 presence), globally the efficiency decrease, as per second principle efficiency. Most favourable conditions is the one with 35% of pre-reforming.

Since the gas out coming from anode contain H2 and CO yet, have been evaluated introduction of anodic recirculation.

3.4 Plant configuration with anodic recirculation (CASE B)

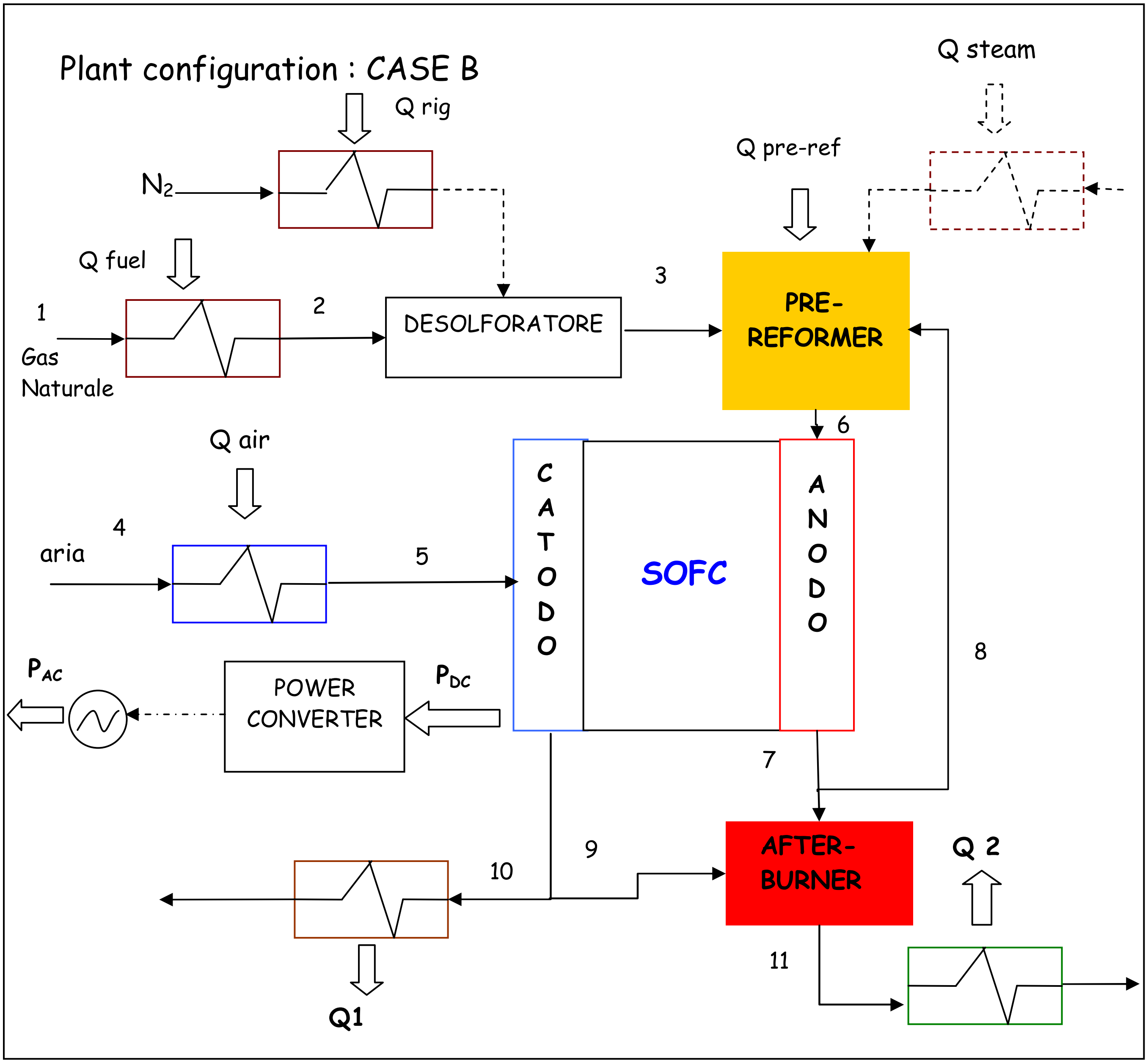

Figura 22 Plant configuration with anodic recirculation

In this case has been considered an anodic gas recirculation of 65%.
Outgoing anode gases contain H2 and CO, so to have the same equivalent moles is possible to reduce fuel inlet to 8,4 mol/h, reducing heat necessary to arrive to 210°C.

Fuel inlet data	35%
Fuel	Gas naturale
Fuel flowrate	8,4mol/h
Temperature	20°C
Pressure	1,1 atm
S/C ratio	2,4

Tabella 19 inlet fuel data CASE B

4	
Fuel heating	
Flowrate	8,4mol/h
Exit temperature	250°C
Inlet temp	40°C
Q fuel	**34 W**

Tabella 20 fuel heating

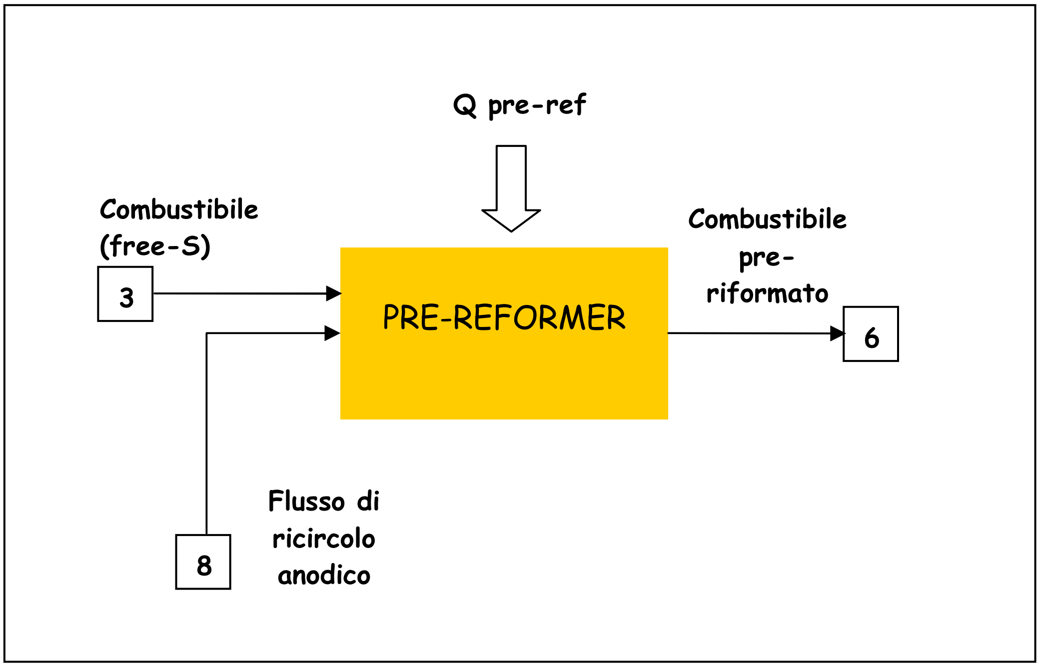

Figura 23 anodic recirculation scheme

Even if recirculated gases are rich of high temperature H_2O, in normal working condition a steam generator is however needed to allow the start of the system.
This plant configuration has been evacuate considering pre-reforming conditions of 35% and 15%, so to compare performance with previous case without an anodic recirculation.
Referring to following table, in both cases are defined the anodic flows:

8 **Anodic recirculation flow**	**35,00%**	**15,00%**
Flow mol/h	49,881	45,305
Temperature	998	862
composition		
H_2O	66%	47,30%
H_2	3,57%	19,50%
CO	3,00%	11,30%
CO_2	27,70%	21,00%

Tabella 21 flow properties anodic recirculation

Can be observed how in 35% pre-reformed case, flow are poor in H_2 but rich in H_2O, while in second case hydrogen presence is higher because electrical current produced (so hydrogen consumption) is lower; in both cases there are a CO_2 concentration higher than 20% at outlet. Inlet cell temperature of recirculation flow is lower when pre-reformer conversion is 15% because of an internal cooling due to reforming reaction.
Pre-reforming concentration at outlet are shown in next table: in both case heat external source are needed to allow conversion, even if the quantity is reduced respect to previous case, because gas coming from anodic flow are in higher temperature conditions.

pre-reformer inlet flow	**35,00%**	**15,00%**
Composition		
CH_4	13,00%	19,30%
CO	2,70%	8,50%
CO_2	23,00%	17,40%
H_2	3,50%	15,90%
H_2O	57,80%	38,90%
T °C	999	864

Tabella 22 pre-reformer inlet flow composition

6 **Pre-reformer exit**	**35%**	**15%**
Exit moles mol/h	67,16	48
Temperature °C	837	770
composition		
CH_4	8,500%	16%

CO	6,500%	10,40%
CO2	20,900%	16,50%
H2	13,700%	21,40%
H2O	50,500%	35,30%
Q pre-ref	**190 W**	**140 W**

Tabella 23 prereformer exit flow

Here below are reported temperature trend (and molar fractions) in pre-reformer in both cases examined;

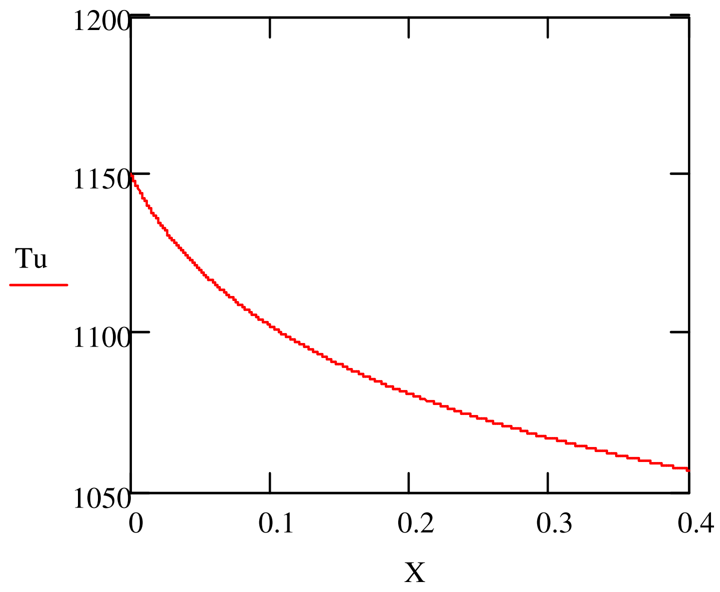

Figure 27 temperature [K] along reformer (15% CASE B)

Air flow in pre-reformer, are directed to the anode side of the stack. To have idea of changes introduced, are presented in next pages a comparison between two configuration of the gases coming from reformer. Performance are reported in table 37.

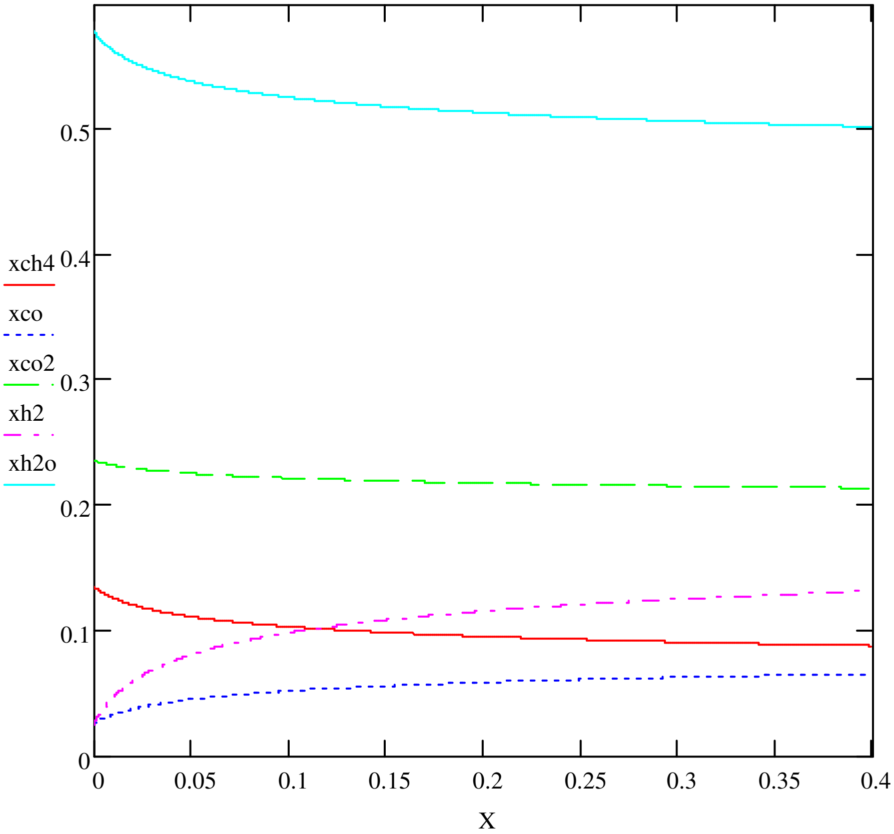

Figure 24 molar fraction along reformer (35% CASE B)

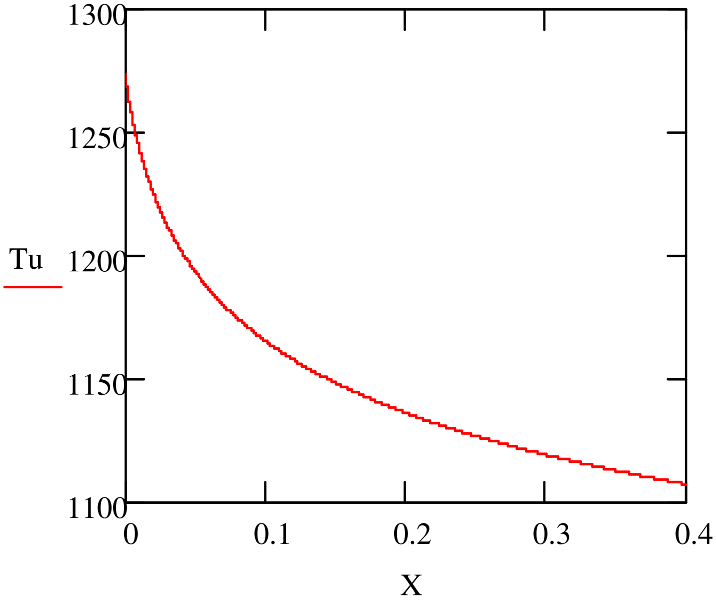

Figure 25 temperature [K] along reformer (35% CASE B)

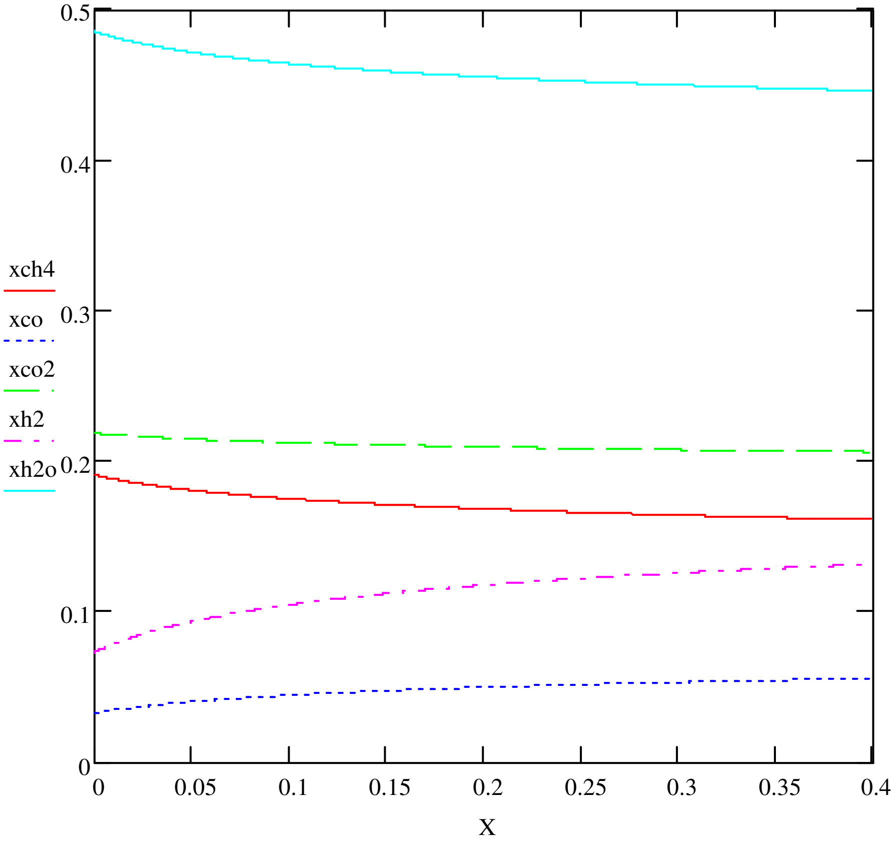

Figure 26 molar fraction along reformer (15% CASE B)

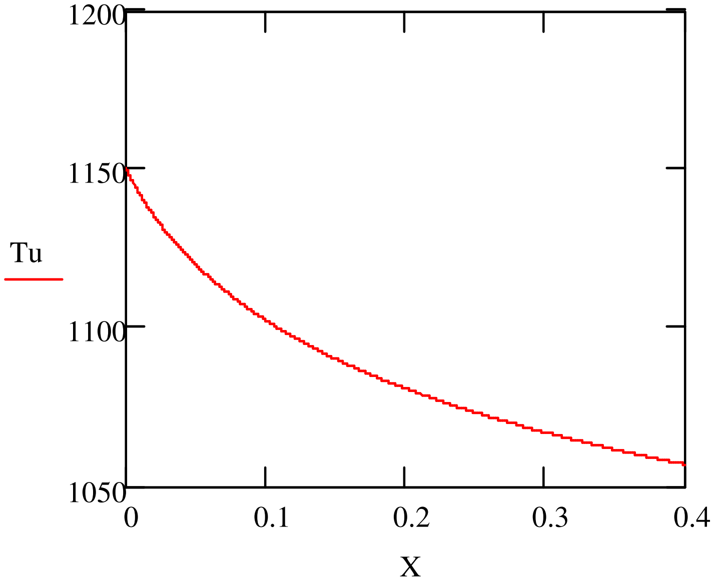

Figure 27 temperature [K] along reformer (15% CASE B)

CASEA		
pre-reformer inlet flow		
Composition	35%	15%
CH4	29%	29%
CO	0%	0%
CO2	0%	0%
H2	0%	0%
H2O	70,60%	70,60%
T°C	1068	982
CASE B		
pre-reformer inlet flow	**35,00%**	**15,00%**
composition		
CH4	13,00%	19,30%
CO	2,70%	8,50%
CO2	23,00%	17,40%
H2	3,50%	15,90%
H2O	57,80%	38,90%
T °C	999	864

Tabella 24 comparison between inlet pre-reformer flows CASE A and CASE B

Fuel Cell Stack	**35%**	**15%**
Inlet flow mol/h	67,16	48,00
Single cell area cm^2	100	100
Cell number	40	40
Current density A/cm^2	0,4355	0,322
Cell voltage V	0,66	0,66
Cell power W	28,743	21,252
Stack power kW	**1,15**	**0,85**
Uf	86%	54%
Air excess	10%	10%
Electric efficiency	49,00%	31,50%

Tabel 25 stack performance CASE B

As is possible to observe comparing table 37 with 26, introducing the anodic recirculation, are obtained an improvement of stack performance in terms of medium current density, stack power and cell efficiency.
In two hypothesis of case B, are obtained a composition of anodic flow quite different, related to power generated by the cell, and other flow characteristic at inlet.

7 **Anode exit**	**35%**	**15%**
Exit flow mol/h	76,74	69,7
Temperature	998	862
Composition		
H2O	66%	47%
H2	3,57%	19,50%
CO	3,00%	11,30%
CO2	27,70%	21,00%
	100%	99%

9 **Cathode exit**	**35%**	**15%**
Inlet air flow	518	520,3
Temperature	979	862
Composition		
O2	18,60%	19,00%
N2	81,40%	81,00%

Tabel 26 anode and cathode exit flows

In next pictures are reported trends of temperature, molar fraction, and current density, at anode-electrolyte interface, in pre-reforming conditions of 35% and 15% of case B.

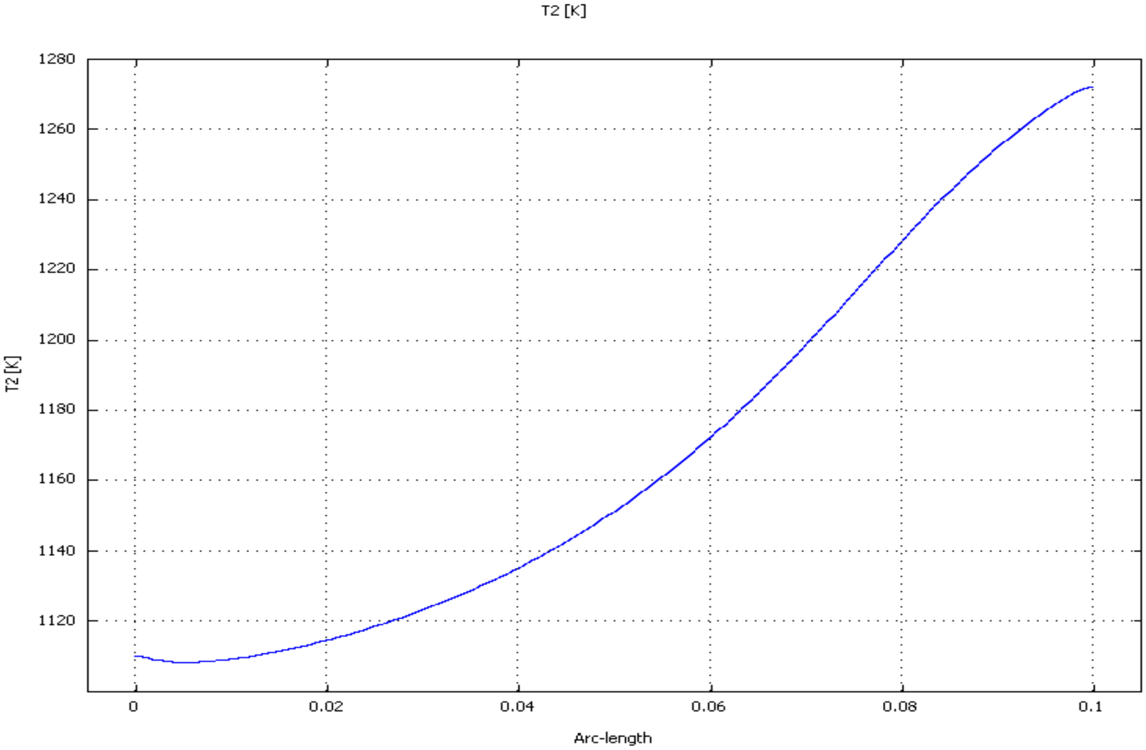

Figura 28 temperature at anode-electrolyte interface (35% pre-ref CASE B)

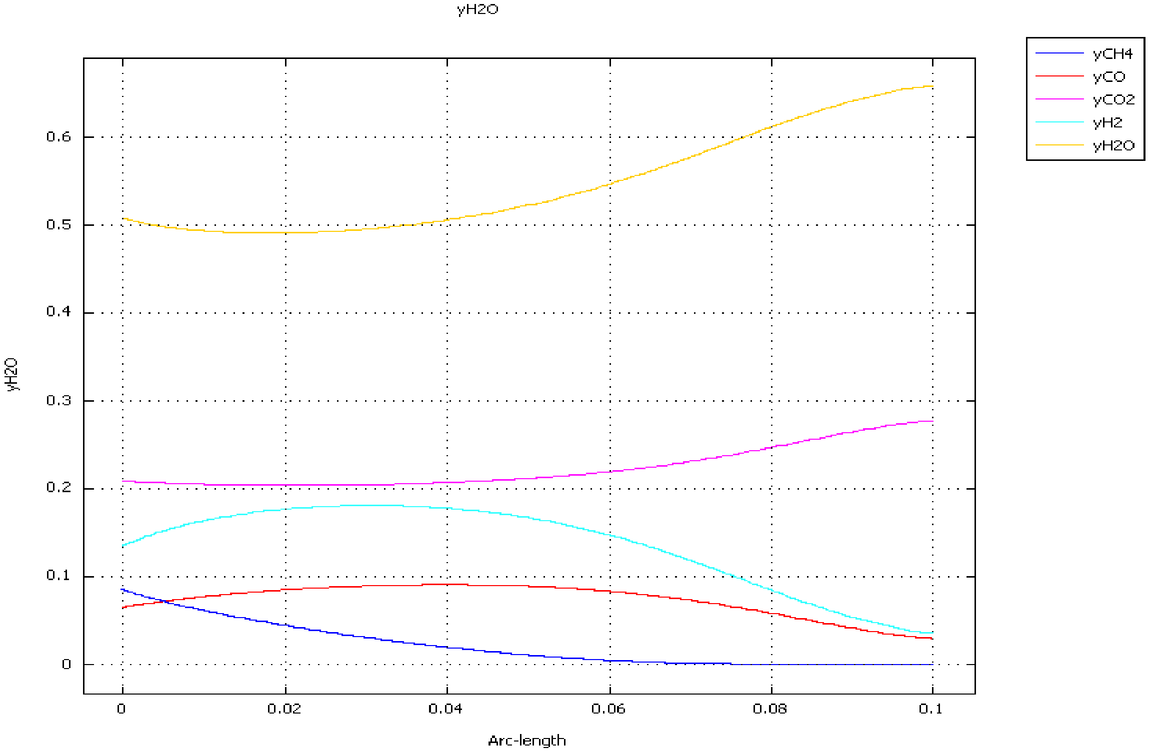

Figure 29 molar fraction at anode-electrolyte interface (35% pre-ref CASE B)

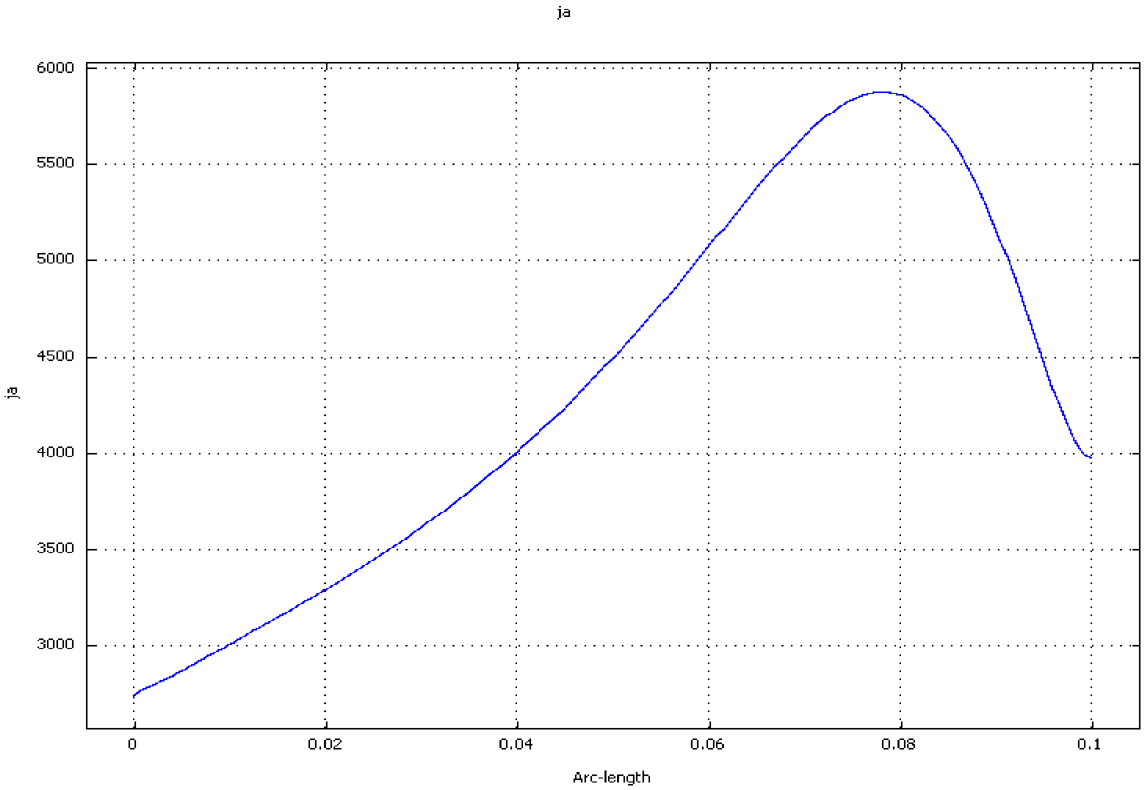

Figura 30 current density [A/m^2] (35% Pre-ref CASE B)

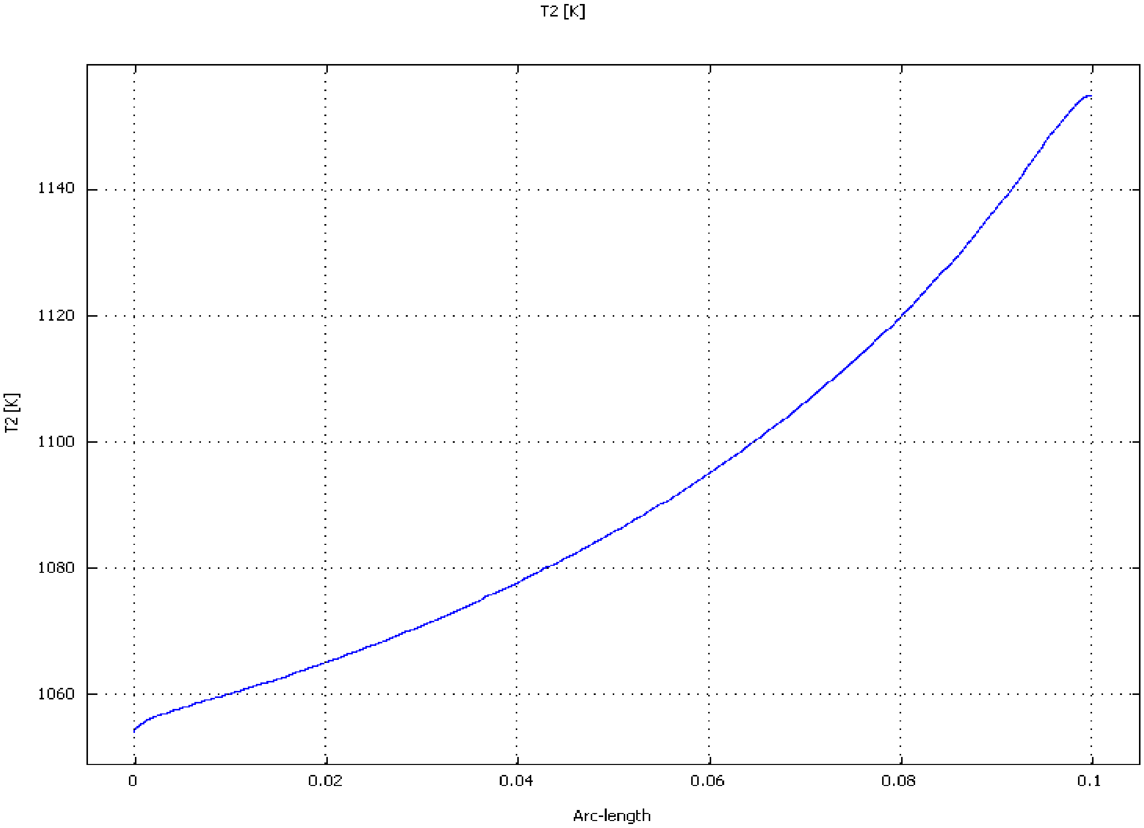

Figura 31 temperature at anode-electrolyte interface (15% Pre-ref CASOB)

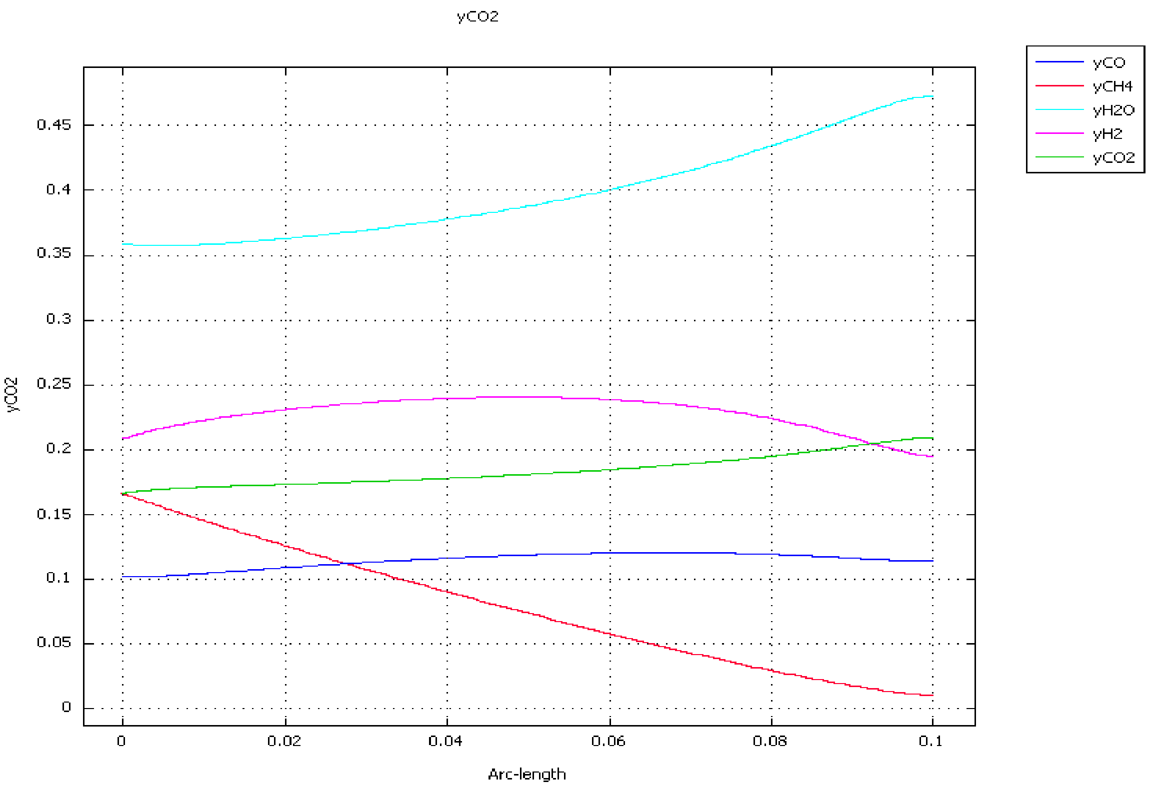

Figura 32 molar fraction at anode-electrolyte (15% Pre-ref CASO B)

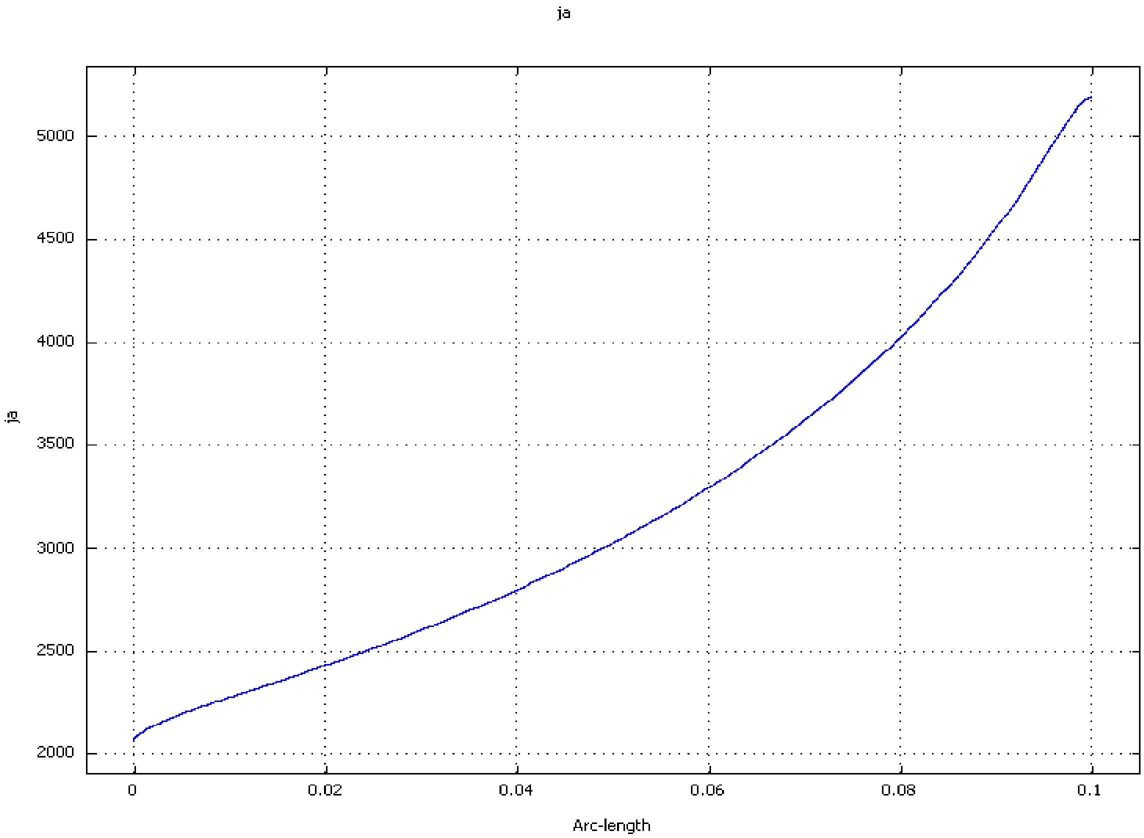

Figura 33 current density [A/m^2] (15% Pre-ref CASE B)

10 **Flusso catodo By-passato**	**35%**	**15%**
moli/h	513,3	500
Temperatura °C	979	862
Composizione		
O2	18,60%	19,00%
N2	81,40%	81,00%
Q disponible 1 [W]	**4067**	**3967**

Tabella 27 Caratteristiche flusso catodico by-passato (CASO B)

	35%	**15%**
Post combustione		
moli aria	4,7	20,3
moli comb	26,859	24,395
Tair	979	862
Tcomb	998	862

Q disponibile 2[W]	**757**	**917**
T°C	1084	1377
11 **composizione in uscita**		
H2O	66%	53,10%
CO2	28,10%	24,40%
N2	5,40%	22,50%

Tabella 28 Caratteristiche flusso in ingresso e uscita dell'after burner (CASOB)

	35%	**15%**
Portata comb [mol/h]	8,4	8,4
mcHi [W]	1870,40	1870,40
Qreg [W]	70	70
Qfuel [W]	34	34
Qpre-ref [W]	190	140
Qsteam [W]		
Qair [W]	3970	3970
Q1 [W]	4067	3967
Q2 [W]	757	917
P [W]	1034,75	765,07
P+Q	1594,75	1435,07
rend I principio	85,26%	76,73%

Qnet [W]	560	670
T media [K]	865	1011,5
Exergia	367,08	472,61
rend II pricipio	74,95%	66,17%

Tabella 29 Prestazioni del sistema CASO

Comparing results from previous table, (case A, table 30), can be observed how in this second case, global efficiency of the system moves from 82% to 87% principally due to power stack increasing.

3.5 SOFC System feed by biogas;

In this paragraph will be analyzed behaviour of the system illustrated in previous pages, fuelled with different sort of fuels. This can allow to have in the future, plats which uses poor fuels directly derived from traditional fuels at low cost; all this should consent to realize simple, small plants as standardized as possible.

Generally speaking, compared with traditional power generation system, high temperature fuel cell, after an opportunity fuel "clean-up" system, can be powered with higher range of fuels.

With this purpose, has been analyzed a valuation of configuration possible with purified dump gas, and gas derived from garbage gasification.

Must be introduced that the use of poor fuels may cause troubles due to pollution content; even if the cell is characterized by high flexibility, its working can be compromised by low quantity poison substances; first of all has been analyzed a cell system feed by biogas keeping constant equivalent hydrogen moles, to be compared with previous model introduced.

Biogas flowrate [mol/h]	20,2
T °C	20°C
Composition	
CO_2	38,89%
CH_4	50%
N_2	11,11%

Tabella 30 inlet byogas composition

As is possible to observe, percentage of inlet methane is quite high, so has been considered a pre-reforming phase of 35%. Plant configuration consequently, remains the same respect to picture 44. Keeping a S/C ratio of 2.4 are needed 24,24 mol/h of water.

Pre-reformer inlet flow properties are reported in table below:

pre reformer inlet flow	
Flowrate	44,44
Temperature °C	1037
Composition	
CH4	22,70%
CO2	17,70%
N2	5,10%
H2O	54,50%

Tabella 31 pre-reformer inlet flow

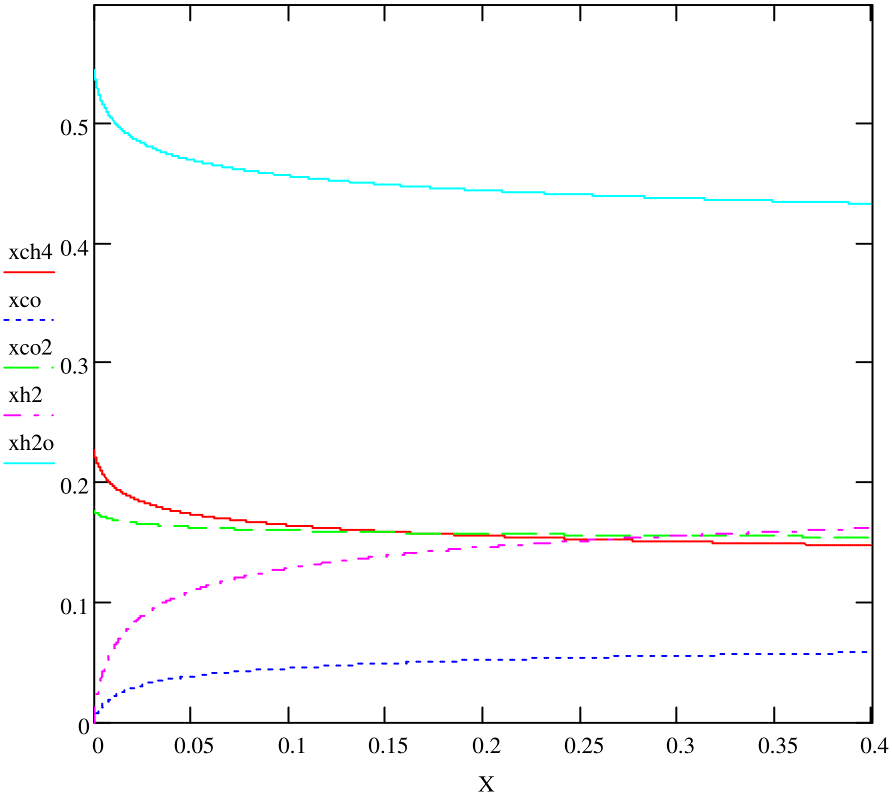

Figura 34 molar fraction along reformer

Molar ratio trend and temperature along reformer are reported in picture 100 and 101. In table 44 and 45 are reported pre-reformer flow exiting composition and cell performance;

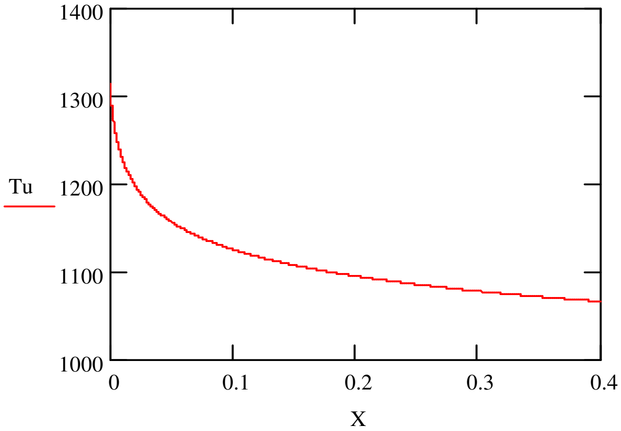

Figura 35 Temperature along reformer [K]

Cell inlet flow	
Flowrate mol/h	49,22
Temperature °C	792
Composition	
CH4	14,70%
CO	5,80%
CO2	15,40%
H2	16,20%
H2O	43,40%
N2	4,50%

Tabella 32 reformer exit flow

Fuel Cell Stack	
BIOGAS	
pre-reforming percentage	**35%**
Inlet flow mol/h	**45,16**
Single cell surface cm^2	100
Cell number	40
Current density A/cm^2	0,4113
Cell voltage V	0,66
Cell power W	27,1458
Stack power kW	**1,085832**
Uf	79%
Air excess	10%
Electric efficiency	47,00%

Tabella 33 stack performance fed by byogas

As is possible to observe in table 45 biogas fuel feed (instead of methane) implies only small decreasing of coefficient of fuel utilization and electric efficiency, respect to similar configuration with pre-reformer of 35%, with and without anodic recirculation, related to less hydrogen at cell inlet. From table 46, also global efficiency is slightly reduced.

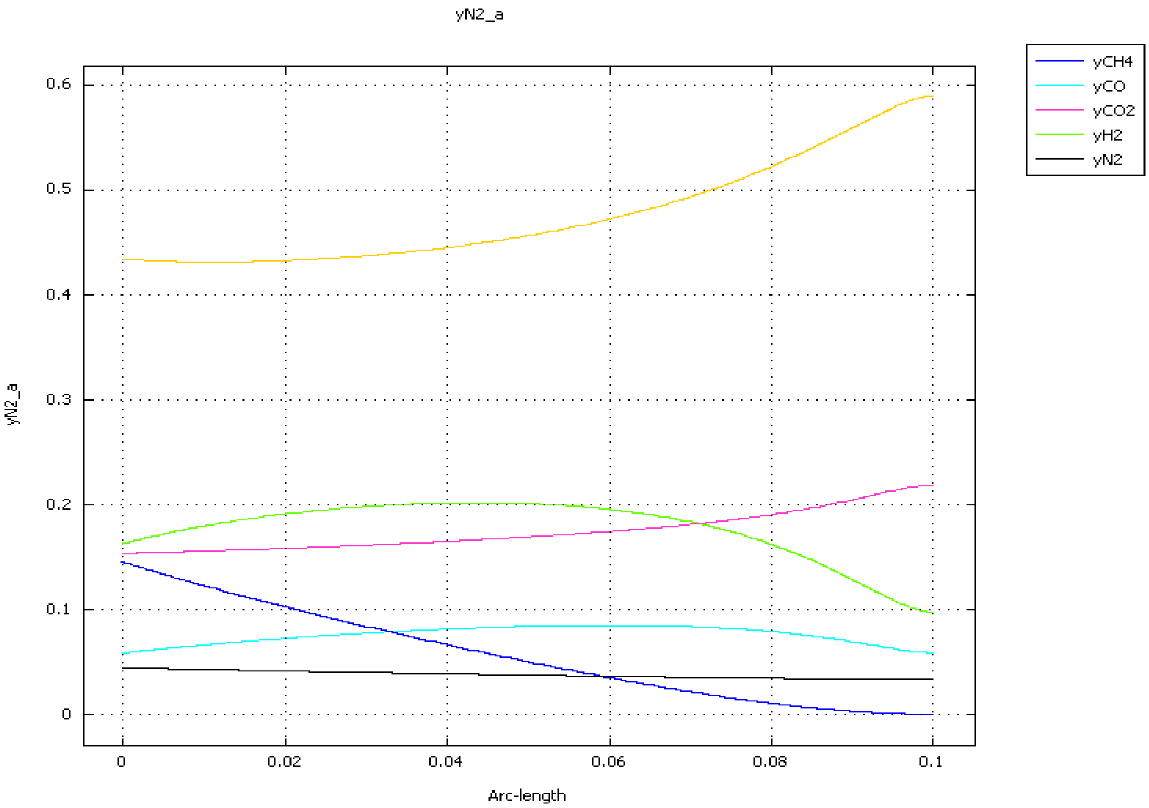

Figura 36 molar fractions at anode-electrolyte interface

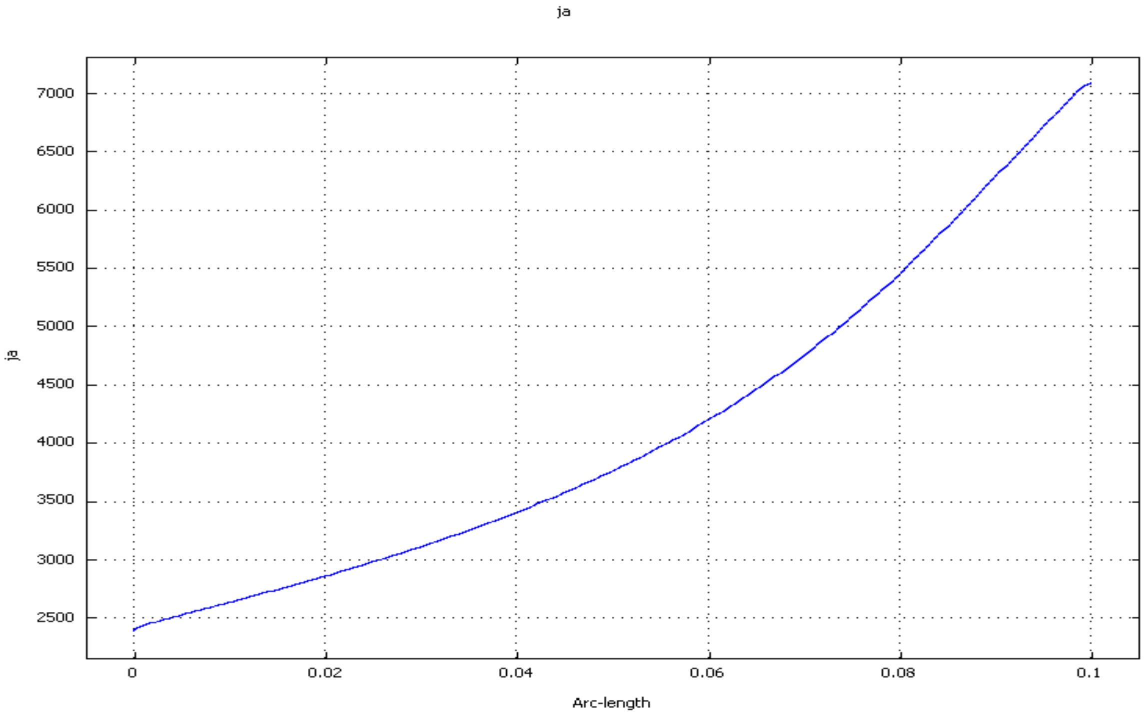

Figura 37 current density [A/m^2]

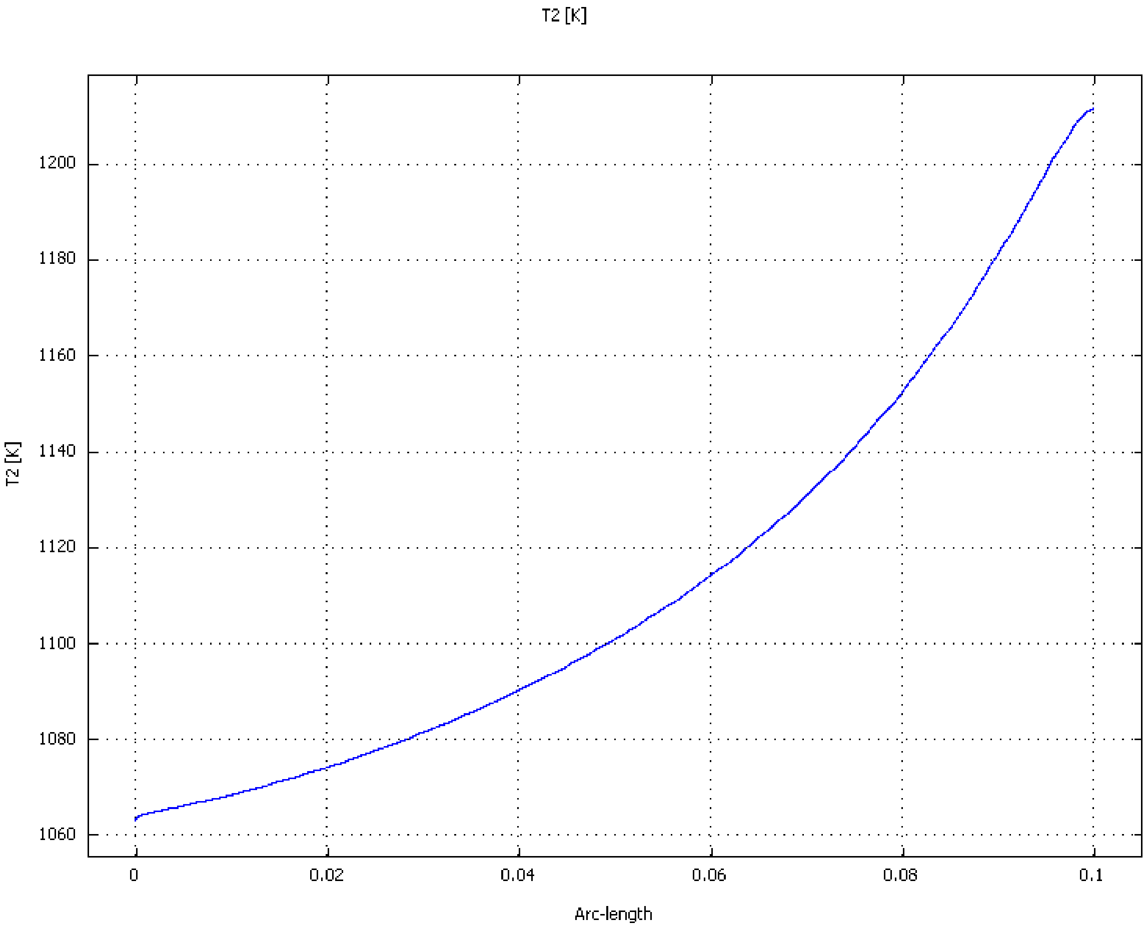

Figura 38 temperature at anode-electrolyte interface

	Biogas
Flowrate Kg/s	0,000158359
mcHi	2236,03
Qsteam	323
Qpre-ref	680
Qfuel	65
Qair	3970
Q1	3843
Q2	2013
P	1019,9
Efficiency	82,19%
Qnet	818
T	800
Ex	513,30
II principle efficinecy	68,57%

Tabella 34 biogas fuel performance

- SOFC system feed by syngases;

flowrate mol/h	80,6
Temperature	20°C
Composition	
H_2	8,11%
H_2O	10,81%
CO	8,11%
CO_2	16,22%
CH_4	8,11%
N_2	48,65%

Tabella 35 composition of singas

Fuel inlet properties are shown in table 47. Methane concentration at inlet is quite low, so it's possible to introduce fuel directly in the stack without necessity of pre-reforming equipment. H2O ratio, instead would cause a value S/C of 1.33, so it needed to be increased to 2. in picture 105 is reported a plant configuration (to note the absence of reforming reactor); in this model, has been consider to approximation to have directly syngas ready to be used, with out any gasification system, and any cleaning system;

Gas and steam are mixed before entering the cell (flow inlet properties in table 48, calculated in the same way to have and equivalent hydrogen moles at cell inlet of cases previously examinees .

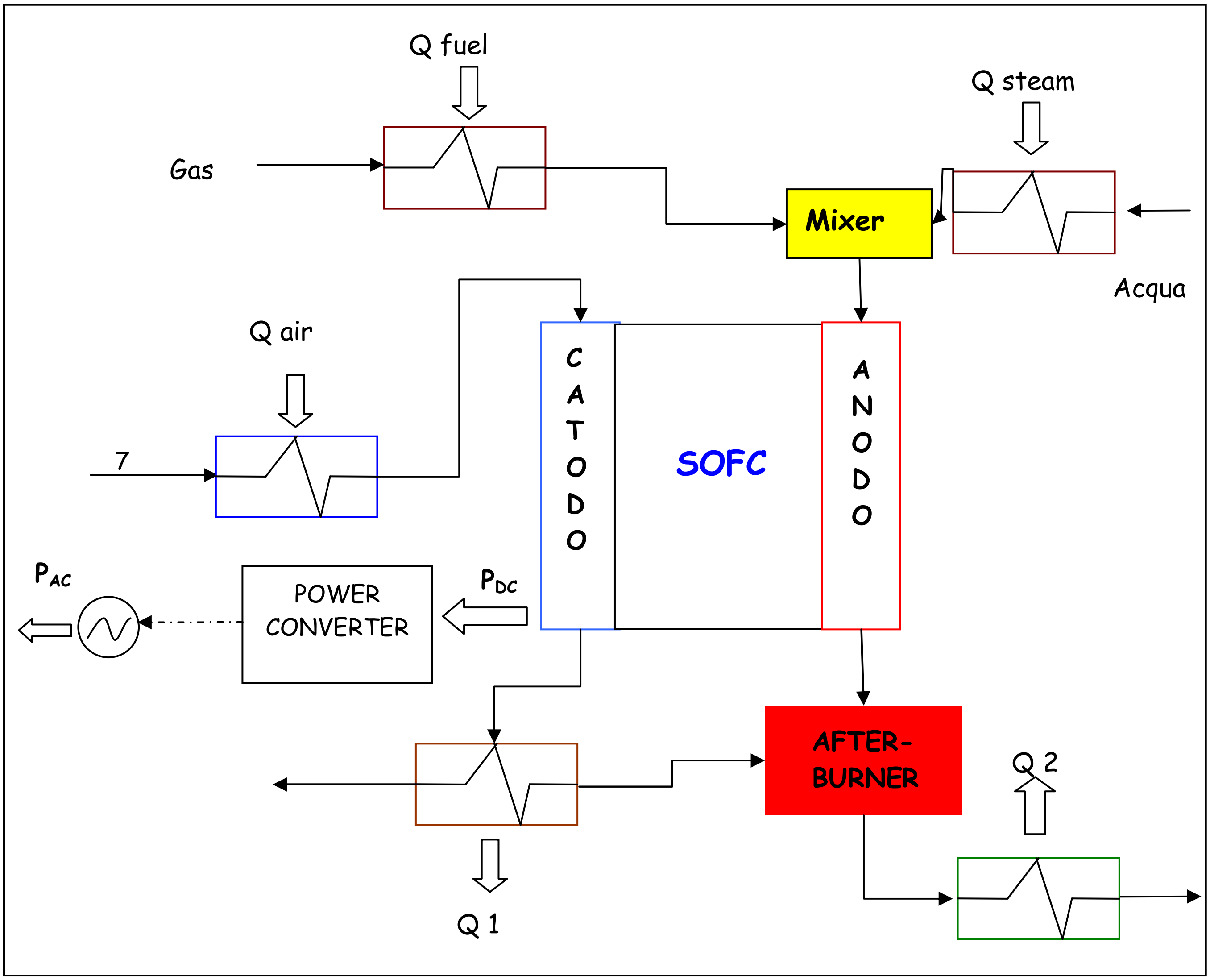

Figura 39 plant scheme fed by singases

Inlet cell flow	
Flowrate mol/h	86
Temperature °C	787
Composition	
CH4	7,60%
CO	7,60%
CO2	15,20%
H2	7,60%
H2O	16,30%
N2	45,70%

Tabella 36 inlet cell flowrate

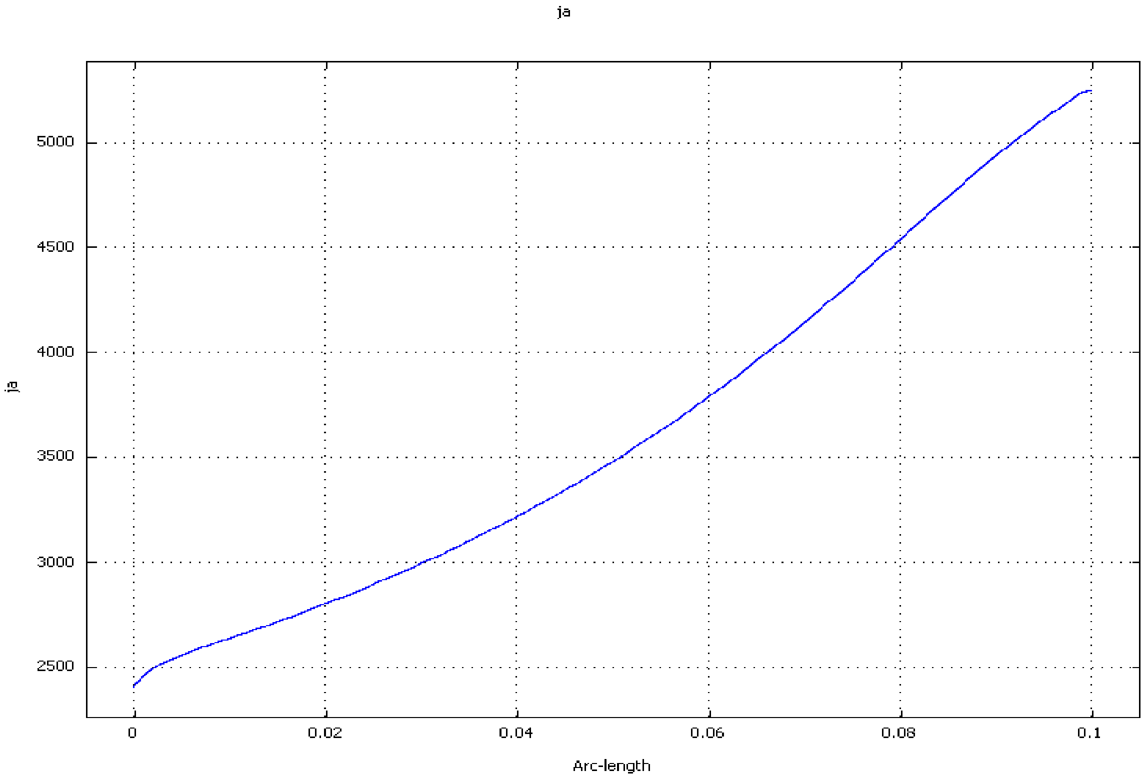

Figura 40 current density [A/m^2]

Stack performance for stack feed by byogas are reported at in table at left: it show how respect to the model feed by methane there are a little power decreasing while the stack electrical efficiency remain at 42%. This is an indication of potentiality of this system also in case where are feed by this kind of fuels;

Fuel Cell Stack	
	Gas di sintesi
pre-reforming percentage	**0%**
Inlet flow mol/h	**85,68**
Single cell surface cm^2	100
Cells number	40
Current density A/cm^2	0,3636
Cell voltage V	0,66
Cell power W	23,9976
Stack power kW	**0,959904**
Uf	75%
Air excess	10%
Electric efficiency	42%

Figura 41 stack performance

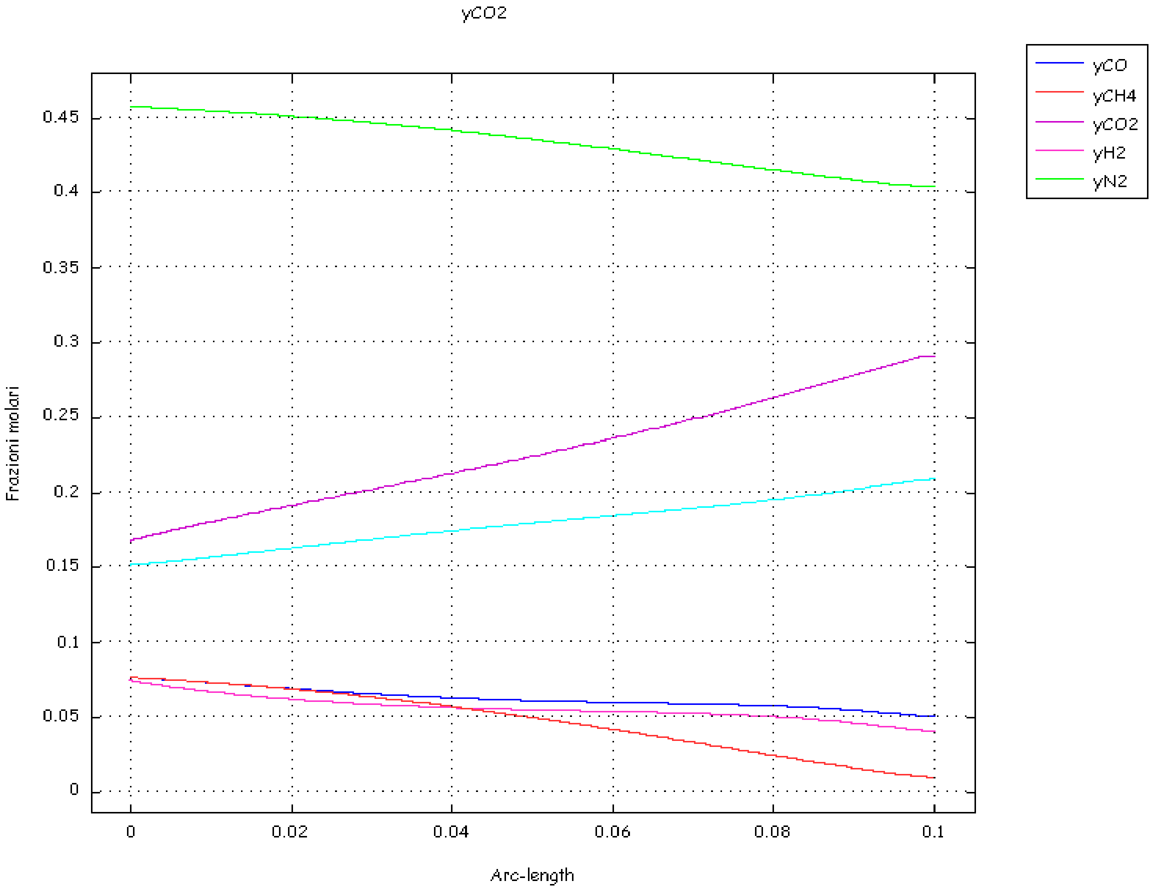

Figura 42 molar fraction at anode-electrolyte interface

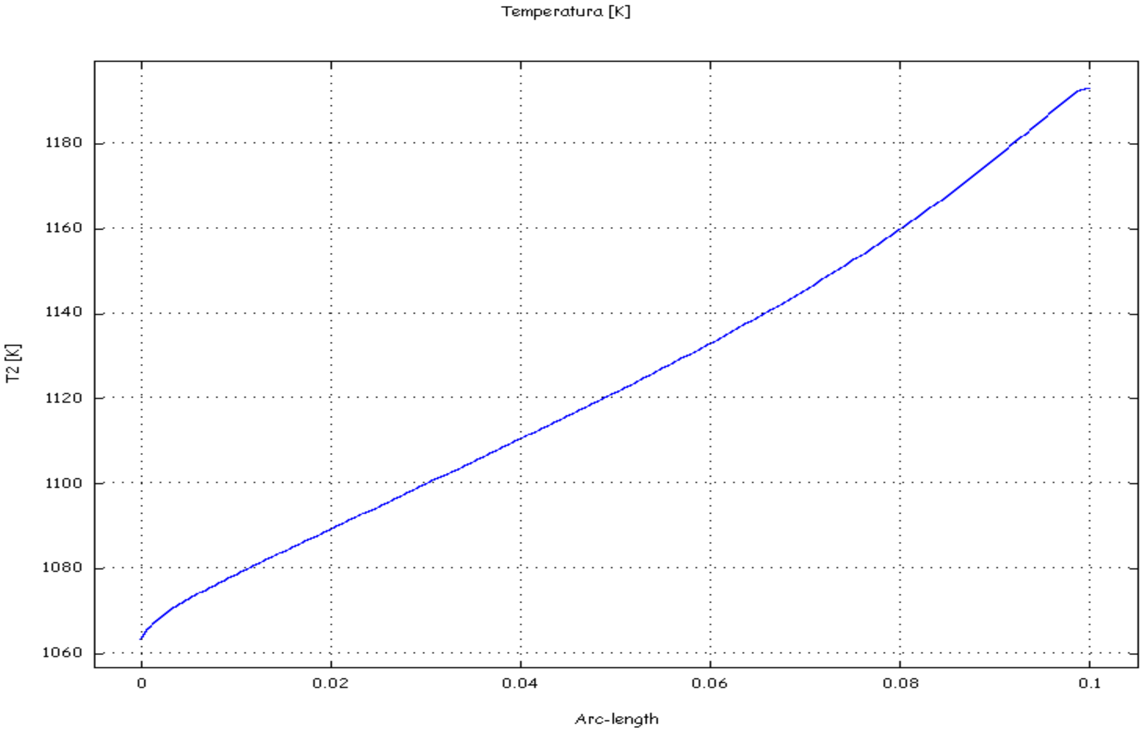

Figura 43 temperature at anode-electrolyte interface

	syngas
flowrate Kg/s	0,000722405
mcHi	2564,54
Qsteam	74
Qpre-ref	
Qfuel	805
Qair	3970
Q1	4193
Q2	1804
P	902,31
Efficiency	79,95%
Qnet	1148
T	964
Ex	793,12
II principle efficiency	66,11%

Tabella 37 SOFC system fed by syngas

In table 49, with syngas feeding are also reported how global efficiency of the system remain around values of 80%.
In table 50 are reported a comparation of the same system feed by methane, syngas and biogas; these last two shown a good global efficiency that decrease from 87% to 79%, while heat available pass from 560 W of methane system to 1148W of the system feed with syngas.
However this last model have a deacrease of power generated of 15% respect to methane system.

	Gas from gasification	Byogas	Methane 35%pre-ref	Methane 35%pre ref with recirculation
Flowrate [mol/h]	80,4	20,2	9,88	8,4
mcHi [W]	2564,54	2236,03	2199,95	1870,40
Qreg [W]	74		70	70
Qsteam [W]		323	315	0
Qpre-ref [W]	649	680	588	190
Qfuel [W]	3970	65	40,2	34
Qair [W]		3970	3970	3970
Q1 [W]	4193	3843	4471	4067
Q2 [W]	1804	2013	1257	757
P [W]	902,31	1019,9	1066,59	1080,74
I principle efficiency	79,95%	82,19%	82,34%	87,72%
Qnet [W]	1148,00	818	744,8	560
II principle efficiency	66,11%	68,57%	73,43%	77,41%

Tabella 38 comparation between system fed by methane (with and without recirculation), byogas, and syngas.

- 4. Stack of SOFC

In this chapter will be analyzed the issues involved passing from single element to a stack of cells;

In the model normally used, the SOFC cell are presented as a multi-layer elements as in the picture below (dimension indicated are the same used on the numerical model); From a mechanical point of view it's quite easy to realize a SOFC system using just a single cell, as analyzed in first chapter.

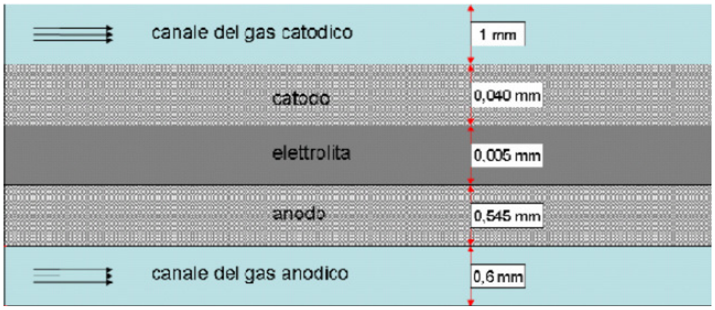

If we decide to replicate this system in a SOFC stack, the things are not so easy, but it's needed to analyze several aspects in order to solve a temperature, leakages and electric contact issues;

To understand the difficulties complexity, it's enough to image to realize a system composed from only two consecutive cells: in the picture below are shown two scheme layer placed in series; the first thing to be noted is that the anode of bottom cell and cathode of the upper one have to be separated from something placed in between;

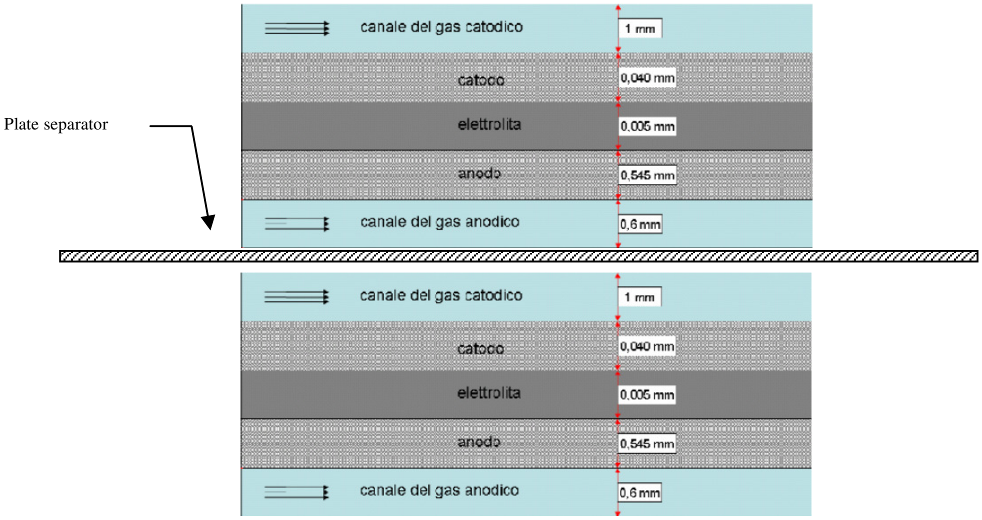

First properties that this "Plate separator" must certainly have are:

- High temperature resistance;
- Electric low conductivity;
- Resistance to corrosion;

From these preliminary characters, a plate like that should be certainly a metallic plate: in particular, in these analyses and experiment, the choice of such material is Crofer 22® (in the appendix is possible to grab more information about specifics).
There is also another aspect to note: the layers putted in contact are two gas channels: they are empty for definition, so to assure an effective contact there should be something that mechanically connect this plate with cell surfaces; these elements were already present in the 3D model presented as "ribs"; These elements are been presented as "disturb element " to the flu dynamics but necessary to the mechanical support of the cell itself;

With these considerations we find out other properties these ribs must have:

- Be a mechanical support for gas channels;
- Be electric conductor;
- Be resistance at high temperature;
- Assure the contact with metallic plate;
- Be mechanically adjustable in order to adapt its shape to guarantee electrical contact in case of cell (or plate interconnector) deformation or initial defect.

Last point is probably the most important: if it's considered the thermal rising from the assembling phase at environment temperature, to the final operation of more than 800 °C, it's possible to imaging the importance of thermal expansion and deformation, especially in the start up phase. A minimum deformation of every element can, in the better cases, cause a bad electric contact, increasing the overall ohm losses and consequently the system performances; In other cases can occur the anticipated mixing of fuels and oxygen that at such high temperature may certainly compromise the whole system safety;
Deformation however can simply be due to component geometry defects: wrinkle surface, initial bending and manual assembling errors of course have their importance to contact aspect;

Starting from results discussed in previous chapters, it's possible to extend the final consideration to mechanical behaviour of the whole system; in particular, looking at the pictures below, are shown the current intensity normally obtained on cell surfaces in most of cases; this current distribution is reasonable applied on the interconnector surface;

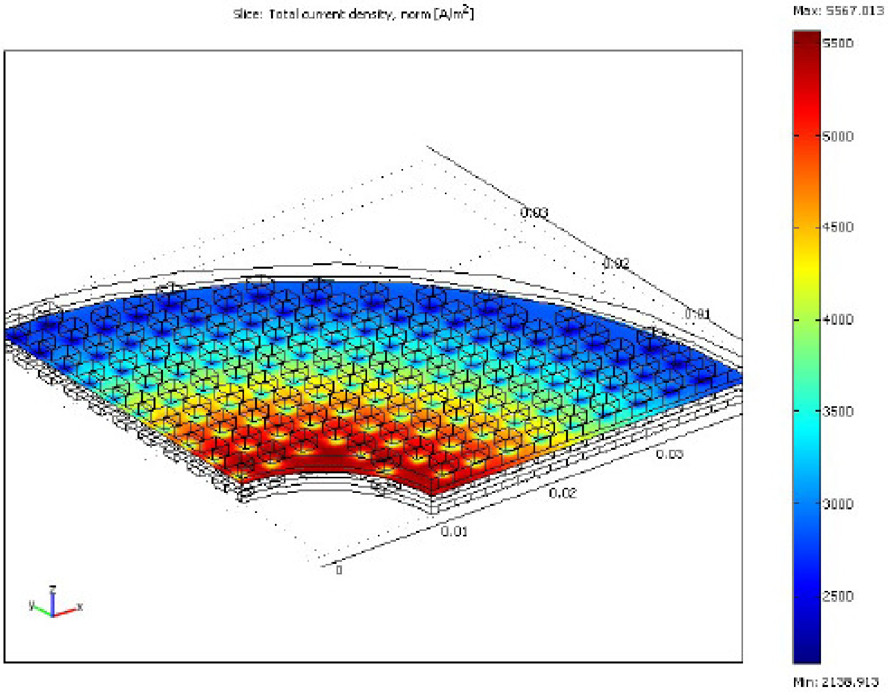

Taking a generic cut section to analyze the problem in two dimension (that could be a generic angle as per shown on the picture on right), the results and considerations obtained from 3d analysis are applied on this sections; From geometric point of view, the results is a simple rectangle (supposed be 1mm thin):

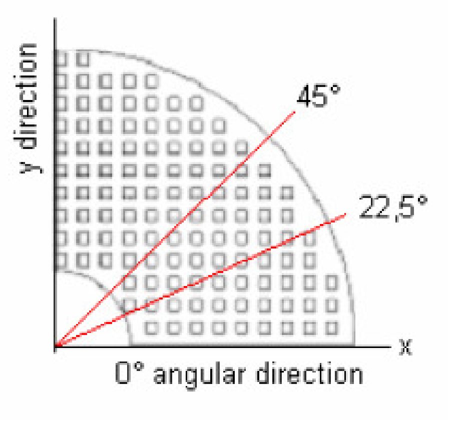

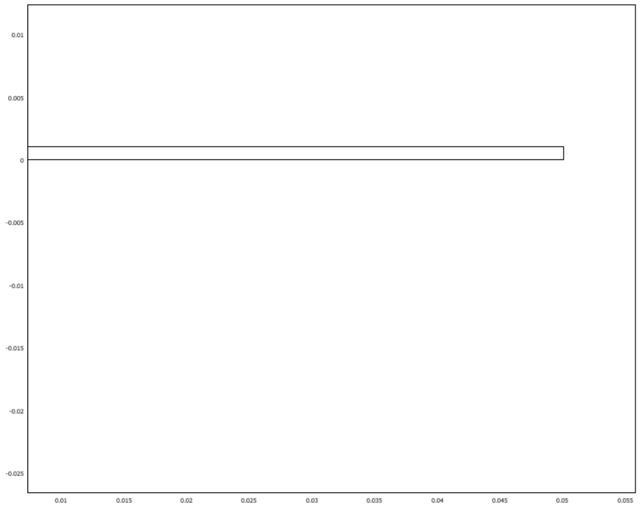

Applying on this geometry, current values results from 3D model as boundary conditions, the current distribution appears in this way:

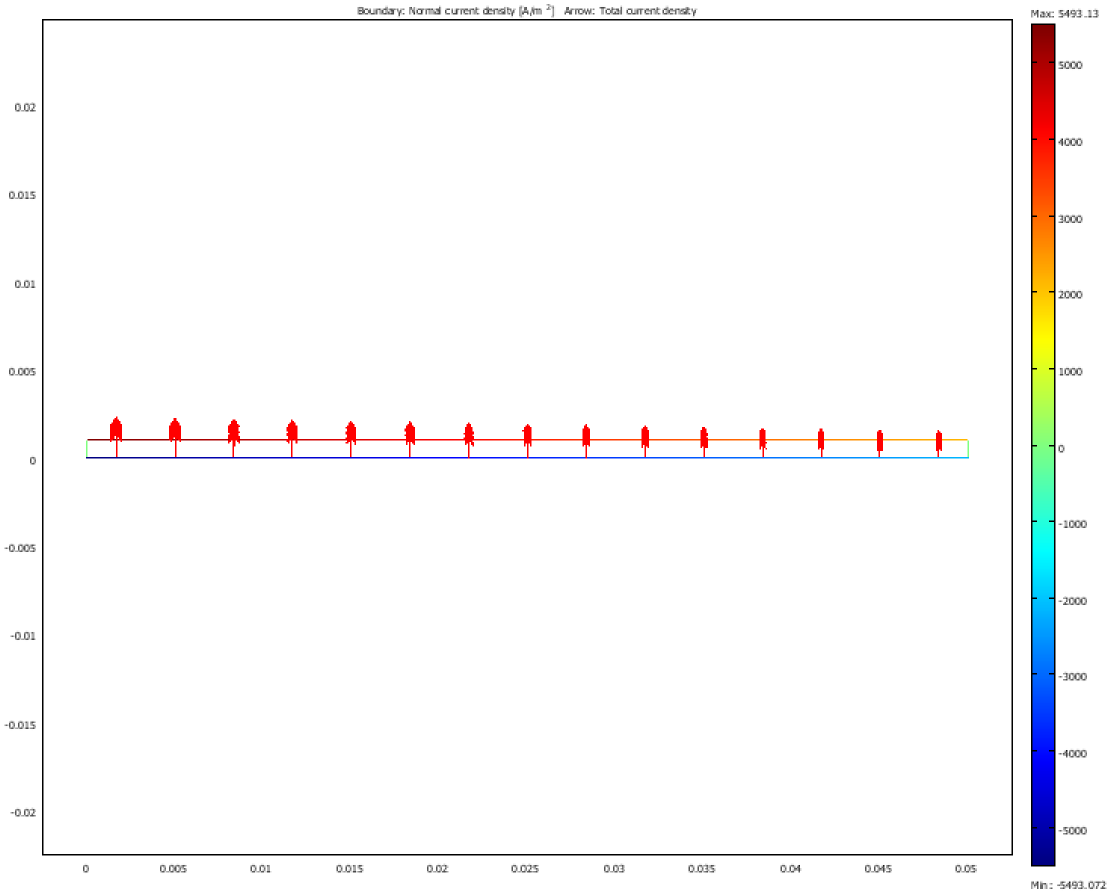

Now the 2D model needed a thermal model to analyze the mechanical behaviour; as per the previous case, are considered initially results obtained from 3D model:

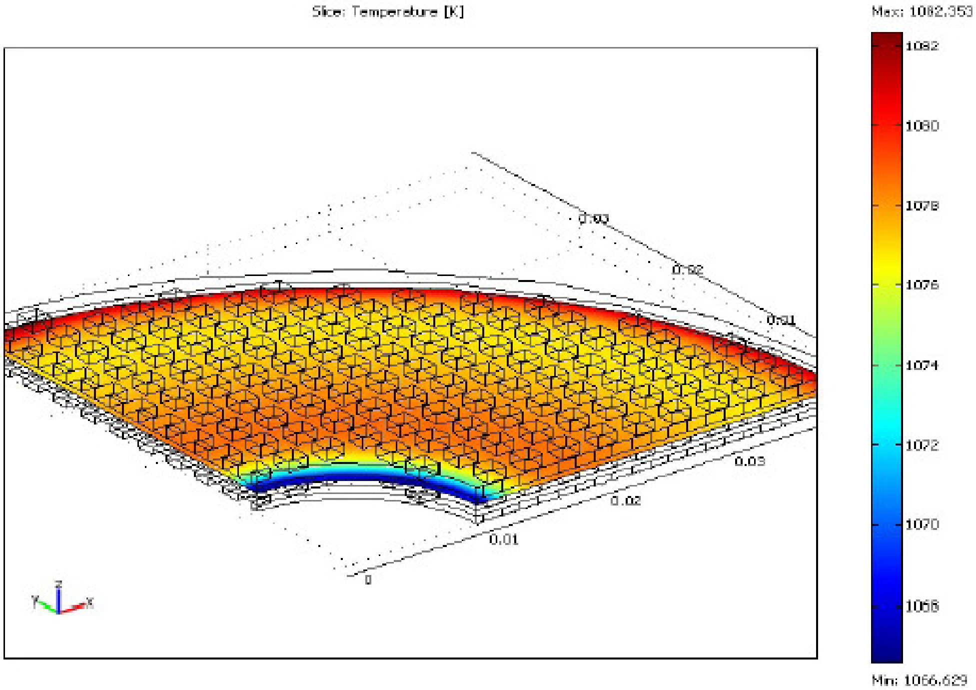

A quick consideration can be done about the temperature displacement:

- A first cooling of surfaced due to “fresh” inlet gases;
- An increasing of temperature in the internal area due to high current density presence;
- A temperature decreasing due to lack of species (and low current density consequently);
- A rising of temperature due to post-burner effect;

From the interconnector point of view, can be applied a similar condition:
- Inlet and outlet temperature are influenced from fresh gas inlet and post burner presence;
- Internal heat generation is due to Joule effect (calculated from current distribution of previous pages);

More over there is another factor to consider before obtain a temperature distribution: the interconnector has the task to keep separate two flows of air and hydrogen (considered in this case but also in many real conditions), that have different velocity (main factor) and different physical fluid properties (secondary importance).

Different cooling capacity on two interconnector sides is evaluated in the simple way below:

$$\frac{\bar{h}_{anode}}{\bar{h}_{cathode}} = \frac{0.332}{0.332}\left(\frac{\mathrm{Re}_{anode}}{\mathrm{Re}_{cathode}}\right)^{0.5}\cdot\left(\frac{\mathrm{Pr}_{anode}}{\mathrm{Pr}_{cathode}}\right)^{0.33} = \left(\frac{\dfrac{\dot{Q}_{anode}}{\nu_{anode}}}{\dfrac{\dot{Q}_{anode}}{\nu_{cathode}}}\right)^{0.5}\cdot\left(\frac{\mathrm{Pr}_{anode}}{\mathrm{Pr}_{cathode}}\right)^{0.33}$$

Considering the following parameters values:

$\dot{Q}_{anode}$ = 1.61 l/min

$\dot{Q}_{cathode}$ = 47.4 l/min

Pr_{anode} = 0.72 (at 1000 °C)

$\mathrm{Pr}_{cathode}$ = 0.753 (at 1000 °C)

$\nu_{anode} = 1.99 * 10^{-4}$ m^2/s

$\nu_{cathode} = 13.4 * 10^{-4}$ m^2/s

Result is: $\bar{h}_{anode} \cong 47\% \ \bar{h}_{cathode}$

At the end of these considerations, conclusion is that the interconnector has a temperature gradient due to:

- High (and low) density current area;
- Differential cooling action by gases at sides;

If include that in the model, the temperature profile in the interconnector section becomes the one showed in the pictures (current density lines are kept on surface to evidence the current distribution);

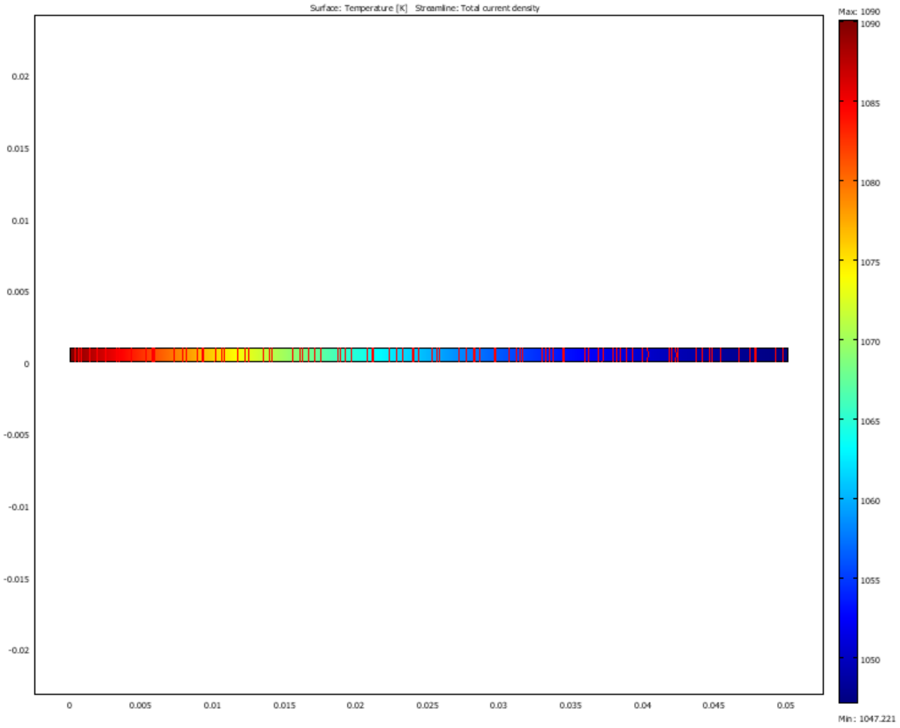

Now it's possible to include thermal deformation in the interconnector model:

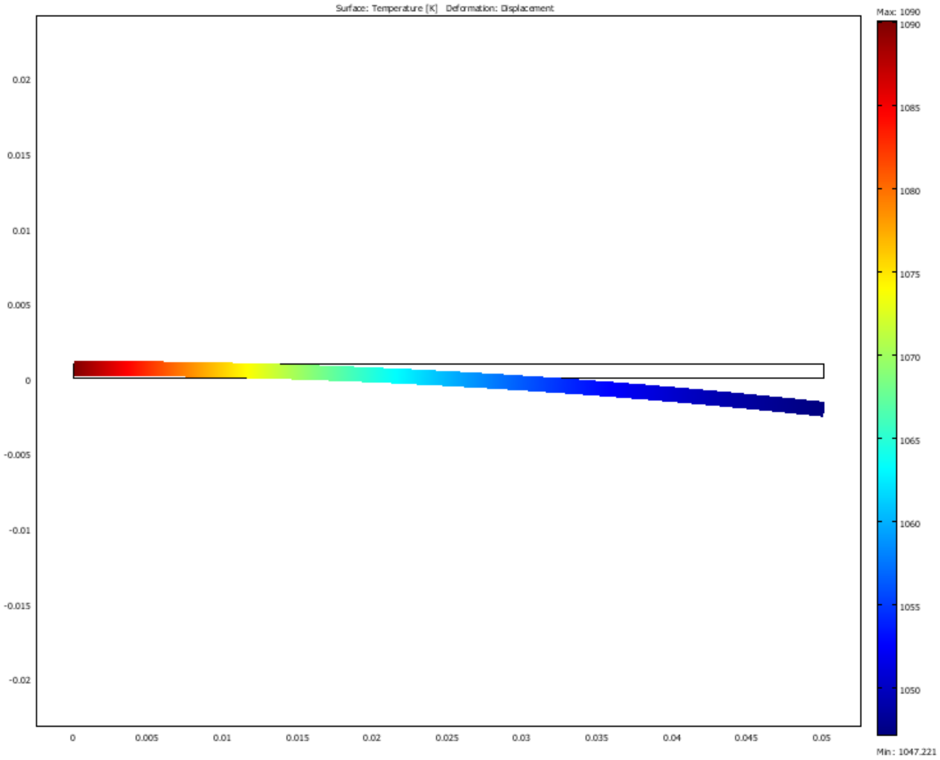

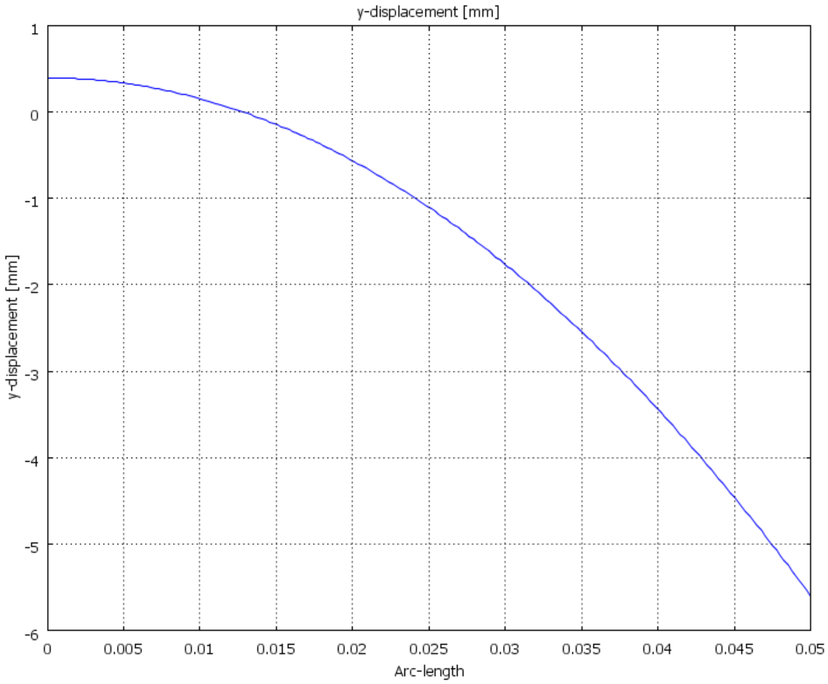

To be noted that displacement (in vertical direction) are been obtained without any reaction force (due to the contact) with ribs; This is of course not the normal condition: indeed, during stack assembling, a certain force compression is applied; as for the sketch below, every ribs (in this case the red arrows) are pressed against the interconnector, to guarantee electric contact and reduce the mechanical deformation due to temperature gradient.

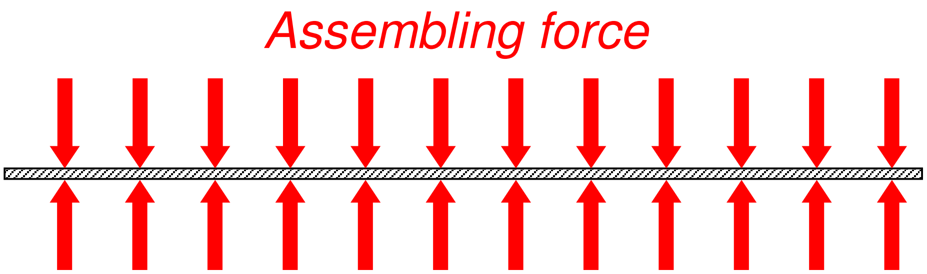

Therefore in the model, has been applied on top and bottom surfaces the preload force, and a weak joint condition that represents the reaction force of ribs under imposed deformation, as per the law:

$$F = K*y$$

With:

F: reaction force
K: elastic constant [N/m]
y: vertical displacement [m]

Including this simple relation in the model, the interconnector deformation depends from the compression load; the graph below show the vertical movement of the interconnector along the cell radius at *1000 °C:* Increasing the load, the maximum vertical displacement are reduced consequently, avoiding (with load rise) contact issues;

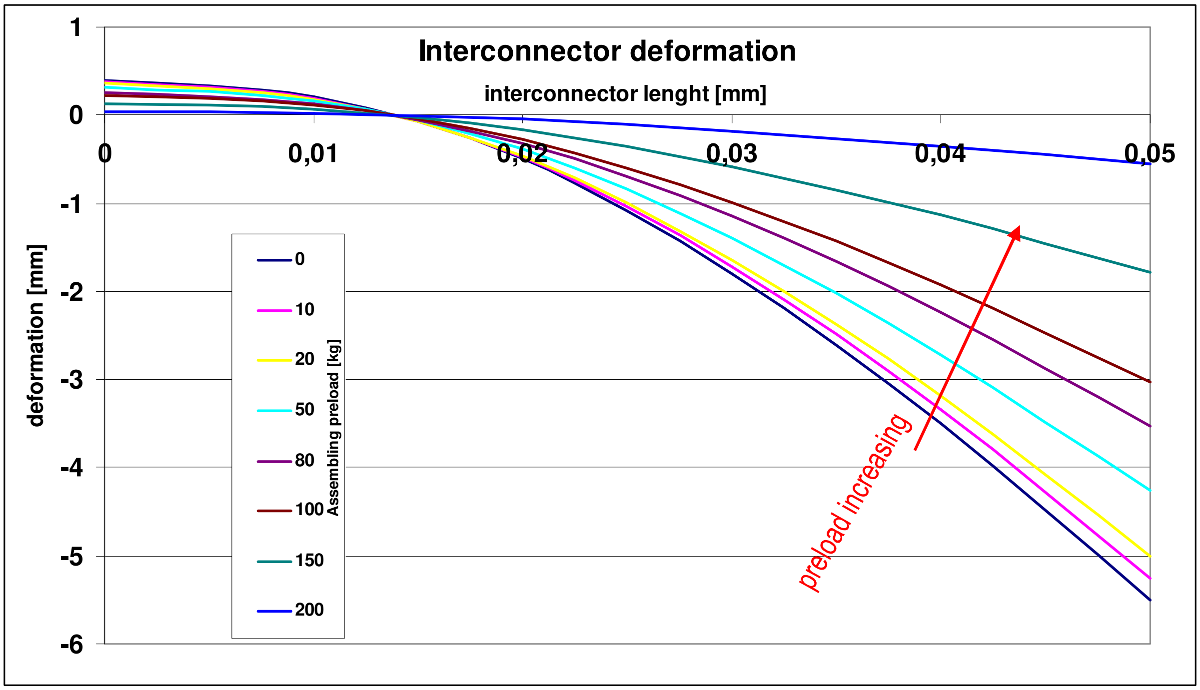

Even if consider the lowest interconnector displacement given applying 1,5 kg/cm2 as initial pressure, comparing with the standard contact rib shape, is possible to observe the same movement order: the following pictures shows some measurement taken by laser measurement on the rib surface: if it's considered the top of the contact as the points at values of -16.5 mm, must be noted that the lowest point of surface are at 0.5mm far.
This deformation from rib side is not due to post operation of some kind of deformation, it's simply after the rib creation process and depends from the kind of technology used.

For example, taking a "co-flows" cells, a cross section gas channel can be imaged as per sketch below:

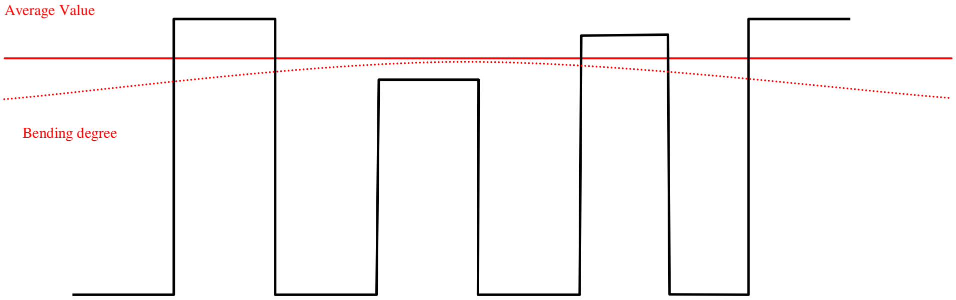

In these drawing, the ribs appears as rectangles with non homogeneous height: this is the normal condition that normally have to be investigated before a stack assembly; in particular, some important values could be the average height values or bending degree that allows to have an idea of what could be the initial contact conditions in every repeating element.

Before stack assembling, usually are performed a surface analysis to define the quality of each element that are going to be installed.

Normally are used laser machine scanners as the one showed below:

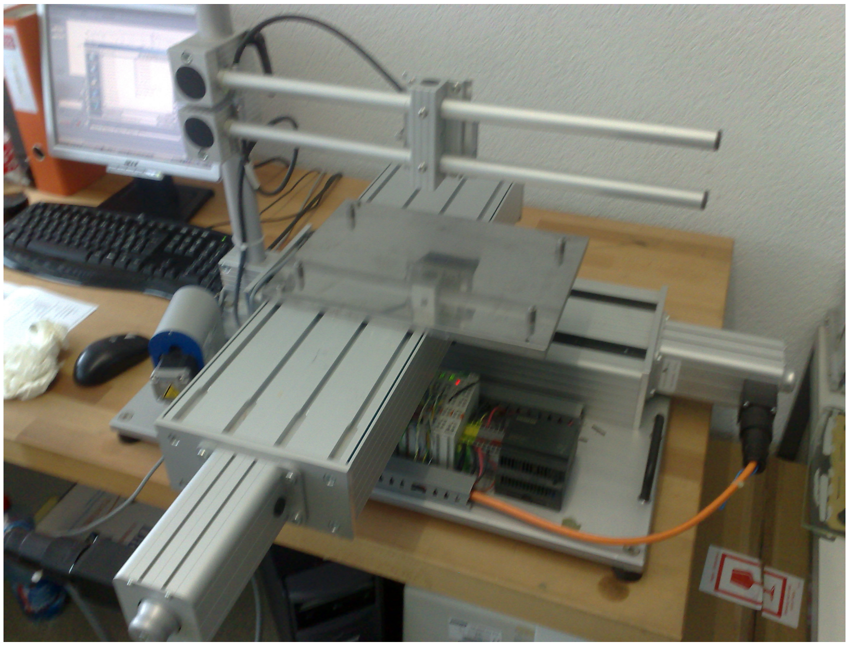

In most cases the analysis interest some reference points or lines: so the analysis can be performed on a fixed path on channels surface that can be easily compared with other elements; This showed here is a channels surface with a generic path of measurement (represented from red line) :

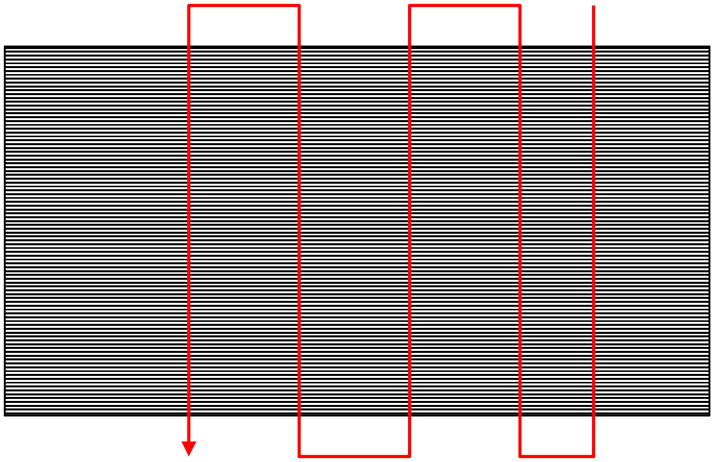

Scope of this test is to analyze different sections and find bending, ribs average values and whatever parameter needed to define the channel quality on the same gas channel;

A typical results may be the following:

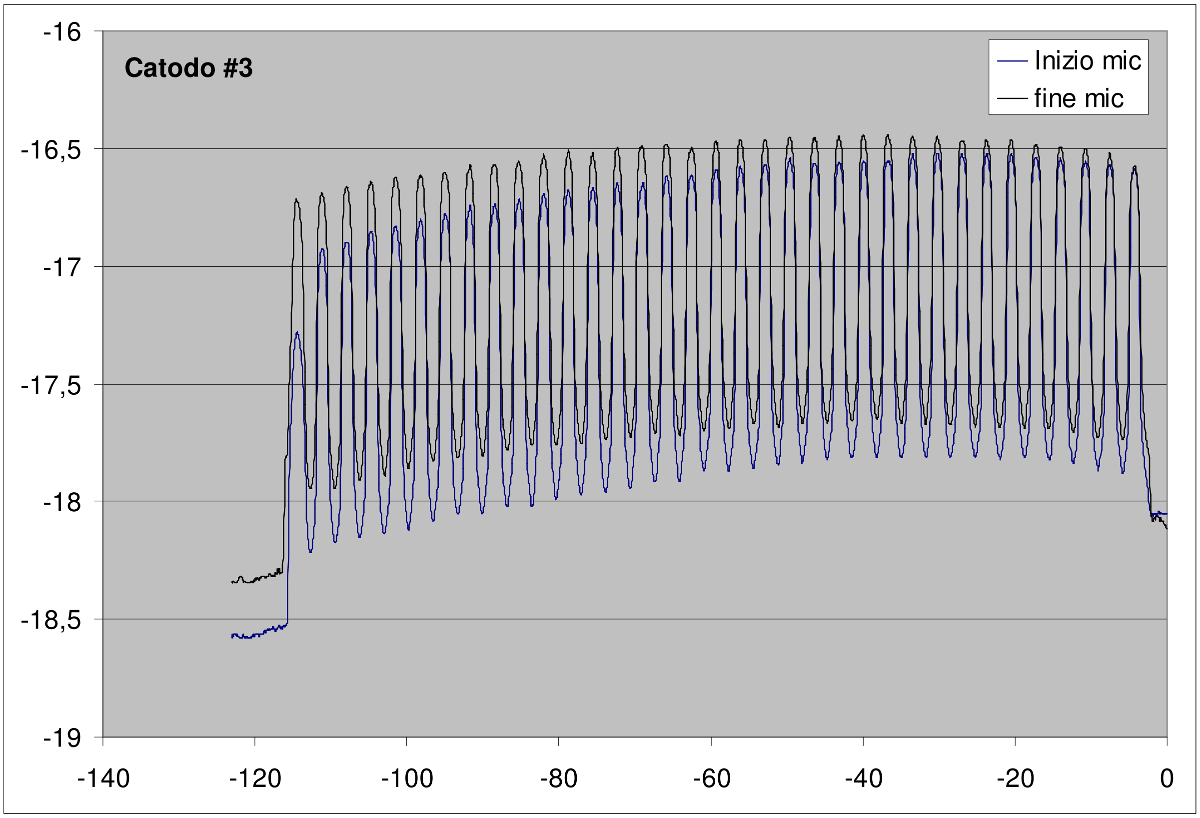

This picture has been created comparing in the same direction (orthogonal to the flow) a generic gas channel surface near to the inlet and outlet section:

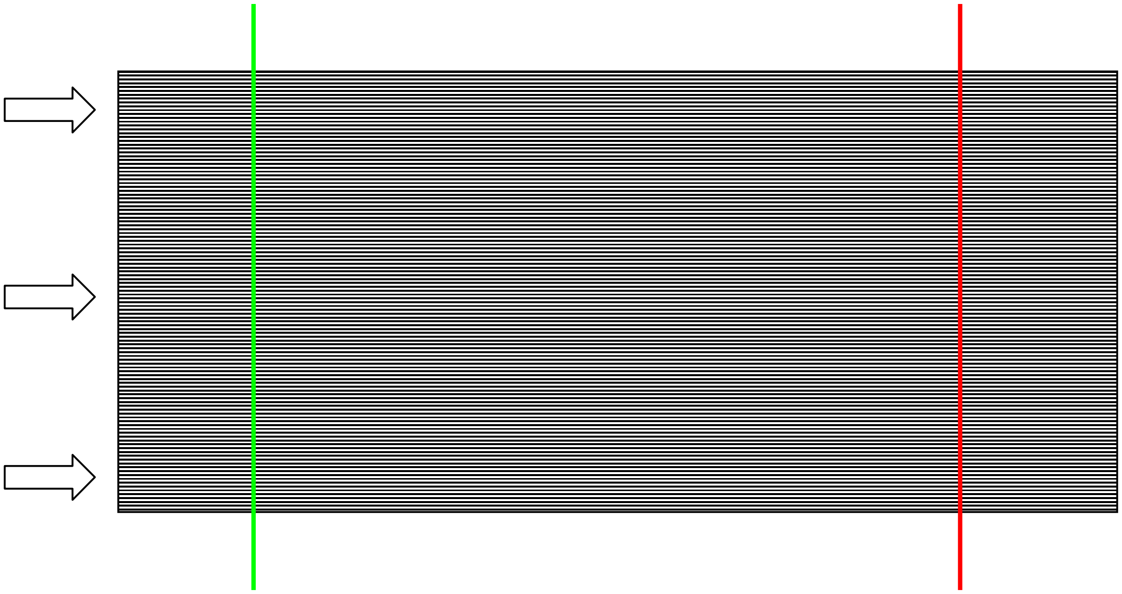

The top and bottom point of the ribs for each section are evidenced here:

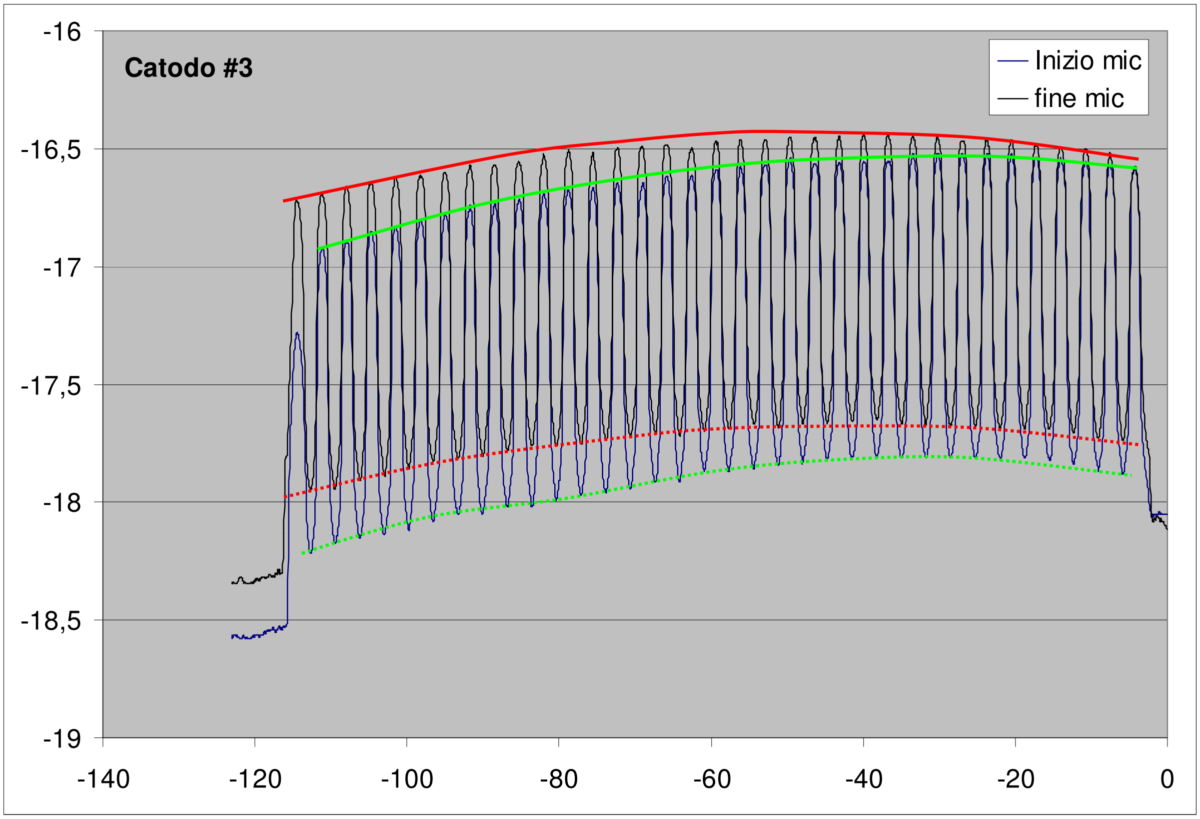

The previous graph evidence the top and bottom point of a single ribs row: appears clear how big can be an initial deformation of the contact elements supposed ideally flat in simulations discussed in previous chapters; in this specific case the contact surface is bended in flow cross section and moreover is sloped in flow direction;

From this analysis can be evidenced two main characters that channels elements should have:

- Elastic behaviour, to be adapted to contact surface under a fixed load;
- Production process to reduce these effects to minimum;

Regarding the second point, one of the most used process is to stamp directly the channels ribs on the interconnector surface:
As explained in the picture, to create ribs geometry directly in the interconnectors, may be used a compression force that press and attach the cathode and anode layers through moulds. In this case of course the interconnector side of the mould will have the ribs shape; respect to what introduced at beginning, in this case, to have a high thickness interconnector helps to avoid deformation due to piston compression;

In most of cases interconnector thickness is a compromise between manufactories resistance process, thermal deformation and electric resistance losses.

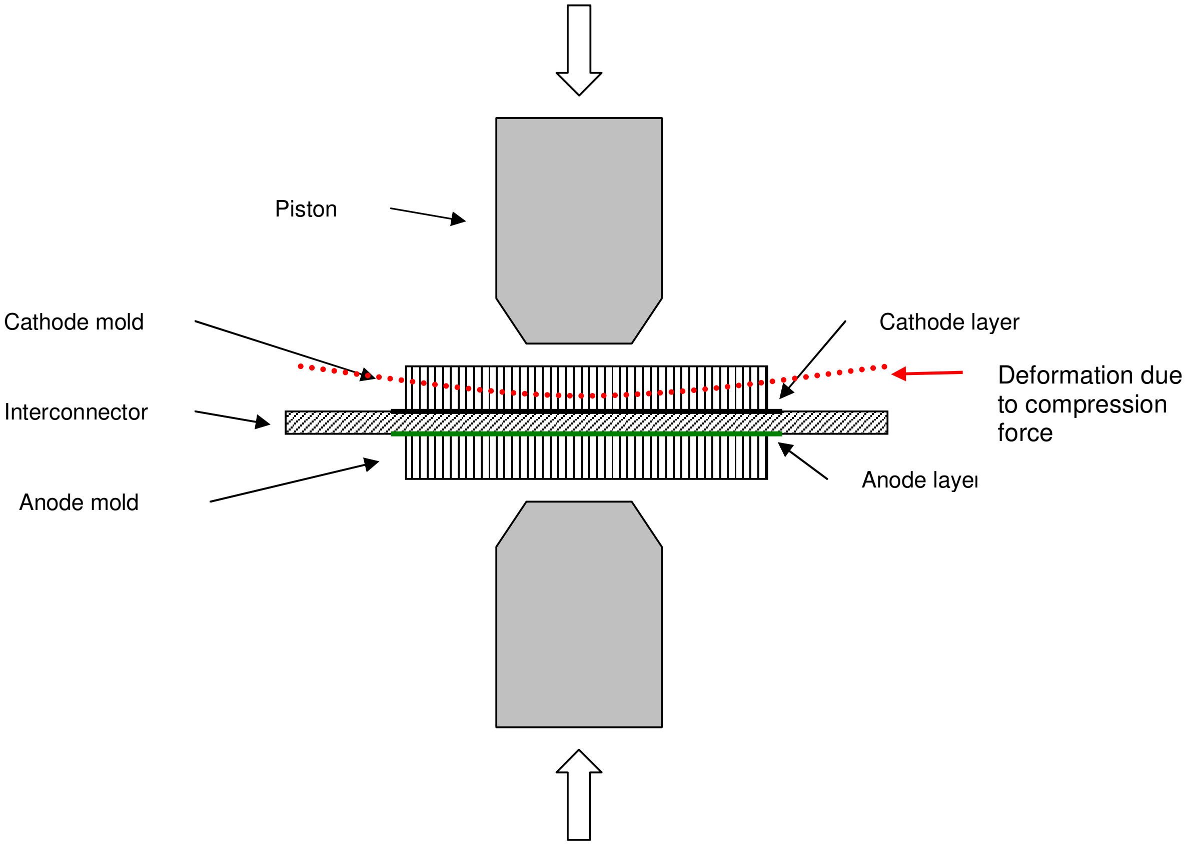

If now extend that to a cell stack assembling, must be noted another issue: the gas containing of the whole system; excluding from this problem all mechanical pipe connections, in every repeating element, must be taken in account to avoid any leakage to prevent first of all any combustion outside the system and with secondary importance cell performance decrease; if it's look back to the previous sketch, and putting attention to gas keeping, it's possible to note how can be difficult to obtain

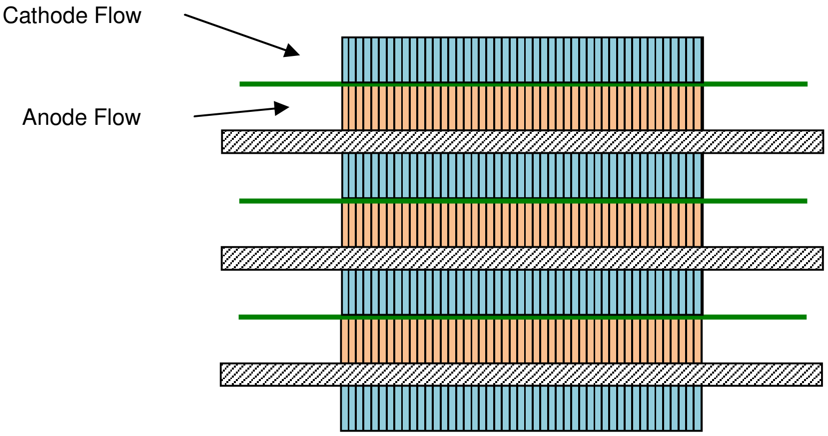

- assembling criteria;

The follow paragraph introduce an idea of concept of repeating element system that can be applied; core of idea is to compress the stack keeping the whole compression system in the cold area, to avoid dimensioning of clamping system in hot environment that implies a waste of material.
Another important point is to create a double contact surface: from what described in previous pages applying a constant force on cell surface, assure the electric contact; in other hand, if the contact is concentred in the centre of the cell, on the edge, may occur leakage issues, especially after the first thermal cycle, when the thermal paste used as gasket became hard and fragile ;

To go over this obstacle, the core of idea is to use this kind of compression and closing system:

First external compression system*, working in cold conditions, to support the main compression force (about 80-90%);*

Secondary internal compression system*, to take remain part and to accomplish other functions that will be analyzed in this document*;

Use the boundary edge of interconnectors, to support part of compression load and assure consequently a better retain;

This solution actually use a cold clamping system, but the presence of something that compress the stack from the inside (even if for small part) makes this compression system an hybrid solution (hot and cold compression).

- **Description of components;**

In the pictures below are shown two sides of the same metallic interconnector; As is possible to observe, there are two different size: the thinner in the centre (to reduce to minimum ohm losses, and a second higher on edge) that assure the contact (and tight) keeping a certain space in the centre and allow the cell presence;
Anode and cathode channels are included in the plate: this means that the length of gas manifold are automatically defined by the plate number;

The plate thickness is 3mm on the borders (to assure resistance to loads and deformation due to thermal gradient) an 1mm in the centre (to reduce electrical losses and save total weight).
Here below some general data:

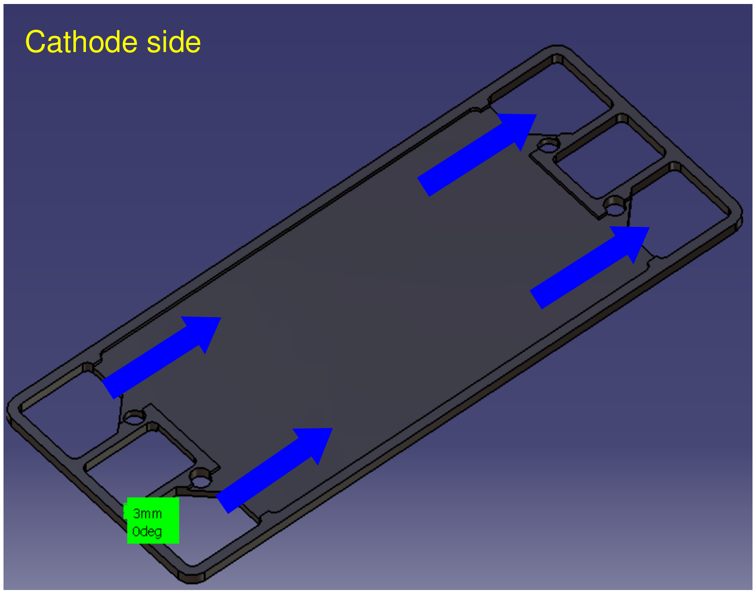

Main dimensions: 192x78mm;

Total weight (including channels): 160g/each

In this case are shown the cathode and anode side, with air (blue) and fuel (red) flows; Of course this is only the preliminary drawing: the flows inlet (and outlet) can for sure be optimized changing the flows dimensions inlet, and move the 4 holes on surface in other position (as shown in next page);

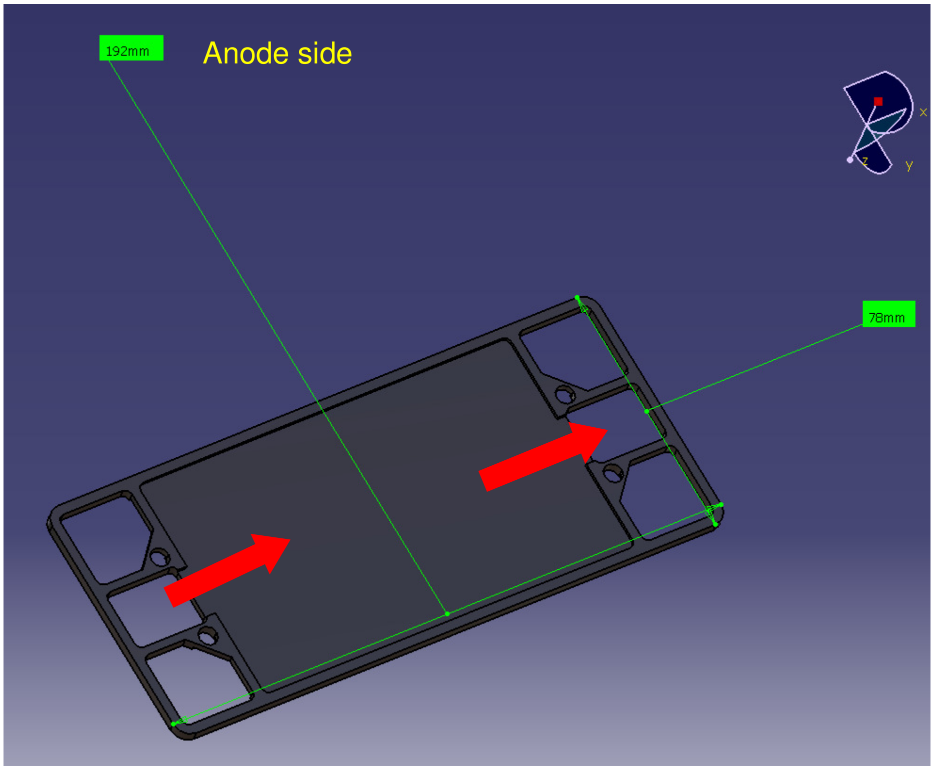

As anticipated, the holes can be moved at border or outside the plate as shown in the picture (adding an eyelets): this will allow to adjust better the inlet flows;

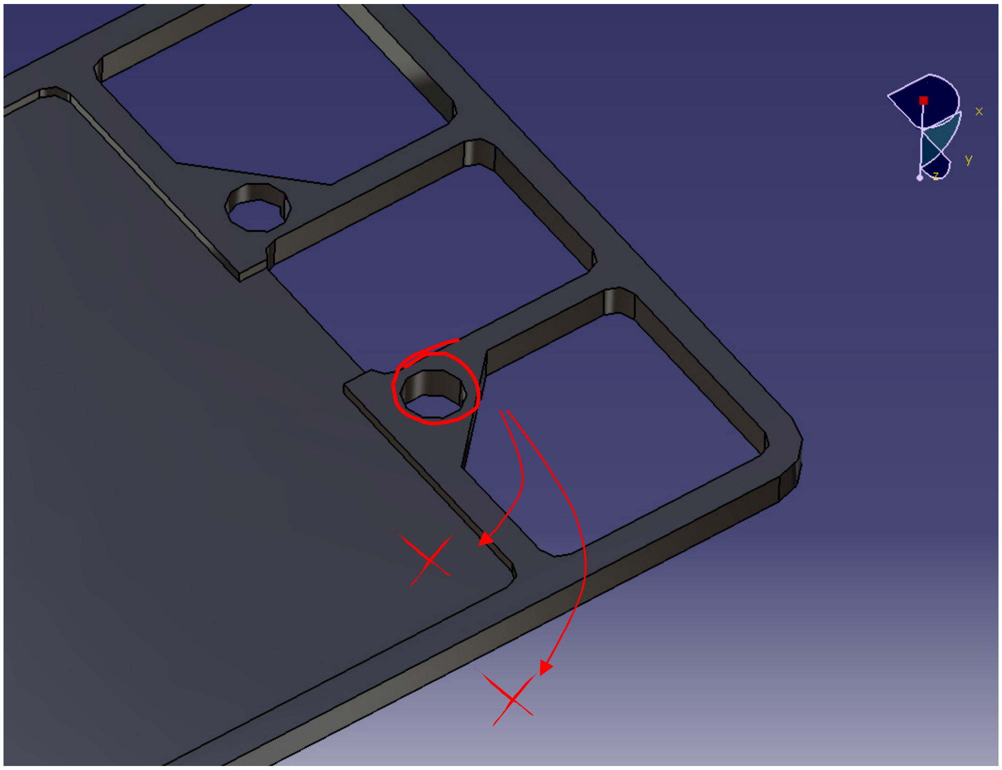

Another modification may be to eliminate completely the three gas channel at outlet, an have an unique conduct where mixing the cell exhausts, and burn them;

The cell considered in this case has the dimensions of 120 x 67mm;

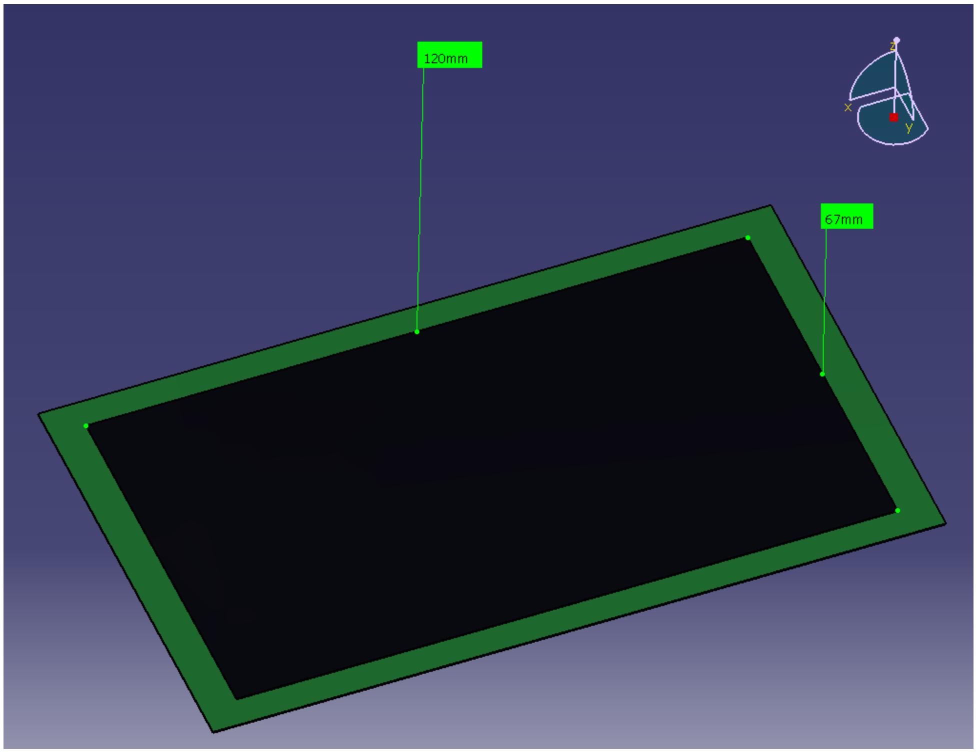

A second component is the one shown on left: it's function is just to create electrical insulation and gasket for channels (as per the cell border). The material can be the same of the cell (NiO mixture) or any other material suitable for this purpose;

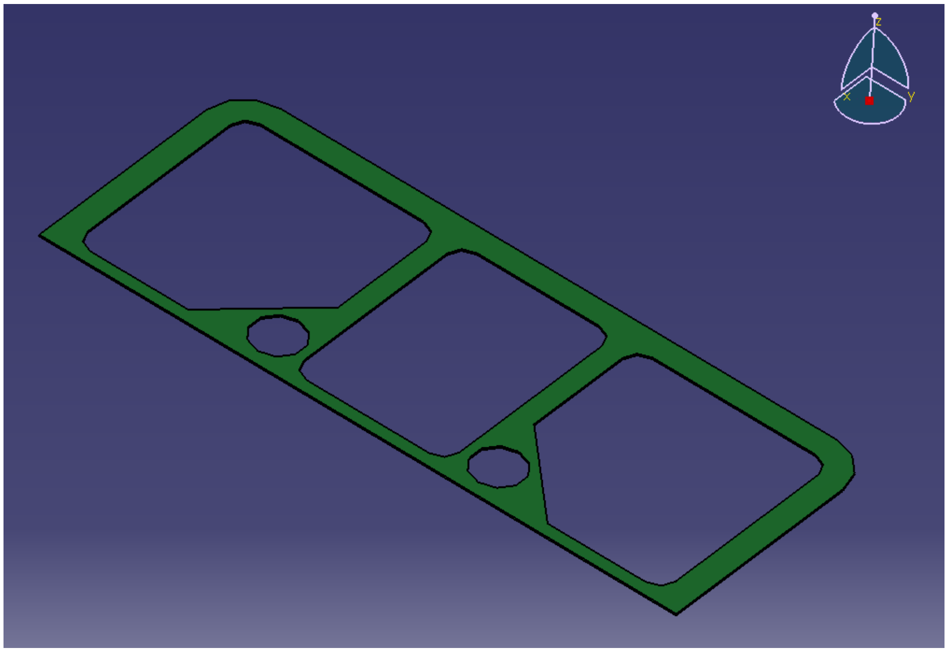

The bottom collector has the function to close the stack and allow the flows to access it (and leave):

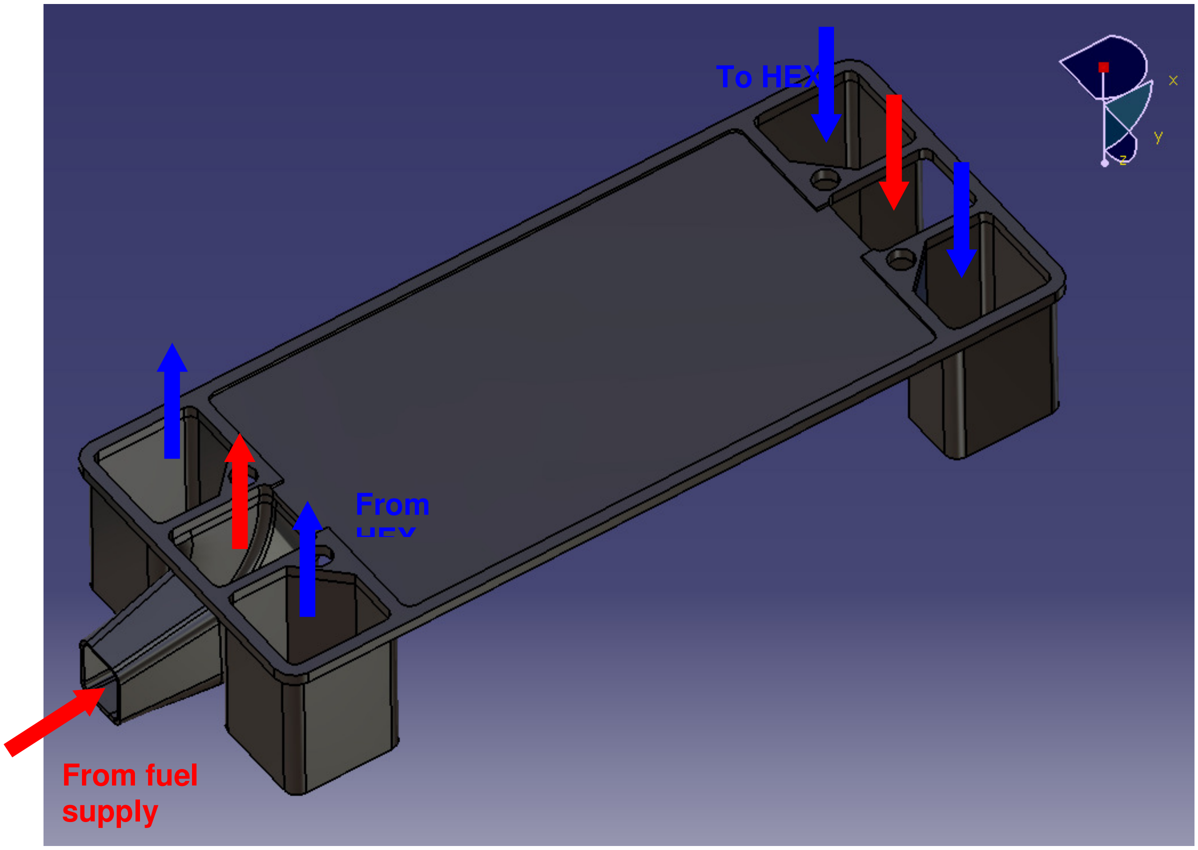

As anticipated in the previous pages, at the outlet may be used a single channel to post-burn remain fuel. The gas inlet/outlet are disposed in this way to be able to connect the stack directly over the heat exchanger;

As per bottom collector, the top has the function to close the stack and receive the vertical force as explained later; for these reasons the part have been designed with reinforce element (to be defined yet);

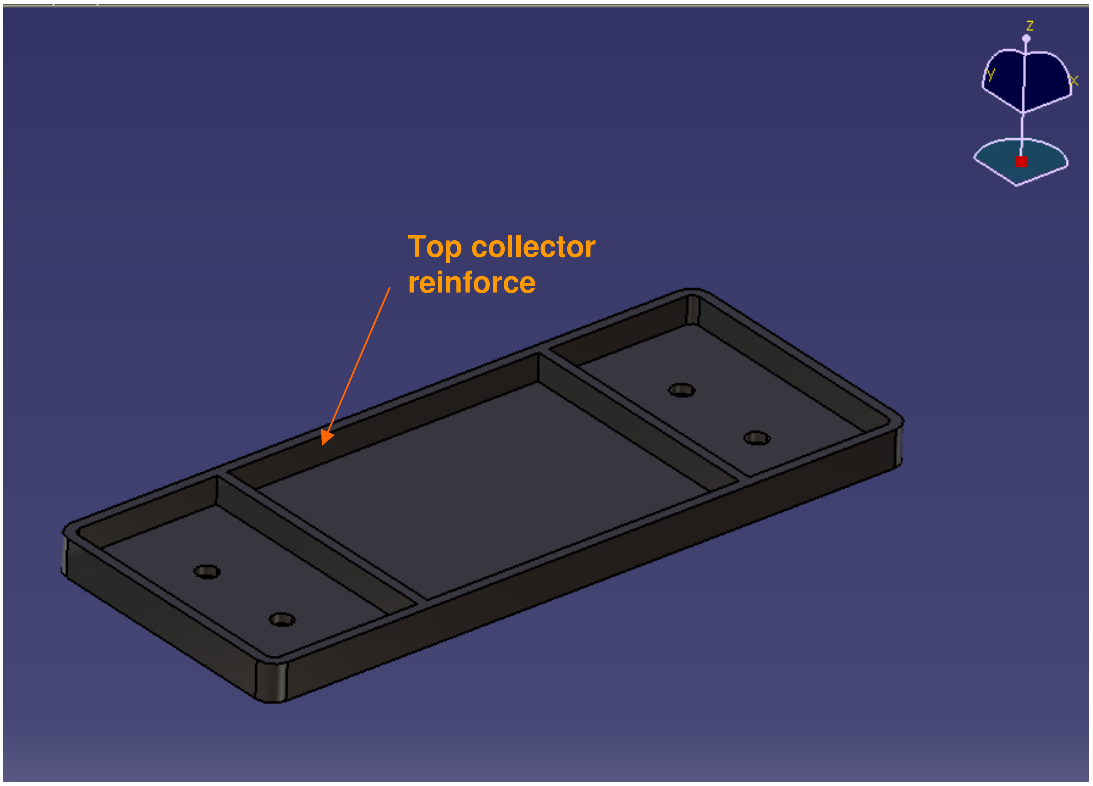

- 4.4 Stack Assembling

The general assembling explosion is shown on the right: the most important elements to note are the tie-rods at the bottom: they cross all assembling element and are surrounded by a ceramic cylinder;

Their function is:

- **pre-compression (closing) of the stack, before installing it in the system;**
- **secondary compression of the stack during functioning (about 10-20% of total force);**
- **Alignment (during assembling and functioning) of all elements;**
- **Electrical power transmission to the top of the stack**
- **Avoid to work in a only cold compression system;**

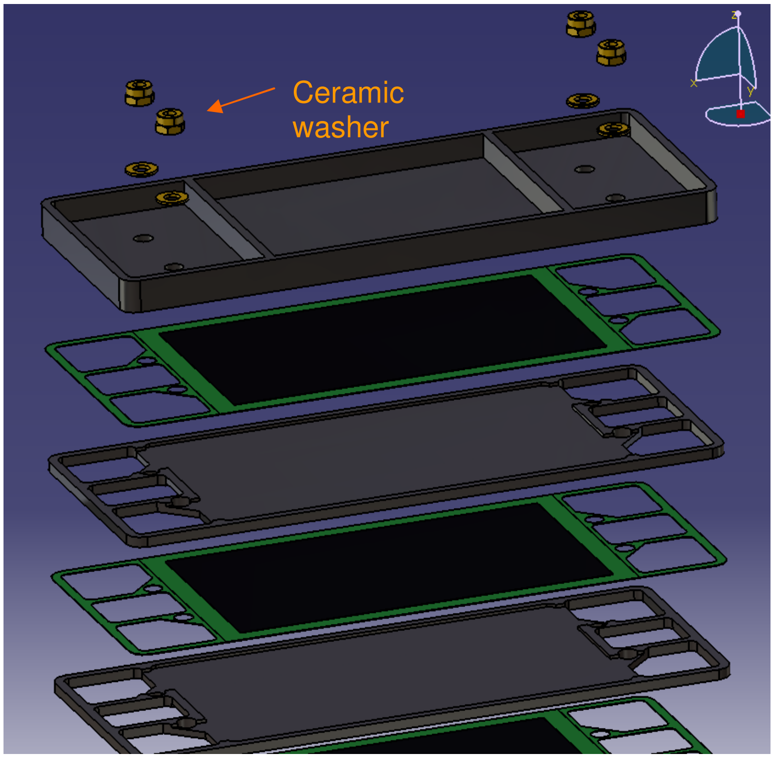

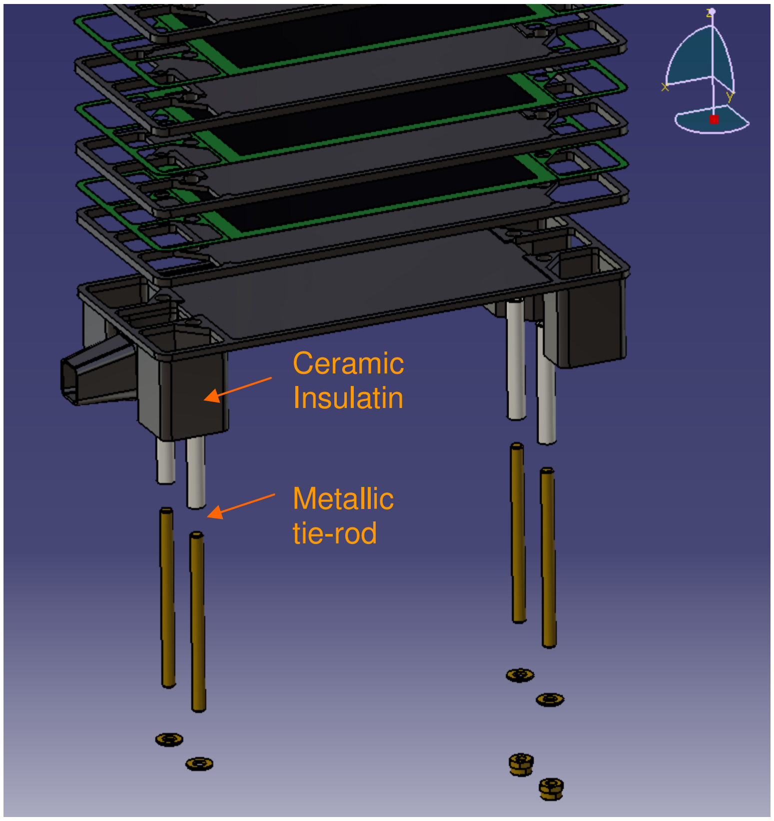

This solution has the advantage that it's possible to assembly and have a pre-compression separately from the rest of the system: the final closed stack does not need any other installation procedure (except consider the bottom connection to heat exchanger); The channels, as anticipated, are included in every single element (*with very low weight increase*), so their length is automatically fixed by elements number.

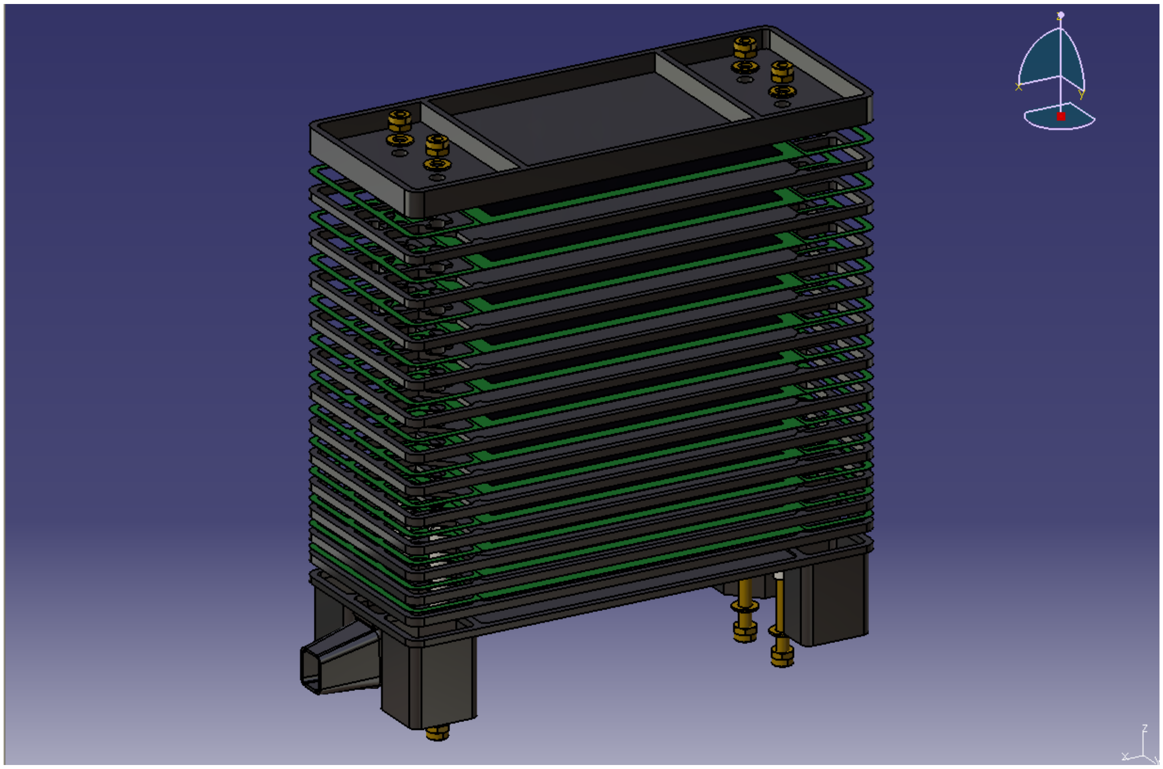

Here below are shown the closed stack of 12 RE. the height is 50.4 mm, including top collector;

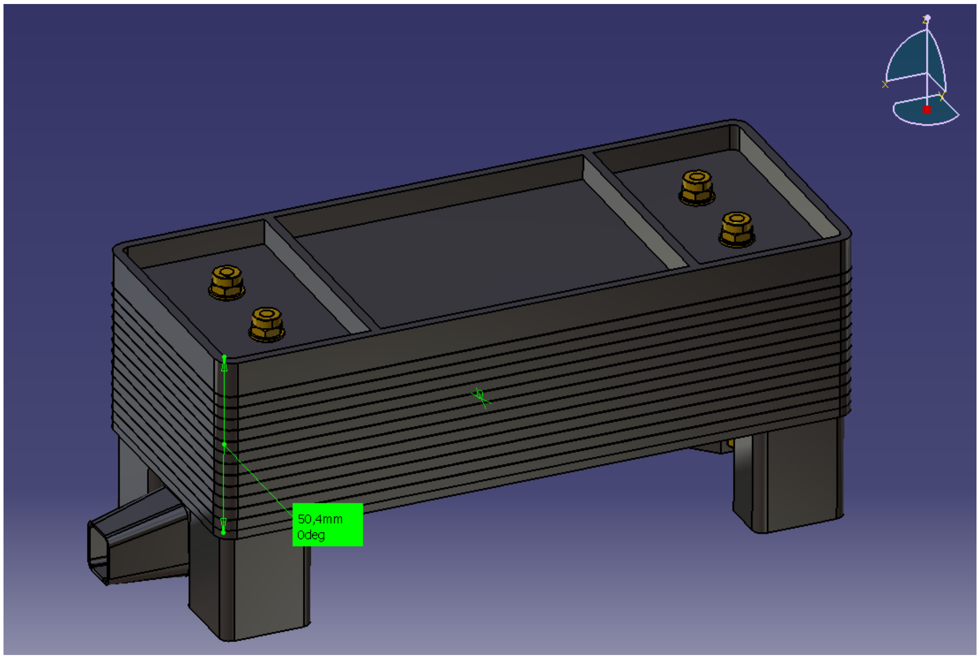

- Applying of first compression force

The tie-rod used are not enough strong to keep the whole compression force; As described in introduction, the scope is to keep compressed the system using and external force, generated through a cold mechanism (that may be a spring or a screw), during the functioning of the system;

The only action to do is to take the already assembled system and apply a force on top through a ceramic force distributor (and at the same time do a thermal insulation action), as shown below:

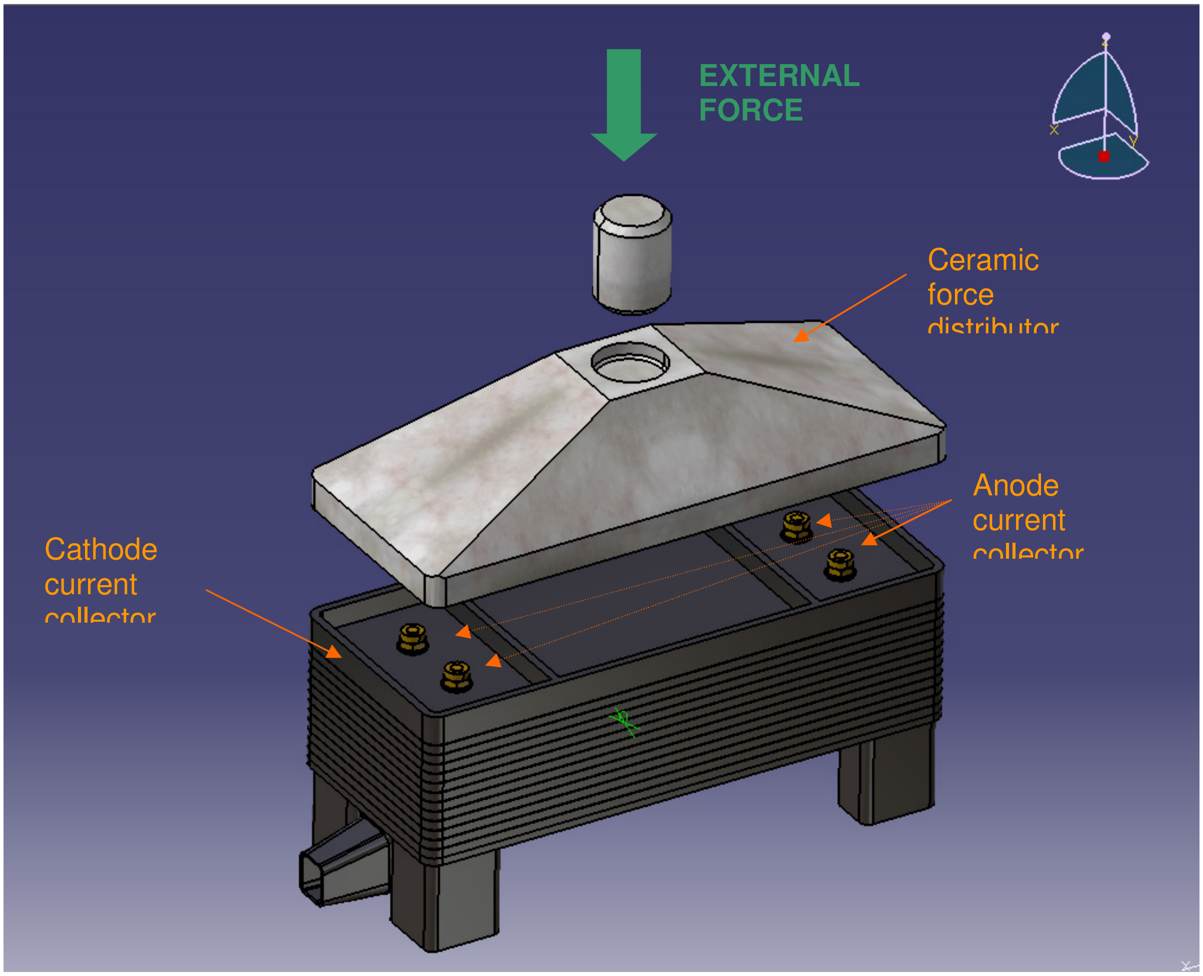

- **Insulating**

Finally the stack can be covered with insulation panels and apply the force;

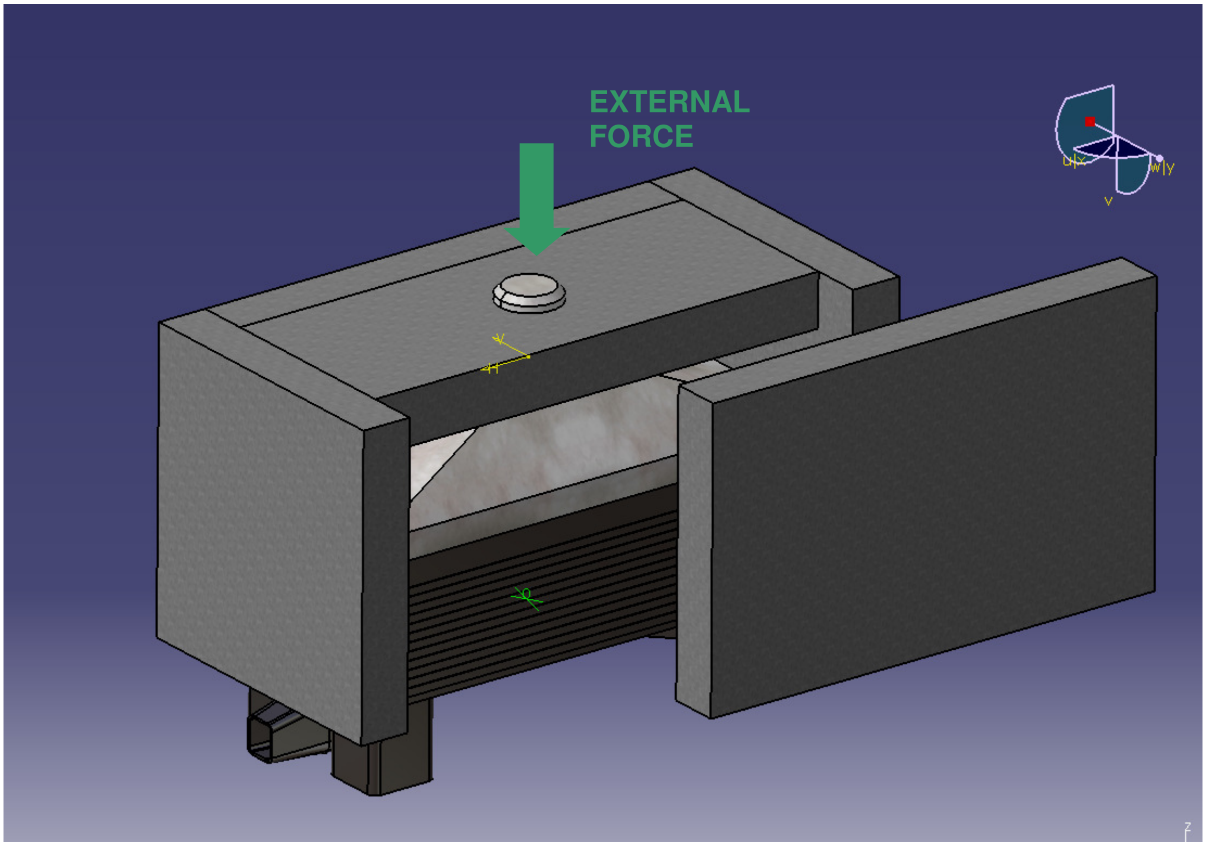

- **Other consideration on force distribution;**

An important consideration regarding the applied force is that the compression external force from outside is discharged on lateral ribs of metallic plate;

This solution assure:

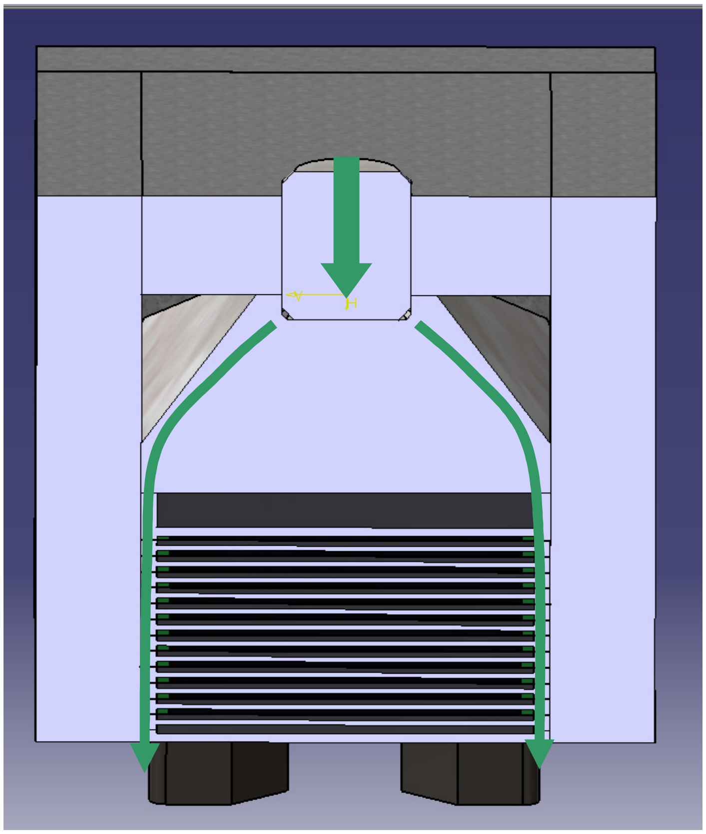

- To reduce to minimum gas losses to outside the cell;
- External load doesn't need to be fine adjusted;
- External load is not supported by cell surface (avoiding mechanical broken for overload);
- Compression directly on metallic plates has an important contribution to contrast deformation (and leakages and contact consequently) due to thermal gradients;

This section shown the anode flow of the system:

Every plate is kept compressed from the tie bars that crossing the interconnectors. To be noted the thickness differences in the centre of interconnectors and the border that guarantee the contact pressure; the upper plate has the function to work as a cap for gas species that are obligated to flow to outlet passing on cell surfaces.

This constructive feature allows to have a modular system: channels length are automatically obtained from the number of interconnectors (and cells) installed in the system.

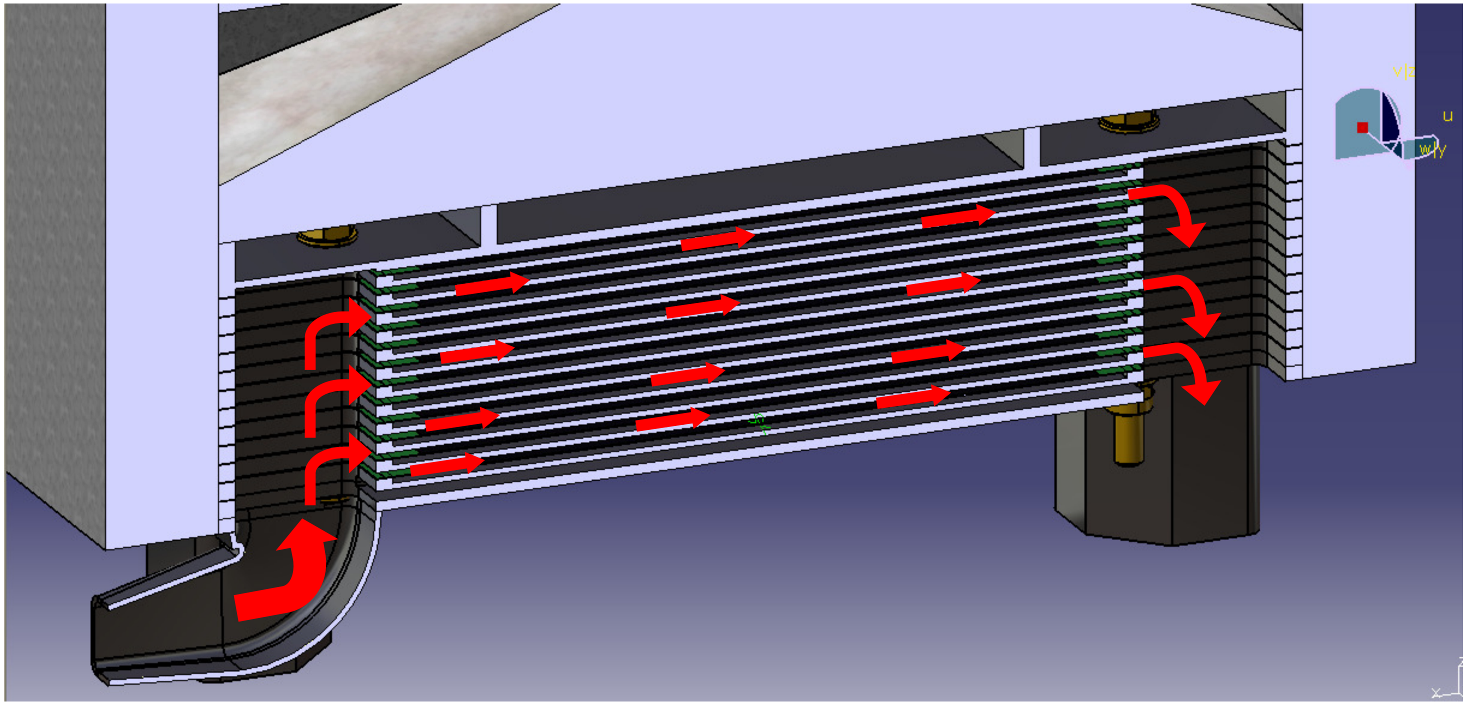

From the cathode side the system works in the same way: the air channels are closed to force the fluid to pass over the cell and exit from other side;

To be noted that flows are left separated in this case;

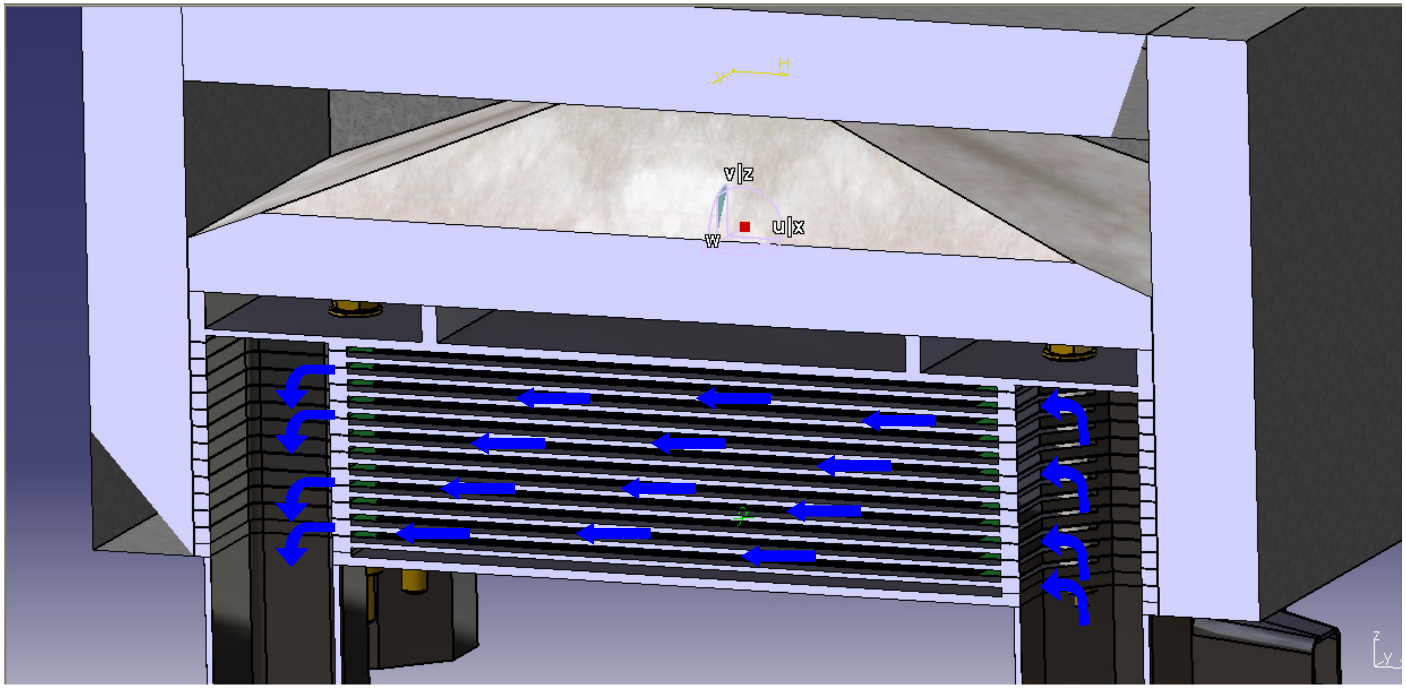

4.5 Contact issues;

As shown in previous paragraph, the contact problem is one of the most important point to take care on cell assembling; from this point of view, during the assembling operation, must have an important role the quality of components used (checked through appropriate inspections), as laser surface investigation;
At the same time must be assured the resistance of component at the thermal gradient deformation; from this last point, a generic stack assemblies as described before, are obligated to have an high interconnector thickness (about 3mm) to reduce to minimum any deformation (and preserve consequently gas retain);

Some consequence of this are listed below:

- Weight of the system;
- Higher cost of material;
- Space required to installation;
- High electric resistance;

The interconnector presented, has the propriety to have tough edge that can limit the bending of surface, in particular, has been seen how part of compression force is supported by borders to increase the bending resistance;

For this reason, the thickness of interconnector in contact with the cell has been reduced to 1mm;

Focus the attention on the cell contact, in this case, instead to maximize the quality of used elements, has been tried to use a flexible connection between cell and interconnector;

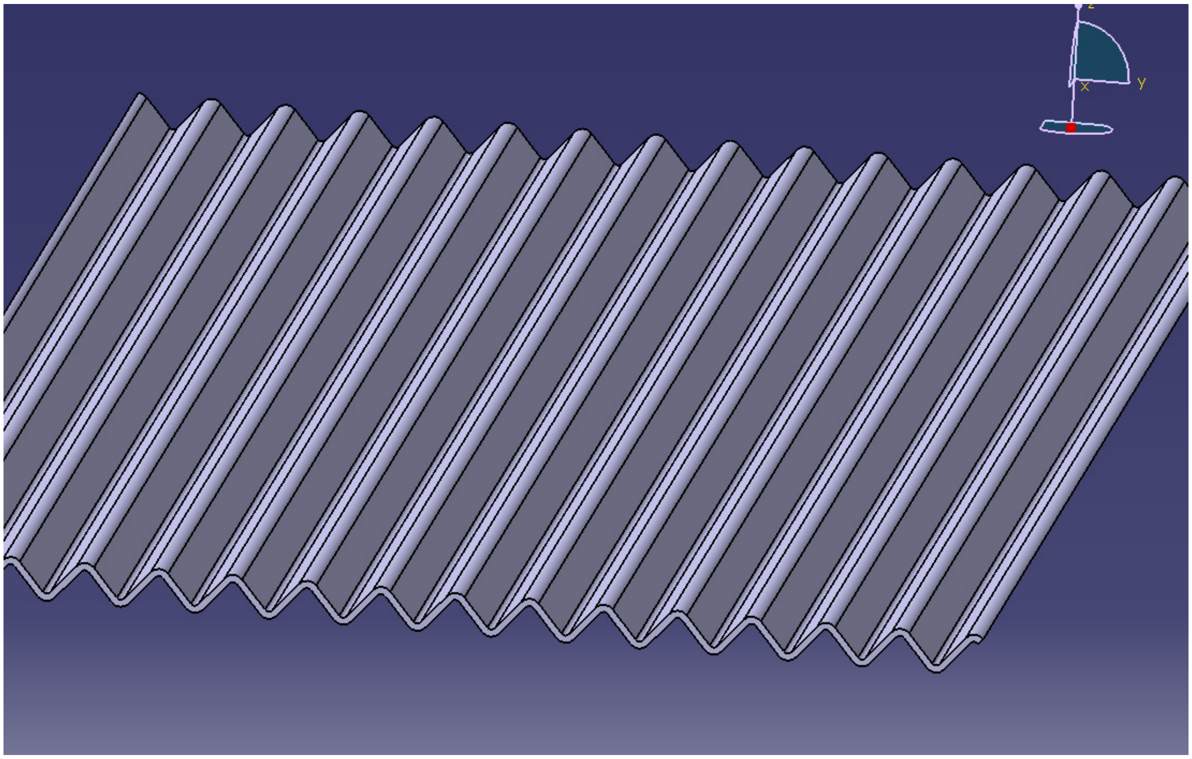

The one in the picture, is a foil of the same material of interconnector (Crofer $22^{®}$), obtained simply from a mould process;

to investigate the contact between interconnector and cell, has been created a new model using the same software (Femlab multiphisics 3.4) used to create 3D cell model.

The foil used has the following dimensions:
Thickness : 0.2mm

Curvature radius: 0.25mm

Length (wavelength): 2.2 mm

Total Height: 1,15mm

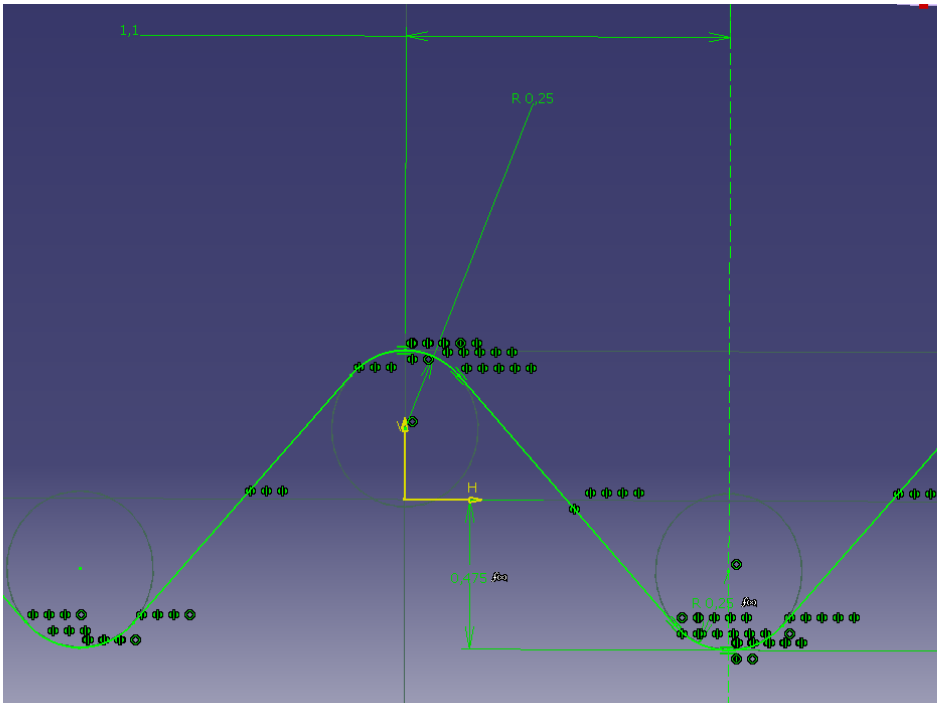

In the picture below are shown a section of two consecutive interconnector, with the foils inserted; obviously the wave direction of the foil are cross displaced respect to flow direction;

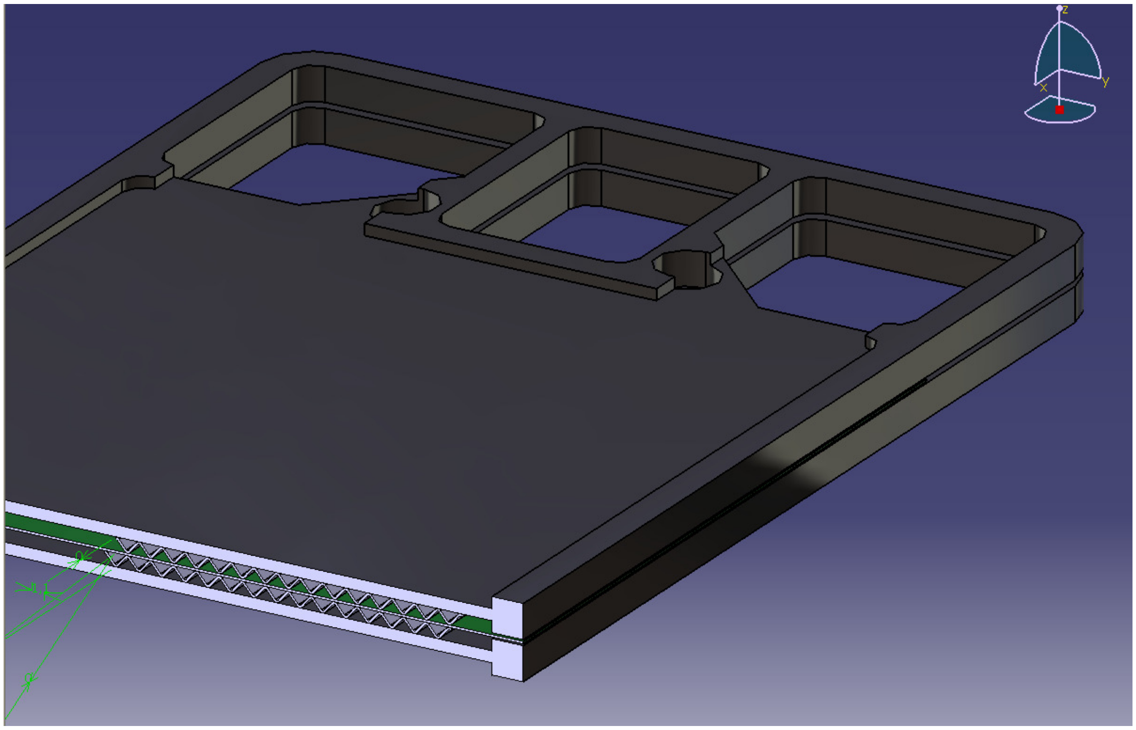

On the pictures below are evidenced all the components of a single repeating element (cell in the centre, foils and interconnectors); must be noted how putting in all in contact, a gap on interconnector border remains (about 0.05mm using this foil geometry): this gap is recovered applying on borders the closing force introduced at beginning of this chapter;

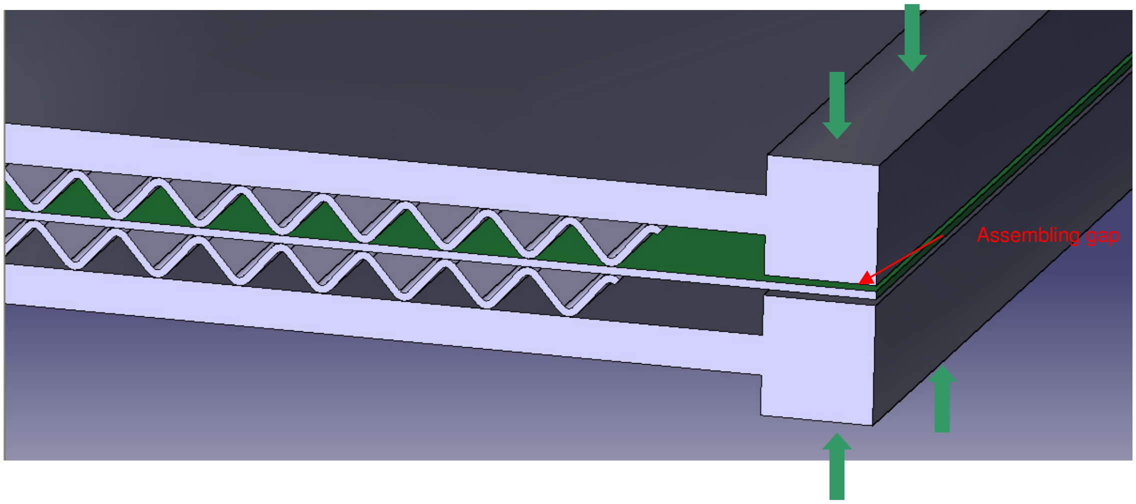

Effectively, once fixed the foil geometry, the system behaviour can be imaged as a spring; The model created has the scope to simulate this spring under different working conditions.

The model has been developed in 2D starting as usual from geometry described, and creating a mesh on it:

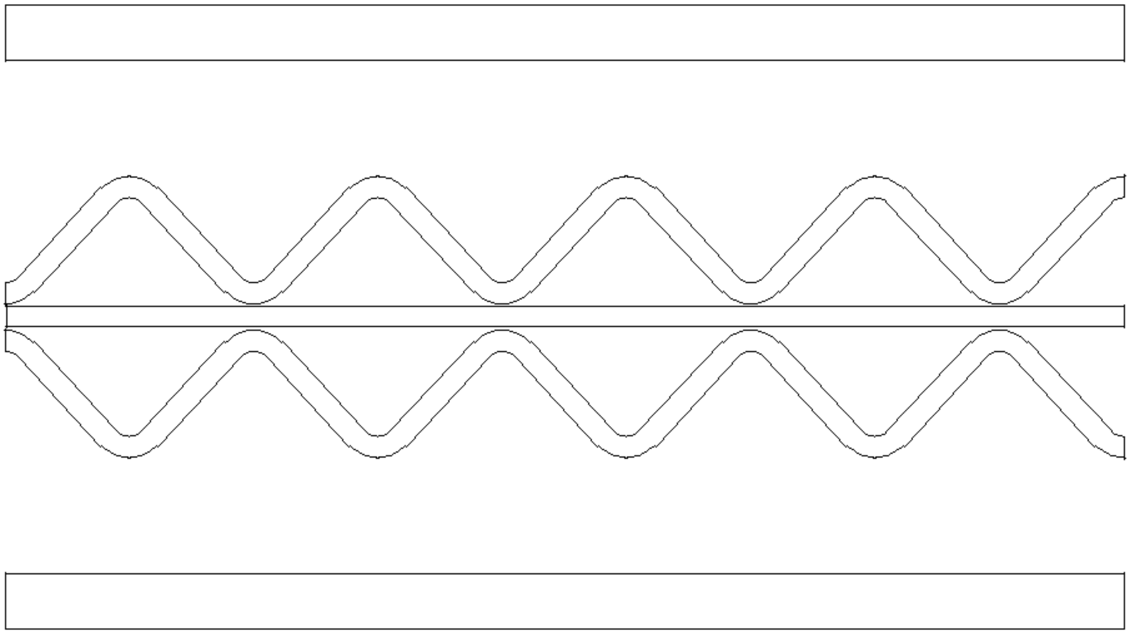

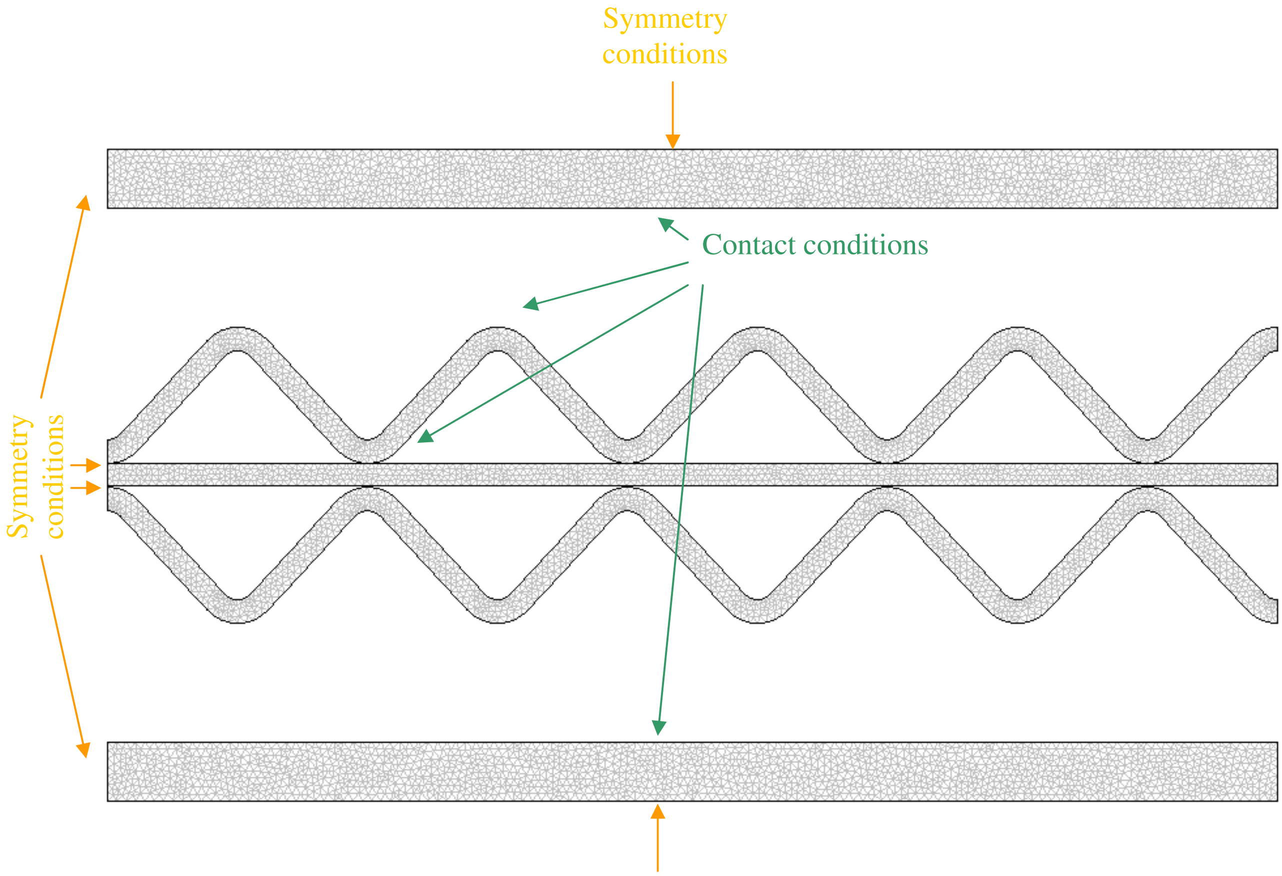

In these images, the interconnector are shown at initial condition (not in contact with foils); more over as boundary condition of the problem, are been applied symmetry condition and contact condition, as per arrows on the pictures;

The model can move the interconnector, arriving to the contact with the foils and proceed with their compression;
In the next picture are shown the Von Mises stress in the materials from the initial contact , increasing the compression arriving at the point that correspond to the gap absence; this condition represent the stack closure condition and trough this model it’s possible to simulate the contact conditions of the cell;

Note the black lines represent the original position of elements before approach the interconnectors;

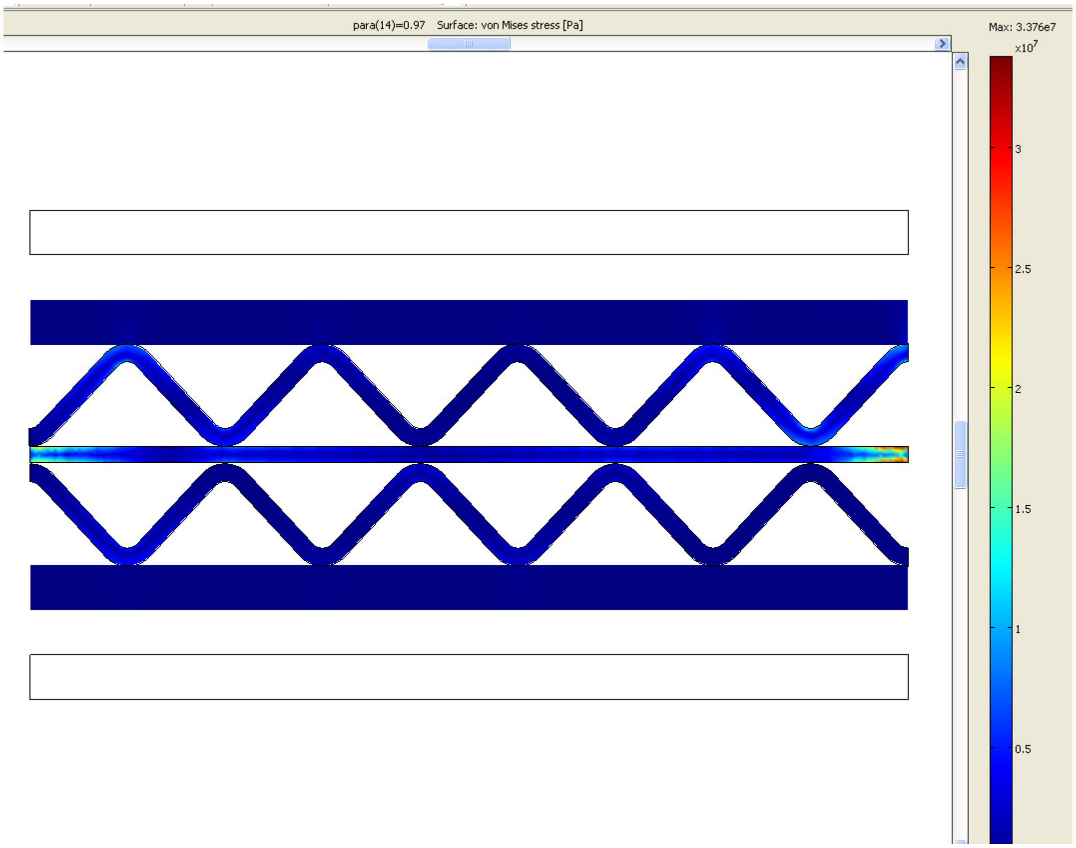

Reducing the distance it’s clear the stress increasing:

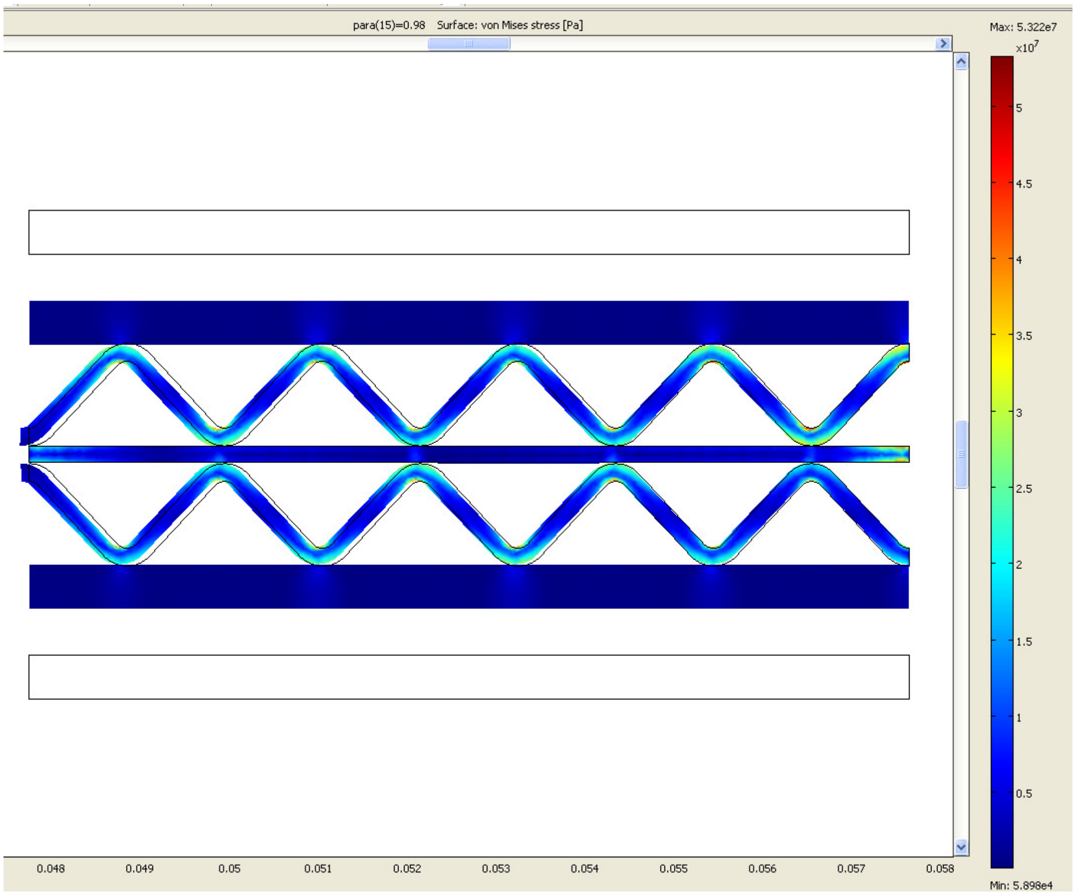

At the closing conditions, the system (an the cell in particular) is loaded in this way:

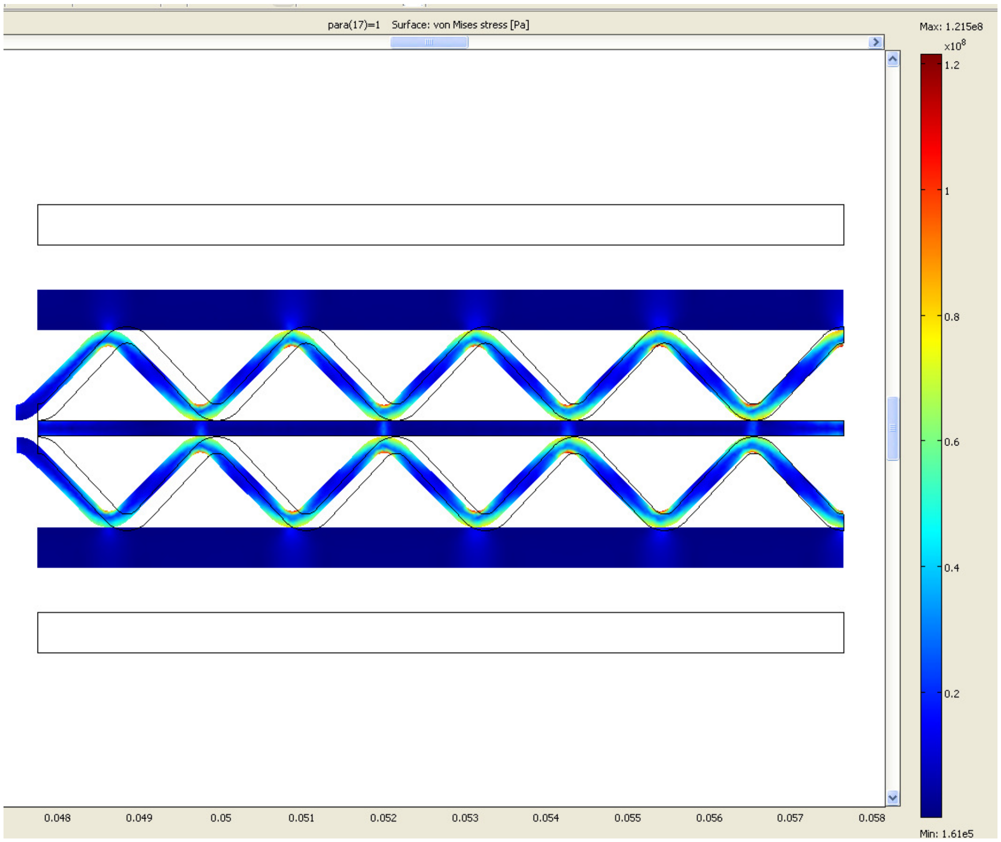

This model is able to investigate mechanical load on cell surface: its ceramic nature makes the cell rather frail (one of the most common problem in the SOFC stacks are cell brakes); for what shown here, this model is able to evaluate stress on cell surface integrate the pre-load effect to rupture cell issues.

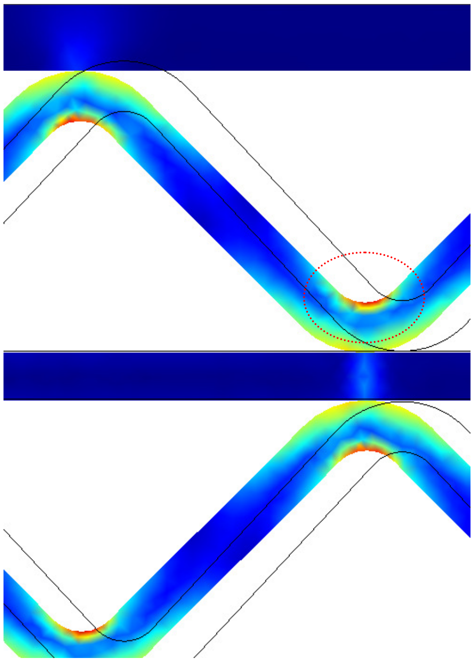

The model is also able to evidence permanent deformation due an excessive compression or bad initial geometry; in the case here reported on the left (inside the red circle) are shown an high stress area due to upper interconnector compression;

Removing the interconnector load, the model show the areas where the deformations have overstepped the elastic field;

In next picture is possible to focus on the same narrow area where a permanent stress are been left on the foils;

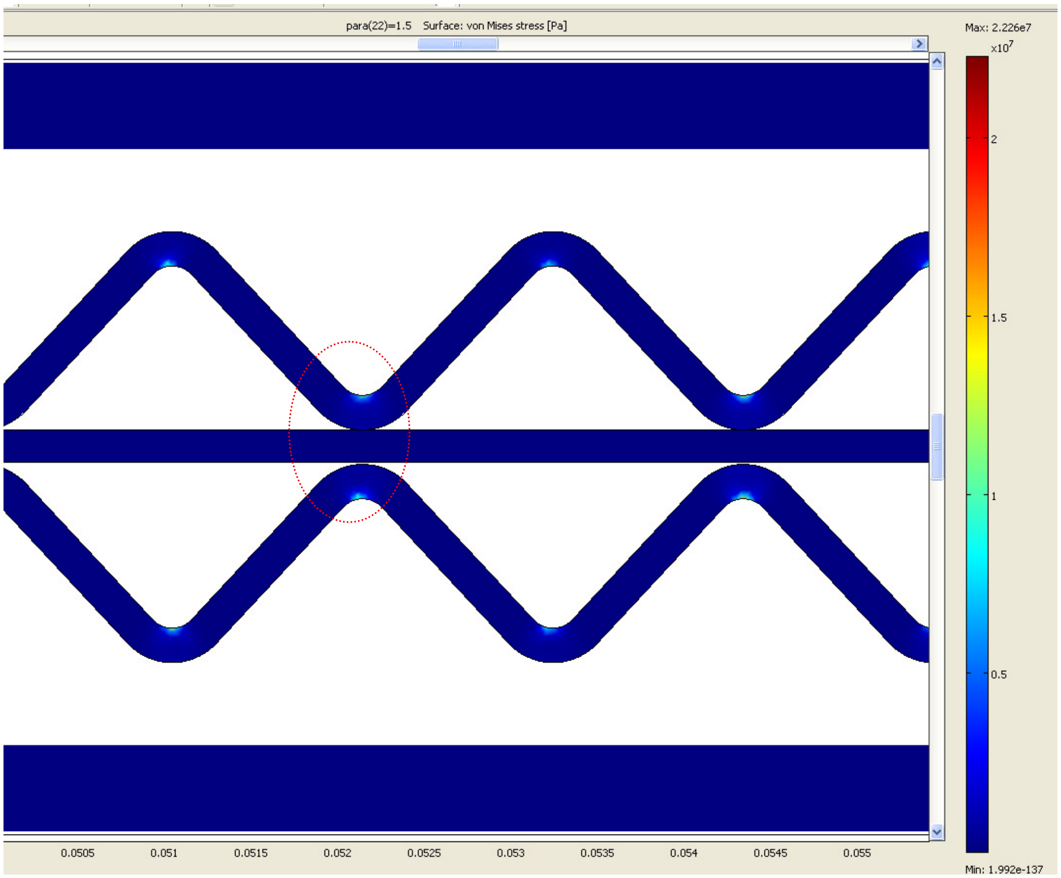

The model has been also integrated with electrical problem in order to analyze current distribution (depending from mechanical contact), and heat production (depending from current distribution);

If consider a current of 0.35 A/cm2 (normal values of current obtainable in experimental system), it’s possible to constrain the model to be crossed by a DC current flow, setting in one side of interconnector the current density, and keeping the other interconnector at ground conditions; Obliviously the mechanical stress due to compression is kept as boundary condition: from that depends contact pressure and consequently current that flows through;

At the end, the results is the following:

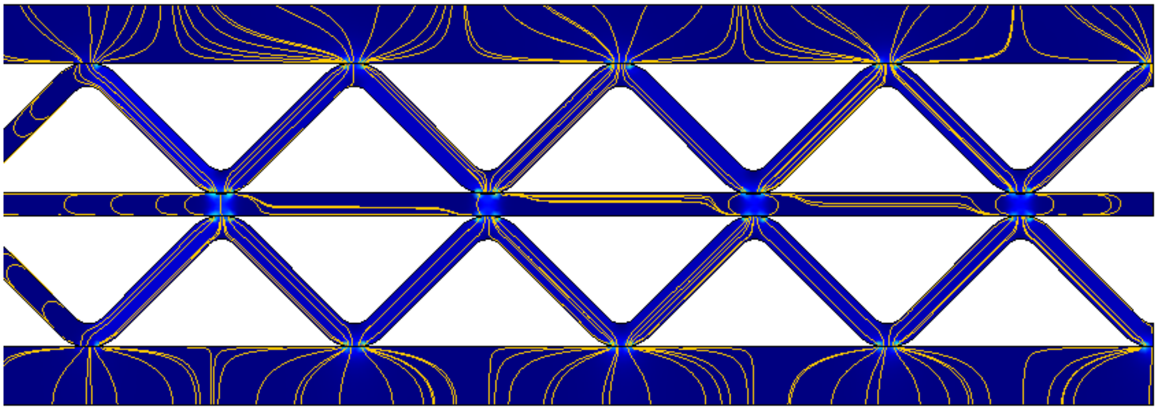

The yellow lines are current lines; as is clearly detectable, the current lines came from interconnector in vertical direction, they start to be concentrated in contact area, then are transmitted to the cell where the current cross the part in horizontal direction and are passed to lower interconnector in the same way;

Including resistivity values in the materials properties, with the same model are possible to get the heat generation due the current flow;
In the picture below are shown this phenomena: to note how the maximum heat source is located on the contact border, where the pressure contact is lower causing an higher electric resistance;

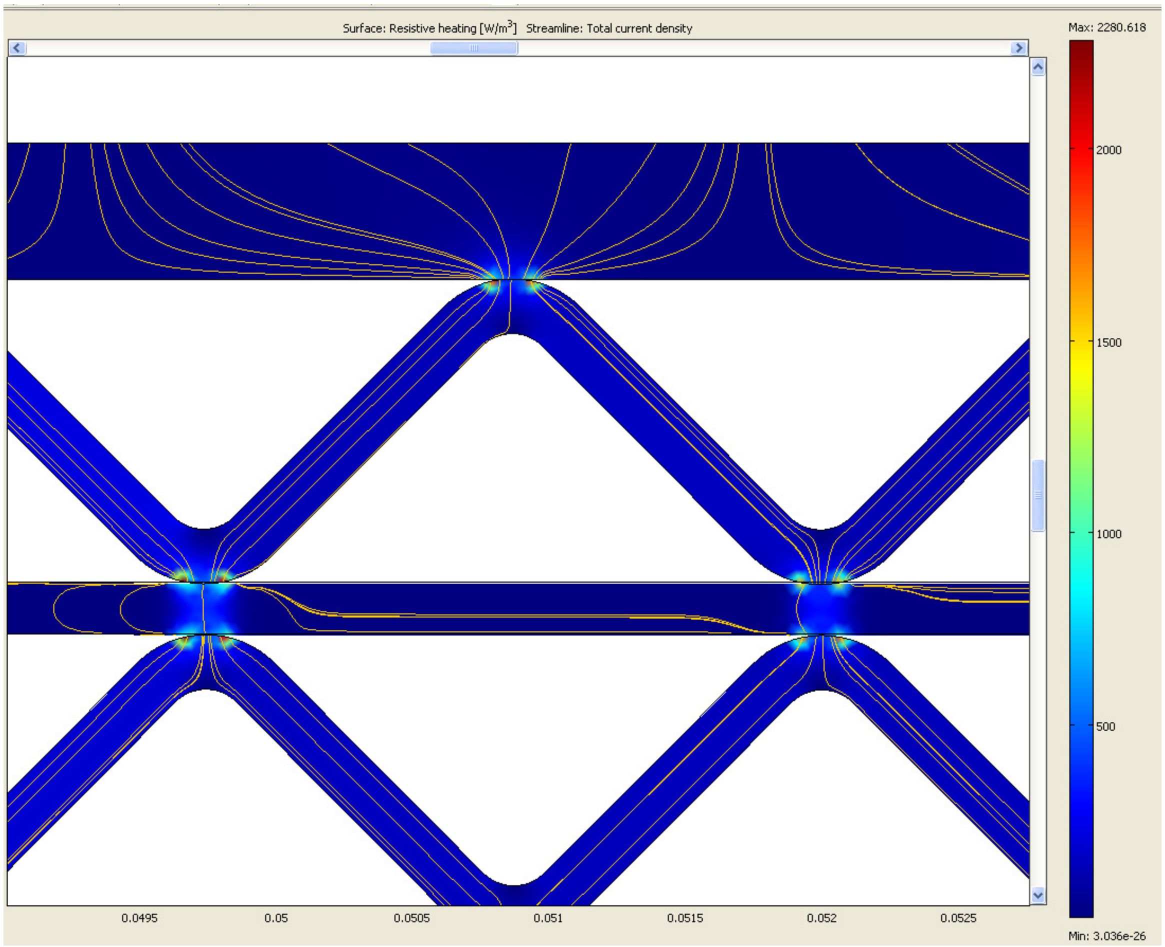

To complete the analysis of foil working, should be considered the fluid-dynamics of it;
In this picture are shown a part of cathode channel (as not been considered entire foil to reduce computation resource);

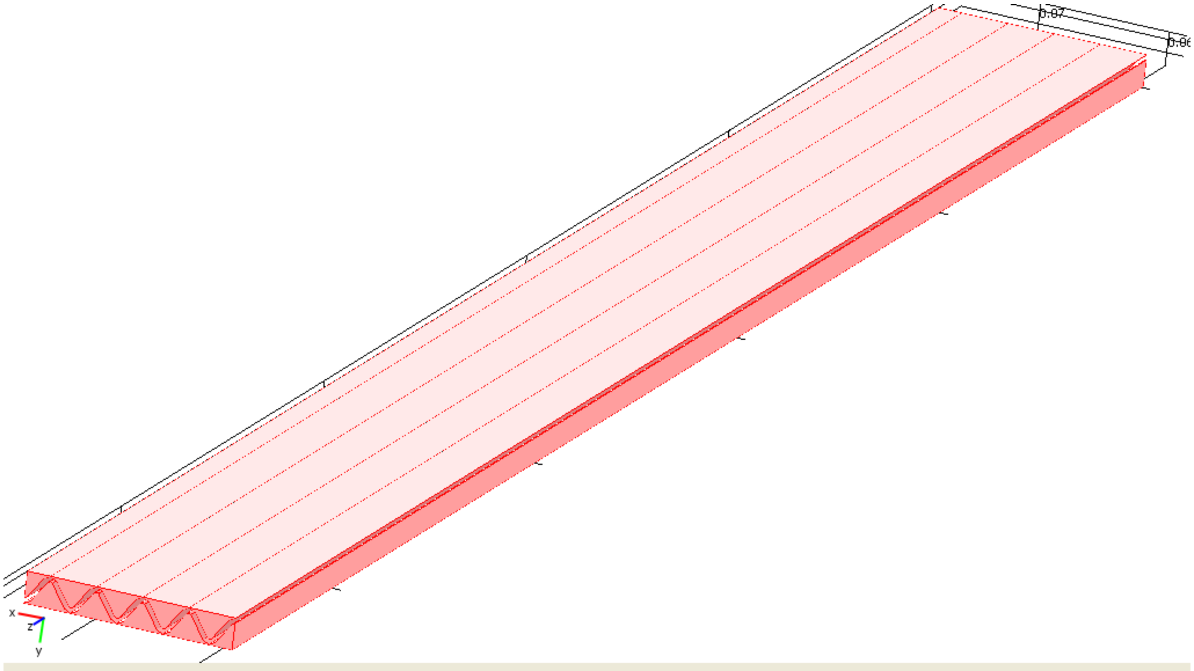

Simulating this gas channels is obtained an interaction between foil and gas:
Pressure drop, in the picture below;

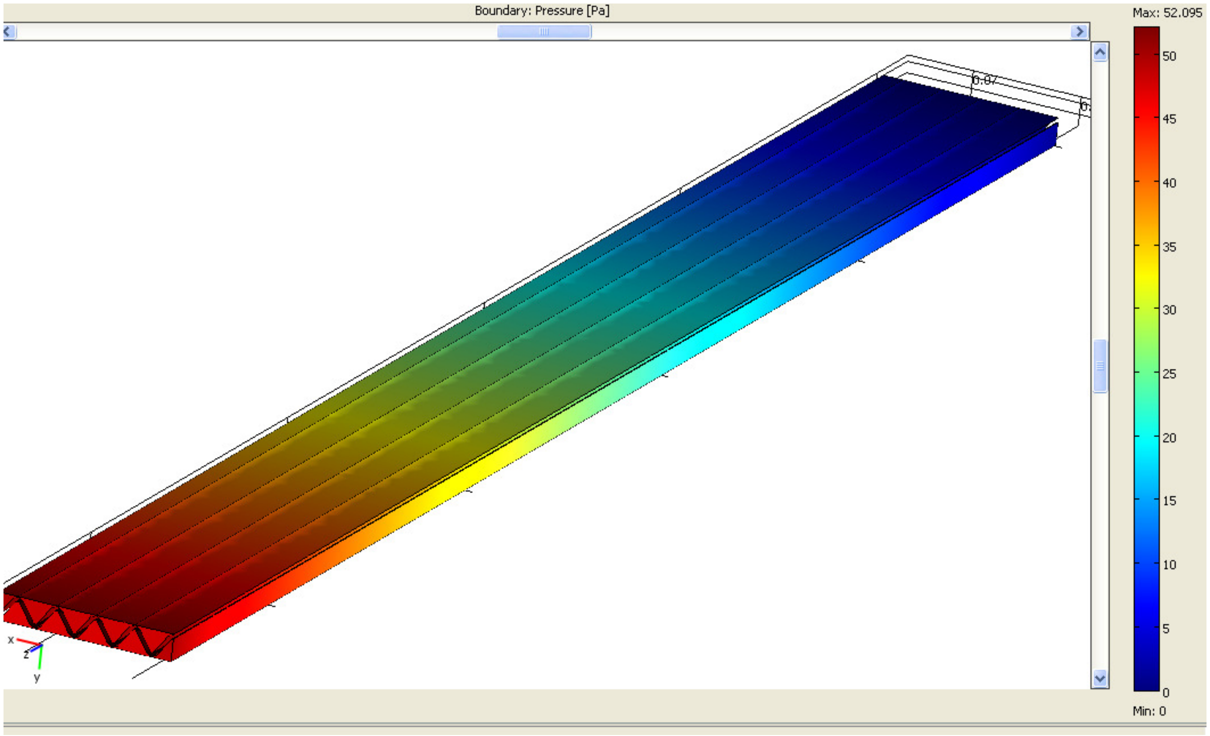

Use this kind of electrical connection inside the stack, implies to have half part on inlet gas not in contact with the cell: consequences of this may observed following pictures where are shown the oxygen concentration entering on left side remains constant on upper side (where there are not electrochemical consumption), and lower side (in contact with cell) where oxygen are consumed along the gas channel;

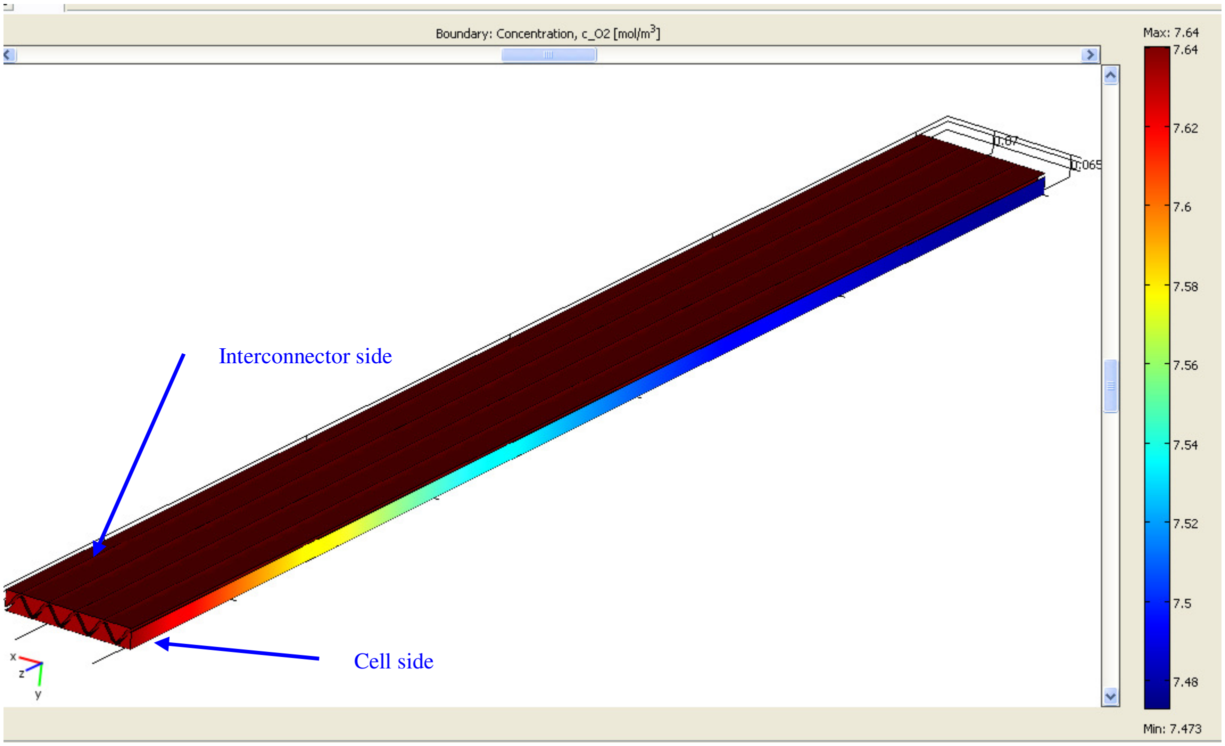

This implies an overall performance degrading of the system cause part of fresh gas inlet in the system take not part to chemical reactions.

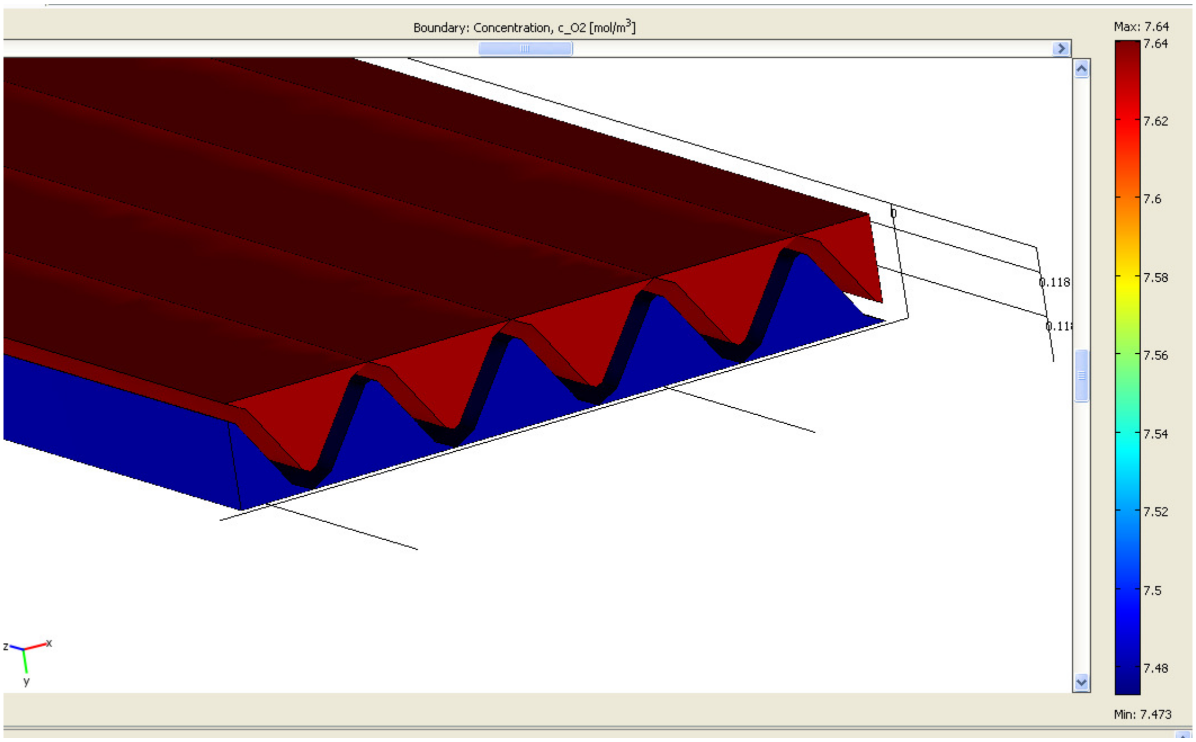

A solution under examination to avoid this issue could be a pre-cutting of the foils before their assembling:
As per picture below, some holes have been opened on the foil surface to create a gas mixing point that makes possible to use part of the gas that normally would not be as in previous case;

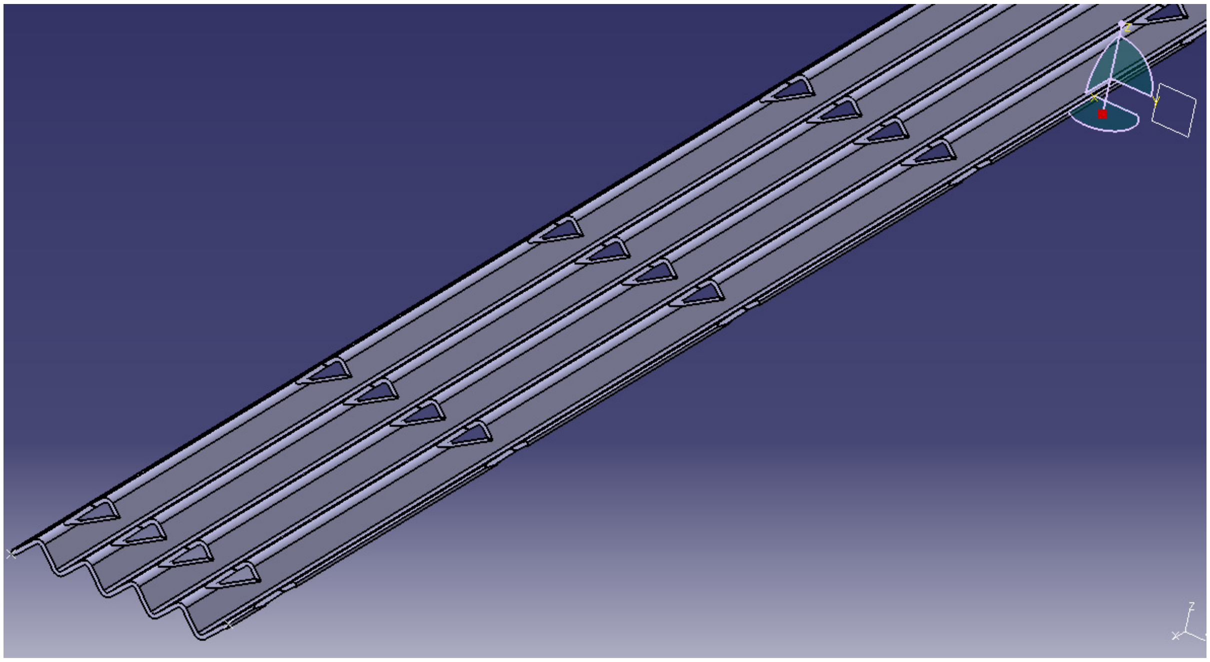

Their use present the following advantages:

- Allow to mix gas on both sides of the foil;
- Studying their position, it’s possible to distribute fresh gas at outlet areas (where normally there are a decreasing of performance due to spices consumption: this situation are still to be investigated but could uniform the temperature gradient on cell surfaces;
- Are easily created by laser cutting or mechanical removal as per the drawing below;

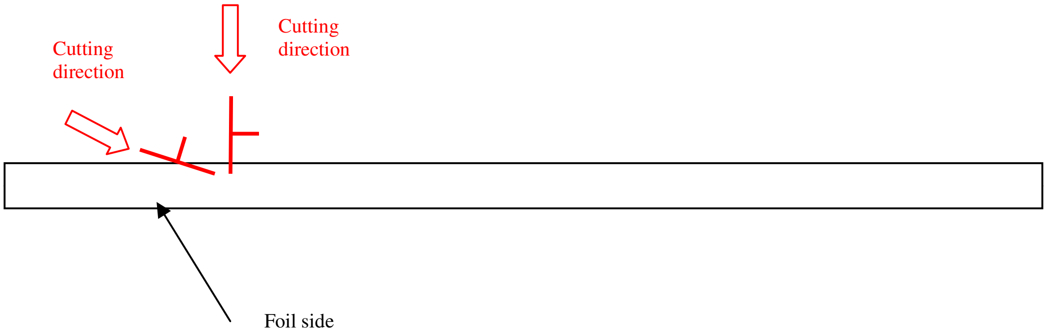

4.6 Conclusion

This fuel cell assembling and compression presents the following advantages:

- **The tie-rod** (covered by the ceramic cylinders), assure the constant alignment of the cells; the only movement allowed is a vertical translation, that reduce to minimum gas losses due to bad positioning of the elements (especially after the stack assembling);

- **The cold compression system:** it's not "completely cold", the compression force from outside insulation is effectively applied through a ceramic piston that cross the insulation, and allows to reduce to minimum thermal losses;

- **The stack assembly is independent: S**ystem assembly is independent from stack assembly: this imply that the stack can be prepared in other location and be inserted in the system in a second time; this feature may results useful if there are necessity to substitute the stack for any reason, or modify their number;

- **Thin metallic interconnector:** metallic plate used are 1mm thin in the cell area surface: that assure a low ohm losses, but at the same time, the 3 mm thin border ribs and the contact to upper and lower plates under compression, assure an high resistance to mechanical deformation. Total weight of the single plate is 160 g;

- **Insulation as secondary element:** The insulation material applied around the stack is just to avoid thermal losses: it's not needed to care about cold air inlet due to a stack depression: as explained in previous points, the stack is closed, and the pressure inside and outside the insulation chamber is the same (as per Flame configuration).

- **Space between cell and metallic plate** are reserved to gas channels; considering thermal expansion, the channels have to be dimensioned to assure contact between cell surface and upper plate.

- No other assembling elements are needed;

- **Possible future improvements:**

- Change positioning of tie-rods;

- Study a better gas inlet (according to the space obtaining changing position of tie-rods as per previous point);

- Consider a common gas channel at cell outlet;

- 5. AfterBurner integration;

In this chapter will be analyzed a combustion model to be used to analyze gas burning at cell outlet; As introduced in cap. 3, the post combustion is needed to recover the chemical energy that are not been used in the cell conversion; In that case have been applied in the thermal model of the cell, an heating source due to high temperature gases presence;

In this case instead, the gas combustion are evaluated as part of the system, where gases coming from the cell are mixed and burned in a chamber;

Thermal heating and pollution creation are considered in the model;

- 5.1 geometry of the model;

The geometry considered in this case has the shape of the drawing on right:

In a ceramic cylinder are inserted an Inconell^{TM} alloy torch; exhaust gases coming from the cell are mixed and burned inside this cylinder to recover remaining chemical energy and warming up the fresh gas;

From this point of view is important to have control of burner outlet temperature and pollution generated by combustion (mainly referred to CO emission);
Here below the combustion system is drawn by CAD systems (the ceramic cylinder is shown as a section);

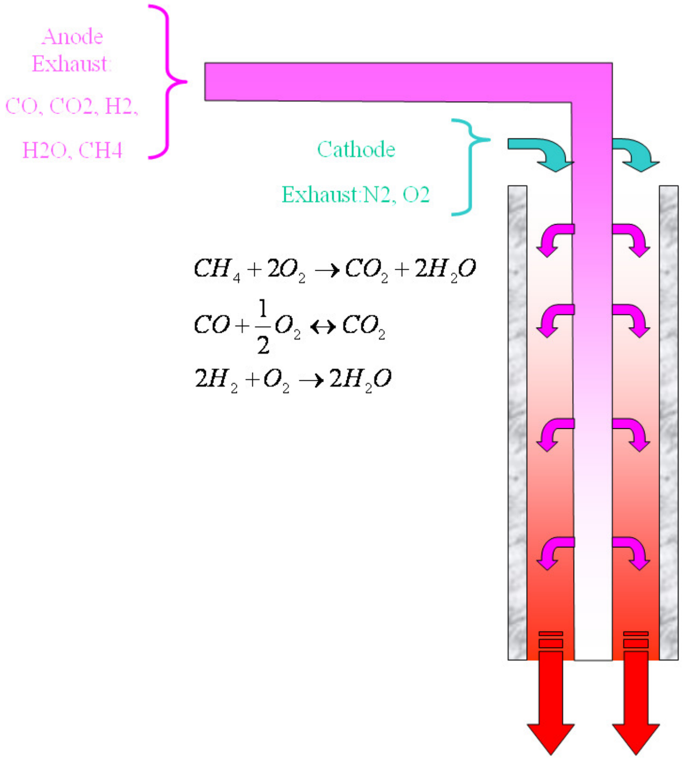

$$CH_4 + 2O_2 \rightarrow CO_2 + 2H_2O$$

$$CO + \frac{1}{2}O_2 \leftrightarrow CO_2$$

$$2H_2 + O_2 \rightarrow 2H_2O$$

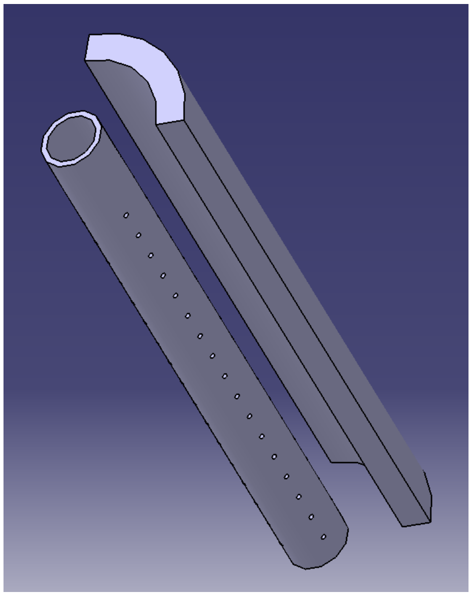

On this drawing are visible holes of 0.8 mm diameter used to allow the gas passing to the combustion chamber;

The combustor model is built as usual, defining the geometry used;
In this case the geometry presents a double symmetry, so just a quarter of the system are considered;

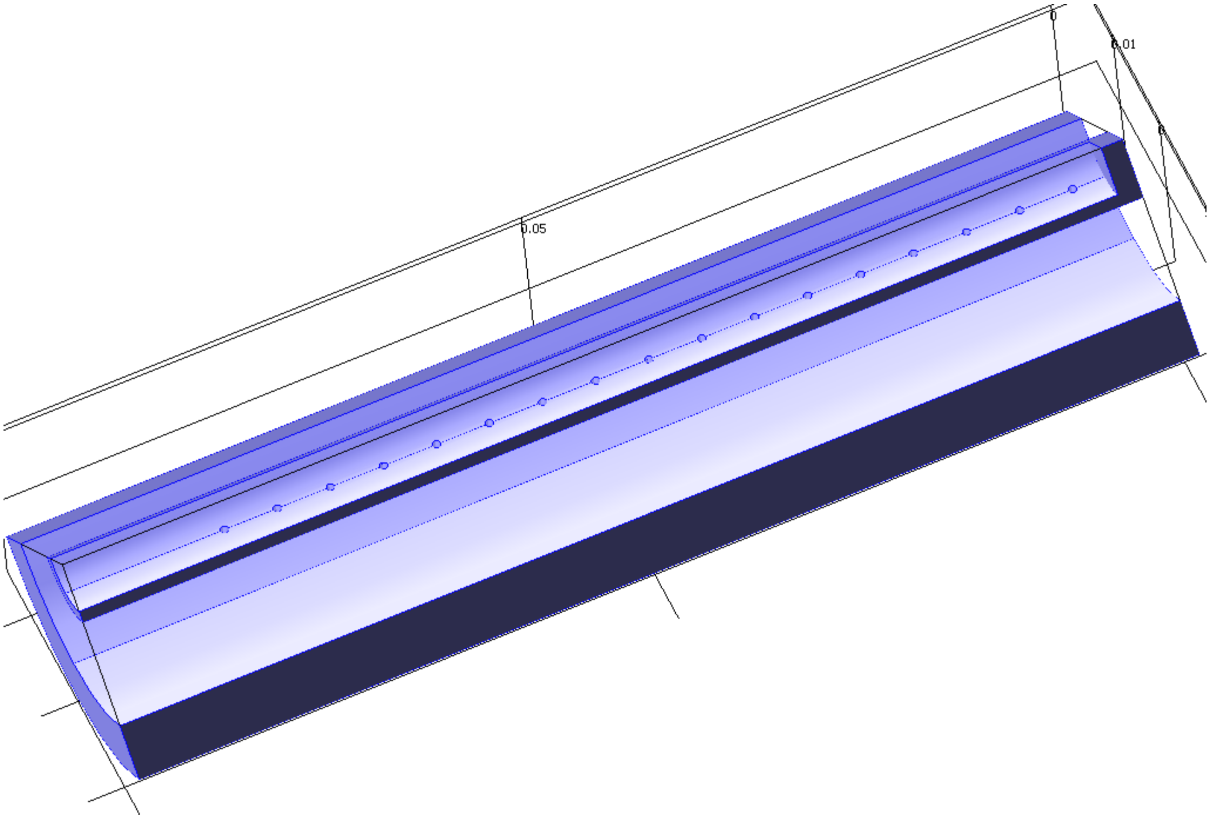
0
0.01
0
0.05

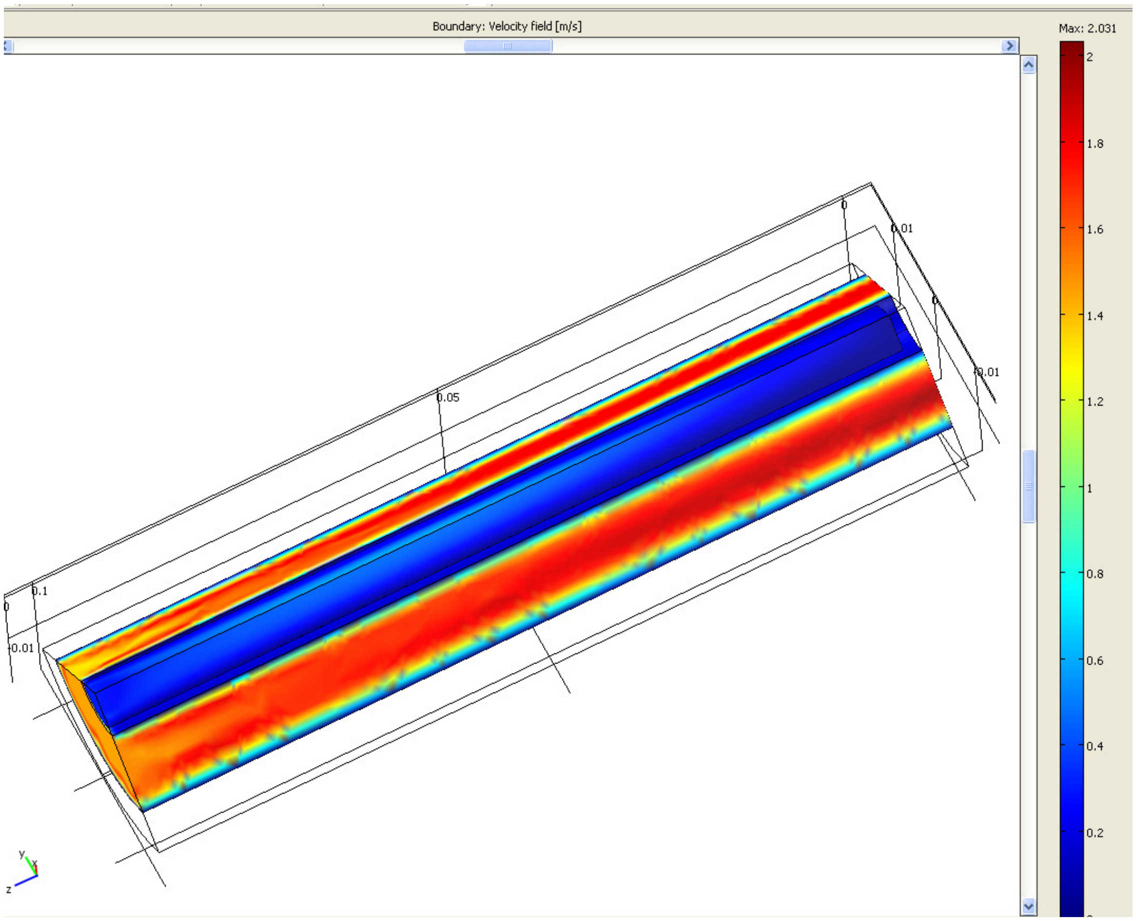
Boundary: Velocity field [m/s]
Max: 2.031
2
1.8
1.6
1.4
1.2
1
0.8
0.6
0.4
0.2
0
0.01
0
0.01
0.05
0
0.1
0.01
y
x
z

In this picture are shown the flow lines coloured according to flow speed; the blue lines are the fuel flow (at low speed): it’s possible to observe that the greater part of fuel are mixed at the beginning of conduct;

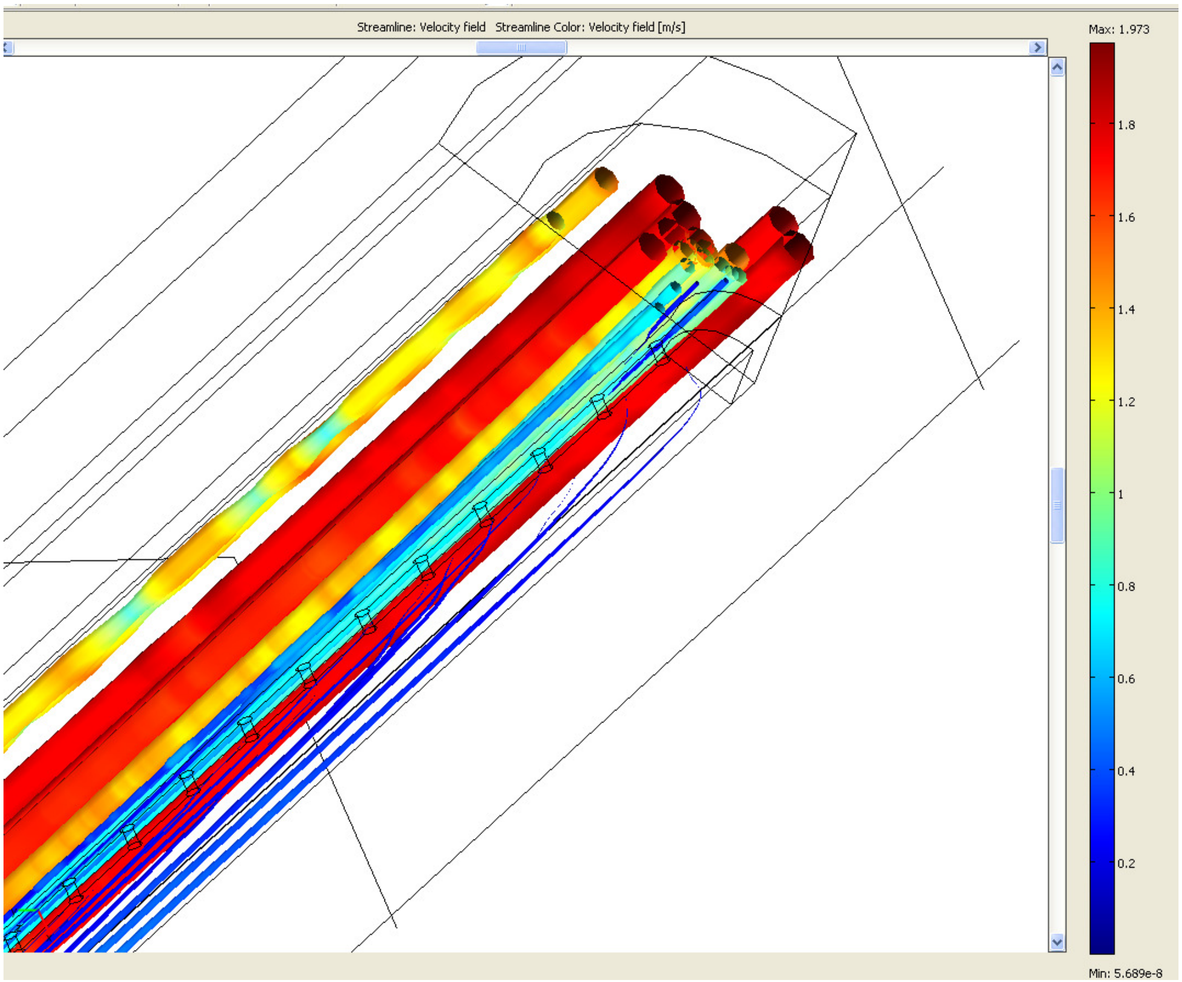

This model define fluid-dynamics behaviour inside the model;

5.2 chemical model;

The combustion model are been created on considerations reported below;

One of chemical reactions used in this model are methane combustion, where air and fuel pre-mixed mixture are hypothesized to generate the following species:

$$CH_4 + 2O_2 \rightarrow CO_2 + 2H_2O$$

Generically, the previous equation can be written as:

$$aA + bB + \ldots \rightarrow eE + fF + \ldots + \Delta h_R^0 ,$$

With a,b,c..etc as stoichiometric coefficient that refer to A,B,C species.

Moreover, the singular species E conservation equation can be written as molar form:

$$\frac{dN_E}{dt} = \dot{N}_{E,i} - \dot{N}_{E,e} + \dot{N}_{E,gen} = \dot{N}_{E,i} - \dot{N}_{E,e} + \dot{w}_E''' V$$

Where

V is volume of reaction zone;

$\dot{w}_E'''$ is production rate of species E per volume unit (assumed uniform in interested volume);

$\frac{dN_E}{dt}$ is the accumulation rates of reaction species E;

$\dot{N}_{E,gen}$ is molar production of species E;

$\dot{N}_{E,i}$ is molar inlet rate of species E;

$\dot{N}_{E,e}$ is molar exit rate of species E;

According these last consideration, the reaction considered at beginning become:

$$\frac{\left(\frac{d[O_2]}{dt}\right)}{-2} = \frac{\left(\frac{d[CH_4]}{dt}\right)}{-1} = \frac{\left(\frac{d[CO_2]}{dt}\right)}{1} = \frac{\left(\frac{d[H_2O]}{dt}\right)}{2} + \dot{w}'''$$

Of course in the previous equation, negative coefficient are assigned to reacting species and positive to products according their stoichiometric coefficient;

Same equation in molar form become:

$$\left\{\frac{1}{-a}\right\}\frac{d[A]}{dt} = \left\{\frac{1}{-b}\right\}\frac{d[B]}{dt} = \ldots = \left\{\frac{1}{e}\right\}\frac{d[E]}{dt} = \left\{\frac{1}{f}\right\}\frac{d[F]}{dt} = \dot{w}'''$$

With $\dot{w}'''$ is reaction rate per unit of volume which is the reaction rate of any species for witch the molar stoichiometric is unity.

However, reaction rate depends from species concentrations: reaction rate expression can be written for a generic reaction $aA + bB + \rightarrow eE$ as:

$\dot{w}_A''' = (-a)\dot{w}'''$

$\dot{w}_E''' = (e)\dot{w}'''$

$\dot{w}''' = k(T) \cdot [A]^{\alpha} \cdot [B]^{\beta}$, where α and β are respectively the reaction orders of species A and B, and overall order of reaction is α+β.

Because the equation $\dot{w}''' = k(T) \cdot [A]^{\alpha} \cdot [B]^{\beta}$ expressed in $\left[\frac{kmol}{m^3 \cdot \sec}\right]$, the k coefficient must have dimension of:

$$k = \frac{kmol}{m^{3(1-\alpha-\beta)} \cdot \sec}$$

Last equation shown as reaction rate increases with concentrations or increased mass reaction species (when α,β > 0);

Generally k is a temperature function given by Arrhenius law:

$$k = A \cdot T^n \cdot e^{\frac{-E}{RT}}$$

With:

E, activation energy
A, pre-exponential factor
T, temperature
n, empirical constant typically varying between 0 and 0.5;

pre-exponential factor A is related to collision number (see appendix of chapter 5 for details), while E is related to the molecular bound energy; Normally the values of these values is quite difficult to find, especially where are involved different kind of reactions. Typically the values are obtained by experimental data;

if uni-molecular reaction $A_2 \rightarrow 2A$ are considered inside a tube reactor, with constant velocity, it's possible to evaluate concentration of species A_2 inside it:

$$-\frac{d[A_2]}{dt} = k[A_2]$$

Using the simplified Arrhenius law $k = A \cdot e^{\frac{-E}{RT}}$, the same reaction can be written as:

$$-\frac{d(\ln[A_2])}{dt} = k = A \cdot e^{\frac{-E}{RT}}$$

Thus, for various temperature, are possible to determine the value of: $-\frac{d(\ln[A_2])}{dt}$;

moreover: $\ln\left\{-\frac{d(\ln[A_2])}{dt}\right\} = \ln\{k\}$

that means that the value $\ln\left\{-\frac{d(\ln[A_2])}{dt}\right\}$ is a line on plane *ln(k)*, *1/T,* with slope of $\frac{-E}{R}$ and A is the intercept of y axis, as per the pictures below:

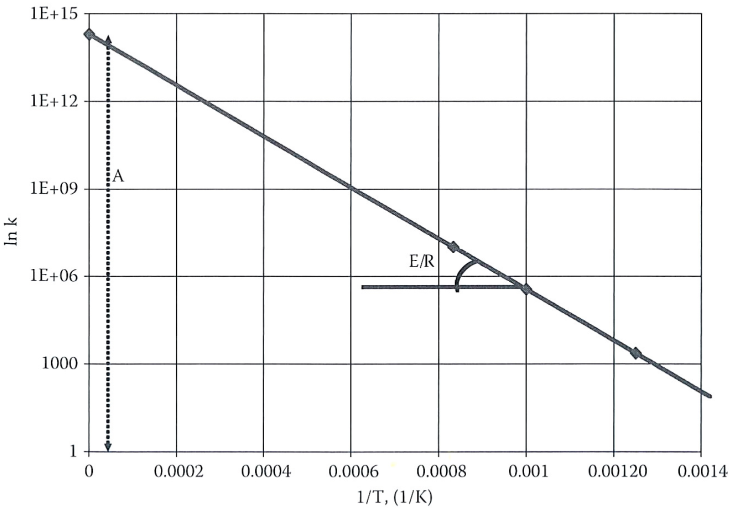

In the following lit are reported the kinetics constants for methane two steps oxidation used for combustion reactions and hydrogen oxidation:

$$CH_4 + \frac{3}{2}O_2 \rightarrow CO + 2H_2O$$

$$\overset{\bullet}{w}_{CH4}^{'''} = A_{CH_4} \cdot T^n \cdot [A]^a \cdot [B]^b \cdot e^{\left(\frac{-E}{RT}\right)}$$

With:

E = 202.6 $\frac{MJ}{kmol}$

A_{CH_4} = 2.8e9

a=-0.3

b=1.3

n=0.2

$$CO + \frac{1}{2}O_2 \rightarrow CO_2$$

$$\overset{\bullet}{w}_{CO}^{'''} = A_{CO} \cdot T^n \cdot [A]^a \cdot [B]^b \cdot [H_2O]^c \cdot e^{\left(\frac{-E}{RT}\right)}$$

With:

A_{CO} = 2.2387e12

E = 167.472 $\frac{MJ}{kmol}$

a = 0.5

b= 1.07

c= 0.4

n=0

$$H_2 + \frac{1}{2} O_2 \rightarrow H_2O$$

$$\overset{\bullet}{w}'''_{CO} = A_{CO} \cdot T^n \cdot [A]^a \cdot [B]^b \cdot [H_2O]^c \cdot e^{\left(\frac{-E}{RT}\right)}$$

$A_{CO} = 2.4547e11$

E = 171.659 $\frac{MJ}{kmol}$

a = 0.85

b= 1.42

c= -0.56

n=0.25

These parameters set velocity of reactions w_r1, w_r2 and w_r3 expressed in $\left[\frac{kmol}{m^3 \cdot \sec}\right]$, that are related to consumption or creation of each species involved as per stoichiometric coefficient ;

5.3 model description;

The model allows to include, concentration of species out coming from cell stack: mainly carbon oxide and dioxide, water, hydrogen, and air; these are imposed as inlet constants, in the circle:

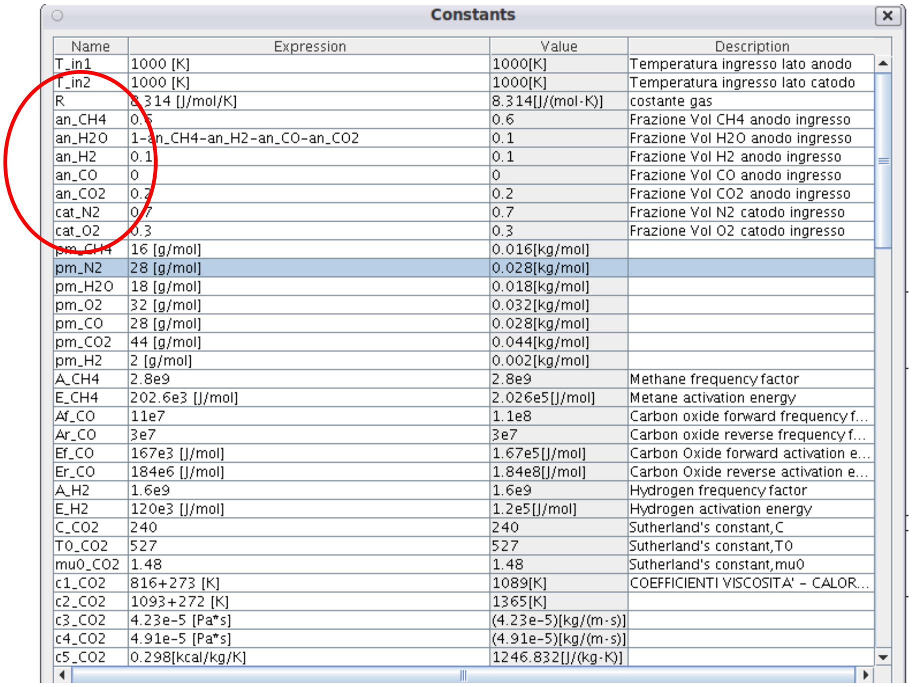

Constants

Name	Expression	Value	Description
T_in1	1000 [K]	1000[K]	Temperatura ingresso lato anodo
T_in2	1000 [K]	1000[K]	Temperatura ingresso lato catodo
R	8.314 [J/mol/K]	8.314[J/(mol·K)]	costante gas
an_CH4	0.6	0.6	Frazione Vol CH4 anodo ingresso
an_H2O	1-an_CH4-an_H2-an_CO-an_CO2	0.1	Frazione Vol H2O anodo ingresso
an_H2	0.1	0.1	Frazione Vol H2 anodo ingresso
an_CO	0	0	Frazione Vol CO anodo ingresso
an_CO2	0.2	0.2	Frazione Vol CO2 anodo ingresso
cat_N2	0.7	0.7	Frazione Vol N2 catodo ingresso
cat_O2	0.3	0.3	Frazione Vol O2 catodo ingresso
pm_CH4	16 [g/mol]	0.016[kg/mol]	
pm_N2	28 [g/mol]	0.028[kg/mol]	
pm_H2O	18 [g/mol]	0.018[kg/mol]	
pm_O2	32 [g/mol]	0.032[kg/mol]	
pm_CO	28 [g/mol]	0.028[kg/mol]	
pm_CO2	44 [g/mol]	0.044[kg/mol]	
pm_H2	2 [g/mol]	0.002[kg/mol]	
A_CH4	2.8e9	2.8e9	Methane frequency factor
E_CH4	202.6e3 [J/mol]	2.026e5[J/mol]	Metane activation energy
Af_CO	11e7	1.1e8	Carbon oxide forward frequency f...
Ar_CO	3e7	3e7	Carbon oxide reverse frequency f...
Ef_CO	167e3 [J/mol]	1.67e5[J/mol]	Carbon Oxide forward activation e...
Er_CO	184e6 [J/mol]	1.84e8[J/mol]	Carbon Oxide reverse activation e...
A_H2	1.6e9	1.6e9	Hydrogen frequency factor
E_H2	120e3 [J/mol]	1.2e5[J/mol]	Hydrogen activation energy
C_CO2	240	240	Sutherland's constant,C
T0_CO2	527	527	Sutherland's constant,T0
mu0_CO2	1.48	1.48	Sutherland's constant,mu0
c1_CO2	816+273 [K]	1089[K]	COEFFICIENTI VISCOSITA' - CALOR...
c2_CO2	1093+272 [K]	1365[K]	
c3_CO2	4.23e-5 [Pa*s]	(4.23e-5)[kg/(m·s)]	
c4_CO2	4.91e-5 [Pa*s]	(4.91e-5)[kg/(m·s)]	
c5_CO2	0.298[kcal/kg/K]	1246.832[J/(kg·K)]	

Setting the inlet molar fraction as boundary conditions, and solving Navier-Stokes in gas domain, concentration problem are solved and reaction rates consequently;

In these picture as shown an example of reactions occurring inside model 2D section that shown velocity of hydrogen and methane consumption;

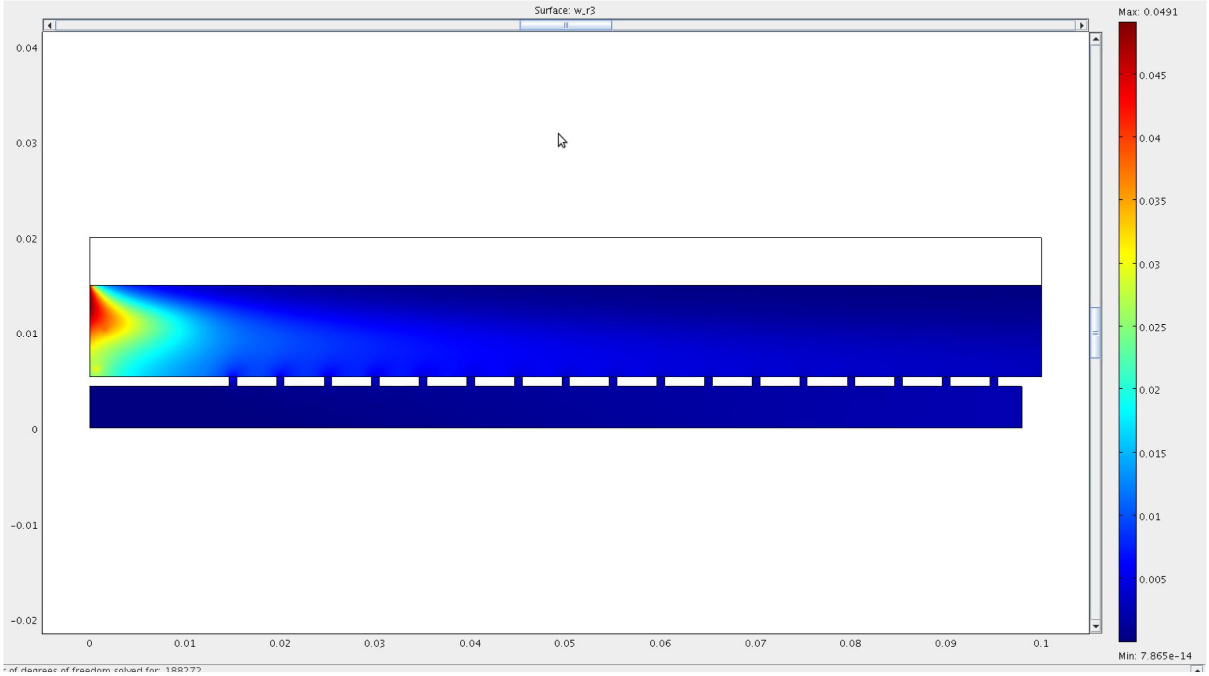

of degrees of freedom solved for: 188272

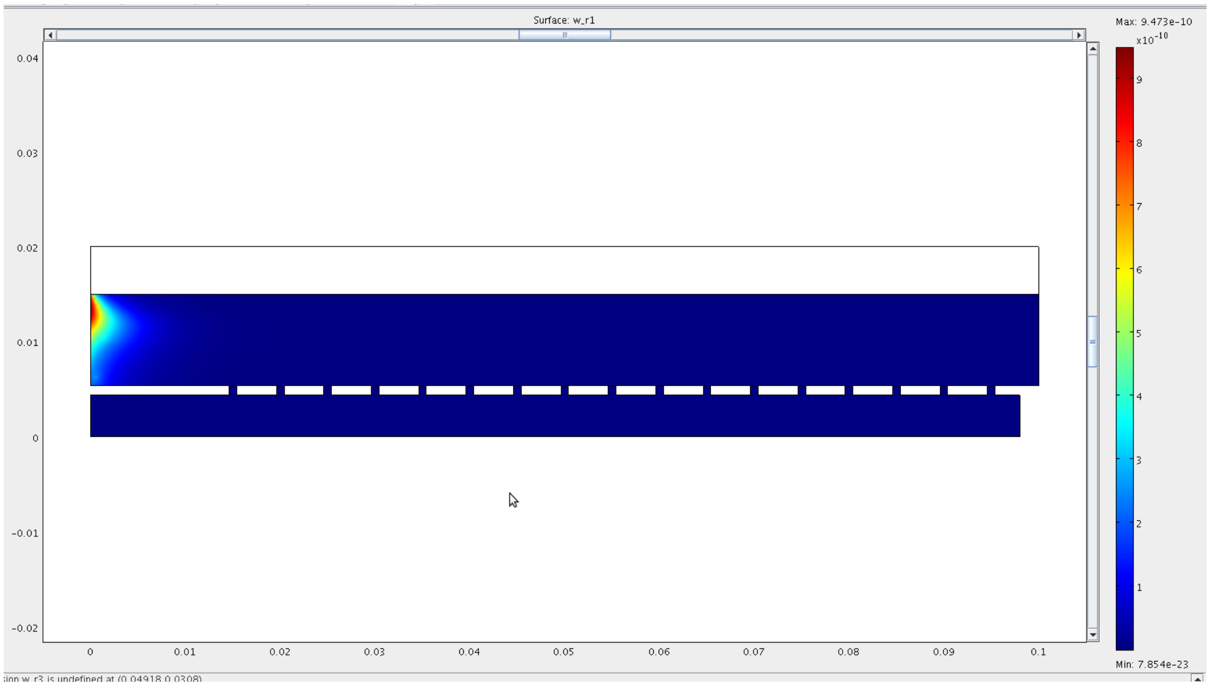

sion w_r3 is undefined at (0.04918,0.0308)

This means that starting from initial species concentration, the model is able to determine composition changing, as evidenced below:

Remaining hydrogen coming from cell is quickly consumed inside the burner :

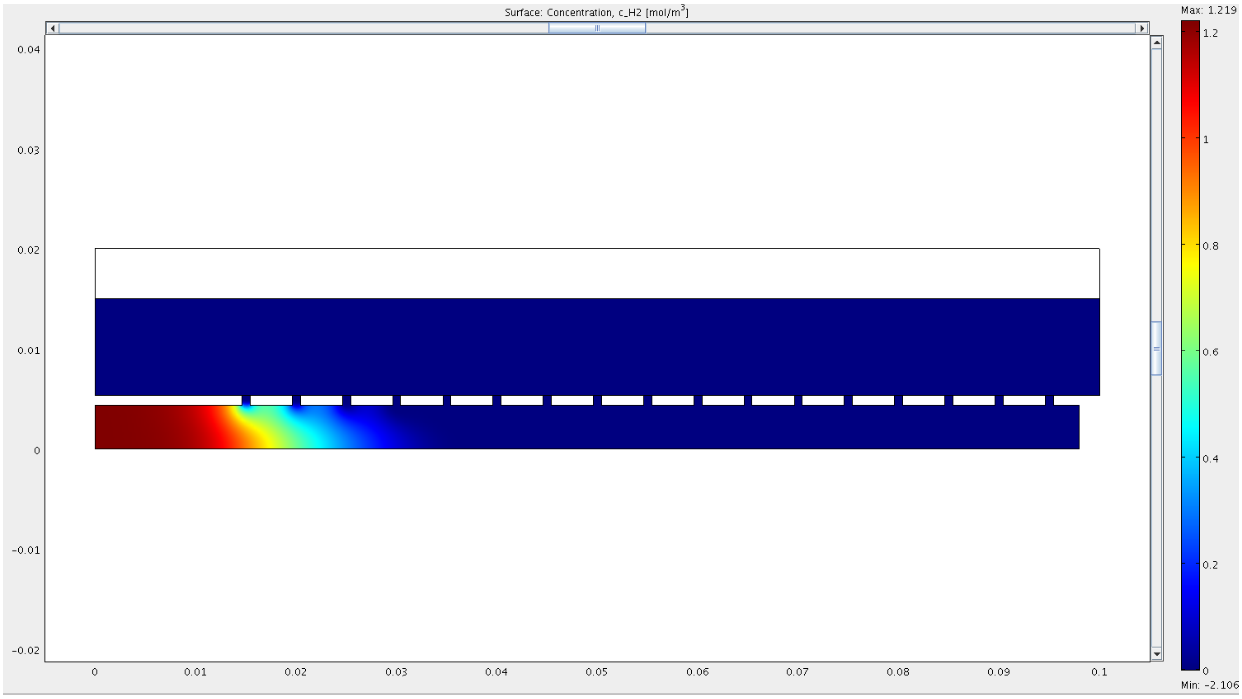

As is visible from the previous picture the hydrogen is consumed mainly in the anodic pipe (for these conditions of flow and initial concentration); in parallel with this, water increasing are visible on the model in the same point evidenced with yellow circle:

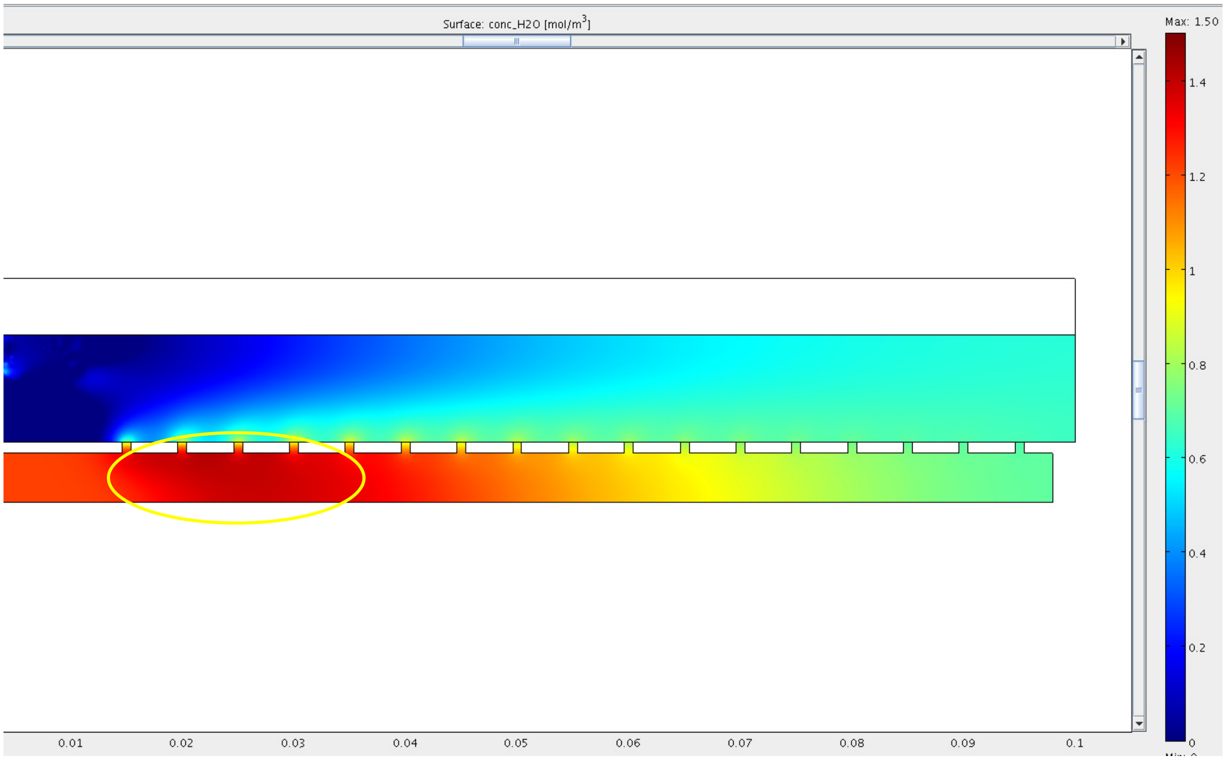

Together with hydrogen, also methane species are consumed:

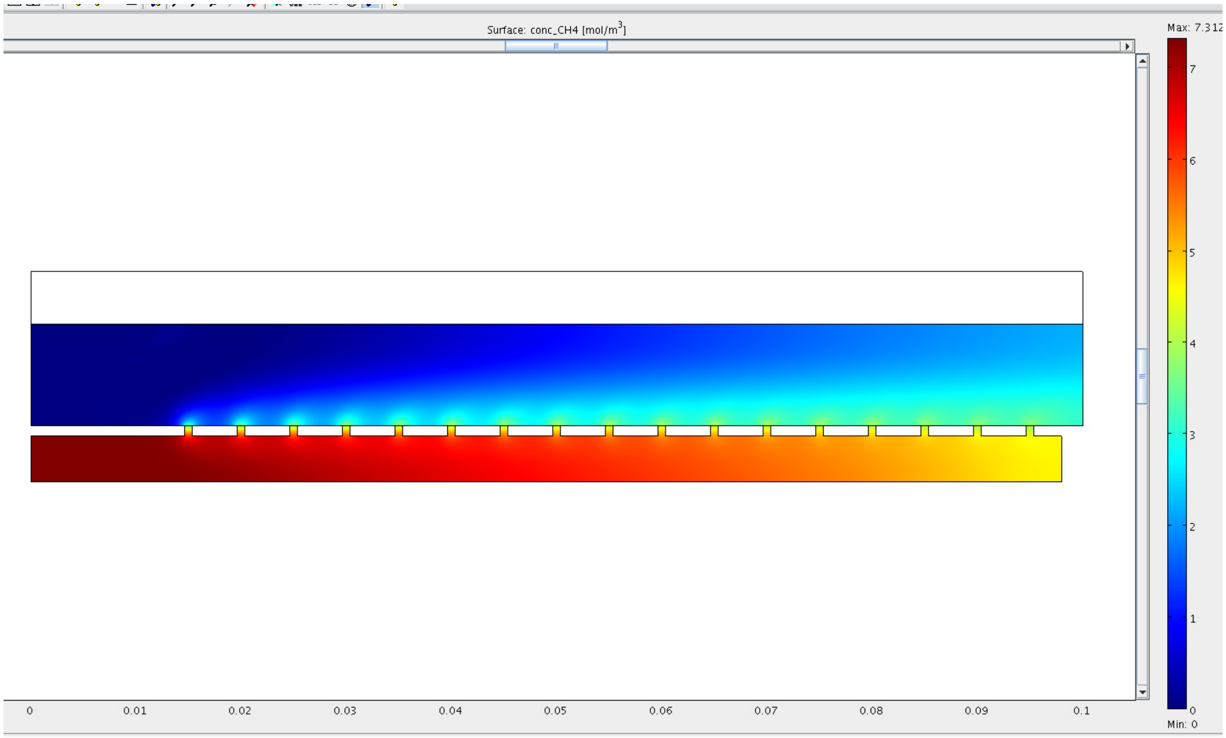

In parallel with this consumption are also produced carbon monoxide in very less quantity as shown in the values range:

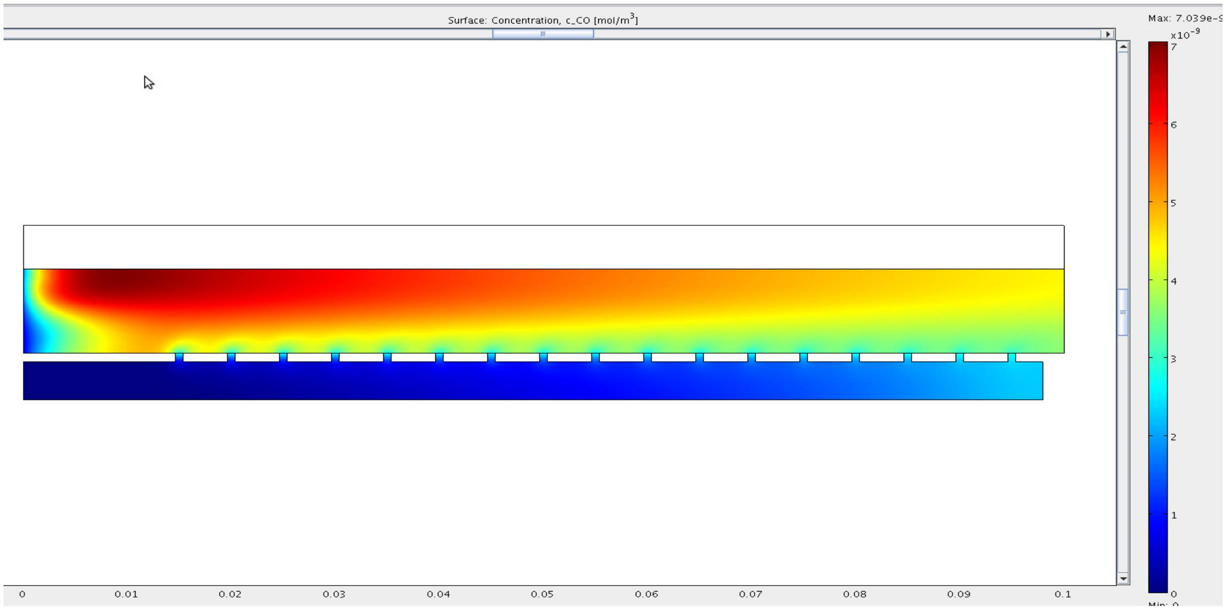

In parallel with species consumption there is an heat production; heat source are set inside flow as follow:

$$CH_4 + \frac{3}{2}O_2 \rightarrow CO + 2H_2O \qquad 324\frac{kJ}{mol}$$

$$CO + \frac{1}{2}O_2 \rightarrow CO_2 \quad 565\frac{kJ}{mol}$$

$$H_2 + \frac{1}{2}O_2 \rightarrow H_2O \quad 286\frac{kJ}{mol}$$

Heat source in the model [W/m^3]:

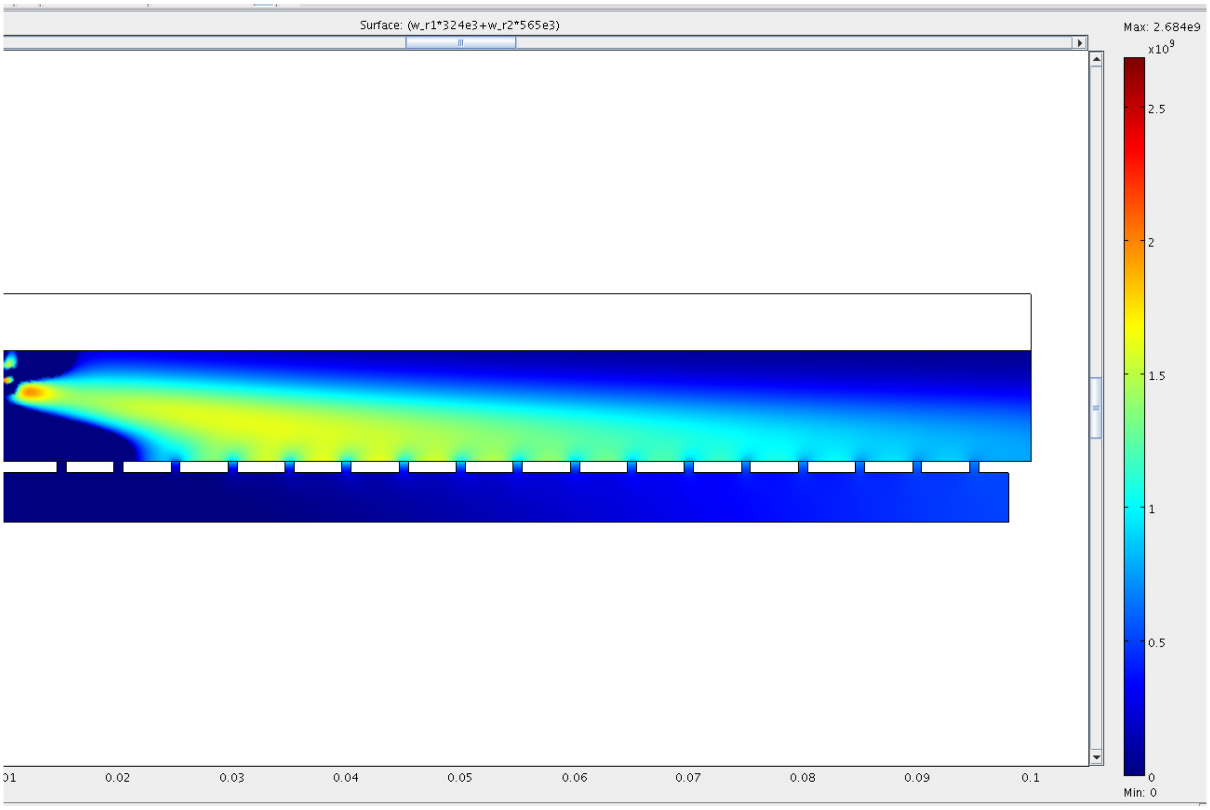

Consequently temperature are influenced by this:

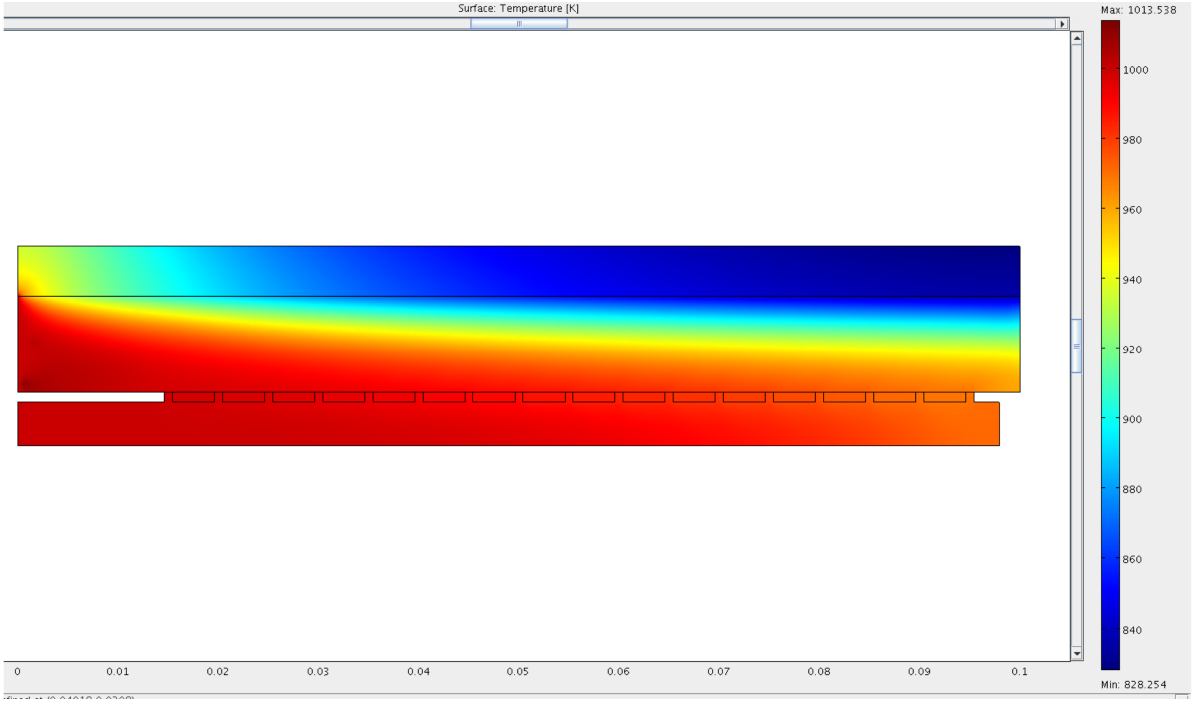

In this model are considered only the CO production reaction shown previously; One of the possible extension of the model will be to include many other pollution creation, standing to the following table: this in an important evaluation to allow to the model to evaluate condition of pollution creation and insert these information in the control system, avoiding these particular conditions;

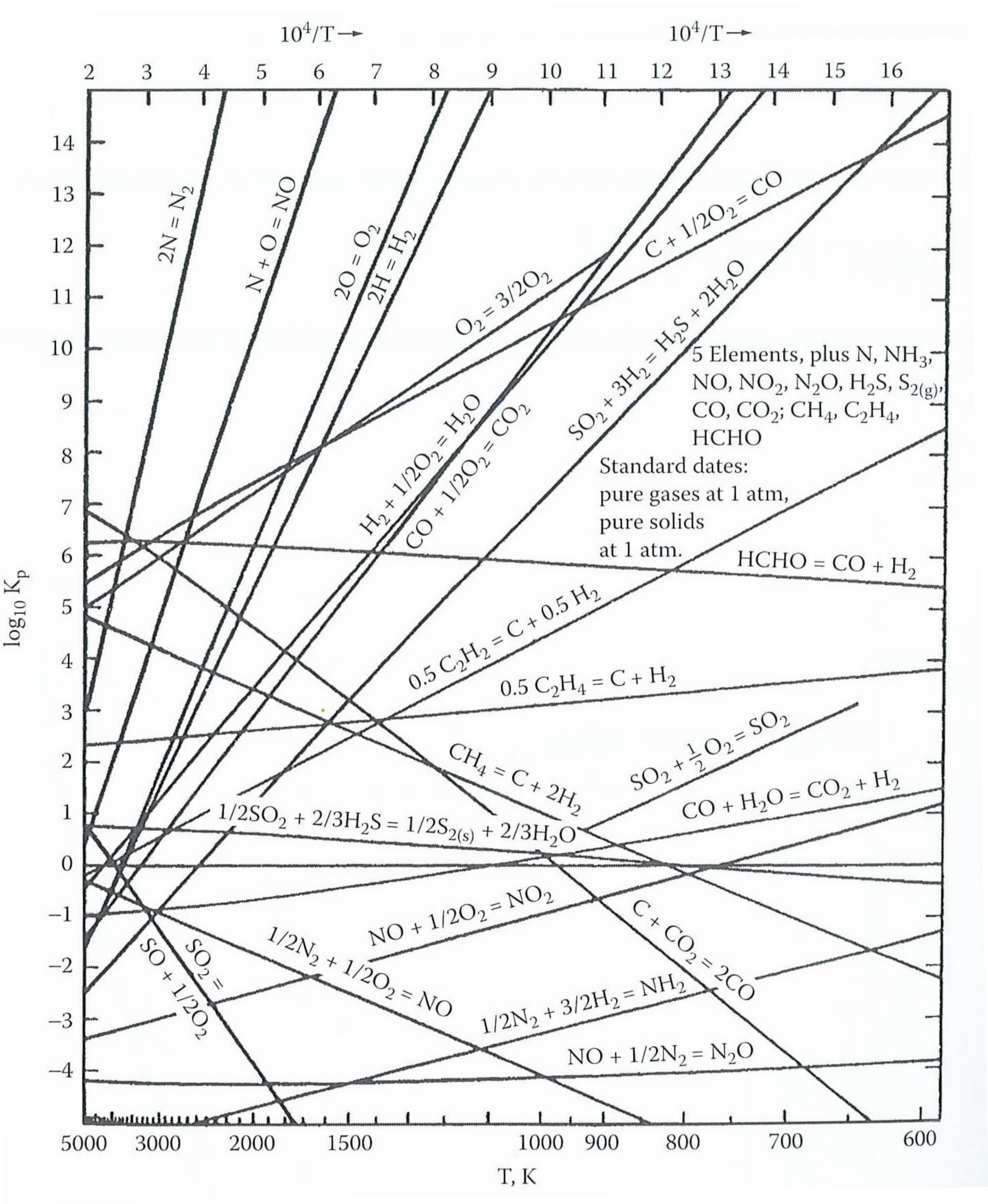

In the next table are reported some CO concentration values (in ppm) measured experimentally from post-combustor model (with same materials, dimensions and flowrate normally used in sofc systems);

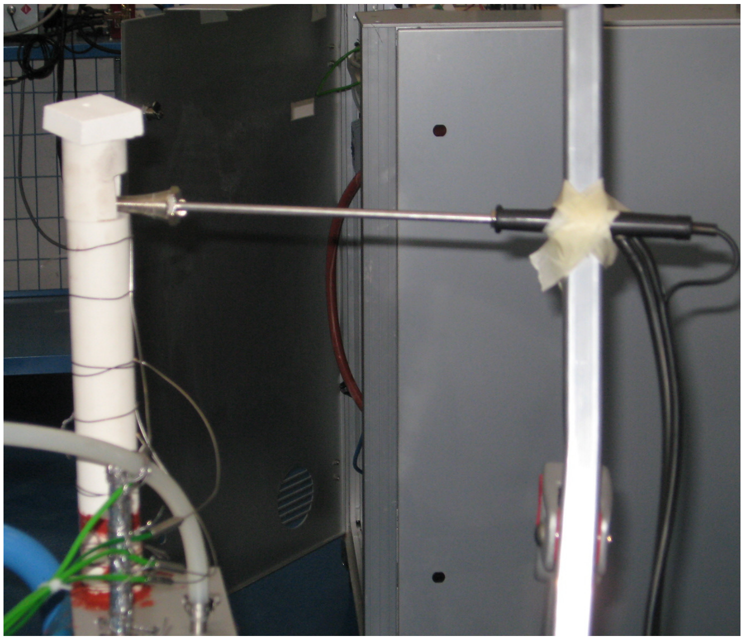


NAT GAS
R 0.0000
CO 00
CO2 -0>-
On/Off
Pump
Send
425

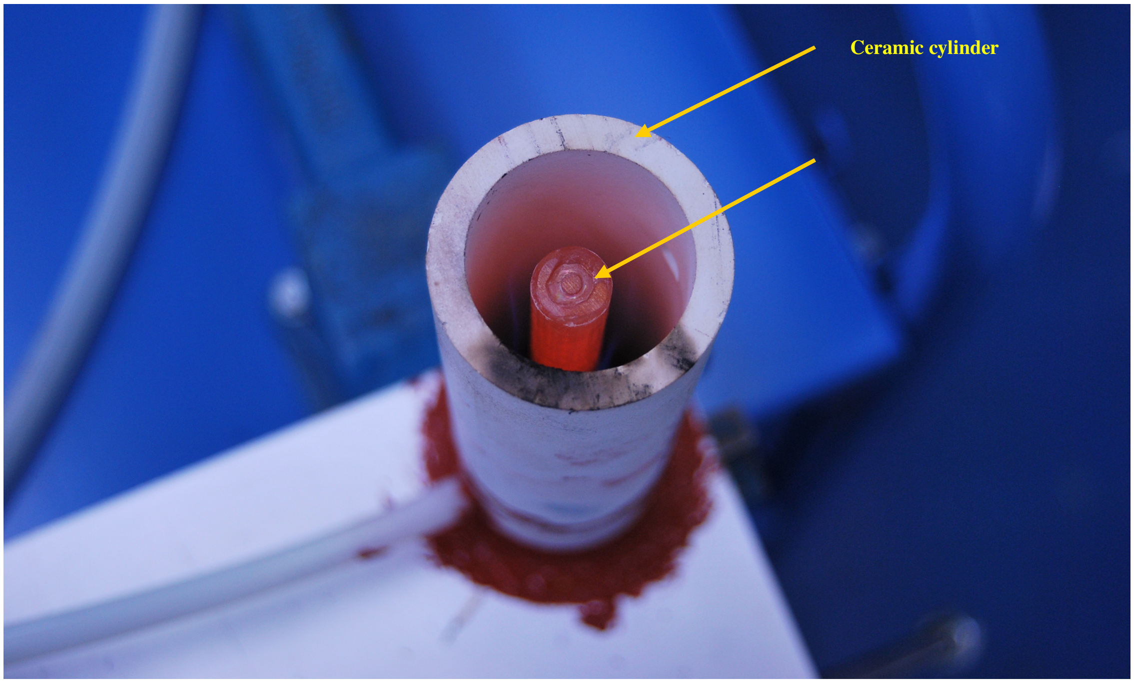
Ceramic cylinder

CO [ppm] measured		**Input gas power [kW]**														
		0,25	**0,5**	**0,8**	**1,0**	**1,3**	**1,6**	**1,9**	**2,1**	**2,4**	**2,7**	**2,9**	**3,2**	**3,5**	**3,8**	**4,0**
λ	**1,0**					54	78	92	88	88	60	37	37	19	6	9
	1,5			18	22	37	46	45	30	28	20	24	30	34	36	45
	2,0			13	11	14	18	25	29	33	48	60	73	80	121	128
	2,5		14	15	13	17	27	42	68	63	66	91	110	114	114	121
	3,0		15	19	21	28	41	60	69	81	39	71	79	76	87	87
	3,5		16	21	25	35	52	71	78	34	39	46	47			
	4,0		15	22	28	39	59	75								
	4,5		16	23	30	44	60									
	5,0		15	23	31	45										
	5,5		14	24	32											
	6,0			22	33											

The graph here reports values in previous table for different gas power input (equivalent to constant flow rate);
It’s possible to note, how there are an initial high CO presence due to lack of air;

If CO production are considered as “burning quality”, best burning conditions are noted for λ values between 1.5 and 2, then CO presence start to increase basically due to cooling down of the system, and high speed of gases that pass through the burner quickly, without time for a complete burning;

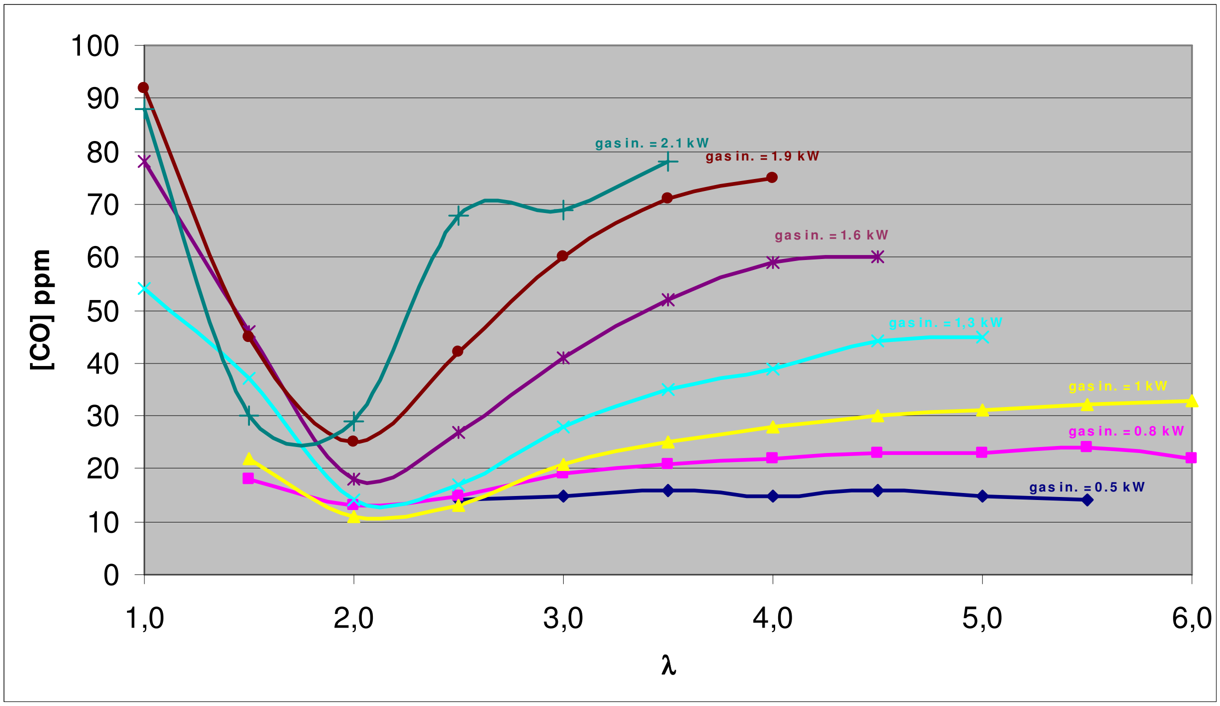

5.4 Results analysis;

Applying model results to experimental data (dot lines), can be evaluated the numeri model accuracies;

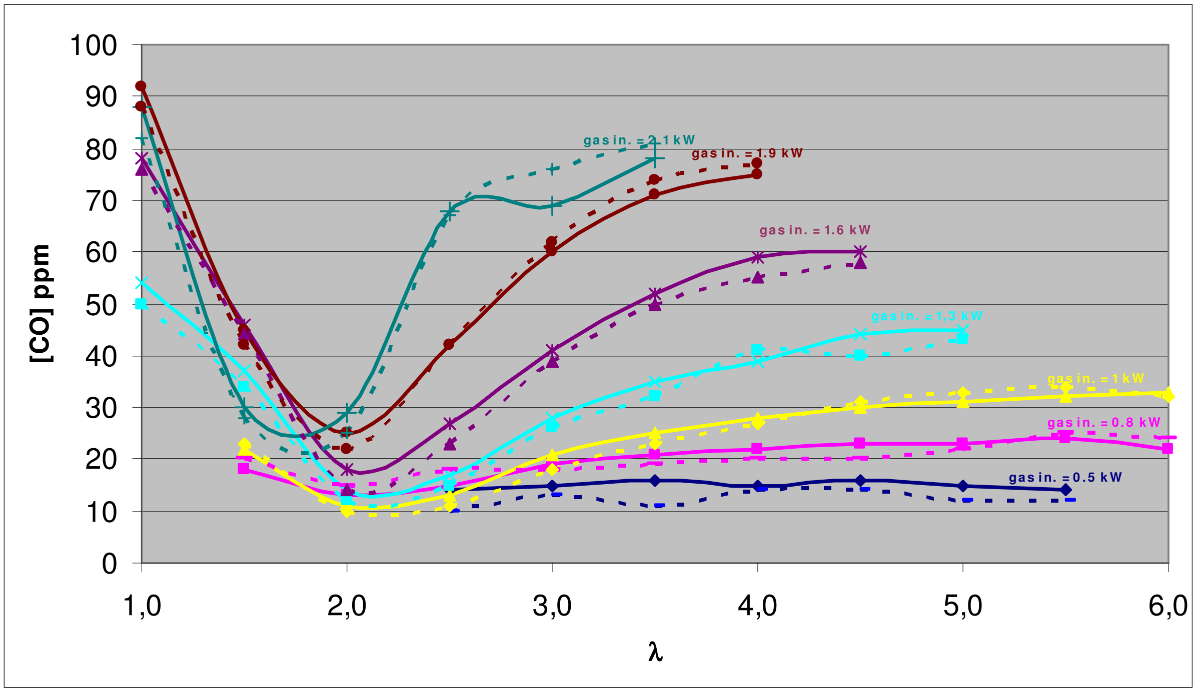

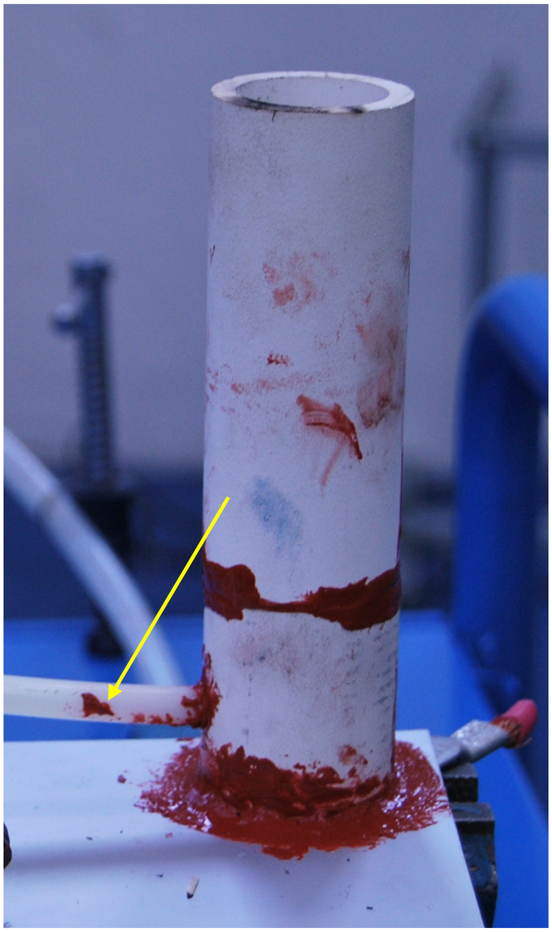

As is possible to observe, starting from power gas input of 2.1 kW, the model start to increase the error factor due to fluid-dynamic at cylinder inlet (realized orthogonal to cylinder axis to allow a easier experimental realization); This is cause of initial turbulence just after cylinder inlet that became evident increasing λ factor;

Appendix: Arrhenius law coefficient calculation;

Collision theory:

This theories assume that reacting molecules first collide, and hypothesizes that chemical reactions will occur only in this collision case;

Collision Number and mean free path;

Molecules contained in a matter travel at distance l_{mean}, before colliding with another molecule;
If a generic molecule A travel for a distance l_{mean} before collide with a second molecule B, then the distance travelled to collide with a third molecule C, will be 2* l_{mean} ;
Consequently it's possible to affirm that distance travelled after collision with n number of molecules will be n* l_{mean} ; the number of this n collisions per unit of time is *Collision Number*;

Average velocity of molecule A can be expressed as:

$$V_{avg} = \sqrt{\frac{8k_B T}{\pi \cdot m_A}}$$

Where:

- m_A, is the mass of molecule A;

- k_B, Boltzmann constant 1.38e-26 kJ/K/molecule;

If now is consider a cylinder of radius σ and length V_{avg} , and n' the number of molecule per unit volume, there are $n'\pi\sigma^2 V_{avg}$ molecule in the cylinder;

The number of collisions in the cylinder per unit of time is:

$$Z_{coll} = \sqrt{2} n' \pi \sigma^2 \sqrt{\frac{8k_B T}{\pi \cdot m_A}}$$

The $\sqrt{2}$ is a correction factor that consider the movement of other molecule (not of a single molecule A);

The time taken for a single collision is the inverse of previous equation, while the average distance travelled by the molecule during this time is called *mean free path* and is calculated by:

$$l_{mean} = \frac{V_{avg}}{\sqrt{2} n' \pi \sigma^2 V_{avg}} = \frac{1}{\sqrt{2} n' \pi \sigma^2}$$

Arrhenius law;

Considering the generic reaction form:

$$A + B \rightarrow products$$

The consumption rate of reagents may depend from:

(number of collision of A and B per unit of volume per time)*(probably of reaction occurring collision);

The probably of reaction depends from various factor such as bond energy ε and species concentrations;

Note that Z_{coll} represent the collision number within the same species A; if now are considered a system of molecules A and B, for the same considerations examinee before, the number of collision between species A and B can be written as:

$$Z_{AB} = \left(N_{avog} * [A]\right) * \left(N_{avog} * [B]\right) \pi \sigma_{AB}^2 \cdot V_{rAB}$$

Where:

- $V_{rAB} = \sqrt{\frac{8k_B T}{\pi \cdot \mu_A}}$
- $\sigma_{AB} = \frac{\sigma_A + \sigma_B}{2}$
- $\mu_{AB} = \frac{m_A \cdot m_B}{m_A + m_B}$

The term $\pi\sigma_{AB}^2$ denotes the cross-sectional area of collision, V_{rAB} the relative, but random, velocity between molecules A and B;

If every collision between A and B results in a consumption of reaction species, the number of consumed molecules of species A (and B) is Z_{AB}. In this case the number of moles consumed is:

$$\left| \dot{W}'''_{hypoth} \right| = \left| \frac{d[A]}{dt}_{hypoth} \right| = \frac{Z_{AB}}{N_{avog}} = \left(\pi \cdot \sigma_{AB}^2 \cdot V_{rAB} \cdot N_{avog}\right) \cdot [A] \cdot [B] = k_{hypoth} \cdot [A] \cdot [B]$$

Where:

$$k_{hypoth} = \pi \cdot \sigma_{AB}^2 \cdot V_{rAB} \cdot N_{avog}$$

This last equations suggests that in 1 cubic meter of volume, about 10^{34} collision per second will results, and the same number is valid for species consumption that correspond to a consumption rate of 10^8 kmol/m^3/sec.

Experiments for various reactive species involved in combustion chemistry, show the more realistic values from 10^{-3} to 10^{-8} kmol/m^3/sec at room temperature and about 10^3 at temperature around 2000 K;

This implies that not all collision results in a chemicals transformations of species, because some molecules collide with greater energy but not others;

From kinetic theory it's found that the fraction of collisions with energy higher than activation energy is given by:

$$F = \exp\left(-\frac{E}{RT}\right)$$

With:

E, activation energy;

Looking at consumed species A:

$$\left|\dot{W}_A'''\right| = \left|\frac{d[A]}{dt}\right| = \frac{Z_{AB}}{N_{avog}} \cdot e^{\frac{-E}{RT}} = k_{hypoth} \cdot e^{\frac{-E}{RT}} \cdot [A] \cdot [B]$$

Last equation requires a correction:

S is the orientation or steric factor: to produce CO2 molecule from CO and O starting atoms, the orientation factors S regards the contact side from “carbon side” or “oxygen side”;
CO2 molecule is O-C-O line molecule, so reaction is facilitated, if oxygen atom collide the CO molecule from carbon side;

$$\left|\dot{W}_A'''\right| = S \cdot k \cdot [A] \cdot [B]$$

Where:

$$k = S \cdot k_{hypoth} \cdot e^{\frac{-E}{RT}} = A \cdot e^{\frac{-E}{RT}}$$

Where A is called *preexponential factor*; the term $e^{\frac{-E}{RT}}$ is the probability that an energetic collision will lead to reaction;

$$A = S \cdot \pi \cdot \sigma_{AB}^2 \cdot V_{rAB} \cdot N_{avog}$$

Where $V_{rAB} \propto T^{\frac{1}{2}}$ and $A \propto T^{\frac{1}{2}} e^{\frac{-E}{RT}}$; the law relating k to temperature is Arrhenius law, generically written as:

$$k = A \cdot T^n \cdot e^{\frac{-E}{RT}}$$

Conclusions

In this work a three-dimensional numerical code for the numerical simulation of a disk-shape anode-supported SOFC, currently produced by InDec B.V, has been developed. Hydrogen and syngas have been used as fuels;

To define the set of the mathematical equations describing the electrochemical and thermo-physical phenomena occurring within the SOFC, a deeply study of literature mathematical models has been provided. In particular, the most used models describing the fundamental processes occurring in the fuel cell individual components has been analyzed and discussed. The resulting mathematical model completely describes transport and electrochemical processes within the fuel cell, also using the conservation of momentum to investigate the SOFC feeding. The defined mathematical model carried out is based on a local balance approach, i.e. the differential form is used in its formulation.

To solve the sets of partial differential equations derived from the SOFC mathematical modelling, the finite element method (FEM) was used. The commercial mathematical software COMSOL Multiphysics® was used to perform the finite element analysis. Even if it allows a complete approach to the numerical modelling of an engineering problem, it is really powerful only for 1D and 2D models as well as 3D models with few degrees of freedom. As a comprehensive analysis of solid oxide fuel cells phenomena requires a multidisciplinary approach (involving chemical reactions, electrical and ionic conduction, and heat transfer) and the computational domain was three-dimensional, many degrees of freedom were necessary. Accordingly, a computer resources management procedure has been setup. It consists of an iterative procedure to reach the solution convergence, called “frozen fields”.

Numerical simulations were performed first to validate the model through experimental data provided by University of Perugia. Main results in this phase can be summarized as:

- the best performing species diffusion and current exchange formulations have been chosen, adopting Fick extended model and Costamagna et al. approach for the exchange current models;

- the pre-exponential constants $A\gamma$ and $C\gamma$ in the anodic and cathodic exchange current and the diffusion parameters by means of the porous microstructure characteristics have been calibrated, by varying them within literature values;

- the results which where obtained with numerical code are mostly coincident till 0.6 volt, showing a total current error everywhere lower than 0.6A. For lower voltage, the code predictive capability decrease for both numerical procedure and experimental data errors.

To establish the range of validity and the accuracy of the code, a hard and important benchmark test was then performed. In fact, the numerical code was subsequently tested versus experimental data obtained varying both fuel flow rate and utilisation coefficient, and by using hydrogen and syngas as fuels. For both the feedings, the agreement between numerical and experimental data was excellent in most cases. Little differences can be observed at high current densities, where the extreme SOFC operation conditions make experimental data less consistent. The percentage errors between numerical and experimental is everywhere within 5%, thus demonstrating a wide range of validity of the numerical code.

Once validated the model, some aspects occurring during cell operation such as the flow field, species concentration, current density and temperature distribution have been pointed out. In particular, some effect affecting SOFC performance were recognized and described. The most important results of the anode-supported SOFC model, using hydrogen or syngas as fuel, are:

- the presence of the ribs strongly affects the gas feeding, producing preferential flow directions;

- the reacting species concentration is lower underneath the ribs, because of the cross-plane and in-plane diffusion effects. Thus under the ribs the produced current is smaller than elsewhere;

- the current density is not uniform in the cell plane, being it affected by reactants distributions at TPB and by the electrolyte resistance which, in turn, is dependent on the cell temperature.

- the fuel cell does not work at uniform temperature, i.e. the furnace temperature. The temperature range is appreciatively of 25°C and the highest temperature is located at the cell outlet, where afterburning reactions occur;

- water shift reaction entirely occurs within the fuel channel. The CO conversion in H_2 is positive elsewhere except at the cell outlet, where the temperature increase inverts the reaction direction;

- in syngas fed SOFC model, the H_2 and CO simultaneous oxidation model is necessary to correctly predict fuel cell behaviour. The parallel H_2 and CO electrochemical sub-model provides a CO contribution of 12.5% on current basis, in all the investigated operating condition. Unfortunately, the lack of experimental data and literature reports about simultaneous oxidation of CO and H_2, prevents a rigorous validation of this result.

The same model (considered in two dimension to save calculation resources) has been used to analyze a SOFC cell inserted in a complete system, paying particular attention to fuel reforming which have been realized using a not stationary and mono-dimension approach;
This model represent a useful instrument to analyze feasibility of SOFC fuel systems fed by different gas types; From this point of view, most significantly results have been obtained evaluation of system fed with poor gases.
Plant that uses gas from garbage, as shown, allows good general performances, even if electric efficiency are reduced of 6% in first case and 16% in the second, if compared with methane system;
However firs principle efficiency are less decreased using this kind of systems; this reductions of global performance consequently have effects on investment costs;

The last part of the present thesis is focused other aspect not analyzed at beginning but anyway important to realization of SOFC system; in particular have been analyzed issues related stack closing: have been possible to observe how is important closing system criteria and material used to realize the system. Thermal deformation and operation repeatability are important too, to improve quality of components and time needed to realize them; Investigation in this direction are strongly required to improve stack functioning and usability at all working condition;

Another aspect that have been analyzed is the exhaust combustion optimization; scope of most SOFC system is to realize something able to be integrated in commercial power generation systems: this scope can not preclude consideration about pollution emission; in particular, a model of post-burner have been developed and tested with methane combustion;

These last two analysis have been developed using the same criteria of first part: define a mathematical problem, assign it to a geometry and solve it using FEM method;

References

[1] Bove, R. and Ubertini, S., 2006, Modeling Solid Oxide Fuel Cell Operation: Approaches, Techniques and Results. Journal of Power Sources, accepted for publication.

[2] Yakabe H., Ogiwara T., Hishinuma M. and Yasuda I., 2001. 3-D model calculation for planar SOFC. Journal of Power Sources, Volume 102, Issues 1-2, pp 144-154.

[3] Perry et al. (1997). Perry's Chemical Engineers' Handbook, 7th ed. McGraw_Hill.

[4] B. Todd, J.B. Young, Thermodinamic and transport properties of gases for use in solid oxide fuel cell modelling, Journal of Power Surces 110 (2002) 186-200.

[5] P. Costamagna, K. Honegger, Modeling of Solid Oxide Heat Exchanger Integrated Stacks and Simulation at High Fuel Utilization, Journal of Electrochem. 145 (1998) 3995-4006.

[6] J.R. Ferguson et al., Journal of Power Surces 58 (1996) 109-122.

[7] T.Yamamura et al., in Solid Oxide Fuel Cell IV, M.Dokiya and al., PV 95-1, p.741, the Electrochemical Society Proceedings Series, Pennington, NJ (1995).

[8] E.Achenbach, Journal of Power Surces 49 (1994) 333.

[9] M.M.A. Khaleel, Z. Lin, P. Singh,W. Surdoval, D. Collin, A finite element analysis modeling tool for solid oxide fuel cell development: coupled electrochemistry, thermal and flow analysis in MARC, J. Power Sources 130 (2004) 136–148.

[10] K.J. Daun et al,. Radiation heat transfer in planar SOFC electrolytes , Journal of Power Sources 157 (2006) 302–310

[11] A.F. Mills, Basic Heat and Mass Transfer, IRWIN, Irwin Heat Transfer Series, 1995.

[12] R. Suwanwarangkul et al., Performance comparison of Fick's, dusty-gas and Stefan–Maxwell models to predict the concentration overpotential of a SOFC anode Journal of Power Sources 122 (2003) 9–18

[13] G. Dotelli, C.M.Mari, Modeling and simulation of the mechanical properties of YSZ/Al2O3 composites: a preliminary study, Solid State Ionics 148 (2002) 527–531.

[14] W. Lehnert, J. Meusinger, F. Thom, Modeling of gas transport phenomena in SOFC anodes, J. Power Sources 87 (2000) 57–63.

[15] B.A. Habeman, J.B. Young, Three-dimensional simulation of chemically reacting gas flows in the porous support structure of an integrated-planar solid oxide fuel cell, Int. Heat Mass Transfer 47 (2004) 3617–3629.

[16] S. Campanari, P. Iora, Comparison of finite volume SOFC models for the simulation of a planar cell geometry, Fuel Cells (1) (2005).

[17] L. Petruzzi, S. Cocchi, F. Fineschi, A global thermo-electrochemical model for SOFC systems design and engineering, Journal of Power Sources 118 (2003) 96–107.

[18] Huayang Zhu, Robert J. Kee, A general mathematical model for analyzing the performance of fuel-cell membrane-electrode assemblies, Journal of Power Sources 117 (2003) 61–74.

[19] A.S. Loselevich, A.A. Kornyshev, Fuel Cells 1 (2001) 40.

[20] T. Setoguchi, K. Okamoto, K. Eguchi, H. Arai, J. Electrochem. Soc. 139 (1992) 2875.

[21] Y. Jiang, A.V. Virkar, J. Electrochem. Soc. 150 (2003) A942.

[22] Y. Matzusaki, M. Hishinuma, I.Yasuda, in: S.C. Singhal, M. Dokiya (Eds.), proceedings of Solid Oxide Fuel Cell VI, PV 99-19, The Electrochemical Society Proceedings Series, Pennington, NJ, 1999, p. 560.

[23] Ronchetti M., Iacobazzi A., Celle a combustibile - stato di sviluppo e prospettive della tecnologia, (2002)

[24] ENEA, Unità di Agenzia per lo Sviluppo Sostenibile, RAPPORTO ENERGIA E AMBIENTE 2005(Gennaio 2006)

[25] Piano nazionale per la riduzione delle emissioni di gas responsabili dell'effetto serra - 2003-2010 MINISTERO DELL'AMBIENTE E TUTELA DEL TERRITORIO MINISTERO DELL'ECONOMIA E FINANZE

[26] Documento di consultazione del 4 aprile 2002 ,Proposte per l'attuazione dei Decreti ministeriali del 24 aprile 2001 per la promozione dell'efficienza energetica negli usi finali.

[27] Subash,C. Singhal, K. Kendall, High temperature solide oxide fuel cell, Fundamental,Design and applications, Elsevier.

[28] J.R. Ferguson, J.M. Fiard, R. Herbin, Three-dimensional numerical simulation for various geometries of solid oxide fuel cells, J. Power Sour. 58 (1996) 109–122.

[29] S.Campanari, P.Iora ,Definition and sensitivity analysis of a finite volume SOFC model for tubular cell geometry, Journal of Power Sources 132 (2004) 113–126.

[30] Chan S.H., Khor K.A., Xia Z.T., A complete polarization model of a solid oxide fuel cell and its sensitivity to the change of component thickness, Journal of Power Sources 93, (2001).

[31] Ugur Pasaogullari and Chao-Yang Wang, Computational fluid dynamics modelling of solid oxide fuel cells, Electrochemical Engine Center, and Department of Mechanical and Nuclear Engineering, The Pennsylvania State University University Park, PA 16802, USA.

[32] M.A. Khaleel, Z. Lina, P. Singh , W. Surdoval , D. Collin, A finite element analysis modeling tool for solid oxide fuel cell development: coupled electrochemistry, thermal and flow analysis in MARC®,Journal of Power Sources 130 (2004) 136–148.

[33] J.J. Hwang, C.K. Chen, D.Y. Lai, Computational analysis of species transport and electrochemical characteristics of a MOLB-type SOFC, Journal of Power Sources 140 (2005) 235–242.

[34] Mads Pagh Nielsen and Søren Knudsen Kær ,Aalborg University,Institute of Energy Technology, Denmark, MODELING A PEM FUEL CELL NATURAL GAS REFORMER.

[35] A. Mary Sukeshini, Bahman Habibzadeh,, Benjamin P. Becker,b Chad A. Stoltz, Bryan W. Eichhorn, and Gregory S. Jackson, Electrochemical Oxidation of H2, CO, and CO/H2 Mixtureson Patterned Ni Anodes on YSZ Electrolytes, Journal of The Electrochemical Society, 153 _4_ A705-A715 _2006_.

[36] A.K.Avci, D.L.Trimm, Z.Ilsen Onsan, Heterogeneus reactor modelling for simulation of catalytic oxidation and steam reforming of methane, Chemical Engineering Science 2001.

[37] D.L.Hoang, S.H. Chan, Modelling of a catalytic autothermal methane reformer for fuel cell applications, Applied catlysis, 2004.

[38] P. Aguiar, C.S. Adjiman, N.P. Brandon, Anode-supported intermediate temperature direct internal reforming solide oxide fuel cell. I: model-based steady-state performance,Journal of power sources, 138,2004.

[39] B.Todd, J.B. Young, Thermodynamic and transport properties of gases for use in solide oxide fuel cell modelling, Journal of power sorces 110,2002,

[40] B.A. Haberman , J.B. Young, Three-dimensional simulation of chemically reacting gas flows in the porous support structure of an integrated planar solid oxide fuel cell, International Journal of Heat and Mass Transfer 47 (2004).

[41] S. Campanari, Thermodynamic model and parametric analysis of a tubular SOFC module, Maggio 2000.

[42] E.Achenbach, Three-dimensional and time-dependant simulation of a planar solid oxide fuel cell stack, Aprile 1994.

[43] R. Herbin,J. Fiard,J. Ferguson, Three-dimensional numerical simulation of the temperature, potential and concentration distributions of a unit cell for various geometries of SOFC.

[44] M. Bernier,J Ferguson, R. Herbin, A3-dimensional planar SOFC stack model.

[45] Polarization effects in intermediate temperature, anode supported Solide Oxide Fuel Cell, Journal of Electrochemical Society 146,1999.

[46] T.Ackman, L.G.J de Haart, W.Lehnert, and D. Stolten, Modelling of mass and heat transport in planar substrate type sofc's, Journal of electrochemical society 150 2003.

[47] R. Suwanwarangkul a, E. Croiset a, E. Entchev b, S. Charojrochkul c, M.D. Pritzker a, M.W. Fowler a, P.L. Douglas a, S. Chewathanakup c, H. Mahaudom, Experimental and modeling study of solid oxide fuel cell operating with syngas fuel, Journal of Power Sources 161 (2006) 308–322.

[48] Dott. Ing. F. Martino ,Dott. M. Zagaroli ,Dott. Ing. C. Riva , Nuove esperienze industriali di valorizzazione energetica dei rifiuti urbani .Il caso della gassificazione.

[49] J.J. Hwang, C.K. Chen, D.Y. Lai, Computational analysis of species transport and electrochemical characteristics of a MOLB-type SOFC, Journal of Power Sources 140 (2005) 235–242.

[50] Institut fur Enrgieverfahrenstechnik, International Energy Agency, Annex II Modelling and evaluation of advanced SOFC.